

NUMERICAL SIMULATION OF INVISCID WAVE-CURRENT
INTERACTION WITH AN FPSO

A Dissertation

by

SANG-YUN BAE

Submitted to the Office of Graduate Studies of
Texas A&M University
in partial fulfillment of the requirements for the degree of

DOCTOR OF PHILOSOPHY

May 2008

Major Subject: Ocean Engineering

NUMERICAL SIMULATION OF INVISCID WAVE-CURRENT
INTERACTION WITH AN FPSO

A Dissertation

by

SANG-YUN BAE

Submitted to the Office of Graduate Studies of
Texas A&M University
in partial fulfillment of the requirements for the degree of

DOCTOR OF PHILOSOPHY

Approved by:

Co-Chairs of Committee,	Richard Mercier
	Moo H. Kim
Committee Members,	Jun Zhang
	Ping Chang
Head of Department,	David V. Rosowsky

May 2008

Major Subject: Ocean Engineering

ABSTRACT

Numerical Simulation of Inviscid Wave-current Interaction
with an FPSO. (May 2008)

Sang-yun Bae, B.S.; M.S., Inha University, Korea

Co-Chairs of Advisory Committee: Dr. Richard Mercier
Dr. Moo H. Kim

This study investigated Floating Production Storage and Offloading (FPSO) responses under wave and current interactions. A higher order boundary element method (HOBEM) was adopted to probe the behavior of an FPSO. Forces and moment of an FPSO were studied under wave and current interactions. The simulations of diffracted and radiated waves were performed in a time domain. Time marching schemes were used for this time domain calculation. The predictor-corrector(P-C) method was used. Boundary integral equations were used to solve each problem with Rankine sources and distributed over the entire calculation domain.

For the far-field boundary condition, Orlandi's truncated open boundary condition was used for an open truncated boundary condition to prevent reflected waves. The current effect was considered an explicit term due to being a moving coordinate. Various current heading angles were also studied. Truncated open boundary, maximum likelihood method, proper element size and shape, modulation function, and Chebyshev filtering were studied to avoid diverged solutions.

From our findings, higher order elements fitted a complicated model such as an FPSO.

We found that this method required considerably fewer elements than the constant panel method in order to obtain reasonable outcomes. Using our developed numerical method, we calculated wave forces and moment, mean drift forces, added mass, and damping coefficients. Conclusively, HOBEM was found to be more effective and more reliable in calculating and predicting wave and current influence on an FPSO. Future studies are needed to develop finer simulation tools for FPSO's large horizontal behavior.

To my parents

ACKNOWLEDGMENTS

I would like to express my sincere gratitude to my advisor, Dr. R. Mercier, for enthusiastic guidance and constant encouragement throughout the research. I also would like to thank the co-chair of my committee, Dr. M.H. Kim, for his caring and helpful advice during my long journey at Texas A&M University. Thanks also goes to Dr. Jun Zhang and Dr. Ping Chang for providing me with valuable suggestions and serving on my dissertation committee.

I am grateful to the staff at Offshore Technology Research Center for their support during my research. I would like to thank Ms. Bobbee Pennington for her thorough proofreading.

A special thanks to my father, Ungjo Bae, my mother, Youngok Shin, my wife, Dr. Hija Park, and my daughter, Kimberly. Without their support and faith in me, this dissertation would never have been completed.

TABLE OF CONTENTS

CHAPTER		Page
I	INTRODUCTION	1
	1.1 Background and motivation	2
	1.2 Mechanics of FPSO Responses in Waves and Current . .	4
	1.2.1 Design parameters	6
	1.3 Literature review	7
	1.3.1 Panel method	8
	1.3.2 Time domain simulation	10
	1.3.3 Treatment for radiation condition	12
	1.3.4 Perturbation methods	13
	1.4 Methodology of present study	15
	1.5 Organization	17
II	THEORETICAL FORMULATION	19
	2.1 Linear wave theory	19
	2.2 Exact boundary value problem	19
	2.2.1 Coordinate systems	19
	2.2.2 Boundary value problem for global coordinate system	22
	2.2.3 Boundary value problem for local coordinate system	25
	2.3 Perturbation method	27
	2.4 Current forces and moments	29
	2.4.1 Components of current	29
	2.4.2 Empirical formulas	30
	2.4.3 Current heading	30
	2.4.4 Munk moment	32
	2.4.5 Double body flow	33
	2.5 Wave forces and moments	35
	2.5.1 Wave drift damping	40
	2.5.2 Equations of motion	41
	2.6 Boundary type solution procedures	44
	2.6.1 Original Trefftz method	44
	2.6.2 Direct method	47
	2.6.3 Common fundamental solutions in BEM	49
	2.7 The boundary integral equation	49

CHAPTER	Page
2.7.1	Weight residual method 49
2.7.2	The Green function 52
2.7.3	Laplace equation with Green function 54
III	NUMERICAL FORMULATION 56
3.1	Discretization 56
3.2	Discretized boundary integral equation 57
3.3	Higher order boundary element method 58
3.3.1	Generation of shape functions 59
3.3.2	Definition of higher order shape functions 62
3.3.3	Discontinuous elements 64
3.3.4	Comparing constant shape function with higher 68
3.3.5	Derivatives in higher order panel 68
3.4	Influence matrix handling 76
IV	STRATEGIES FOR CONVERGENCE IN SIMULATION AND NUMERICAL RESULTS 79
4.1	Truncated open boundary condition 79
4.1.1	General idea 79
4.1.2	Numerical treatment 83
4.2	Maximum likelihood method 88
4.3	Guidelines for elements generation 91
4.4	Time stepping methods 93
4.4.1	Saw-tooth instability 96
4.4.2	Chebyshev filtering scheme 97
4.5	Modulation function 98
4.6	Overview of THOBEM, WAMIT, and TiMIT 101
4.6.1	The limitations 101
4.6.2	Process in general 102
4.6.3	The differences 102
4.7	Simulation results 104
4.7.1	A case study for convergence test with various time grid sizes 105
4.7.2	Diffraction study 106
4.7.3	Mean drift force 113
4.7.4	Radiation study 117
4.7.5	Current effect study 124
4.7.6	The influence of the current on wave length 145
4.7.7	The influence of the current on wave elevation 148
4.7.8	Current effect with headings 151

CHAPTER	Page
V SUMMARY AND CONCLUSIONS	165
5.1 Conclusions	165
5.2 Future works	167
REFERENCES	168
APPENDIX A	176
APPENDIX B	178
APPENDIX C	179
APPENDIX D	181
APPENDIX E	183
APPENDIX F	185
VITA	285

LIST OF TABLES

TABLE		Page
2.1	Formulas for linear wave theory I.	20
2.2	Formulas for linear wave theory II.	21
2.3	Fundamental solutions for BEM.	50
4.1	Comparison of the simulation programs: THOBEM, WAMIT ver. 5.4, and TiMIT.	104
4.2	Dimensions of the GoM FPSO.	109
4.3	Parametric study for radiated wave.	117
4.4	Expectations of the current effect with diffracted waves.	128
4.5	Change of wave amplitudes due to collinear and adverse current effect in the upstream and downstream.	150

LIST OF FIGURES

FIGURE	Page
1.1	FPSO experiment under wind and wave load (Provided Courtesy of Offshore Technology Research Center in College Station, Texas, USA). 1
1.2	Moored floating production facilities. 3
2.1	Exact boundary value problem with two coordinate systems. 22
2.2	Definition of the simple Green function. 53
3.1	General procedures for a solid modeling. 57
3.2	Two-dimensional linear shape functions. 60
3.3	Quadratic shape functions. 61
3.4	Schematics of the nine nodes and six nodes elements. 62
3.5	Distribution of the discontinuous elements along the intersection of the two boundary surfaces. 65
3.6	Shape functions for a lower order panel with four nodes. 69
3.7	Shape functions for a higher order panel with eight nodes. 70
3.8	Shape functions for a higher order panel with nine nodes I. 71
3.9	Shape functions for a higher order panel with nine nodes II. 72
3.10	Relationship between the global and the local coordinates system for a quadrilateral curved element. 73
4.1	Domain size and wave probe positions to investigate phase velocities at truncated open boundary. 84
4.2	Phase velocity at open truncated boundary. 86

FIGURE	Page	
4.3	Relationship between phase velocity at open boundary and diffraction forces in surge and sway.	87
4.4	Examples of MLM.	90
4.5	Circular domain for an FPSO with one-way biased elements.	92
4.6	Circular domain for an FPSO with two-way biased elements.	93
4.7	Circular domain for hemisphere with inner and outer regions.	94
4.8	Circular domain for hemisphere with inner and outer regions, and smaller elements on the open boundary.	94
4.9	Comparison of modulation function effect until $t/T = 2, 4,$ and $6.$	100
4.10	Convergence test for time steps per nondimensional time 20, 30, 40, and 50.	107
4.11	Convergence test for time steps per nondimensional time 60, 70, 80, and 90.	107
4.12	Convergence test for time steps per nondimensional time 100, 110, 120, and 130.	108
4.13	Convergence test for time steps per nondimensional time 140, 150, and 160.	108
4.14	Perspective view of an FPSO in the rectangular domain.	110
4.15	Comparison of THOBEM and WAMIT in time history of wave forces and moment.	111
4.16	Comparison of THOBEM and WAMIT of the first order forces and moment in various frequencies.	112
4.17	Comparison of THOBEM and WAMIT results for mean drift forces and moment with diffracted waves.	114
4.18	The first and second component of the mean drift forces and moment in THOBEM with diffracted waves.	115

FIGURE	Page
4.19	Comparison of THOBEM and WAMIT of the velocity potential. 116
4.20	Time history of forces and moment from radiated wave in surge. 119
4.21	Time history of forces and moment from radiated wave in heave. 120
4.22	Added mass and damping coefficients in x direction when body oscillates in surge. 121
4.23	Added mass and damping coefficients in z direction when body oscillates in surge. 122
4.24	Added mass and damping coefficients in x direction when body oscillates in heave. 123
4.25	Added mass and damping coefficients in z direction when body oscillates in heave. 125
4.26	Current effect with diffracted waves for (a) head sea(adverse current) effect (b) following sea(collinear current) effect. 126
4.27	Time history of forces and moment for diffracted waves ($\omega = 0.6(rad/sec)$) with current effect ($F_n = \mp 0.01$). 127
4.28	Time history of forces and moment for diffracted waves ($\omega = 0.6(rad/sec)$) with current effect ($F_n = \mp 0.03$). 129
4.29	Time history of forces and moment for diffracted waves ($\omega = 0.6(rad/sec)$) with (a) adverse and (b) collinear current effect. 131
4.30	Surge forces for diffracted waves in various frequencies with head sea (adverse current) effect. 132
4.31	Surge forces for diffracted waves in various frequencies with head sea (adverse current) effect. 133
4.32	Surge forces for diffracted waves in various frequencies with following sea (collinear current) effect. 134
4.33	Surge forces for diffracted waves in various frequencies with following sea (collinear current) effect. 135

FIGURE	Page
4.34	Current effect with radiated waves in (a) surge with the positive Froude number and (b) heave with the negative Froude number. 136
4.35	Added mass in surge with radiated waves at various frequencies for (a) incident wave frequencies and (b) encounter frequencies when the FPSO oscillates in surge. 137
4.36	Damping coefficient in surge with radiated waves in various frequencies for (a) incident wave frequencies and (b) encounter frequencies when the FPSO oscillates in surge. 138
4.37	Added mass in heave with radiated waves at various frequencies for (a) incident wave frequencies and (b) encounter frequencies when the FPSO oscillates in surge. 139
4.38	Damping coefficient in heave with radiated waves in various frequencies for (a) incident wave frequencies and (b) encounter frequencies when the FPSO oscillates in surge. 140
4.39	Added mass in surge with radiated waves at various frequencies for (a) incident wave frequencies and (b) encounter frequencies when the FPSO oscillates in heave. 141
4.40	Damping coefficient in surge with radiated waves in various frequencies for (a) incident wave frequencies and (b) encounter frequencies when the FPSO oscillates in heave. 142
4.41	Added mass in heave with radiated waves at various frequencies for (a) incident wave frequencies and (b) encounter frequencies when the FPSO oscillates in heave. 143
4.42	Damping coefficient in surge with radiated waves in various frequencies for (a) incident wave frequencies and (b) encounter frequencies when the FPSO oscillates in heave. 144
4.43	Change of wave length due to collinear and adverse current effects. 147
4.44	Change of wave amplitude due to collinear and adverse current effects. 149
4.45	Current effect with diffracted waves in various headings for head sea (adverse current) cases. 152

FIGURE	Page
4.46	Current effect with diffracted waves in various headings for following sea (collinear current) cases. 153
4.47	Surge forces with diffracted waves in various frequencies for head sea (adverse current) effect. Wave and current heading angles are -5 and 175 degrees respectively. 155
4.48	Sway forces with diffracted waves in various frequencies for head sea (adverse current) effect. Wave and current heading angles are -5 and 175 degrees respectively. 156
4.49	Heave forces with diffracted waves in various frequencies for head sea (adverse current) effect. Wave and current heading angles are -5 and 175 degrees respectively. 157
4.50	Roll moments with diffracted waves in various frequencies for head sea (adverse current) effect. Wave and current heading angles are -5 and 175 degrees respectively. 158
4.51	Pitch moments with diffracted waves in various frequencies for head sea (adverse current) effect. Wave and current heading angles are -5 and 175 degrees respectively. 159
4.52	Yaw moments with diffracted waves in various frequencies for head sea (adverse current) effect. Wave and current heading angles are -5 and 175 degrees respectively. 160
4.53	Surge forces with diffracted waves in various frequencies for head sea (adverse current) effect at Froude number is 0.03. Wave heading angles are -5, -10, -15, and -30. Current heading angles are 175, 170, 165, 150 degrees. 162
4.54	Sway forces with diffracted waves in various frequencies for head sea (adverse current) effect at Froude number is 0.03. Wave heading angles are -5, -10, -15, and -30. Current heading angles are 175, 170, 165, 150 degrees. 163
4.55	Yaw moments with diffracted waves in various frequencies for head sea (adverse current) effect at Froude number is 0.03. Wave heading angles are -5, -10, -15, and -30. Current heading angles are 175, 170, 165, 150 degrees. 164

FIGURE	Page
C.1	Sequence of the process for numerical calculation 180
F.1	Surge forces for diffracted waves in various frequencies with head sea (adverse current) effect. Wave and current heading angles are -10 and 170 degrees respectively. 186
F.2	Sway forces for diffracted waves in various frequencies with head sea (adverse current) effect. Wave and current heading angles are -10 and 170 degrees respectively. 187
F.3	Heave forces for diffracted waves in various frequencies with head sea (adverse current) effect. Wave and current heading angles are -10 and 170 degrees respectively. 188
F.4	Roll moments for diffracted waves in various frequencies with head sea (adverse current) effect. Wave and current heading angles are -10 and 170 degrees respectively. 189
F.5	Pitch moments for diffracted waves in various frequencies with head sea (adverse current) effect. Wave and current heading angles are -10 and 170 degrees respectively. 190
F.6	Yaw moments for diffracted waves in various frequencies with head sea (adverse current) effect. Wave and current heading angles are -10 and 170 degrees respectively. 191
F.7	Surge forces for diffracted waves in various frequencies with head sea (adverse current) effect. Wave and current heading angles are -15 and 165 degrees respectively. 192
F.8	Sway forces for diffracted waves in various frequencies with head sea (adverse current) effect. Wave and current heading angles are -15 and 165 degrees respectively. 193
F.9	Heave forces for diffracted waves in various frequencies with head sea (adverse current) effect. Wave and current heading angles are -15 and 165 degrees respectively. 194
F.10	Roll moments for diffracted waves in various frequencies with head sea (adverse current) effect. Wave and current heading angles are -15 and 165 degrees respectively. 195

FIGURE	Page
F.11	Pitch moments for diffracted waves in various frequencies with head sea (adverse current) effect. Wave and current heading angles are -15 and 165 degrees respectively. 196
F.12	Yaw moments for diffracted waves in various frequencies with head sea (adverse current) effect. Wave and current heading angles are -15 and 165 degrees respectively. 197
F.13	Surge forces for diffracted waves in various frequencies with head sea (adverse current) effect. Wave and current heading angles are -30 and 150 degrees respectively. 198
F.14	Sway forces for diffracted waves in various frequencies with head sea (adverse current) effect. Wave and current heading angles are -30 and 150 degrees respectively. 199
F.15	Heave forces for diffracted waves in various frequencies with head sea (adverse current) effect. Wave and current heading angles are -30 and 150 degrees respectively. 200
F.16	Roll moments for diffracted waves in various frequencies with head sea (adverse current) effect. Wave and current heading angles are -30 and 150 degrees respectively. 201
F.17	Pitch moments for diffracted waves in various frequencies with head sea (adverse current) effect. Wave and current heading angles are -30 and 150 degrees respectively. 202
F.18	Yaw moments for diffracted waves in various frequencies with head sea (adverse current) effect. Wave and current heading angles are -30 and 150 degrees respectively. 203
F.19	Surge forces for diffracted waves in various frequencies with head sea (adverse current) effect. Wave and current heading angles are zero and 175 degrees respectively. 204
F.20	Sway forces for diffracted waves in various frequencies with head sea (adverse current) effect. Wave and current heading angles are zero and 175 degrees respectively. 205

FIGURE	Page
F.21	Heave forces for diffracted waves in various frequencies with head sea (adverse current) effect. Wave and current heading angles are zero and 175 degrees respectively. 206
F.22	Roll moments for diffracted waves in various frequencies with head sea (adverse current) effect. Wave and current heading angles are zero and 175 degrees respectively. 207
F.23	Pitch moments for diffracted waves in various frequencies with head sea (adverse current) effect. Wave and current heading angles are zero and 175 degrees respectively. 208
F.24	Yaw moments for diffracted waves in various frequencies with head sea (adverse current) effect. Wave and current heading angles are zero and 175 degrees respectively. 209
F.25	Surge forces for diffracted waves in various frequencies with head sea (adverse current) effect. Wave and current heading angles are zero and 170 degrees respectively. 210
F.26	Sway forces for diffracted waves in various frequencies with head sea (adverse current) effect. Wave and current heading angles are zero and 170 degrees respectively. 211
F.27	Heave forces for diffracted waves in various frequencies with head sea (adverse current) effect. Wave and current heading angles are zero and 170 degrees respectively. 212
F.28	Roll moments for diffracted waves in various frequencies with head sea (adverse current) effect. Wave and current heading angles are zero and 170 degrees respectively. 213
F.29	Pitch moments for diffracted waves in various frequencies with head sea (adverse current) effect. Wave and current heading angles are zero and 170 degrees respectively. 214
F.30	Yaw moments for diffracted waves in various frequencies with head sea (adverse current) effect. Wave and current heading angles are zero and 170 degrees respectively. 215

FIGURE	Page
F.31	Surge forces for diffracted waves in various frequencies with head sea (adverse current) effect. Wave and current heading angles are zero and 150 degrees respectively. 216
F.32	Sway forces for diffracted waves in various frequencies with head sea (adverse current) effect. Wave and current heading angles are zero and 150 degrees respectively. 217
F.33	Heave forces for diffracted waves in various frequencies with head sea (adverse current) effect. Wave and current heading angles are zero and 150 degrees respectively. 218
F.34	Roll moments for diffracted waves in various frequencies with head sea (adverse current) effect. Wave and current heading angles are zero and 150 degrees respectively. 219
F.35	Pitch moments for diffracted waves in various frequencies with head sea (adverse current) effect. Wave and current heading angles are zero and 150 degrees respectively. 220
F.36	Yaw moments for diffracted waves in various frequencies with head sea (adverse current) effect. Wave and current heading angles are zero and 150 degrees respectively. 221
F.37	Surge forces for diffracted waves in various frequencies with head sea (adverse current) effect. Waves heading angles and current heading angles are 5 and 175 degrees respectively. 222
F.38	Sway forces for diffracted waves in various frequencies with head sea (adverse current) effect. Wave and current heading angles are 5 and 175 degrees respectively. 223
F.39	Heave forces for diffracted waves in various frequencies with head sea (adverse current) effect. Wave and current heading angles are 5 and 175 degrees respectively. 224
F.40	Roll moments for diffracted waves in various frequencies with head sea (adverse current) effect. Wave and current heading angles are 5 and 175 degrees respectively. 225

FIGURE	Page
F.41	Pitch moments for diffracted waves in various frequencies with head sea (adverse current) effect. Wave and current heading angles are 5 and 175 degrees respectively. 226
F.42	Yaw moments for diffracted waves in various frequencies with head sea (adverse current) effect. Wave and current heading angles are 5 and 175 degrees respectively. 227
F.43	Surge forces for diffracted waves in various frequencies with head sea (adverse current) effect. Waves heading angles and current heading angles are 10 and 170 degrees respectively. 228
F.44	Sway forces for diffracted waves in various frequencies with head sea (adverse current) effect. Wave and current heading angles are 10 and 170 degrees respectively. 229
F.45	Heave forces for diffracted waves in various frequencies with head sea (adverse current) effect. Wave and current heading angles are 10 and 170 degrees respectively. 230
F.46	Roll moments for diffracted waves in various frequencies with head sea (adverse current) effect. Wave and current heading angles are 10 and 170 degrees respectively. 231
F.47	Pitch moments for diffracted waves in various frequencies with head sea (adverse current) effect. Wave and current heading angles are 10 and 170 degrees respectively. 232
F.48	Yaw moments for diffracted waves in various frequencies with head sea (adverse current) effect. Wave and current heading angles are 10 and 170 degrees respectively. 233
F.49	Surge forces for diffracted waves in various frequencies with head sea (adverse current) effect. Waves heading angles and current heading angles are 30 and 150 degrees respectively. 234
F.50	Sway forces for diffracted waves in various frequencies with head sea (adverse current) effect. Wave and current heading angles are 30 and 150 degrees respectively. 235

FIGURE	Page
F.51	Heave forces for diffracted waves in various frequencies with head sea (adverse current) effect. Wave and current heading angles are 30 and 150 degrees respectively. 236
F.52	Roll moments for diffracted waves in various frequencies with head sea (adverse current) effect. Wave and current heading angles are 30 and 150 degrees respectively. 237
F.53	Pitch moments for diffracted waves in various frequencies with head sea (adverse current) effect. Wave and current heading angles are 30 and 150 degrees respectively. 238
F.54	Yaw moments for diffracted waves in various frequencies with head sea (adverse current) effect. Wave and current heading angles are 30 and 150 degrees respectively. 239
F.55	Surge forces for diffracted waves in various frequencies with following sea (collinear current) effect. Wave and current heading angles are -5 degrees. 240
F.56	Sway forces for diffracted waves in various frequencies with following sea (collinear current) effect. Wave and current heading angles are -5 degrees. 241
F.57	Heave forces for diffracted waves in various frequencies with following sea (collinear current) effect. Wave and current heading angles are -5 degrees. 242
F.58	Roll moments for diffracted waves in various frequencies with following sea (collinear current) effect. Wave and current heading angles are -5 degrees. 243
F.59	Pitch moments for diffracted waves in various frequencies with following sea (collinear current) effect. Wave and current heading angles are -5 degrees. 244
F.60	Yaw moments for diffracted waves in various frequencies with following sea (collinear current) effect. Wave and current heading angles are -5 degrees. 245

FIGURE	Page
F.61	Surge forces for diffracted waves in various frequencies with following sea (collinear current) effect. Wave and current heading angles are -10 degrees. 246
F.62	Sway forces for diffracted waves in various frequencies with following sea (collinear current) effect. Wave and current heading angles are -10 degrees. 247
F.63	Heave forces for diffracted waves in various frequencies with following sea (collinear current) effect. Wave and current heading angles are -10 degrees. 248
F.64	Roll moments for diffracted waves in various frequencies with following sea (collinear current) effect. Wave and current heading angles are -10 degrees. 249
F.65	Pitch moments for diffracted waves in various frequencies with following sea (collinear current) effect. Wave and current heading angles are -10 degrees. 250
F.66	Surge forces for diffracted waves in various frequencies with following sea (collinear current) effect. Wave and current heading angles are -15 degrees. 251
F.67	Sway forces for diffracted waves in various frequencies with following sea (collinear current) effect. Wave and current heading angles are -15 degrees. 252
F.68	Heave forces for diffracted waves in various frequencies with following sea (collinear current) effect. Wave and current heading angles are -15 degrees. 253
F.69	Roll moments for diffracted waves in various frequencies with following sea (collinear current) effect. Wave and current heading angles are -15 degrees. 254
F.70	Pitch moments for diffracted waves in various frequencies with following sea (collinear current) effect. Wave and current heading angles are -15 degrees. 255

FIGURE	Page
F.71	Surge forces for diffracted waves in various frequencies with following sea (collinear current) effect. Wave and current heading angles are -30 degrees. 256
F.72	Sway forces for diffracted waves in various frequencies with following sea (collinear current) effect. Wave and current heading angles are -30 degrees. 257
F.73	Heave forces for diffracted waves in various frequencies with following sea (collinear current) effect. Wave and current heading angles are -30 degrees. 258
F.74	Roll moments for diffracted waves in various frequencies with following sea (collinear current) effect. Wave and current heading angles are -30 degrees. 259
F.75	Pitch moments for diffracted waves in various frequencies with following sea (collinear current) effect. Wave and current heading angles are -30 degrees. 260
F.76	Surge forces for diffracted waves in various frequencies with following sea (collinear current) effect. Wave and current heading angles are zero and -5 degrees respectively respectively. 261
F.77	Sway forces for diffracted waves in various frequencies with following sea (collinear current) effect. Wave and current heading angles are zero and -5 degrees respectively. 262
F.78	Heave forces for diffracted waves in various frequencies with following sea (collinear current) effect. Wave and current heading angles are zero and -5 degrees respectively. 263
F.79	Roll moments for diffracted waves in various frequencies with following sea (collinear current) effect. Wave and current heading angles are zero and -5 degrees respectively. 264
F.80	Pitch moments for diffracted waves in various frequencies with following sea (collinear current) effect. Wave and current heading angles are zero and -5 degrees respectively. 265

FIGURE	Page
F.81	Surge forces for diffracted waves in various frequencies with following sea (collinear current) effect. Wave and current heading angles are zero and -10 degrees respectively respectively. 266
F.82	Sway forces for diffracted waves in various frequencies with following sea (collinear current) effect. Wave and current heading angles are zero and -10 degrees respectively. 267
F.83	Heave forces for diffracted waves in various frequencies with following sea (collinear current) effect. Wave and current heading angles are zero and -10 degrees respectively. 268
F.84	Roll moments for diffracted waves in various frequencies with following sea (collinear current) effect. Wave and current heading angles are zero and -10 degrees respectively. 269
F.85	Pitch moments for diffracted waves in various frequencies with following sea (collinear current) effect. Wave and current heading angles are zero and -10 degrees respectively. 270
F.86	Surge forces for diffracted waves in various frequencies with following sea (collinear current) effect. Wave and current heading angles are 5 and -5 degrees respectively respectively. 271
F.87	Sway forces for diffracted waves in various frequencies with following sea (collinear current) effect. Wave and current heading angles are 5 and -5 degrees respectively. 272
F.88	Heave forces for diffracted waves in various frequencies with following sea (collinear current) effect. Wave and current heading angles are 5 and -5 degrees respectively. 273
F.89	Roll moments for diffracted waves in various frequencies with following sea (collinear current) effect. Wave and current heading angles are 5 and -5 degrees respectively. 274
F.90	Pitch moments for diffracted waves in various frequencies with following sea (collinear current) effect. Wave and current heading angles are 5 and -5 degrees respectively. 275

FIGURE	Page
F.91	Surge forces for diffracted waves in various frequencies with following sea (collinear current) effect. Wave and current heading angles are 10 and -10 degrees respectively respectively. 276
F.92	Sway forces for diffracted waves in various frequencies with following sea (collinear current) effect. Wave and current heading angles are 10 and -10 degrees respectively. 277
F.93	Heave forces for diffracted waves in various frequencies with following sea (collinear current) effect. Wave and current heading angles are 10 and -10 degrees respectively. 278
F.94	Roll moments for diffracted waves in various frequencies with following sea (collinear current) effect. Wave and current heading angles are 10 and -10 degrees respectively. 279
F.95	Pitch moments for diffracted waves in various frequencies with following sea (collinear current) effect. Wave and current heading angles are 10 and -10 degrees respectively. 280
F.96	Surge forces for diffracted waves in various frequencies with following sea (collinear current) effect. Wave and current heading angles are 15 and -15 degrees respectively respectively. 281
F.97	Heave forces for diffracted waves in various frequencies with following sea (collinear current) effect. Wave and current heading angles are 15 and -15 degrees respectively. 282
F.98	Roll moments for diffracted waves in various frequencies with following sea (collinear current) effect. Wave and current heading angles are 15 and -15 degrees respectively. 283
F.99	Pitch moments for diffracted waves in various frequencies with following sea (collinear current) effect. Wave and current heading angles are 15 and -15 degrees respectively. 284

CHAPTER I

INTRODUCTION

Consideration of wave induced forces is the critical starting point for the design of marine structures. In the past five decades, the importance of wave related problems have led to the introduction of highly interesting topics such as theoretical analysis, numerical modeling, and experimental studies. Experimental studies are one-of-a-kind solutions for explaining the complex phenomena of wave, current, wind, and body interactions. For example, figure 1.1 shows an FPSO experiment under a complicated ocean environment.

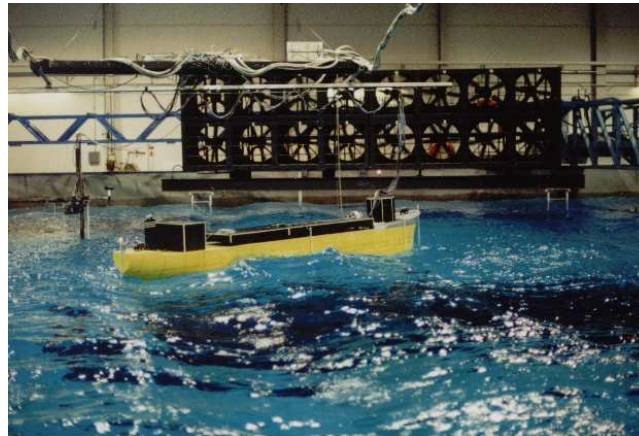


FIGURE 1.1. FPSO experiment under wind and wave load (Provided Courtesy of Offshore Technology Research Center in College Station, Texas, USA).

One of the major limitation for research in this area is cost due to the marine struc-

This dissertation follows the style and format of the *Journal of Fluid Mechanics*.

tures' scale and harsh environments. Therefore, numerical simulation is an alternative solution for use in running preliminary experimental tests. Numerical simulation has also made wonderful contributions in the application of mathematical background theories.

1.1 Background and motivation

Most floating production systems were installed in about 150 to 400 ft deep water in 1990s. During the last ten years the production zones moved to seas more than ten times deeper than in the past. Therefore, more precise studies are needed to calculate response of the moored floating bodies. The major classes of floating production systems or units are illustrated in figure 1.2 and listed as follows:

- floating production, storage, and offloading vessels (FPSOs),
- semisubmersible floating production systems (FPSs), or semisubmersible floating production units (FPUs),
- spar buoys,
- tension leg platforms (TLPs).

Floating production facilities were initially installed in the mid 70's. The first ship-shaped production facility was installed in 1974 by Arco Indonesia Inc. The capacity was 66,000 dwt. In 1975, Hamilton Brothers installed a barge type floating production facility on Argyll field in the North Sea. One year later, another floating production facility was launched near Madura Island in Indonesia.

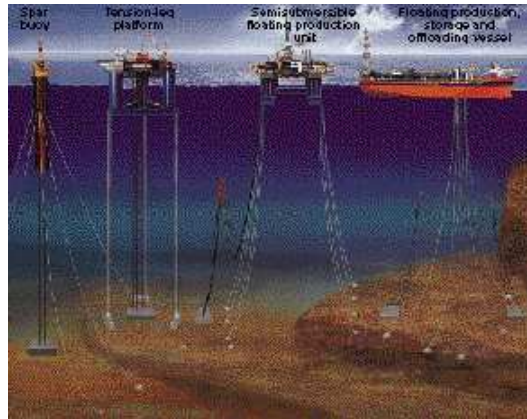


FIGURE 1.2. Moored floating production facilities.

These early models required either storage facilities such as a storage barge or pipelines to onshore terminals. In 1977, Shell installed a 60,000 dwt FPSO at Castellon field offshore of Spain in 377 ft. of water. The early FPSO mooring design was based on tanker offloading systems such as catenary anchored-leg moored buoys (CALMs) and single-point buoy moorings (SPMs). By the late 1980s, only ten FPSOs were working worldwide.

In the 1990s, FPSOs started to gain the spotlight. Fifty-five FPSOs were installed in the 1990s and the FPSO business grew rapidly. Floating installations are primarily designed for oil production. One advantage of the FPSO is its large storage capacity for produced oil, which is especially needed in remote areas where pipeline infrastructure is nonexistent.

Other mooring production system concepts require floating storage vessels, shuttle-tanker terminals, or pipelines to onshore. Considering operation costs, separate facilities are more expensive than integrated ones. The initial costs of FPSO are less expensive than two other facilities such as an FPU/FSO (Pennwell 1998).

Although the FPSO possesses significant economic advantage over other production system concepts(TLPs, SPARS, etc.), the ship form does not naturally have very good station-keeping and seakeeping performance. Furthermore, the mechanics of turret-moored FPSO responses combined with wind, wave, and current are not as well understood as other floating system concepts, such as TLPs and SPARS.

This study is motivated by the need to better understand the hydrodynamics of turret-moored FPSOs. A turret-moored FPSO is susceptible to large mean yaw drift angles and relatively large low frequency drift motions. These slowly varying quantities are the key to determining tensions in mooring lines and risers. Due to the potentially large mean yaw position, accurate determination of the body headings is crucial.

1.2 Mechanics of FPSO Responses in Waves and Current

The main issues in global design of FPSOs are:

- **large relative vertical motions:** heave and pitch. The main focus of the studies is on the greenwater. Due to the large vertical motion, FPSO may be slammed on the deck by waves, and this may cause improper operation of the FPSO.
- **large horizontal motions:** surge, sway, and yaw. If the FPSO is moored by either a single point mooring(SPM) or a turret mooring system(TMS), it will be free to yaw. Therefore, it may adopt a large yaw angle with different wave and current headings.
- **large roll motions:** FPSO employs a ship-shaped body moving like a ship. Like a ship motion, it may experience a large roll motion. A large roll angle may

cause discomfort during operation. Certain types of stabilization equipment have been devised to avoid a resonance effect to roll, such as bilge keels, and anti-rolling tanks.

Numerical modeling of the motion of a moored large displacement body is generally accomplished by using the boundary element method (Brebbia & Dominguez 1977, 1989, 1992; Beer 2001). This method is based on the assumption of inviscid wave-body interactions. This approach yields accurate estimates of first-order diffraction and radiation effects, especially as these effects determine the vessel responses at the exciting wave frequencies.

However, the nonlinear forcing of low frequency resonant motions is caused by a combination of both viscous and inviscid effects, particularly in extreme waves combined with a strong current.

Inviscid mean and slowly-varying drift forces and moments are generated by a number of mechanisms:

- i) A major contribution to horizontal drift force arises from the relative vertical motion between the surface piercing body and the wave. This results in some of the body surface being submerged in the water while other parts of the body are not. The difference of relative vertical motion around the waterline results in a non-zero mean force.
- ii) The quadratic velocity term in Bernoulli's equation.
- iii) Effects associated with finite-amplitude body motions in an inertial frame of reference.

- iv) Contribution from the second-order velocity potential. This mechanism does not generate mean drift loads, only dynamic loads.
- v) The Munk moment associated with asymmetric streamlines when the current has an oblique angle relation to a ship. More details can be found in Faltinsen (1990).

The viscous drift force is primarily due to the wave-current interaction with a vessel. Zhao, Flatinsen, Krokstad & Aanesland (1988) confirmed that current velocities of 1 (m/s) may very well represent a 50% increase in drift forces on a large volume body.

1.2.1 Design parameters

In turret mooring system design, several design variables must be considered. Both the location of the turret and direction of the external excitation are used to determine the effects of parameters on the system dynamics:

- **hydrodynamic properties:**
 - the hydrodynamic and hydrostatic properties of the hull
 - the magnitude and direction of the external excitation (current, wave, and wind)
- **mooring systems:** turret, mooring lines, and risers
 - the size and position of the turret with respect to the vessel
 - the number, length, pretension, orientation and material of the mooring lines and risers

- the fraction of the turret diameter where the mooring lines are attached
- the gap between the turret and the vessel

1.3 Literature review

The moving body in the fluid with wave has a long historical background. The fundamental study of marine hydrodynamics originates with Froude (1868) and Michell (1898). Michell (1898) probed the waves produced by an actual ship. He proposed the first analytical solution for ship motion, the thin ship theory. Michell's main idea was that the inclination of the tangent plane at any point of its surface to the vertical median plane is small. Accordingly, the waves that arise from the parts at the stem and stern are dominant in the ship motion. Michell's theory requires some restrictions as follows:

- **ideal fluid assumption:** The fluid is assumed to be inviscid and the flow is irrotational. Therefore, the motion can only be specified under potential framework with necessary boundary conditions.
- **slender body assumption:** The hull must have a small ratio of beam to length so that its surface slope relative to the centerplane is small.
- **no wave breaking:** The wave height generated by the ship must be small compared to its length so that the square of the particle velocity is negligible in comparison with ship speed.
- **no defects in the body:** The ship is assumed to be under proper operational condition. It can not have experienced any sinkage or trim.

The slender body assumption has faced difficulties because of the geometric characteristics of ships. Moreover, the results do not possess good agreement in low frequencies and at high forward speeds. To overcome these problems, researchers have studied various methods. The following subsections review the panel method, time-domain simulation, treatment for radiation condition, and perturbation method.

1.3.1 Panel method

Over the past sixty years, several panel methods have been developed and adopted to overcome the difficulty of strip theory. Among three different panel methods (constant panel, higher order element, and panel free), Hess & Smith (1964) pioneered the constant panel method. They distributed a source that develops a flow without a free surface so that their calculation domain is equivalent to double body flow with a rigid free surface.

The body was subdivided into a number of quadrilateral elements and sources were deployed as constant strength. The body boundary conditions were satisfied at the center of each quadrilateral element. Each panel had to satisfy the body boundary conditions and unknowns obtained from solving the system of simultaneous equations. With this procedure, the boundary integral equation is changed to a system of linear equations for unknown source strength. The potentials, velocities, and pressures at the centroid of each panel can then be determined from this source strength. This is often referred to as the constant panel method. A large number of panels are commonly required to achieve accurate results in many applications such as computation of second order forces. It is commonly known that the constant panel method may have difficulty providing an accurate gradient of the velocity potential. Nakos &

Sclavounos (1991) used the constant panel method. They spread Rankine sources to a three-dimensional ship hull and calculated the steady and time harmonic potential flows with a forward velocity.

Higher order element methods have been developed to overcome the deficiencies of the constant panel method. More details for what is its referring to deficiencies are described in Chapter III. Most higher order methods use quadratic and triangular panels in three dimensional problems. The strength of source are deployed over a panel as the first or the second order degree polynomials. It may require less effort in the total process of the computational task in comparison to the constant panel method due to the requirement of less panels for the reasonable outcome. Hsin, Kerwin & Newman (1993) applied B-splines and developed a higher order panel method. Teng & Eatock-Taylor (1995) developed a higher order boundary element method (HOBEM) code to solve the wave, current, and body interactions in the frequency domain.

Lee, Maniar, Newman & Zhu (1997) have presented a geometry independent higher order method which separates the geometric and hydrodynamic representations. The velocity potential is described by B-splines. It allows accurate geometrical descriptions and flexibility of potential discretization. Later, Qiu (2001) provided a panel-free method (PFM) based on the desingularized Green's formula to solve the radiation problem of a floating body in time domain. He used the velocity potential due to a non-impulsive velocity obtained from the boundary integral equation in terms of source strength distribution. The geometry of a body surface is mathematically represented by Non-Uniform Rational B-splines(NURBS). Qiu, Peng & Hsiung (2003) used PFM for diffraction and radiation problems to compare with Wigley hull in the time domain. More recently, Kim & Shin (2003) used NURBS to solve three-dimensional

radiation and diffraction problems.

Independently, several researchers developed HOBEM. Liu (1988) developed HOBEM for wave body interaction in linear problems. Liu, Kim & Lu (1991) applied this method to linear wave and body interaction problems. They compared the performance of HOBEM with a constant panel method. Boo (1993) subsequently applied HOBEM to the wave resistance problem in the frequency domain and the fully non-linear wave tank problem in the time domain. Later, HOBEM was extended to the second order problem by Liu, Kim & Kim (1995). A simple Green function was used in HOBEM so that this Green function automatically satisfies the free surface boundary and radiation conditions at far field.

1.3.2 Time domain simulation

After a calculation domain is discretized, either time or frequency domain will be chosen to calculate hydrodynamic properties. For zero speed problems, the frequency domain approach is quite successful and has become a routine process for the design of large offshore structures.

Chang (1977), Inglis & Price (1982), and Guevel & Bougis (1982) have used three dimensional constant panels to obtain solutions of ship motion in the frequency domain. This panel method in a frequency domain has been employed for ship seakeeping analysis using a zero speed Green function with a speed correction. The results based on this Green function came out unsatisfactory due to computational complication. To overcome the difficulties in the complexity of Green function with a speed correction, Wu & Eatock-Taylor (1987) derived a different Green function for the problem of constant forward speed in regular waves. They derived a single integral from the original

Green function. The original Green function was expressed in a double integral for a unit oscillating source with constant forward speed. More recently, Noblesse & Yang (2004*a*, 2004*b*) and Yang, Lohner & Noblesse (2004) proposed a simpler Green function for forward speed.

An alternative approach is to formulate the ship motion problem directly in the time domain. When forward speed is involved, the Green function in the time domain is a simpler form and requires less computational effort than the Green function used in a frequency domain. Finkelstein (1957), Stoker (1957), and Ogilvie (1964) researched a direct method for a time domain solution. The zero forward speed problem has been discussed in detail by Wehausen (1967, 1971). Beck & Liapis (1987) investigated the transient motion problem. Korsmeyer, Lee, Newman & Sclavounos (1988), and Beck & King (1989) studied the radiation problem in a zero Froude number case.

The early stage of the time domain simulation is formally related to the frequency domain results via Fourier transforms. In the linear time domain formulation, the time dependent Green function is applied to derive a boundary integral equation at the mean wetted surface of the body under the assumptions of small body motion and small amplitude incident waves. The action of the linearized radiation and the diffraction forces on the body can be described in terms of convolution integrals of the arbitrary motion with impulse functions. These methods were developed by Beck & King (1989), and Kin and Yue(1994).

A combined time domain simulation scheme was developed by Qiu, Peng & Hsiung (2003) to take into account the nonlinear effect of incident waves. In their works, the radiation and diffraction forces were computed at the mean wetted surface by applying the impulse response function. The Froude-Krylove forces and restoring forces

were computed at the instantaneous wetted surface under the incident wave profile.

Maneuvering force, rudder effect, and viscous damping were studied by Seiber(2000) and Qie et al. (2001a, 2001b). These nonlinear forces and effects were investigated by considering the varied hydrodynamic coefficients on various waterlines. Added mass, damping and restoring force coefficients were precomputed in the time domain for respective wetted surfaces chosen at body draft. Next the instantaneous wetted body surface was interpolated at each time step. This method showed promising improvement for motion prediction, particularly for roll. Additional efforts may require that the various positions of the hull be panelized. The free surface nonlinearity, an exact boundary problem, was researched by Lin & Yue(1990), Magee(1994), and Danmeier(1999). An exact body boundary condition is imposed on an instantaneous wetted surface in a linear time domain model. The free surface boundary condition remains linear so that the time independent Green function can still be applied. These studies imply that applying an exact body boundary condition may improve the simulation for large amplitude motions.

1.3.3 Treatment for radiation condition

In the time domain simulation of free surface waves, the calculation domain needs to be truncated to reduce computational cost for practical purposes. There are several methods to treat the open boundary condition. For instance, Longuet-Higgins & Cokelet (1976) applied a periodic condition to the open boundary. This method can be applied only when the incoming wave is periodic.

Dommermuth & Yue (1987) used a matching technique. This technique consists of matching inner numerical solutions with outer ones and satisfies the radiation condi-

tions. This method can only be applied when outer solutions are known. Jagannathan (1988) used a special numerical scanning method in this two dimensional nonlinear wave simulation to improve performance. Cointe (1989) used a sponge layer. When the damping factors are properly modeled, it demonstrates good performance. However, increasing computational domain size makes increasing the degree of freedom. Generally, the size of the damping zone is more than one wave length in the wave direction. Oliveira (2000) compared the sponge layer boundary condition with the open truncated boundary. He recommended 1.5 wave lengths for the sponge layer widths to obtain the best results.

Orlanski (1976) first applied the Sommerfeld radiation condition with special numerical treatments to the open boundary condition. Many researchers employed the Sommerfeld/Orlanski condition as their numerical method. For instance, Isaacson & Cheung (1992), Cheung(1991), and Jagannathan(1998) used the Sommerfeld/Orlanski radiation condition. This condition is also used in a time domain higher order boundary element method (THOBEM). Please refer to Chapter IV for more details.

1.3.4 Perturbation methods

The linear diffraction theory for regular waves may extend to a second approximation on the basis of the Stokes expansion procedure. Variables describing the flow (i.e. wave elevation, velocity potential, etc.) are expanded as a power series and rearranged according to the order of the perturbation parameters. This is called the perturbation method. As an example of this method, Stokes second order wave theory was developed similarly.

The method involves two inhomogeneous free surface boundary conditions and an

inhomogeneous radiation condition. These inhomogeneous conditions make it extremely difficult to obtain an exact solution. Several researchers have presented a Green function as an exact solution. Most of these pioneer works failed to satisfy these inhomogeneous boundary conditions.

Subsequent studies were attempted in order to correct these deficiencies. These methods generally involve the decomposition of the potential at second order into free and forced components. Free components satisfied homogeneous terms and forced components satisfied inhomogeneous terms. A free surface boundary condition and a radiation condition at second order were modified by the forced term.

Another approach has been considered without using a second order potential. When the wave loading on bodies is the only factor to consider, the wave forces at second order can be obtained without evaluating the second order potential explicitly. An asymptotic form of the second order potential can be obtained by using the Haskind reciprocal relationship. This asymptotic form of the potential is known as a weakly radiation condition and this may be used to provide a far field closure of the solution. Molin (1979) proposed that this approach is applicable to three dimensional structures of arbitrary shape. He showed second order quantities for a small pile in a finite water depth.

The following studies have been done by Rahman (1984) and Eatock-Taylor & Hung (1987). They showed a regular wave diffraction around a bottom mounted surface piercing circular cylinder in three dimensions. Rahman (1987) and Abul-Azm & Williams (1988) performed a truncated circular cylinder in three dimensions. Williams & Abul-Azm (1990) applied this method to an array of vertical cylinders in three dimensions. Molin (1979) used an asymptotic expansion to get a second order potential in three

dimensions. The following studies have been done for a second order potential by Eatock-Taylor & Hung (1987), and Abul-Azm & Williams (1988). Their solutions were mutually in accord. Wu & Eatock-Taylor (1990) showed an analytic solution in two dimensions. It was compared with Vada (1987)'s numerical solution.

1.4 Methodology of present study

The methodology of present study is that of using a higher order panel method to get diffracted or radiated forces in the time domain. If the current speed is small, the effects of flow separation may be negligible and this problem can be formulated within the framework of the potential theory.

Keulegan-Carpenter (K-C) number can be considered as an indicator whether the flow separation occurs or not. When K-C number is less than three, flow separation can be neglected (Isaacson & Cheung 1992). Zhao, Flatinsen, Krokstad & Aanesland (1988) proved by their experiment that flow separation does not occur when K-C number is less than one with a hemisphere case. Another limitation is a current speed. This speed is less than the maximum wave-induced velocity. Under these conditions, potential theory reasonably matches with experimental results. The current effect problem can be solved with an undisturbed free surface boundary condition. Due to the rigid free surface, this is called a double body flow problem.

The perturbation method is adopted for the free surface boundary condition. The major difficulties associated with the fully nonlinear free surface problem arise from the two nonlinear free surface boundary conditions. These conditions are applied on the instantaneous free surface while the position of the instantaneous free surface is unknown in the previous time step. To overcome these difficulties, the instantaneous

free surface has been defined by a Taylor series expansion from the still water level. Isaacson & Cheung (1992) used the perturbation method. They defined two small parameters: the wave slope parameter $\epsilon (= H/\lambda)$ and the current speed parameter $\delta (U/\sqrt{gL})$. They are independent of each other. Similarly, these small parameters are used in the present study. The original boundary value problem can be divided into a zeroth order time independent problem at $O(\delta)$ and a first order unsteady problem at $O(\epsilon)$ including $O(\epsilon\delta)$.

HOBEM is used to solve this boundary value problem. An advanced element method makes the entire boundary surface discretized into a set of curved surface elements. Higher order interpolation functions were used to describe the velocity potential on each element. Liu, Kim & Lu (1991) compared HOBEM with constant panel methods (CPM). The use of the HOBEM has certain benefits in comparison to conventional CPM. HOBEM can handle a problem with less elements as opposed to CPM so that total computational efforts can be reduced.

Another advantage of using HOBEM is for calculating second order quantities where the velocity potential and its derivatives are needed exactly at the intersection of free surface and body surface. Liu, Kim & Kim (1995) showed second order mean wave loads and double frequency wave loads on the TLP. Using constant panels is known to be inaccurate in the computation of the second order spatial derivatives of the velocity potential on integral surfaces.

To complete the time domain simulation, the kinematic and dynamic free surface boundary conditions were updated using predictor-corrector(P-C) method. At the intersection of the free surface and radiation boundaries, discontinuous elements were used to circumvent a Dirichlet-Dirichlet corner problem. The discontinuous elements

can also be used between bodies with sharp edges or corners. In addition, in order to perform the numerical simulation in the truncated domain, the open boundary condition should be added.

The developed THOBEM program was used to investigate the effects of the constant current and wave interactions on an FPSO. The simulation results are compared and discussed with wave analysis Massachusetts institute of technology (WAMIT) in the case of a zero Froude number. Simulation results with constant current effect are compared with TiMIT. The suite of programs called TiMIT performs a linear seakeeping analysis for bodies with or without forward speed. For the verification of THOBEM code, a hemisphere was studied as a simple large three-dimensional body. With confidence in these simulation results, FPSO problems are solved.

1.5 Organization

In Chapter II, exact boundary value problems are defined and formulated by using a perturbation method. First order wave forces and second order mean drift forces are formulated. Constant current effects are considered. For the current force, empirical formulas, Munk moment, and double body flow are presented. In the last section of the Chapter II, boundary integral equation is briefly mentioned.

In Chapter III, all numerical procedures are presented on the basis of the theoretical formulations of the previous chapter. The Green function is presented as the fundamental solution. The use of discretized Laplace equation and boundary conditions are discussed. HOBEM is presented in detail.

In Chapter IV, several numerical strategies for the convergence in the long time step

simulation for the FPSO are discussed. Maximum likelihood method is presented as a solution for the reduction of total simulation time. Proper size of both domain and element shape is discussed. The time stepping method is discussed. As a solution to avoid saw-tooth problem, Chebyshev filtering scheme is presented. Impulse-response function is discussed as an alternative simulation method in the time domain. Simulation results are provided. Hemisphere and FPSO are simulated by THOBEM, WAMIT, and TiMIT.

Chapter V consists of conclusions and discussions.

The appendices provide useful information on open source numerical libraries, software development tools, Linux cluster, several fundamental formulas, and derivations.

CHAPTER II

THEORETICAL FORMULATION

2.1 Linear wave theory

Linear wave theory is known as a core theory for ocean surface waves in offshore and coastal engineering. This section does not intend to repeat theory fundamentals. This section rather provides a brief review of linear wave theory using tables 2.1 and 2.2. These tables are used as a reminder or a help to understand the following exact boundary value problems.

2.2 Exact boundary value problem

The theoretical formulations show the interactions of regular waves and uniform currents with a large three-dimensional body. Regular incoming waves propagate to the positive x-direction and currents flow in the opposite direction with velocity U .

2.2.1 Coordinate systems

Two Cartesian coordinate systems are introduced. One is global coordinate $\vec{x}_0 = (x_0, y_0, z_0)$ and the other is the local coordinate that moves with the mean forward speed $\vec{x} = (x, y, z)$. The z-axis is positive upward. The origin of the coordinate system is located on the undisturbed mean free surface. With steady current U , the steady moving coordinate system is

Velocity potential

Finite: $\phi = \frac{gA \cosh k(z+h)}{\omega \cosh kh} \cos(\omega t - kx)$

Infinite: $\phi = \frac{gA}{\omega} e^{kz} \cos(\omega t - kx)$

Dispersion relation

Finite: $\frac{\omega^2}{g} = k \tanh kh$

Infinite: $\frac{\omega^2}{g} = k$

Relation wave length and period

Finite: $\lambda = \frac{g}{2\pi} T^2 \tanh \frac{2\pi}{\lambda} h$

Infinite: $\lambda = \frac{g}{2\pi} T^2$

Incident wave profile

Finite: $\eta = A \sin(\omega t - kx)$

Infinite: $\eta = A \sin(\omega t - kx)$

TABLE 2.1 Formulas for linear wave theory I.

Dynamic pressure	Finite:	$p_D = \rho g A \frac{\cosh k(z+h)}{\cosh kh} \sin(\omega t - kx)$
	Infinite:	$p_D = \rho g A \sin(\omega t - kx)$
x-axis velocity component	Finite:	$V_x = \omega A \frac{\cosh k(z+h)}{\sinh kh} \sin(\omega t - kx)$
	Infinite:	$V_x = \omega A e^{kz} \sin(\omega t - kx)$
z-axis velocity component	Finite:	$V_z = \omega A \frac{\sinh k(z+h)}{\sinh kh} \cos(\omega t - kx)$
	Infinite:	$V_z = \omega A e^{kz} \cos(\omega t - kx)$
x-axis acceleration component	Finite:	$a_x = \omega^2 A \frac{\cosh k(z+h)}{\sinh kh} \cos(\omega t - kx)$
	Infinite:	$a_x = \omega^2 A e^{kz} \cos(\omega t - kx)$
z-axis acceleration component	Finite:	$a_z = -\omega^2 A \frac{\sinh k(z+h)}{\sinh kh} \sin(\omega t - kx)$
	Infinite:	$a_z = -\omega^2 A e^{kz} \sin(\omega t - kx)$

TABLE 2.2 Formulas for linear wave theory II.

$$\vec{x} = (x, y, z) = (x_0 - Ut, y_0, z_0), \quad (2.1)$$

where t is time.

Figure 2.1 shows an exact boundary value problem with two coordinates systems.

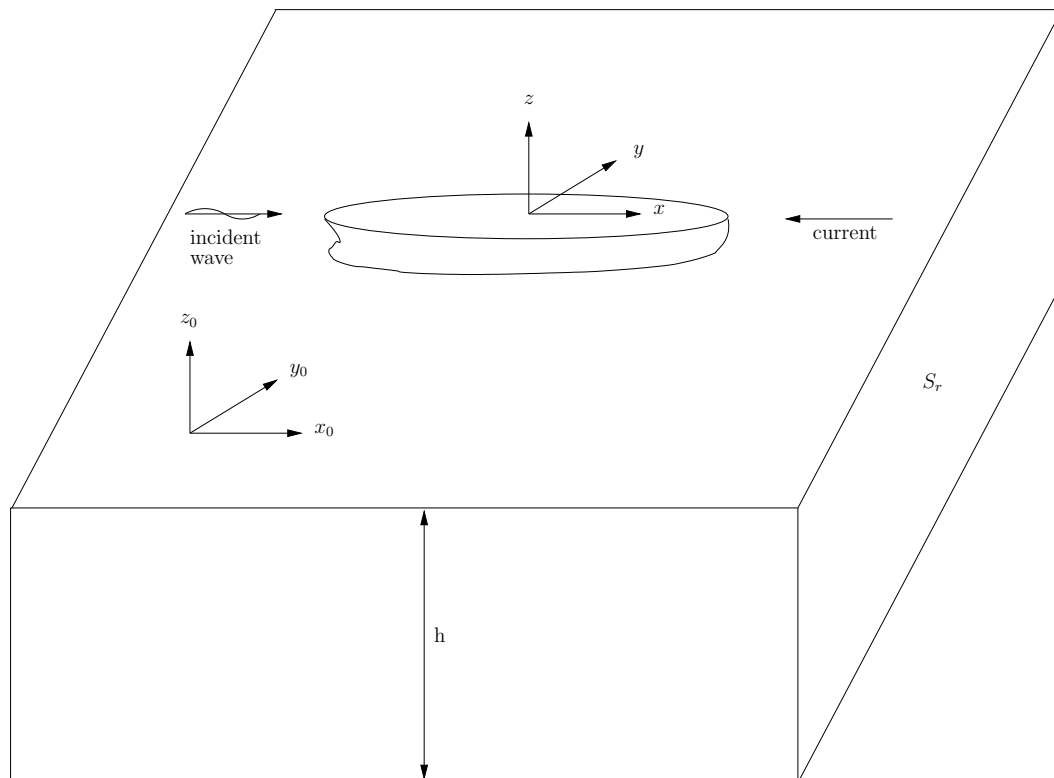


FIGURE 2.1. Exact boundary value problem with two coordinate systems.

2.2.2 Boundary value problem for global coordinate system

Since the ideal fluid is considered, the fluid is incompressible and the flow is irrotational. A surface tension is neglected. With an ideal fluid assumption, the properties

of the fluid can be described within the potential framework. Total velocity potential is $\Phi(\vec{x}_0, t)$. The fluid velocity vector $\vec{V}(\vec{x}_0, t)$ can be defined as $\nabla\Phi(\vec{x}_0, t)$. As a governing equation, the Laplace equation in the fluid domain is

$$\nabla^2\Phi = 0. \quad (2.2)$$

The fluid pressure $p(\vec{x}_0, t)$ is given by Bernoulli's equation

$$p - p_a = -\rho \left(\Phi_t + \frac{1}{2} \nabla\Phi \cdot \nabla\Phi + gz_0 + \text{constant} \right), \quad (2.3)$$

where ρ is the fluid density. g is the gravitational acceleration. p_a is the atmospheric pressure.

The free surface elevation can be defined as

$$z_0 = \hat{\eta}(x_0, y_0, t). \quad (2.4)$$

On the free surface, the kinematic boundary condition should be satisfied. This means that no fluid particles can leave on the free surface. This boundary condition can be satisfied with

$$\frac{D}{Dt}(\hat{\eta} - z_0) = 0 \quad \text{on } z_0 = \hat{\eta}, \quad (2.5)$$

where the total derivative is

$$\frac{D}{Dt} \equiv \frac{\partial}{\partial t} + \vec{V} \cdot \nabla. \quad (2.6)$$

The kinematic free surface boundary condition is

$$\frac{\partial \hat{\eta}}{\partial t} + \nabla \Phi \cdot \nabla \hat{\eta} = \frac{\partial \Phi}{\partial z_0} \quad \text{on } z_0 = \hat{\eta} \quad (2.7)$$

by the total derivative of the equation (2.5). An additional boundary condition should be imposed on the free surface. The dynamic free surface boundary condition means that the pressure on the free surface is atmospheric. From Bernoulli's equation (2.3), this boundary condition can be defined as

$$\frac{\partial \Phi}{\partial t} + \frac{1}{2} \nabla \Phi \cdot \nabla \Phi + g z_0 = 0 \quad \text{on } z_0 = \zeta. \quad (2.8)$$

The body surface is assumed impermeable so that no fluid enters or leaves on its surface. For a fixed body in a moving fluid, the body boundary condition can be satisfied with

$$\vec{V}_b \cdot \vec{n} = \vec{n} \cdot \nabla \Phi = 0. \quad (2.9)$$

When a body is moving with the velocity \vec{V}_b , the normal velocity on the body surface is equal to that of the adjacent fluid. This boundary condition can be treated appropriately by

$$\left(\vec{V}_b - \nabla \Phi \right) \cdot \nabla = 0, \quad (2.10)$$

where \vec{n} is the unit normal vector in a positive normal direction to be into the fluid domain.

The bottom boundary is assumed that no fluid can penetrate it. It does not move so there is no local velocity. This boundary condition is defined as

$$\frac{\partial \Phi}{\partial n} = 0. \quad (2.11)$$

The last boundary condition is the radiation condition. The waves generated by a body should propagate away from the body. This condition is expressed as

$$\Phi \sim \frac{Ae^{kz}}{\sqrt{r}} \sin(kr - \omega t + \epsilon), \quad (2.12)$$

where $r = \sqrt{x^2 + y^2}$ is a large horizontal distance from the body.

2.2.3 Boundary value problem for local coordinate system

For convenience, a local coordinate system is used for this study because a steady current effect can be taken into account more easily. The velocity potential and the wave elevation are redefined in this steady moving reference frame as follows:

$$\begin{aligned} \Phi(x_o - Ut, y_o, z_o, t) &= \phi(x, y, z, t), \\ \hat{\eta}(x_o - Ut, y_o, t) &= \eta(x, y, t). \end{aligned} \quad (2.13)$$

According to the Lorentz transformation, the partial derivative of velocity potential is

$$\frac{\partial}{\partial t} \Phi(x_o - Ut, y_o, z_o, t) = \left(\frac{\partial}{\partial t} - U \frac{\partial}{\partial x} \right) \phi(x, y, z, t). \quad (2.14)$$

Similarly, the time derivative for the wave elevation is

$$\frac{\partial}{\partial t} \hat{\eta}(x_o - Ut, y_o, t) = \left(\frac{\partial}{\partial t} - U \frac{\partial}{\partial x} \right) \eta(x, y, z, t). \quad (2.15)$$

The Laplace equation and boundary conditions can define the new velocity potential ϕ and the wave elevation η . The Laplace equation under local coordinates system is satisfying with the fluid domain is

$$\nabla^2 \phi = 0. \quad (2.16)$$

A free surface has two boundary conditions. The kinematic boundary condition is

$$\frac{\partial \eta}{\partial t} - U \frac{\partial \eta}{\partial x} + \nabla \phi \cdot \nabla \eta - \frac{\partial \phi}{\partial z} = 0, \quad (2.17)$$

and the dynamic boundary condition is

$$\frac{\partial \phi}{\partial t} - U \frac{\partial \phi}{\partial x} + \frac{1}{2} \nabla \phi \cdot \nabla \phi + g\eta = 0. \quad (2.18)$$

These free surface conditions include a current effect explicitly as considered when

a local coordinates moves. Boundary conditions for a body surface and a bottom surface are as follows:

$$\frac{\partial \phi}{\partial n} = \vec{V}_s \cdot \vec{n} \quad \text{on the body surface,} \quad (2.19)$$

$$\vec{n} \cdot \nabla \phi = 0 \quad \text{on the bottom surface.} \quad (2.20)$$

This boundary value problem has the same assumption under the potential framework. In the following section, this predefined boundary value problem will be derived to solve the wave-current body interaction problem using the perturbation method.

2.3 Perturbation method

It is difficult to solve the exact location of a free surface at each time step especially when a body pierces into a free surface. In the previous section, these boundary values were defined as an instantaneous wetted surface. This is called an exact boundary value problem or a fully nonlinear problem. To consider this free surface nonlinearity, the influence matrix needs to be calculated and inverted at every time step. As the free surface moves to a new position, this influence matrix also changes. The influence matrix only contains distance information between the source point and the field point.

The Stokes perturbation procedure is based on the assumptions of small wave amplitudes and small body motions. All the physical variables are perturbed with respect to the mean free surface and the mean wetted body surface. Therefore, all the lo-

cation information does not change over time. Here, this influence matrix consists of time independent values. For this reason, calculating the influence matrix and its inversion matrix is required only once. This matrix can be applied to different wave conditions unless it has numerical difficulties. Two independent parameters are introduced. One is the wave steepness parameter ϵ and the other is the current speed parameter δ :

$$\epsilon = \frac{H}{\lambda}, \quad \delta = \frac{U}{\sqrt{gL}}, \quad (2.21)$$

where H is the wave height. λ is the wave length. L is the characteristic length of the body.

The velocity potential and the wave elevation can be extended from the mean free surface. Both are rearranged by the order of the parameters as follows:

$$\phi(\vec{x}, t) = \underbrace{\bar{\phi}(\vec{x})}_{O(\delta)} + \underbrace{\epsilon\phi^{(1)}(\vec{x}, t)}_{O(\epsilon, \epsilon\delta)} + \underbrace{\epsilon^2\phi^{(2)}(\vec{x}, t)}_{O(\epsilon^2, \epsilon^2\delta, \dots)}, \quad (2.22)$$

$$\eta(\vec{x}, t) = \underbrace{\bar{\eta}(\vec{x})}_{O(\delta^2)} + \underbrace{\epsilon\eta^{(1)}(\vec{x}, t)}_{O(\epsilon, \epsilon\delta)} + \underbrace{\epsilon^2\eta^{(2)}(\vec{x}, t)}_{O(\epsilon^2, \epsilon^2\delta, \dots)}, \quad (2.23)$$

where $\bar{\phi}$ is the zeroth order steady disturbance potential. $\phi^{(1)}$ and $\phi^{(2)}$ are the time dependent first and second order velocity potentials.

In this perturbation expansion, the order of magnitudes of two independent parameters may be defined as $O(\delta) > O(\epsilon) > O(\epsilon\delta)$. All the terms in series higher than $O(\delta)$ or $O(\epsilon, \epsilon\delta)$ are neglected because these higher parameters are small enough.

2.4 Current forces and moments

A current effect is considered as one of the causes of the slow drift motion. An FPSO is considered in the potential theory so that the current effect can be similarly treated as a constant forward speed of a ship in the still water. Due to the current effect, the forces acting on an FPSO can be replaced with the forces that make a ship move forward. Either empirical formulas or a double body potential can be used for this study.

2.4.1 Components of current

The components of current were proposed by the 10th ISSC. The surface current velocity U is divided into the following components:

$$U = U_t + U_w + U_s + U_m + U_{set-up} + U_d, \quad (2.24)$$

where U_t is the tidal component. U_w is the component generated by local wind. U_s is the component generated by Stokes drift. U_m is the component from major ocean circulation, if any, depending on geographical location. U_{set-up} is the component due to set-up phenomena and storm surges. U_d is the local density-driven current governed by strong density jumps in the upper ocean.

U_t and U_s will be discussed in the next few subsections.

2.4.2 Empirical formulas

Empirical formulas may be used to calculate current forces and moments on an FPSO. These empirical formulas assume a small Froude number (F_n). Wave frequency damping is neglected.

An empirical formula is

$$F_L = \frac{0.075}{(\log_{10} Rn - 2)^2} \frac{1}{2} \rho A_w U^2 \cos\beta |\cos\beta|, \quad (2.25)$$

where β is the angle between the current velocity and longitudinal x-axis. A_w is the wetted surface of the ship. F_L is the longitudinal direction drag force due to the friction. R_n is $UL|\cos\beta|/\nu$.

As an alternative, the generalized Hughes (1954) formula is

$$F_L = \frac{0.066(1+f)}{(\log_{10} Rn - 2.03)^2} \frac{1}{2} \rho A_w U^2 \cos\beta |\cos\beta|, \quad (2.26)$$

where f is the form factor found in the experiments. f is between 0.2 and 0.4 when $\beta = 0$. f may be up to 0.8 when the flow separates in the stern.

2.4.3 Current heading

When the current direction is not close to the longitudinal axis of the ship, the cross-flow principle may be used to evaluate the transverse current force and the current yaw moment on the ship. This cross-flow principle has the following assumptions.

- the flow separates due to cross-flow past the ship
- longitudinal current components do not influence the transverse forces on a cross-section
- the transverse force on a cross-section is mainly due to the separated flow effects on the pressure distribution around the ship

Transverse current force(F_T) is

$$F_T = \frac{1}{2}\rho \left[\int_L dx C_D(x) D(x) \right] U^2 \sin \beta |\sin \beta|, \quad (2.27)$$

where L is the length of a ship. C_D is the drag coefficient for the cross-flow and $D(x)$ is the sectional draft.

C_D value may be evaluated when cross-flow passes an infinitely long cylinder with the cross-sectional area of the ship at the longitudinal coordinate x . The important parameters influencing C_D are as follows:

- instance free-surface effects
- beam-draft ratio
- bilge radius
- bilge keel dimensions
- Reynolds number

Yaw moment(F_Y) is

$$F_Y = \frac{1}{2}\rho \left[\int_L dx C_D(x) D(x) x \right] U^2 \sin \beta |\sin \beta| + \frac{1}{2} U^2 (A_{22} - A_{11}) \sin 2\beta, \quad (2.28)$$

where A_{11} is the added mass in surge and A_{22} is the added mass in sway.

$$A_{22}(x) = -\rho \int_{W_0} \phi_2 n_2 ds, \quad (2.29)$$

where W_0 is the wetted cross-sectional surface.

2.4.4 Munk moment

The last term of the equation (2.28) is used for Munk moment. This moment can be derived from the non-separated potential theory. First, rigid free surface condition and strip theory are used: Second, x-derivatives to y- and z- derivatives are neglected. After these procedures, ϕ satisfies the two-dimensional Laplace equation in the cross-sectional plane. Then, body boundary conditions are

$$\frac{\partial \phi}{\partial n} = -n_2 U \sin \beta \quad (2.30)$$

and

$$\phi = -U \sin \beta \phi_2, \quad (2.31)$$

where ϕ_2 is normalized by two-dimensional sway velocity potential at zero frequency.

Bernoulli's equation excluding hydrostatic pressure is

$$p + \frac{\rho}{2} \left[\left(\frac{\partial \Phi}{\partial x} \right)^2 + \left(\frac{\partial \Phi}{\partial y} \right)^2 + \left(\frac{\partial \Phi}{\partial z} \right)^2 \right] = p_0 + \frac{1}{2} \rho U^2 \quad (2.32)$$

and

$$\begin{aligned} p &= -\rho U \cos \beta \frac{\partial \phi}{\partial x} - \rho U \sin \beta \frac{\partial \phi}{\partial y} - \frac{1}{2} \rho \left[\left(\frac{\partial \Phi}{\partial x} \right)^2 + \left(\frac{\partial \Phi}{\partial y} \right)^2 + \left(\frac{\partial \Phi}{\partial z} \right)^2 \right] \\ &= \frac{\rho}{2} U^2 \sin 2\beta \frac{\partial \phi_2}{\partial x} + \rho U^2 \sin^2 \beta \left\{ \frac{\partial \phi_2}{\partial y} - \frac{1}{2} |\nabla \phi|^2 \right\}. \end{aligned} \quad (2.33)$$

The yaw moment can be written as

$$\begin{aligned} F_6 &= \frac{\rho}{2} U^2 \sin 2\beta \int_L dx x \int_{W_0} \frac{\partial \phi_2}{\partial x} n_2 ds \\ &+ \rho U^2 \sin^2 \beta \int_L ds x \int_{W_0} \left\{ \frac{\partial \phi_2}{\partial y} - \frac{1}{2} |\nabla \phi_2|^2 \right\} n_2 ds. \end{aligned} \quad (2.34)$$

Faltinsen (1990) showed a good agreement in the experiment when $\beta = 1/2\pi$. Munk moment is maximum when $\beta = 1/4\pi$.

2.4.5 Double body flow

The Neumann-Kelvin linearization works well for slender bodies. However, for more blunt bodies, the approximation of the body boundary condition is unsatisfactory.

As an alternative to improve the body-boundary condition, the double-body approximation includes a perturbation of the uniform stream. The steady potential is

$$\Phi^{db} = -U_0x + \phi^{db}, \quad (2.35)$$

which satisfies the following boundary-value problem:

$$\nabla^2 \Phi^{db} = 0, \quad (2.36)$$

$$\frac{\partial \Phi^{db}}{\partial z} = 0 \quad \text{on } z = 0, \quad (2.37)$$

$$\vec{n} \cdot \nabla \Phi^{db} = 0 \quad \text{on } \bar{S}_b, \quad (2.38)$$

$$\nabla \Phi^{db} \rightarrow (-U_0, 0, 0) \quad \text{on } R_1 \rightarrow \infty. \quad (2.39)$$

According to Newman (1978), the double-body m-terms can be written as

$$\begin{aligned} (m_1, m_2, m_3) &= -(\vec{n} \cdot \nabla) \nabla \Phi^{db} \\ &= -\left(n_1 \frac{\partial^2 \Phi^{db}}{\partial x^2} + n_2 \frac{\partial^2 \Phi^{db}}{\partial x \partial y} + n_3 \frac{\partial^2 \Phi^{db}}{\partial x \partial z} \right. \\ &\quad \left. n_1 \frac{\partial^2 \Phi^{db}}{\partial y \partial x} + n_2 \frac{\partial^2 \Phi^{db}}{\partial y^2} + n_3 \frac{\partial^2 \Phi^{db}}{\partial y \partial z} \right) \end{aligned}$$

$$n_1 \frac{\partial^2 \Phi^{db}}{\partial z \partial x} + n_2 \frac{\partial^2 \Phi^{db}}{\partial z \partial y} + n_3 \frac{\partial^2 \Phi^{db}}{\partial z^2}) \quad (2.40)$$

and

$$\begin{aligned} (m_4, m_5, m_6) &= \vec{r}_g \times (m_1, m_2, m_3) - \vec{n} \times \nabla \Phi^{db} \\ &= \vec{r}_g \times (m_1, m_2, m_3) \\ &\quad + \left(n_3 \frac{\partial \Phi^{db}}{\partial y} - n_2 \frac{\partial \Phi^{db}}{\partial z} + n_1 \frac{\partial \Phi^{db}}{\partial z} \right. \\ &\quad \left. + n_3 \frac{\partial \Phi^{db}}{\partial x} + n_2 \frac{\partial \Phi^{db}}{\partial x} + n_1 \frac{\partial \Phi^{db}}{\partial y} \right). \end{aligned} \quad (2.41)$$

2.5 Wave forces and moments

Under the potential flow assumption, the pressure distribution over the body surface can be determined by the unsteady Bernoulli's equation. This study employed a perturbation method and included the current effect. For convenience, the Bernoulli's equation can be expressed in a local coordinates system as follows:

$$p = -\rho \left(\frac{\partial \phi}{\partial t} - U \frac{\partial \phi}{\partial x} + \frac{1}{2} \nabla \phi \cdot \nabla \phi + gz \right). \quad (2.42)$$

After the velocity potential is determined, the wave forces and moments can be obtained by carrying out an integration of the pressure over the instantaneous wetted body surface S_i .

$$\vec{F} = \int_{S_i} p \vec{n} dS. \quad (2.43)$$

$$\vec{M} = \int_{S_i} p (\vec{n} \times \vec{r}) dS. \quad (2.44)$$

These moments are calculated relative to the center of gravity, not to the origin. Unfortunately, the actual position of the body, S_i is unknown. To determine forces and moments, the perturbation method is adopted. A fluctuation of the still water level on a body can be replaced with a mean wetted body contour line. The integration on the instantaneous wetted body surface can be separately treated in the equation (2.45):

$$\int_{S_i} F(\vec{x}) dS = \int_{S_b} F(\vec{x}) dS + \int_{S_o} F(\vec{x}) dS, \quad (2.45)$$

where S_b is the mean body wetted surface and S_o is an oscillatory disturbance of the mean body wetted surface over the still water level.

The equation (2.45) can be approximated as

$$\int_{S_o} F(\vec{x}) dS \approx \int_{W_o} \int_{S_o}^n F(\vec{x}) dz dl, \quad (2.46)$$

where W_o denotes the water line contour and l denotes the distance measured along the water line contour.

The pressure p_i on the instantaneous body surface can also be expanded by a Taylor series from the mean water line.

$$p_i = p_o + \vec{\alpha} \cdot \nabla p_o + \left(\frac{1}{2} \vec{\alpha} \cdot \nabla^2 \right) p_o + \dots \quad (2.47)$$

p_o , the pressure around mean position of the body can also be expressed by a perturbation series as follows:

$$p_o = \bar{p} + \epsilon p^{(1)} + \epsilon^2 p^{(2)} + \dots \quad (2.48)$$

The expanded pressure terms can be collected by equal powers of ϵ in the equations (2.49) - (2.51):

$$\bar{p}_i = \bar{p}. \quad (2.49)$$

$$p_i^{(1)} = p^{(1)} + \left(\vec{\Xi}^{(1)} + \vec{\Omega}^{(1)} \times \vec{r} \right) \cdot \nabla \bar{p}. \quad (2.50)$$

$$\begin{aligned} p_i^{(2)} &= p^{(2)} + \left[\vec{\Xi}^{(2)} + \left(\vec{\Omega}^{(2)} \times \vec{r} \right) + \vec{\Omega}^{(1)} \times \left(\vec{\Omega}^{(1)} \times \vec{r} \right) \right] \cdot \nabla \bar{p} \\ &+ \left(\vec{\Xi}^{(1)} + \vec{\Omega}^{(1)} \times \vec{r} \right) \cdot \nabla p^{(1)} + \frac{1}{2} \left[\left(\vec{\Xi}^{(1)} + \vec{\Omega}^{(1)} \times \vec{r} \right) \cdot \nabla \right]^2 \bar{p}. \end{aligned} \quad (2.51)$$

From the Bernoulli's equation and the perturbation series for the potential, the components of the pressure series on the average wetted surface can be obtained as follows:

$$\bar{p} = -\rho \left(gz + \frac{1}{2} \nabla \bar{\phi} \cdot \nabla \bar{\phi} - \frac{1}{2} U^2 \right). \quad (2.52)$$

$$p^{(1)} = -\rho \left(\nabla \bar{\phi} \cdot \nabla \phi^{(1)} + \frac{\partial \phi^{(1)}}{\partial t} - U \frac{\partial \phi^{(1)}}{\partial x} \right). \quad (2.53)$$

$$p^{(2)} = -\rho \left(\frac{1}{2} \nabla \phi^{(1)} \cdot \nabla \phi^{(1)} + \nabla \bar{\phi} \cdot \nabla \phi^{(2)} + \frac{\partial \phi^{(1)}}{\partial t} - U \frac{\partial \phi^{(1)}}{\partial x} \right). \quad (2.54)$$

As mentioned earlier, we assumed that δ is small so that the terms of $O(\delta^2)$ in \bar{p} is neglected.

The steady contribution at $O(\delta)$ is then given as

$$\bar{\vec{F}} = \int_{S_b} \bar{p}_i \bar{\vec{n}} dS = \begin{Bmatrix} 0 \\ 0 \\ \rho g \forall \end{Bmatrix} \quad (2.55)$$

and

$$\bar{\vec{M}} = \int_{S_b} \bar{p}_i (\bar{\vec{n}} \times \bar{\vec{r}}) dS = \rho g \forall \begin{Bmatrix} y_b \\ -x_b \\ 0 \end{Bmatrix}, \quad (2.56)$$

where \forall is the total displacement of the body. x_b and y_b are the center of the body.

The unsteady first order forces and moments can then be obtained from collecting the terms of $O(\epsilon)$ and $O(\epsilon\delta)$. For convenience, we leave out the over-bar which denotes the values on the mean position. The first order forces and moments are given as:

$$\begin{aligned}
\vec{F}^{(1)} &= \int_{S_b} \left(p_i^{(1)} \bar{\vec{n}} + \bar{p}_i \bar{\vec{n}}^{(1)} \right) dS \\
&= -\rho \int_{S_b} \left(\frac{\partial \phi^{(1)}}{\partial t} - U \frac{\partial \phi^{(1)}}{\partial x} + \nabla \phi^{(1)} \cdot \nabla \bar{\phi} \right) \bar{\vec{n}} dS + \vec{F}_{hs}^{(1)} \quad (2.57)
\end{aligned}$$

and

$$\begin{aligned}
\vec{M}^{(1)} &= \int_{S_b} \left[p_i^{(1)} (\bar{\vec{r}} \times \bar{\vec{n}}) + \bar{p}_i \bar{\vec{\Omega}}^{(1)} \times (\bar{\vec{r}} \times \bar{\vec{n}}) \right] dS \\
&= -\rho \int_{S_b} \left(\frac{\partial \phi^{(1)}}{\partial t} - U \frac{\partial \phi^{(1)}}{\partial x} + \nabla \phi^{(1)} \cdot \nabla \bar{\phi} \right) (\bar{\vec{r}} \times \bar{\vec{n}}) dS + \vec{M}_{hs}^{(1)}. \quad (2.58)
\end{aligned}$$

In addition, $\vec{F}_{hs}^{(1)}$ and $\vec{M}_{hs}^{(1)}$ are the first order hydrostatic pressure contributions due to the body motion:

$$\vec{F}_{hs}^{(1)} = -\rho g A_{wl} \left(\bar{\Xi}_3^{(1)} + y_f \Omega_1^{(1)} - x_f \Omega_2^{(1)} \right) \vec{k} \quad (2.59)$$

and

$$\vec{M}_{hs}^{(1)} = -\rho g \int_{S_b} (\bar{\vec{r}} \times \bar{\vec{n}}) \left(\bar{\Xi}_3^{(1)} + y_f \Omega_1^{(1)} - x_f \Omega_2^{(1)} \right) dS, \quad (2.60)$$

where A_{wl} is the area of the water line surface. x_f and y_f are the center of the buoyancy of A_{wl} . The centers of gravity and buoyancy are on the same vertical axis so that the value of the moments in the equation (2.56) becomes zero.

Although only the first order potential is considered, the integral over the oscillatory wetted surface contributes to the second order quantities. These second order forces and moments come from the quadratic terms of the first order quantities.

2.5.1 Wave drift damping

This study was performed under the small wave amplitude condition and viscous forces were not taken into account. Under these assumptions, a wave damping coefficient is an important damping force for slowly varying motions. A wave drift damping is proportional to the square of an incoming wave amplitude. This drift damping is also proportional to the slowly varying velocity of the body. Therefore, this slowly varying damping can be considered as the effect of the second order mean drift force with respect to slowly varying forward speed of the body.

This study adopted the same method proposed by Wichers & Huijsmans (1984). The drift force with current speed can be expressed with a Taylor expansion as the equation (2.61). This force can expand with respect to the drift velocity. This velocity may be a small forward velocity of the body or current speed.

$$\bar{F} = \bar{F}^{(0)} + U \frac{\partial \bar{F}^{(1)}}{\partial U} + \dots, \quad (2.61)$$

where $\bar{F}^{(0)}$ is the wave drift force on a body with zero forward speed.

The second term contains the body forward velocity or current speed. This term $\partial \bar{F}^{(1)} / \partial U$ indicates a wave drift damping coefficient. The central difference can be used to calculate the second term numerically.

$$\left(\frac{\partial \bar{F}^{(1)}}{\partial U}\right)_{U=0} = \frac{\bar{F}(U) - \bar{F}(-U)}{2\Delta U}. \quad (2.62)$$

2.5.2 Equations of motion

The motions of a floating body may be subsequently obtained from applying Newton's second law. The response can be calculated by solving the equation of motion. Assuming that the motion is harmonic, the total exciting force acting on the body may be divided into the added mass force, radiation damping force, and hydrostatic force. The typical equation of motion is shown with $\vec{X} = \{\Xi_1, \Xi_2, \Xi_3, \Omega_1, \Omega_2, \Omega_3\}^T$.

$$(M + M_A)\frac{\partial \vec{X}}{\partial t^2} + B\frac{\partial \vec{X}}{\partial t} + C\vec{X} = \begin{Bmatrix} \vec{F}_{ext} \\ \vec{M}_{ext} \end{Bmatrix}. \quad (2.63)$$

The restoring force coefficients C are the only geometric dependent and can be obtained from hydrostatic calculation. The hydrostatic coefficients in matrix C are defined as:

$$C(3,3) = \rho g \int_{S_b} n_z dS$$

$$C(3,4) = \rho g \int_{S_b} y n_z dS$$

$$C(3,5) = -\rho g \int_{S_b} x n_z dS$$

$$\begin{aligned}
C(4,4) &= \rho g \int_{S_b} y^2 n_z dS + \rho g \forall (z_b - z_g) \\
C(4,5) &= \rho g \int_{S_b} x y n_z dS \\
C(4,6) &= -\rho g \forall x_b + m g x_g \\
C(5,5) &= \rho g \int_{S_b} x^2 n_z dS + \rho g \forall (z_b - z_g) \\
C(5,6) &= -\rho g \forall y_b + m g y_g,
\end{aligned} \tag{2.64}$$

where $C(i, j) = C(j, i)$ for all (i, j) except for $C(4, 6)$ and $C(5, 6)$.

The other values of the indices (i, j) are

$$C(i, j) = 0. \tag{2.65}$$

For a body in the free stable buoyancy, the following relations hold

$$m = \rho \forall, \quad x_b = x_g \quad y_b = y_g \tag{2.66}$$

and

$$C(4,4) > \rho g \forall z_g, \quad C(5,5) > \rho g \forall z_g, \tag{2.67}$$

where m is the body mass and (x_g, y_g, z_g) are the coordinates of the center of gravity

as defined in the previous section.

M is a symmetric mass matrix shown in the equation (2.68). This consists of the body mass and the moment of inertia.

$$M = \begin{bmatrix} m & 0 & 0 & 0 & mz_g & -my_g \\ 0 & m & 0 & -mz_g & 0 & mx_g \\ 0 & 0 & m & my_g & -mx_g & 0 \\ 0 & -mz_g & my_g & I_{11} & I_{12} & I_{13} \\ mz_g & 0 & -mx_g & I_{21} & I_{22} & I_{23} \\ -my_g & -mx_g & 0 & I_{31} & I_{32} & I_{33} \end{bmatrix} \quad (2.68)$$

The moments of inertia (I_{ij}) are defined in terms of the corresponding radius of the gyration (r_{ij}).

$$I_{ij} = \rho \forall r_{ij} |r_{ij}|. \quad (2.69)$$

The added mass coefficients M_A and the radiation damping coefficient B can be obtained from the solution of the radiation problem. From the equations (2.57) and (2.58), first order forces and moments can be obtained. Then this forces and moments can be divided into the terms proportional to the body acceleration and the velocity as follows:

$$F_{ij} = -M_{A_{ij}} \frac{\partial^2 X_j}{\partial t^2} - B_{ij} \frac{\partial X_j}{\partial t}, \quad (2.70)$$

where j is the direction of the motion, either transversal or rotational. The i is the

direction of the force.

Similarly, the wave exciting forces \vec{F}_{ext} and the moment \vec{M}_{ext} are evaluated from the solution of the diffraction problem.

2.6 Boundary type solution procedures

Boundary element method(BEM) is one of the boundary type solution procedures. After Trefftz performed a BEM calculation (Hunter & Pullan 2003) to get the contraction coefficient of a round jet issuing from an infinite tank in 1917, it has been applied to many engineering fields such as ocean engineering, foundations, aerodynamics, etc., particularly in fields with infinite or semi-infinite domains. It is because these engineering problems can be solved by the boundary discretization when the object is governed by the linear and homogeneous differential equation.

2.6.1 Original Trefftz method

The basic idea of boundary element methods was proposed first by Trefftz in 1926. The original Trefftz method is an indirect formulation. When functions satisfy the differential equations, these can be used as an approximated solution inside the domain. The solution of the problem can be approximated by the superposition of the functions. These functions have the unknown parameters to be determined. These approximated functions can satisfy the boundary conditions by collocation, least square, or the Galerkin method.

The Laplace equation is described as an example of Trefftz method. Poisson equation's homogeneous form describes the calculation domain in this study. The bound-

ary value problem requires solving a Laplace equation with boundary conditions. The Laplace equation is

$$\nabla^2\phi = 0 \quad (\text{in } \Omega). \quad (2.71)$$

We can sort out boundary conditions simply with two categories:

- essential conditions: $\phi = \bar{\phi}$ on Γ_1
- natural conditions: $\frac{\partial\phi}{\partial n} = \frac{\partial\bar{\phi}}{\partial n}$ on Γ_2 ,

where ϕ and $\partial\phi/\partial n$ are potentials and its derivatives in the normal direction respectively. Ω denotes the object domain. Γ_1 , and Γ_2 denote its boundaries. $\bar{\phi}$ and $\partial\bar{\phi}/\partial n$ are the specified values on the boundary.

The potential $\phi(p)$ at arbitrary point p is approximated by the superposition of functions as follows:

$$\phi(p) \approx \tilde{\phi}(p) = a_1\phi_1^* + a_2\phi_2^* + \cdots + a_N\phi_N^* = \{a_1 \cdots a_N\}^T \cdot \{\phi_1^* \cdots \phi_N^*\}, \quad (2.72)$$

where N is the total number of the functions and $\{a_1 \cdots a_N\}^T$ denotes the vector of unknown parameters.

Similarly, the derivative of the equation (2.72) is

$$\frac{\partial\phi(p)}{\partial n} \approx \frac{\partial\tilde{\phi}(p)}{\partial n} = \{a_1 \cdots a_N\}^T \cdot \left\{ \frac{\partial\phi_1^*}{\partial n} \cdots \frac{\partial\phi_N^*}{\partial n} \right\}. \quad (2.73)$$

Both the equations (2.72) and (2.73) as approximated solutions satisfy the equation (2.71) so that the residuals yield. The residuals at point p are

$$R_1 \equiv \tilde{\phi} - \bar{\phi} = \{a\}^T \cdot \{\phi^*(p)\} - \bar{\phi} \neq 0, \quad (2.74)$$

where p on Γ_1

and

$$R_2 \equiv \frac{\partial \tilde{\phi}}{\partial n} - \frac{\partial \bar{\phi}}{\partial n} = \{a\}^T \cdot \left\{ \frac{\partial \phi^*}{\partial n}(p) \right\} - \frac{\partial \bar{\phi}}{\partial n} \neq 0, \quad (2.75)$$

where p on Γ_2

So far, the solution of the problem is approximated by the superposition of the functions that satisfy the Laplace equation. Accordingly, the approximated solution satisfies the boundary condition. This approximated solution makes some residuals or errors in the boundary. To reduce these residuals, the original Trefftz method adopts a collocation method. R_1 and R_2 as in the equations (2.74) and (2.75) respectively are forced to vanish at the boundary collocation points. To minimize residuals in the collocation points, the least square and the Galerkin method are commonly used. In the Galerkin method, R_1 and R_2 are minimized by

$$\int_{\Gamma_1} \frac{\partial \tilde{\phi}}{\partial n} R_1 d\Gamma - \int_{\Gamma_2} \tilde{\phi} R_2 d\Gamma = 0. \quad (2.76)$$

The general procedures for the original Trefftz method are summarized as below:

Compose approximated solution
by superposition of interpolating functions.

↓

Get residuals of boundary conditions.

↓

Minimize residuals with
collocation, least square, and the Galerkin method.

↓

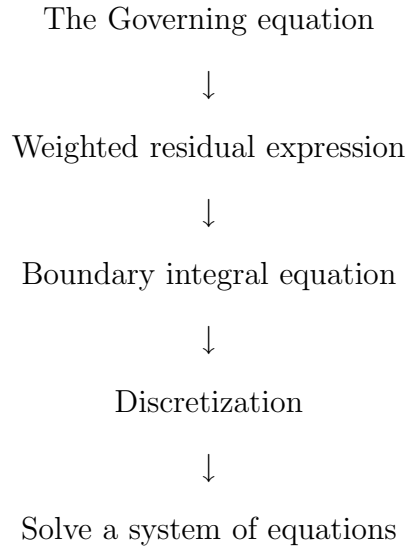
Solve a system of equations.

For more details and examples, Brebbia & Dominguez (1989) and Beer (2001) are good references.

The Trefftz method has some advantages when compared with the Ritz method. When the solution of the differential equation is known, the actual boundary conditions can be approximated. Accordingly, the solutions that precisely satisfy the differential equations can be used for approximating boundary conditions with minimized residuals. It also has some application issues in the engineering field. Generally, the original Trefftz method is known to be unsuitable for writing general purpose programs because the accuracy is not satisfactory and its convergence cannot be assured. The solution of differential equations also needs to be as simple as possible to reduce computation time.

2.6.2 Direct method

An alternative approach for boundary type solution is a direct method. Its general procedures are as follows:



To solve the equation (2.71), the weighted residual method is introduced. We make a weak formula with fundamental solutions.

$$\int_{\Omega} (\nabla^2 \phi) W d\Omega = 0. \quad (2.77)$$

Integrating twice by parts to make $\nabla^2 W$,

$$\begin{aligned} (\nabla \phi) W - \int_{\Omega} \nabla \phi \cdot \nabla W d\Omega &= 0 \\ \int_{\Gamma} \frac{\partial \phi}{\partial n} W d\Gamma - \int_{\Omega} \nabla \phi \cdot \nabla W d\Omega &= 0 \\ \int_{\Gamma} \frac{\partial \phi}{\partial n} W d\Gamma - \phi \nabla W + \int_{\Omega} \phi (\nabla^2 W) d\Omega &= 0 \\ \int_{\Gamma} \frac{\partial \phi}{\partial n} W d\Gamma - \int_{\Gamma} \frac{\partial W}{\partial n} \phi d\Gamma + \int_{\Omega} \phi (\nabla^2 W) d\Omega &= 0 \end{aligned} \quad (2.78)$$

2.6.3 Common fundamental solutions in BEM

These fundamentals in BEM can be applied in many engineering fields. Table (2.3) provides a fundamental solution with BEM. The next section 2.7 shows BEM in relation to the velocity potential problem.

2.7 The boundary integral equation

The boundary integral equation will be discussed as a method to solve a Laplace equation with boundary conditions. Jaswon (1963) showed that this boundary integral equation of potential theory could be solved to a tolerable accuracy. He performed not only Fredholm's first and second kind integral equations but the coupled one as well. Symm (1963) alternatively used Green's formula. He took field points to lie on the boundary itself and then identified the connecting boundary values and normal derivatives of a harmonic function. This procedure yielded integral equation formulations covering the mixed boundary value problems of potential theory.

2.7.1 Weight residual method

In order to obtain the proper boundary integral equation, a Laplace-type boundary value problem is first considered.

$$\nabla^2 u = 0, \quad \text{in } \Omega_o, \quad (2.79)$$

$$u = \bar{u}, \quad \text{on } \Gamma_1, \quad (2.80)$$

One-dimensional	
Laplace	equation $\frac{\partial^2 u^*}{\partial x^2} + \delta_0 = 0$
	solution $u^* = \frac{r}{2}$
Diffusion	equation $\frac{\partial u^*}{\partial x} - \frac{1}{k} \frac{\partial u^*}{\partial t} + \delta_0 \delta(t) = 0$
	where, k is the diffusivity
	solution $u^* = -\frac{H(t)}{\sqrt{4\pi kt}} \exp\left(-\frac{r^2}{4kt}\right)$
	where, $r = x $
	H is the unite step function
Two-dimensional	
Laplace	equation $\frac{\partial^2 u^*}{\partial x^2} + \frac{\partial^2 u^*}{\partial y^2} + \delta_0 = 0$
	solution $u^* = \frac{1}{2\pi} \log\left(\frac{1}{r}\right)$
Diffusion	equation $\frac{\partial^2 u^*}{\partial x^2} + \frac{\partial^2 u^*}{\partial y^2} - \frac{1}{k} \frac{\partial u^*}{\partial t} = 0$
	where, k is the diffusivity
	solution $u^* = -\frac{1}{(4\pi kt)^{\frac{3}{2}}} \exp\left(-\frac{r^2}{4kt}\right)$
	where, $r = \sqrt{x^2 + y^2}$
Three-dimensional	
Laplace	equation $\frac{\partial^2 u^*}{\partial x^2} + \frac{\partial^2 u^*}{\partial y^2} + \frac{\partial^2 u^*}{\partial z^2} + \delta_0 = 0$
	solution $u^* = \frac{1}{4\pi r}$
	where, $r = \sqrt{x^2 + y^2 + z^2}$

TABLE 2.3 Fundamental solutions for BEM.

$$v = \frac{\partial u}{\partial n} = \bar{v}, \quad \text{on } \Gamma_2, \quad (2.81)$$

where Ω_0 in the equation (2.79) is a fluid domain. Γ_1 in the equation (2.80) is an essential (Dirichlet) boundary condition and Γ_2 in the equation (2.81) is natural (Neumann).

The weighted residual statement for this boundary value problem can be expressed as the equation (2.82).

$$\int_{\Omega_o} \nabla^2 u u^* d\Omega + \int_{\Gamma_2} (\bar{v} - v) u^* d\Gamma + \int_{\Gamma_1} (u - \bar{u}) \frac{\partial u^*}{\partial n} d\Gamma = 0. \quad (2.82)$$

The inner product of the errors and weight functions are used. u^* is a known weight function or a trial function. Using the Green's second identity, the first term in the equation (2.82) can be rewritten as

$$\int_{\Omega_o} \nabla^2 \nabla^* + \int_{\Gamma} \left(u^* \frac{\partial u}{\partial n} - u \frac{\partial u^*}{\partial n} d\Gamma \right), \quad (2.83)$$

where $\partial u / \partial n = v$.

Substitution of the equation (2.83) into (2.82) leads to

$$\begin{aligned} \int_{\Omega_o} u \nabla^2 u^* d\Omega_o &= - \int_{\Gamma_1} \left(u^* v - u \frac{\partial u^*}{\partial n} \right) d\Gamma - \int_{\Gamma_2} \left(u^* v - u \frac{\partial u^*}{\partial n} \right) d\Gamma \\ &\quad - \int_{\Gamma_1} \left(u - \bar{u} \frac{\partial u^*}{\partial n} \right) d\Gamma - \int_{\Gamma_2} (\bar{v} - v) u^* d\Gamma, \end{aligned} \quad (2.84)$$

or generally,

$$\int_{\Omega_o} u \nabla^2 u^* d\Omega_o = - \int_{\Gamma} u^* v d\Gamma + \int_{\Gamma} u v^* d\Gamma. \quad (2.85)$$

The equation (2.85) represents the general integral equation with the prescribed boundary conditions. From this procedure, a boundary integral equation will be set. Its discretized form will be discussed in the following section. Detailed procedures to derive the boundary integral equation can be found in Brebbia & Dominguez (1989) and Beer (2001).

2.7.2 The Green function

A simple Green function is adopted as a fundamental solution of a Laplace equation. The three-dimensional Green function is

$$G(x, y, z; x_i, y_i, z_i) = \frac{1}{R}, \quad (2.86)$$

where

$$R = \sqrt{(x - x_i)^2 + (y - y_i)^2 + (z - z_i)^2}. \quad (2.87)$$

This is equivalent to the velocity potential generated by a simple Rankine source. The advantages of this Green function come from its simplicity. It is the only function of the distance between two node points. It is easy for a general problem to be extended when compared with other complicated Green functions. Figure 2.2 shows the simple

Green function.

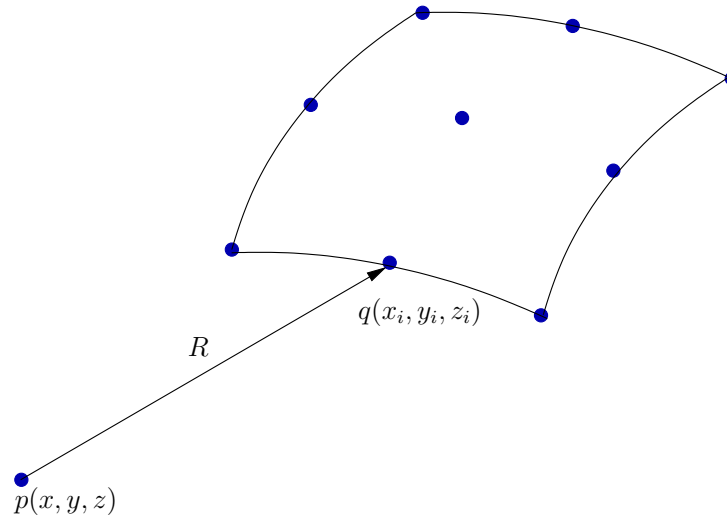


FIGURE 2.2. Definition of the simple Green function.

For convenience, we assume that the water depth is constant and the body is symmetric with respect to the xz plane. Then we can use respective image sources so that the integrating surface can be reduced to half of the body surface, free surface, and open boundary surface. In this case the Green function should be given as

$$G = \frac{1}{R_1} + \frac{1}{R_2} + \frac{1}{R_3} + \frac{1}{R_4}, \quad (2.88)$$

where

$$R_1 = \sqrt{(x - x_i)^2 + (y - y_i)^2 + (z - z_i)^2}. \quad (2.89)$$

$$R_2 = \sqrt{(x - x_i)^2 + (y + y_i)^2 + (z - z_i)^2}. \quad (2.90)$$

$$R_3 = \sqrt{(x - x_i)^2 + (y - y_i)^2 + (z + z_i + 2h)^2}. \quad (2.91)$$

$$R_4 = \sqrt{(x - x_i)^2 + (y + y_i)^2 + (z + z_i + 2h)^2}. \quad (2.92)$$

2.7.3 Laplace equation with Green function

The Laplace equation has a weighting term as follows:

$$\nabla^2 G(p, q) = \hat{c}(p)\delta(p, q), \quad (2.93)$$

where δ is Dirac delta function. $p = (x, y, z)$ and $q = (x_i, y_i, z_i)$ are the coordinates of the field and the source point, respectively. $\hat{c}(p)$ is a solid angle.

Substituting the equation (2.93) to the equation (2.85) yields the boundary integral equation as follows:

$$\hat{c}(p)\phi(p) + \int_{\Gamma} \frac{\partial G(p, q)}{\partial n(q)} \phi(q) d\Gamma = \int_{\Gamma} G(p, q) \frac{\partial \phi(q)}{\partial n(q)} d\Gamma. \quad (2.94)$$

The boundary Γ can be divided into the body surface (S_B), free surface (S_F), and open boundary (S_R). The equation (2.94) can be rewritten as follows:

$$\begin{aligned} \hat{c}(p)\phi(p) &= \int_{S_F \cup S_R} G(p, q) \frac{\partial \phi(q)}{\partial n(q)} d\Gamma + \int_{S_B} \frac{\partial G(p, q)}{\partial n(q)} \phi(q) d\Gamma \\ &= - \int_{S_F \cup S_R} \frac{\partial G(p, q)}{\partial n(q)} \phi(q) d\Gamma + \int_{S_B} G(p, q) \frac{\partial \phi(q)}{\partial n(q)} d\Gamma. \end{aligned} \quad (2.95)$$

The following Chapter III shows how to solve the equation (2.95) numerically.

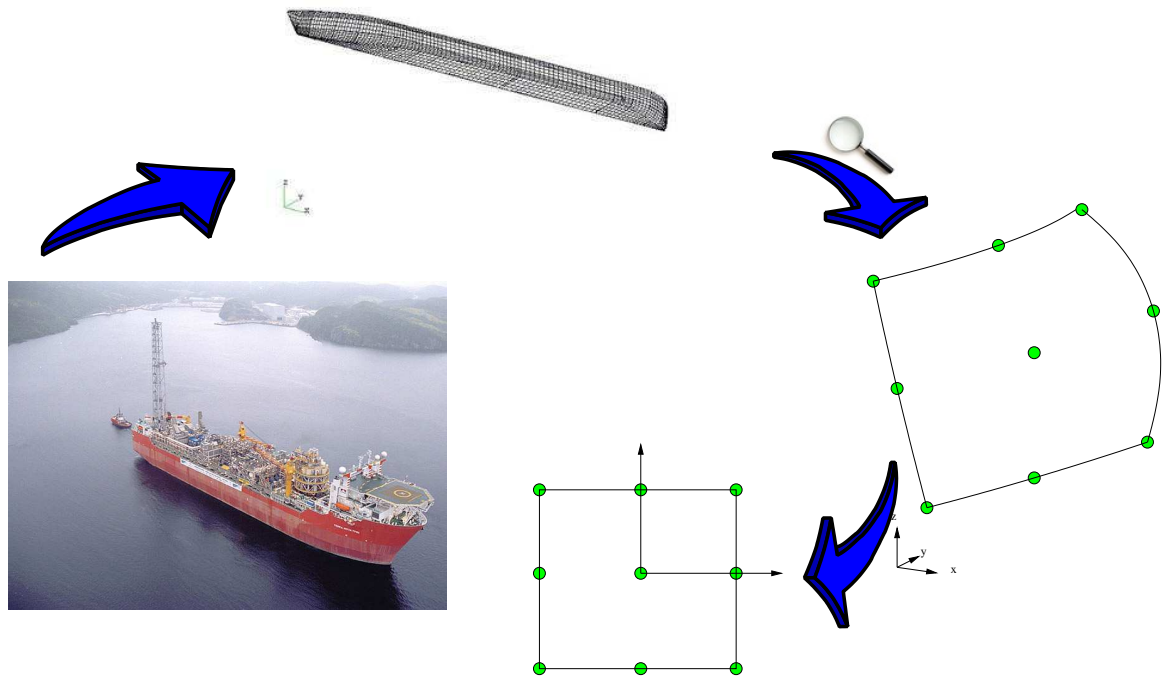
CHAPTER III

NUMERICAL FORMULATION

In the previous chapter, the boundary integral equation was defined. To solve the equation (2.95) numerically, it has to be transformed to the discretized linear algebraic equations. The whole boundary surface is composed of a number of panels or elements where the physical variables and geometries are represented. This procedure is called a boundary element method. The next section will show general concepts of the numerical modeling which helps understand the numerical strategies in Chapter IV.

3.1 Discretization

Numerical modeling is a transforming process from the mathematical to the visual (Boresi, Chong & Saigal 2003). In the present study, a partial differential equation needs to be solved as a boundary and an initial value problem. Since this process is mathematical, the next step is to create a panel along the surface which is called a calculation domain. The modeling process is used not only for the boundary element method but it has also been applied in many engineering fields. For example, a new ship model can be tested in many other fields. Shipowners would like to know the shape of a ship before they build. Structure engineers might want to know if the new built ship can meet a classification before launching. Remodeling engineers may be interested in what kinds of effect their remodeled skyscraper could have on the skyline of the city. These processes are specifically called a solid modeling as illustrated in figure 3.1.



Permission is granted to copy, distribute and/or modify this document under the terms of the GNU Free Documentation License, Version 1.2 or any later version published by the Free Software Foundation; with no Invariant Sections, no Front-Cover Texts, and no Back-Cover Texts. Subject to disclaimers.

FIGURE 3.1. General procedures for a solid modeling.

After generating a model, each panel has a geometric information with the earth-fixed Cartesian coordinates system. This can be transformed into a local or intrinsic coordinate system. Through this process, a three-dimensional model can be generated from solid two-dimensional elements.

3.2 Discretized boundary integral equation

The discretized Laplace equation can be written as follows:

$$-\sum_{j=1}^{n_0} G_{ij} \left(\frac{\partial \phi}{\partial n} \right)_j + \sum_{j=n_0+1}^n H_{ij} \phi_j = \sum_{j=n_0+1}^n G_{ij} \left(\frac{\partial \phi}{\partial n} \right)_j - \sum_{j=1}^{n_0} H_{ij} \phi_j$$

and $i = 1, 2, \dots, n,$ (3.1)

where n_0 is the number of nodes on the free and open boundary surface. The n is the total number of nodes on the discretized domain.

The boundary equation (2.95) can be rearranged by ϕ and its normal derivative. The boundary integral equation (3.1) can be changed to a simpler form after rearranging it into a linear algebraic equation below.

$$\sum_{j=1}^n H_{ij} \phi_j = \sum_{j=1}^n G_{ij} \left(\frac{\partial \phi}{\partial n} \right)_j. \quad (3.2)$$

The coefficients H_{ij} and G_{ij} correspond respectively to the integrals of the Green function and its normal derivatives over each element.

3.3 Higher order boundary element method

Several panel methods were found in the literature for the present study. The constant panel method and the higher order panel method were the two most common methods used among the previous studies. There are several disadvantages to the constant panel method:

- The curved surface is approximated by flat panels. Singularity strength over the surface is discontinuous across panel boundaries.

- An excessive number of panels may be required to represent portions of surfaces with large curvature, which may result in expensive computational efforts to achieve desirable accuracy.
- The quadrilateral panels may have a leakage problem at the nodes and along the edges of adjacent panels.

These deficiencies can be solved by using a higher order panel. A higher order panel uses a B-spline curve between the nodes within the same element to approximate a curved surface. Accordingly, a higher order panel requires fewer panels to get an appropriate result.

3.3.1 Generation of shape functions

To generate shape functions is an intuitive job (Beer 2001). The shape function only requires the following properties:

$$N_n(\xi_n) = 1.$$

$$N_n(\xi_i) = 0 \quad \text{for } i \neq n. \quad (3.3)$$

Equation(3.3) shows that only the weighted node should be one and the others zero. When applying shape function to the weighted node point, the total summation of the weights equals one. For example, when one defines one's own shape function and the weighted intrinsic coordinate is (-1, +1), one can apply it to all one's defined shape function. All the values must be identical to zero except the weighted node.

For more simplicity, a two-dimensional linear shape function can be considered as shown in figure 3.2.

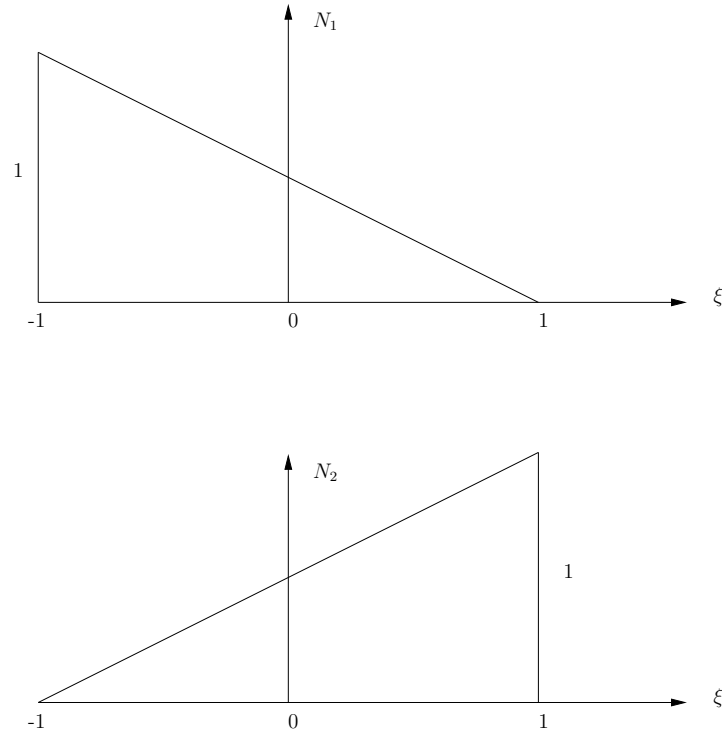


FIGURE 3.2. Two-dimensional linear shape functions.

$$N_1 = \frac{1}{2}(1 - \xi).$$

$$N_2 = \frac{1}{2}(1 + \xi). \quad (3.4)$$

Equation(3.4) is satisfied by equation(3.3).

Figure 3.3 illustrates two-dimensional quadratic shape functions. The main idea of quadratic shape functions is that the middle node can be defined by quadratic

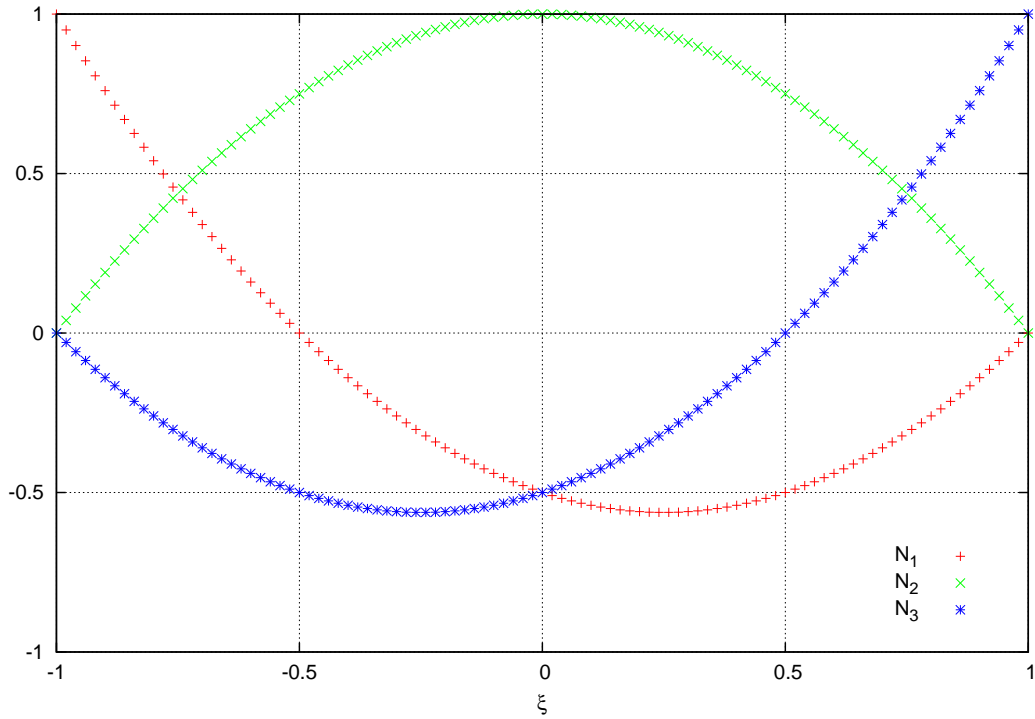


FIGURE 3.3. Quadratic shape functions.

function. Here, N_2 is defined as in the equation(3.5). Next, the weighed value by N_2 has to be reduced on both ends of the nodes. It has been done simply by subtracting from linear shape function to the middle node.

$$N_1 = \frac{1}{2}(1 - \xi) - \frac{1}{2}N_2.$$

$$N_2 = 1 - \xi^2.$$

$$N_3 = \frac{1}{2}(1 + \xi) - \frac{1}{2}N_2. \quad (3.5)$$

3.3.2 Definition of higher order shape functions

The entire calculation domain can be represented by quadrilateral or triangular elements. In the present study, higher order panels are used for all discretized boundary surface. First, a body geometry and other surfaces are discretized by quadratic isoparametric quadrilateral(or triangular) elements. Next, physical variables and geometries on each element can be interpolated by higher order shape functions.

Nine nodes quadrilateral and six nodes triangular elements are used for the study as in figure 3.4.

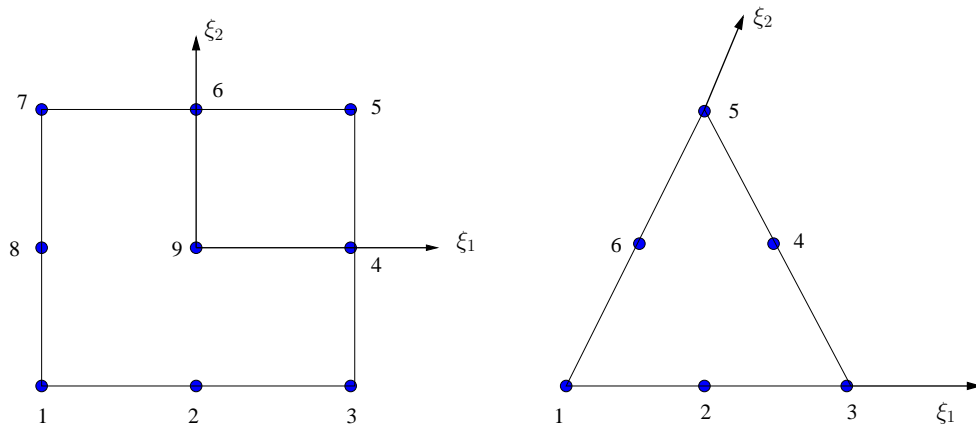


FIGURE 3.4. Schematics of the nine nodes and six nodes elements.

The shape functions for the quadrilateral elements are given as

$$N_1 = \frac{1}{4}\xi_1\xi_2(\xi_1 - 1)(\xi_2 - 1),$$

$$N_2 = -\frac{1}{2}\xi_2(\xi_1^2 - 1)(\xi_2 - 1),$$

$$\begin{aligned}
N_3 &= \frac{1}{4}\xi_1\xi_2(\xi_1 + 1)(\xi_2 - 1), \\
N_4 &= -\frac{1}{2}\xi_1\xi_2(\xi_1 + 1)(\xi_2 - 1), \\
N_5 &= \frac{1}{4}\xi_1\xi_2(\xi_1 + 1)(\xi_2 + 1), \\
N_6 &= -\frac{1}{2}\xi_1\xi_2(\xi_1 - 1)(\xi_2 + 1), \\
N_7 &= \frac{1}{4}\xi_1\xi_2(\xi_1 - 1)(\xi_2 + 1), \\
N_8 &= -\frac{1}{2}\xi_1\xi_2(\xi_1 - 1)(\xi_2 - 1), \\
N_9 &= \xi_1\xi_2(\xi_1 - 1)(\xi_2 - 1). \tag{3.6}
\end{aligned}$$

The triangular elements are given as

$$\begin{aligned}
N_1 &= \xi_1(2\xi_1 - 1), \\
N_2 &= 4\xi_1\xi_2, \\
N_3 &= \xi_2(2\xi_2 - 1), \\
N_4 &= 4\xi_2(1 - \xi_1 - \xi_2), \\
N_5 &= (1 - \xi_1 - \xi_2)(1 - 2\xi_1 - 2\xi_2),
\end{aligned}$$

$$N_6 = 4\xi_1(1 - \xi_1 - \xi_2), \quad (3.7)$$

where ξ_1 and ξ_2 are coordinates of the local elements.

The triangular elements may be used if the body or other boundary surface is difficult to discretize by quadrilateral elements.

3.3.3 Discontinuous elements

When two different boundary surfaces meet, the nodes on the intersection of each boundary have identical geometric information. The influence matrix may be singular due to the nodes. This is called a corner problem. This problem can be summarized as in the three cases below:

- Dirichlet-Neumann condition(D-N)
- Neumann-Neumann conditions(N-N)
- Dirichlet-Dirichlet conditions(D-D)

For the (D-N) and (N-N) case, the influence matrix can be rearranged as a non-singular matrix by using multiple nodes at the intersection of the boundary. For the (D-D) case, the influence matrix becomes singular because two rows of the influence matrix are identical. The boundary value problem may not be solved by multiple nodes scheme in this (D-D) case. Therefore, a discontinuous elements technique should be employed.

The (D-D) case can occur at the intersection of the free surface and truncated open boundary surface because the velocity potentials can be defined from both boundary

surfaces. To overcome this (D-D) problem, discontinuous elements are used along the intersection of two boundaries. The nodes on the intersection move the element inward. In this study, the discontinuity parameter, $\tau = 1/3$ is used along the intersection of free surface and the open boundary as shown in figure 3.5.

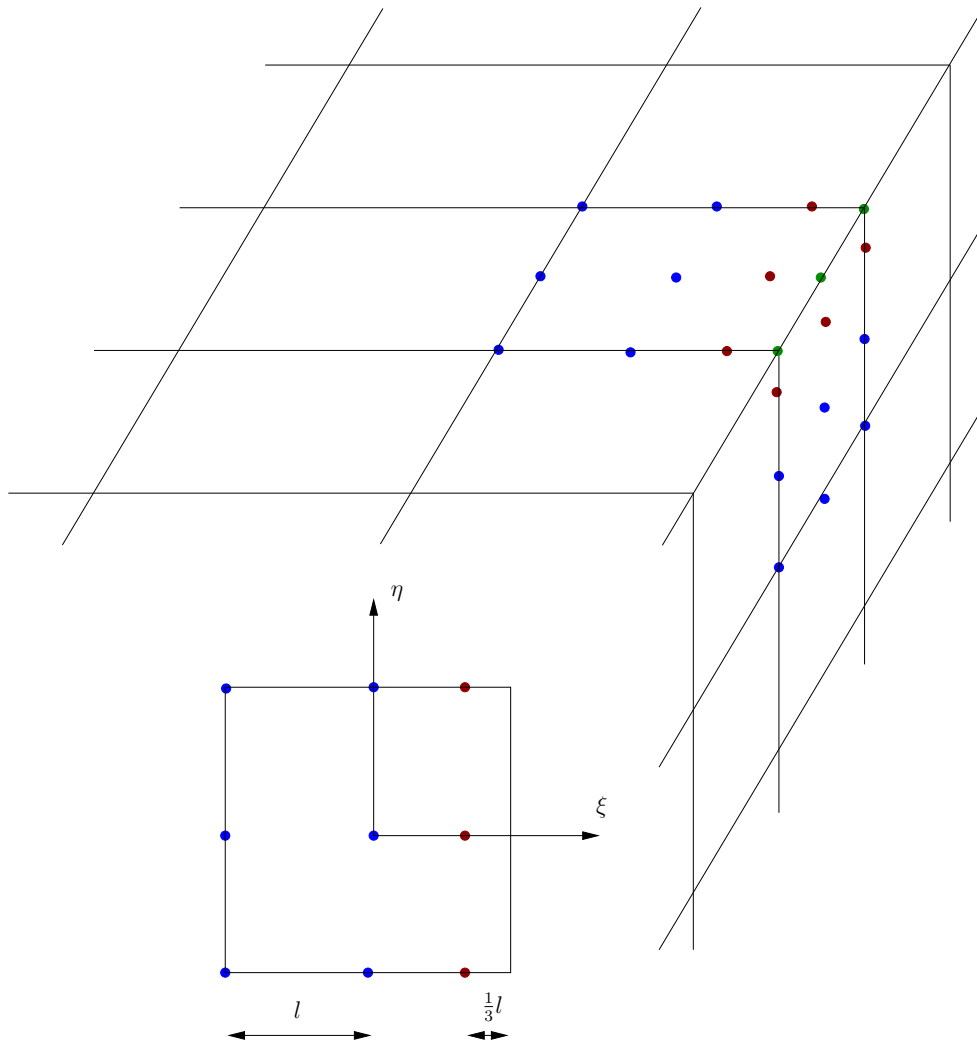


FIGURE 3.5. Distribution of the discontinuous elements along the intersection of the two boundary surfaces.

This discontinuity parameter τ can vary in the range of $0 < \tau \leq 1$ for the quadratic element. The shape functions for the one-sided discontinuous element with a discontinuity parameter $\tau = \frac{1}{3}$ are given as follows:

$$\begin{aligned}
N_1 &= \frac{1}{10}\xi_1\xi_2(3\xi_1 - 2)(\xi_2 - 1), \\
N_2 &= -\frac{1}{4}(\xi_1 + 1)(3\xi_1 - 2)(\xi_2 - 1), \\
N_3 &= \frac{9}{20}\xi_1\xi_2(\xi_1 + 1)(\xi_2 - 1), \\
N_4 &= -\frac{9}{10}\xi_1(\xi_1 + 1)(\xi_2^2 - 1), \\
N_5 &= \frac{9}{20}\xi_1\xi_2(\xi_1 + 1)(\xi_2 + 1), \\
N_6 &= -\frac{1}{4}(\xi_1 + 1)(3\xi_1 - 2)(\xi_2 + 1), \\
N_7 &= \frac{1}{10}\xi_1\xi_2(3\xi_1 - 2)(\xi_2 + 1), \\
N_8 &= -\frac{1}{5}\xi_1(3\xi_1 - 2)(\xi_2^2 - 1), \\
N_9 &= \frac{1}{2}(\xi_1 + 1)(3\xi_1 + 2)(\xi_2^2 - 1). \tag{3.8}
\end{aligned}$$

For the two-sided discontinuous elements:

$$\begin{aligned}
N_1 &= \frac{1}{25}\xi_1\xi_2(3\xi_1 - 2)(3\xi_2 - 2), \\
N_2 &= -\frac{1}{10}\xi_2(\xi_1 + 1)(3\xi_1 - 2)(3\xi_2 - 2), \\
N_3 &= \frac{9}{50}\xi_1\xi_2(\xi_1 + 1)(3\xi_2 - 2), \\
N_4 &= -\frac{9}{20}\xi_1(\xi_1 + 1)(\xi_2 + 1)(3\xi_2 - 2), \\
N_5 &= \frac{81}{100}\xi_1\xi_2(\xi_1 + 1)(\xi_2 + 1), \\
N_6 &= -\frac{9}{20}\xi_2(\xi_1 + 1)(3\xi_1 - 2)(\xi_2 + 1), \\
N_7 &= \frac{9}{50}\xi_1\xi_2(3\xi_1 - 2)(\xi_2 + 1), \\
N_8 &= -\frac{1}{10}\xi_1(3\xi_1 - 2)(\xi_2 + 1)(3\xi_2 - 2), \\
N_9 &= \frac{1}{4}(\xi_1 + 1)(\xi_2 + 1)(3\xi_1 - 2)(3\xi_2 - 2). \tag{3.9}
\end{aligned}$$

More details for the discontinuous element can be found in Brebbia & Dominguez (1989) and Boo (1993).

3.3.4 Comparing constant shape function with higher

Shape functions are illustrated in figures 3.6, 3.7, 3.8, and 3.9. In the constant panel shown in figure 3.6, the weights are deployed with linear functions. Whereas, in the higher order panel shown in figures 3.8 and 3.9 weights are deployed with quadratic functions. The higher order panels with a bubble mode and a non-bubble mode are illustrated in figures 3.7 and 3.9. The bubble mode in figure 3.9 shows a smoother surface gradient with a more concentrated weighted area. However, reducing the surface gradient and increasing the concentrated weighted area do not guarantee robustness nor do they have a good agreement. The quality of the solution depends upon the geometric complexity.

3.3.5 Derivatives in higher order panel

The higher order boundary element assigns the velocity potential at each node point. For this study, a nine nodes quadrilateral isoparametric element is used. This quadrilateral element can transform a curved boundary element in Cartesian coordinates to a local element in $\xi_1 - \xi_2$ coordinates. This describes both the geometry of the element and the variation of dependent variables.

Figure 3.10 shows a local element in a global coordinates system. In this figure, the position vector \vec{R} can be defined as

$$\vec{R} = x(\xi_1, \xi_2)\vec{i} + y(\xi_1, \xi_2)\vec{j} + z(\xi_1, \xi_2)\vec{k}. \quad (3.10)$$

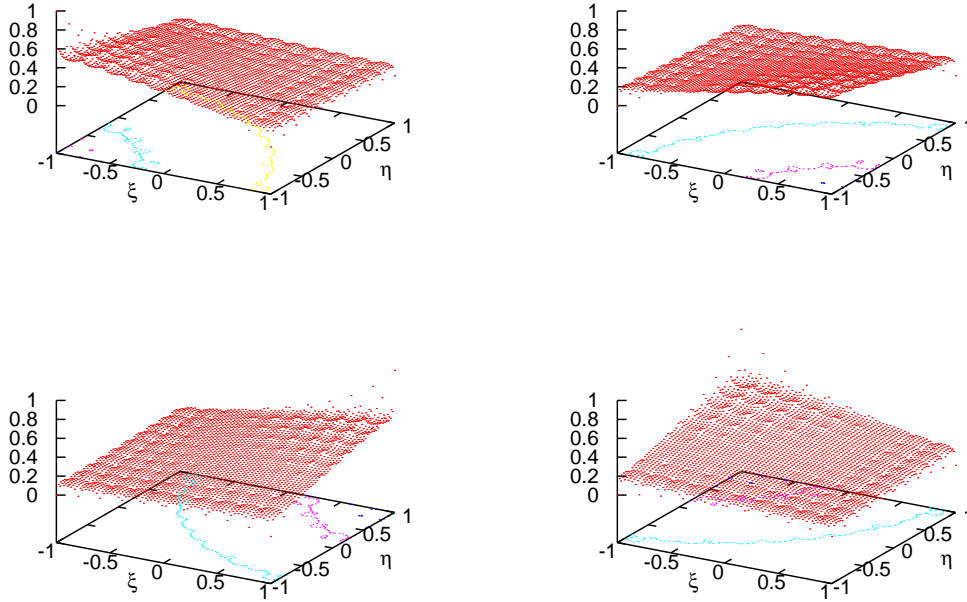


FIGURE 3.6. Shape functions for a lower order panel with four nodes.

$$R_1 = \frac{\partial R}{\partial \xi_1} \quad \text{and} \quad R_2 = \frac{\partial R}{\partial \xi_2}. \quad (3.11)$$

The mapping of the body surfaces is:

$$x = \sum_{j=1}^s N_j(\xi_1, \xi_2) x_j,$$

$$y = \sum_{j=1}^s N_j(\xi_1, \xi_2) y_j,$$

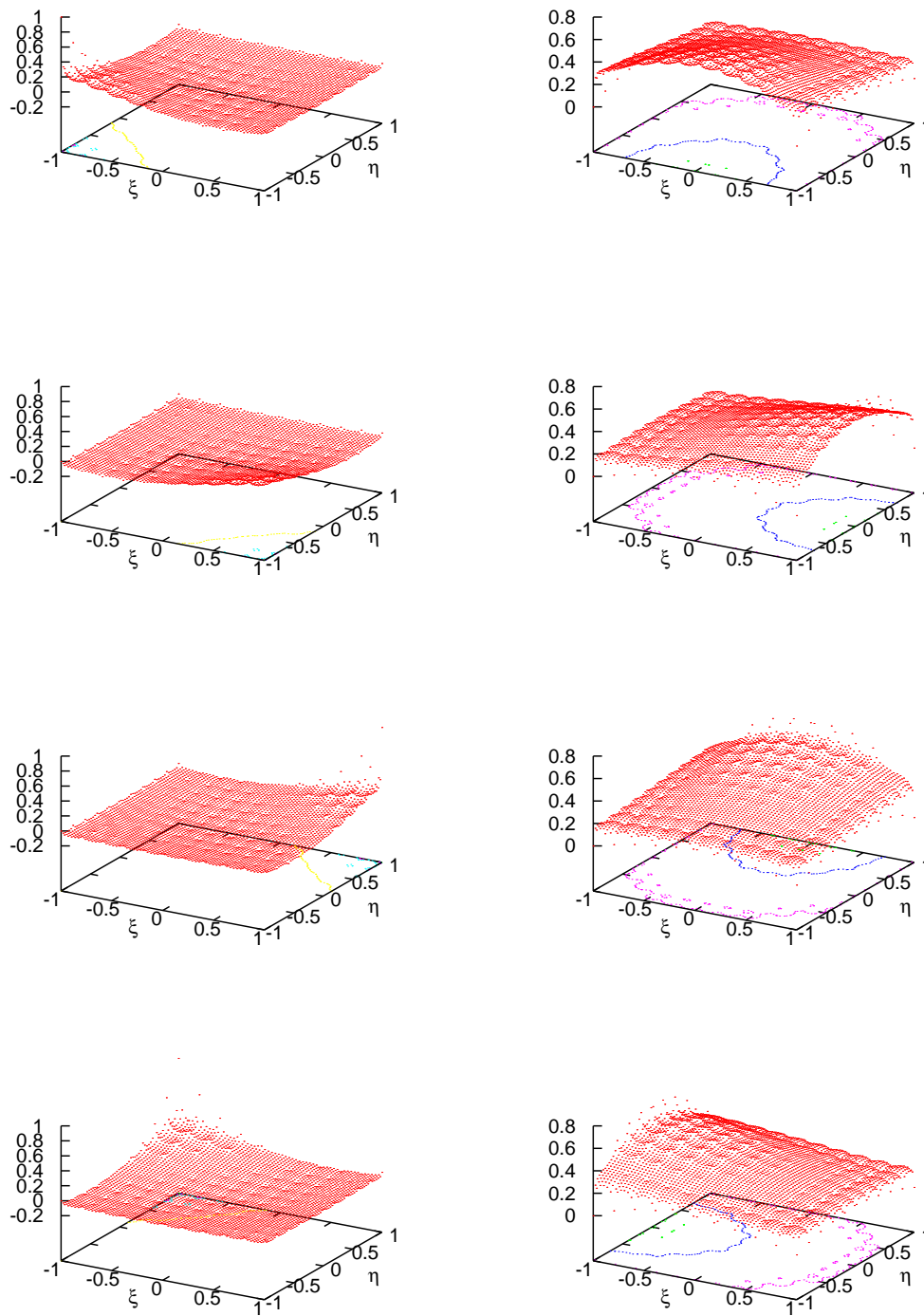


FIGURE 3.7. Shape functions for a higher order panel with eight nodes.

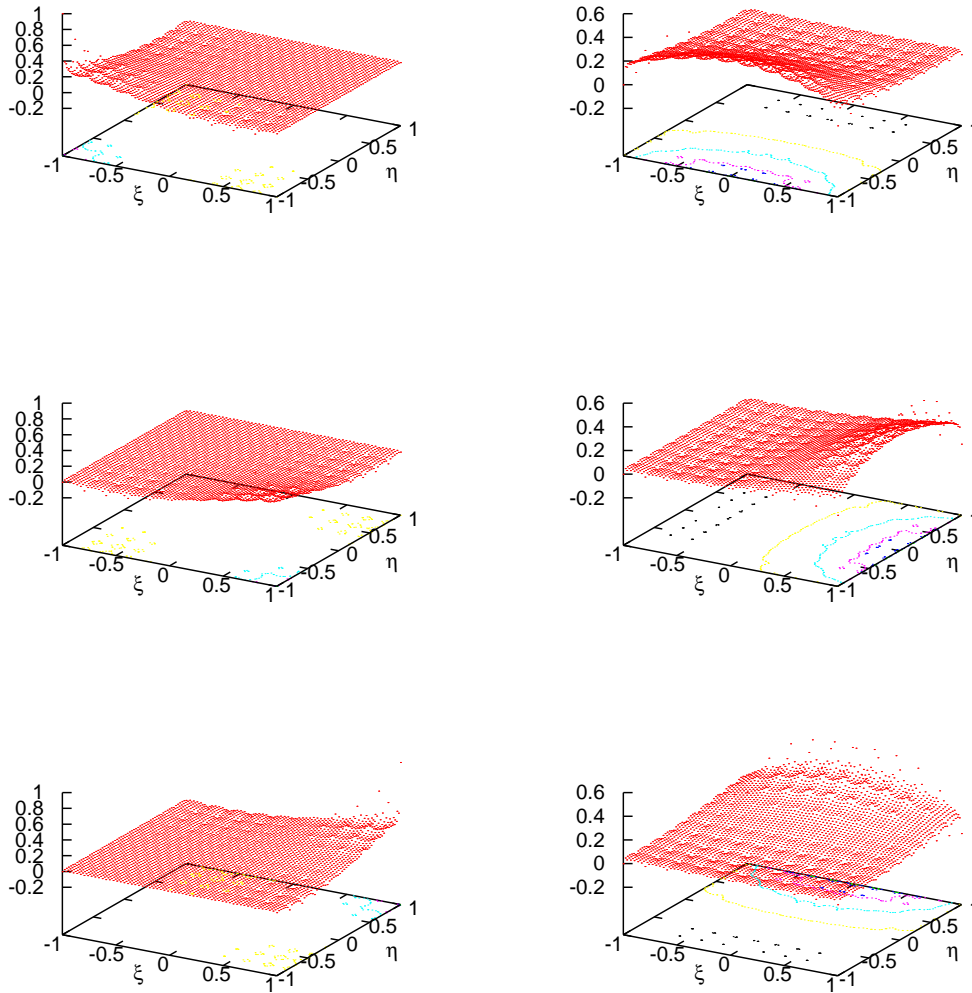


FIGURE 3.8. Shape functions for a higher order panel with nine nodes I.

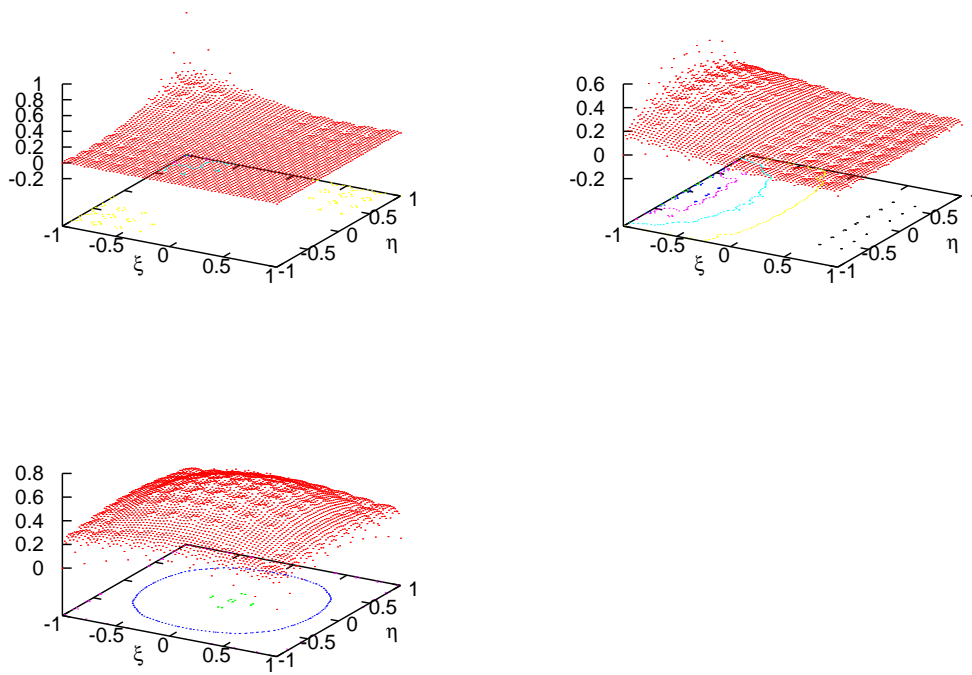


FIGURE 3.9. Shape functions for a higher order panel with nine nodes II.

$$z = \sum_{j=1}^s N_j(\xi_1, \xi_2) z_j, \quad (3.12)$$

where s is the total number of nodes at a higher order panel.

Using the definition of shape function, the velocity potential and its derivatives are as follows:

$$\phi = \sum_{j=1}^s N_j(\xi_1, \xi_2) \phi_j.$$

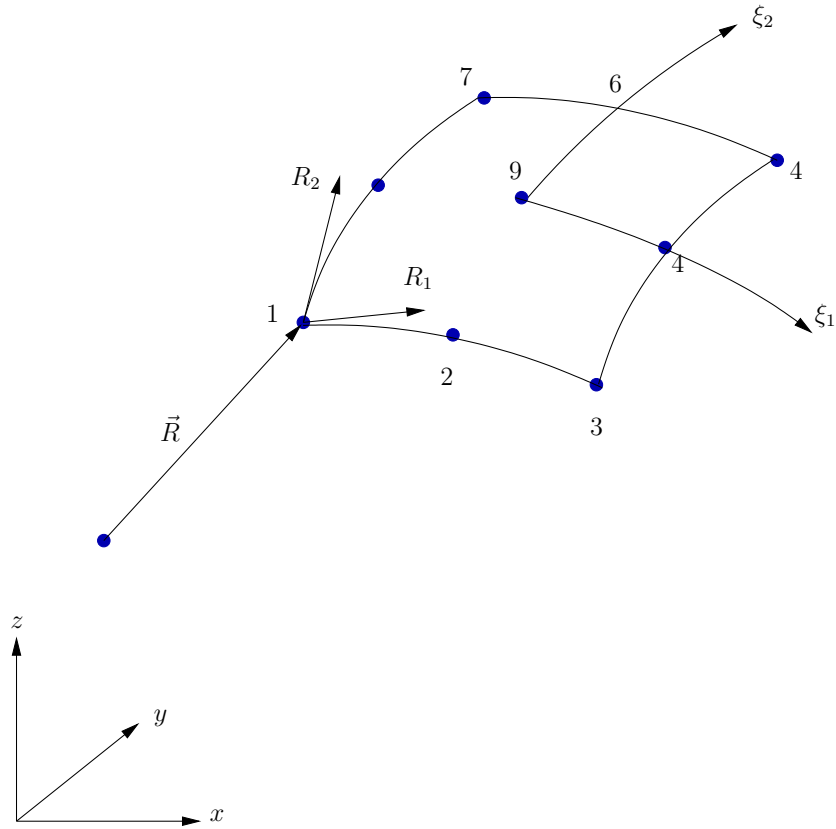


FIGURE 3.10. Relationship between the global and the local coordinates system for a quadrilateral curved element.

$$\frac{\partial \phi}{\partial n} = \sum_{j=1}^s N_j(\xi_1, \xi_2) \left(\frac{\partial \phi}{\partial n} \right)_j. \quad (3.13)$$

The unit normal vector in the curvilinear reference system can be written as

$$\vec{n} = \frac{\frac{\partial \vec{R}}{\partial \xi_1} \times \frac{\partial \vec{R}}{\partial \xi_2}}{\left| \frac{\partial \vec{R}}{\partial \xi_1} \times \frac{\partial \vec{R}}{\partial \xi_2} \right|} = (n_x, n_y, n_z), \quad (3.14)$$

where n_x , n_y , and n_z are defined as

$$n_x = \frac{\left(\frac{\partial y}{\partial \xi_1} \frac{\partial z}{\partial \xi_2} - \frac{\partial y}{\partial \xi_2} \frac{\partial z}{\partial \xi_1} \right)}{\sqrt{(n_x^2 + n_y^2 + n_z^2)}},$$

$$n_y = \frac{\left(\frac{\partial z}{\partial \xi_1} \frac{\partial x}{\partial \xi_2} - \frac{\partial x}{\partial \xi_1} \frac{\partial z}{\partial \xi_2} \right)}{\sqrt{(n_x^2 + n_y^2 + n_z^2)}},$$

and

$$n_z = \frac{\left(\frac{\partial x}{\partial \xi_1} \frac{\partial y}{\partial \xi_2} - \frac{\partial y}{\partial \xi_1} \frac{\partial x}{\partial \xi_2} \right)}{\sqrt{(n_x^2 + n_y^2 + n_z^2)}}. \quad (3.15)$$

The normal derivative of the potential is:

$$\frac{\partial \phi}{\partial n} = \frac{\partial \phi}{\partial x} n_x + \frac{\partial \phi}{\partial y} n_y + \frac{\partial \phi}{\partial z} n_z. \quad (3.16)$$

From the chain rule and the equation (3.16), the velocity potential on the local coordinate system can be defined as:

$$\begin{Bmatrix} \frac{\partial \phi}{\partial \xi_1} \\ \frac{\partial \phi}{\partial \xi_2} \\ \frac{\partial \phi}{\partial n} \end{Bmatrix} = \begin{bmatrix} \frac{\partial x}{\partial \xi_1} & \frac{\partial y}{\partial \xi_1} & \frac{\partial z}{\partial \xi_1} \\ \frac{\partial x}{\partial \xi_2} & \frac{\partial y}{\partial \xi_2} & \frac{\partial z}{\partial \xi_2} \\ \frac{\partial n}{\partial x} & \frac{\partial n}{\partial y} & \frac{\partial n}{\partial z} \end{bmatrix} \begin{Bmatrix} \frac{\partial \phi}{\partial x} \\ \frac{\partial \phi}{\partial y} \\ \frac{\partial \phi}{\partial z} \end{Bmatrix} \quad (3.17)$$

or

$$\begin{pmatrix} \frac{\partial \phi}{\partial \xi_1} \\ \frac{\partial \phi}{\partial \xi_2} \\ \frac{\partial \phi}{\partial n} \end{pmatrix} = J \begin{pmatrix} \frac{\partial \phi}{\partial x} \\ \frac{\partial \phi}{\partial y} \\ \frac{\partial \phi}{\partial z} \end{pmatrix}, \quad (3.18)$$

where J is the Jacobian matrix defined in the equation (3.18).

The velocity potential can be derived from the equation (3.18) on the boundary surface in the global coordinates system and it can be written as:

$$\begin{pmatrix} \frac{\partial \phi}{\partial x} \\ \frac{\partial \phi}{\partial y} \\ \frac{\partial \phi}{\partial z} \end{pmatrix} = J^{-1} \begin{pmatrix} \frac{\partial \phi}{\partial \xi_1} \\ \frac{\partial \phi}{\partial \xi_2} \\ \frac{\partial \phi}{\partial n} \end{pmatrix}. \quad (3.19)$$

The derivatives of the velocity potential and the components of the Jacobian matrix with respect to the local coordinates can be expressed as:

$$\frac{\partial \phi}{\partial \xi_1} = \sum_{j=1}^s \left(\frac{\partial N_j}{\partial \xi_1} \right) \phi_j, \quad \frac{\partial \phi}{\partial \xi_2} = \sum_{j=1}^s \left(\frac{\partial N_j}{\partial \xi_2} \right) \phi_j \quad (3.20)$$

and

$$\frac{\partial \vec{x}}{\partial \xi_1} = \sum_{j=1}^s \left(\frac{\partial N_j}{\partial \xi_1} \right) \vec{x}_j, \quad \frac{\partial \vec{x}}{\partial \xi_2} = \sum_{j=1}^s \left(\frac{\partial N_j}{\partial \xi_2} \right) \vec{x}_j. \quad (3.21)$$

Similarly, the second order derivatives of the velocity potential can also be calculated so that the local derivatives of the velocity can be written as follows:

$$\frac{\partial^2 \phi}{\partial x \partial \xi_1} = \sum_{j=1}^s \left(\frac{\partial N_j}{\partial \xi_1} \right) \frac{\partial \phi}{\partial x_j}, \quad \frac{\partial^2 \phi}{\partial x \partial \xi_2} = \sum_{j=1}^s \left(\frac{\partial N_j}{\partial \xi_2} \right) \frac{\partial \phi}{\partial x_j}. \quad (3.22)$$

$$\frac{\partial^2 \phi}{\partial y \partial \xi_1} = \sum_{j=1}^s \left(\frac{\partial N_j}{\partial \xi_1} \right) \frac{\partial \phi}{\partial y_j}, \quad \frac{\partial^2 \phi}{\partial y \partial \xi_2} = \sum_{j=1}^s \left(\frac{\partial N_j}{\partial \xi_2} \right) \frac{\partial \phi}{\partial y_j}. \quad (3.23)$$

$$\frac{\partial^2 \phi}{\partial z \partial \xi_1} = \sum_{j=1}^s \left(\frac{\partial N_j}{\partial \xi_1} \right) \frac{\partial \phi}{\partial z_j}, \quad \frac{\partial^2 \phi}{\partial z \partial \xi_2} = \sum_{j=1}^s \left(\frac{\partial N_j}{\partial \xi_2} \right) \frac{\partial \phi}{\partial z_j}. \quad (3.24)$$

A higher order panel has the advantage in calculation of the first and the second partial derivatives. This panel method yields more accurate derivatives of the velocity potential in contrast to the constant panel method. The wave, current, and body interaction problem includes the first and the second order derivatives both in the free surface boundary and the body boundary conditions. This also includes the first and the second order derivatives of the velocity potential and the wave elevation.

3.4 Influence matrix handling

Whichever numerical method is chosen, one will need to follow the procedures. The summary of the procedure is as follows: First, the time harmonic solutions corresponding to the first and the second terms of the series expansion are solved for a given steady-state incident wave field. Second, the incident wave field is represented by a superposition of the fundamental first-order solutions of particular frequency

components in the absence of the body. Third, the boundary value problem is recast into integral equations using the wave source potential as a Green function. Finally, the integral equation is solved by a panel method for the unknown velocity potential or the source strength on the body surface. The last step needs matrix inversion of the influence matrix and requires a large portion of the total simulation time.

Several numerical schemes have been developed. The iterative method is most frequently used so far. Celebi (1997) showed several iterative methods. He treated free surface boundaries as an instantaneous wetted body surface so that every time step requires an inversion matrix. Since an inversion matrix does not need to save for the reuse, in this case, an iterative solver may work better to get a reasonably approximated solution. Although cpu time for inversion matrix is critical for the total simulation time, direct method is used for the present study. The influence matrix consists of time independent variables so that the matrix inversion is only required once. Gauss-Jordan Elimination has been used in the previous studies for an inverse influence matrix. The Gauss-Jordan is a direct method and it guarantees convergence. The only weakness of this method is that it takes relatively longer time for solving a large problem. An FPSO simulation requires a large number of elements so that the efficient handling of an inversion matrix process is one of the critical factors in terms of the total simulation time. For time efficiency, single digit Gauss elimination with factorization(SGEFA) is introduced in the THOBEM program. SGEFA is a direct method and adopts lower and upper triangular matrices (LU) decomposition similar to other preconditioned methods. SGEFA has been very successful and verified appropriate for the present study. The SGEFA is part of SLATEC that is a common numerical library project. SLATEC is the acronym for the Sandia, Los Alamos, Air Force Weapons Laboratory Technical Exchange Committee. A brief explanation of

SLATEC is found in Appendix B.

CHAPTER IV

STRATEGIES FOR CONVERGENCE IN SIMULATION AND NUMERICAL RESULTS

Convergence is one of the typical problems involved in time domain simulation. To improve convergence, the following four factors must be taken into account. First, the robust numerical implementation of a far-field closure must be considered. Second, the body and mean free surface intersection area must be treated with caution. Third, a stable numerical algorithm is required for integration on the free surface. Finally, an efficient matrix solver must be selected properly for the large, dense, and unsymmetrical matrix.

4.1 Truncated open boundary condition

4.1.1 General idea

When a surface piercing body is located in an unbounded region, radiation condition must be considered as being the infinite domain for the uniqueness of the solution. An open truncated boundary is an artificial boundary condition set up in order to handle an infinite domain with limited computational resources. An improper treatment of an artificial boundary causes significant reflected waves and influences the entire calculation domain as well. To avoid huge reflection, techniques have been developed and are categorized as three parts:

- an artificial damping zone or sponge layer

- a partial differential equation(i.e. Sommerfeld condition)
- an hybrid or combined method

An artificial damping zone has the advantage of being easy to apply and also that of having good reflection properties for a wide range of frequencies. The disadvantage is that this technique requires an additional large size of the calculation domain for good absorption. In contrast to this, the partial differential equation type of the truncated boundary (i.e. the Sommerfeld radiation condition) involves a smaller size of the calculation domain. It was originally derived from spatially and temporarily periodic conditions of a potential function. The Sommerfeld radiation condition is applied to estimate the time-dependent phase velocity on the boundary of the flow that comes from the boundary conditions on the truncated surface for a next time step. This technique assumes a locally and momentarily periodic condition of the flow on a truncated surface so that phase velocity can be determined by the outflow of the scattered waves.

In time domain, the Sommerfeld radiation condition for a scattered potential is given as

$$\sqrt{r} \left(\frac{\partial \phi_s}{\partial t} + C \frac{\partial \phi_s}{\partial r} \right) = 0 \quad \text{as } r \rightarrow \infty. \quad (4.1)$$

The Sommerfeld condition still needs the infinity of the distance r that is a radial distance from the body. On the basis of the Sommefeld condition, the truncated open boundary was introduced by Orlanski (1976). When the radial distance from the body is finite, the value within the parenthesis can be zero at a proper phase velocity. The normal phase velocity can be treated on the truncated open boundary

surface more efficiently. Scattered velocity potential is given as

$$\phi_s = A(x, y, z)F(k_x x + k_y y - \omega t), \quad (4.2)$$

where k_x and k_y are the local wave numbers in x and y directions respectively. A in the equation (4.2) is the amplitude by disturbance. Differentiating the equation (4.2) with respect to the normal direction to the outer truncated open boundary is given as

$$\frac{\partial \phi_s}{\partial t} + C \frac{\partial \phi_s}{\partial n} - C \frac{\phi_s}{A} \frac{\partial A}{\partial n} = 0 \quad \text{on the truncated edge.} \quad (4.3)$$

The third term may be neglected because the amplitude of the first order scattered wave decays as $1/\sqrt{r}$ and the third term is $1/(kr)$ smaller than the first two terms. It becomes negligible when the truncated open boundary is located sufficiently distant from the body. Through equations (4.2) and (4.3), the infinite radial distance can be eliminated from the equation (4.1) and is rearranged as below:

$$\frac{\partial \phi_s}{\partial t} + C \frac{\partial \phi_s}{\partial n} = 0 \quad \text{on the truncated edge.} \quad (4.4)$$

$\partial \phi_s / \partial n$ is the fluid velocity at the edge between the free surface and the truncated open boundary outward normal on the boundary surface. $C(x, y, z, t)$ is the phase velocity determined numerically.

Orlanski (1976) used the leap frog method to get a phase velocity numerically. The characteristic of waves is assumed to have a slope equal to $\Delta x / \Delta t$. The phase velocity is extrapolated as

$$\begin{aligned} & \frac{\phi(n_i, \tau + 1) - \phi(n_i, \tau - 1)}{\Delta t} \\ &= -\frac{C}{\Delta x} [\phi(n_i, \tau + 1) + \phi(n_i, \tau - 1) - 2\phi(n_{i-1}, \tau)], \end{aligned} \quad (4.5)$$

where n_i represents the node points in the truncated open boundary. n_{i-1} is the interior node point next to the open boundary. The time level τ is the instant time when the computation is performed. $\tau - 1$ and $\tau + 1$ are the previous and the following time levels respectively.

When the simulation performs at time level τ , the phase velocity can be obtained numerically using the information from the previous time levels and the interior nodes next to the open boundary. The phase velocity at time level τ is given as

$$C = -\frac{\Delta x}{\Delta t} \frac{\phi(n_i - 1, \tau) - \phi(n_i - 1, \tau - 2)}{\phi(n_i - 1, \tau) + \phi(n_i - 1, \tau - 2) - 2\phi(n_i - 2, \tau - 1)}. \quad (4.6)$$

With a time-dependent phase velocity on the truncated surface in the Sommerfeld radiation condition, an irregular wave train can be treated and transmitted as a series of periodic waves in time.

The multi-frequencies wave case can be treated as

$$\prod_{i=1}^N \left(\frac{\partial \phi_s}{\partial t} + C_i \frac{\partial \phi_s}{\partial n} \right) = 0 \quad \text{on the truncated edge.} \quad (4.7)$$

The disadvantage is that the waves treated in C_i term can travel without severe reflected waves. Therefore, it is not a very elegant solution for a problem with multi-

frequencies.

This study concerns only the monochromatic wave. The Orlanski condition is used here for the open boundary. Step by step descriptions are as follows: First, a calculation domain can be well-arranged as a boundary value problem. The free surface possesses the Dirichlet condition with a known value ϕ_s . The body and truncated open boundary has the Neumann condition with a known value $\partial\phi_s/\partial n$. Second, to prevent reflected waves on the truncated boundary, the Orlanski open boundary condition is used to determine the values of the ϕ_s and η at the node point on the truncated edges. The value of $\partial\phi/\partial n$ on the edges can be calculated by a quadratic interpolation formula from the known value of ϕ_s on the free surface. It can also be obtained from the dynamic free surface condition. This study employs this method.

The Orlanski condition can also work with a scattered wave elevation and it is given as

$$\frac{\partial\eta}{\partial t} + C\frac{\partial\eta}{\partial n} = 0. \quad (4.8)$$

The equations (4.4) and (4.8) in this study were applied separately or in combination. The results were nearly identical so it has been unnecessary to apply both equations at the same time.

4.1.2 Numerical treatment

The truncated open boundary needs a numerical treatment for the robustness of the simulation. The phase velocities C , $\partial\phi/\partial t$, and $\partial\phi/\partial n$ are very small, zero, or even negative values when waves pass through the truncated open boundary nodes. To

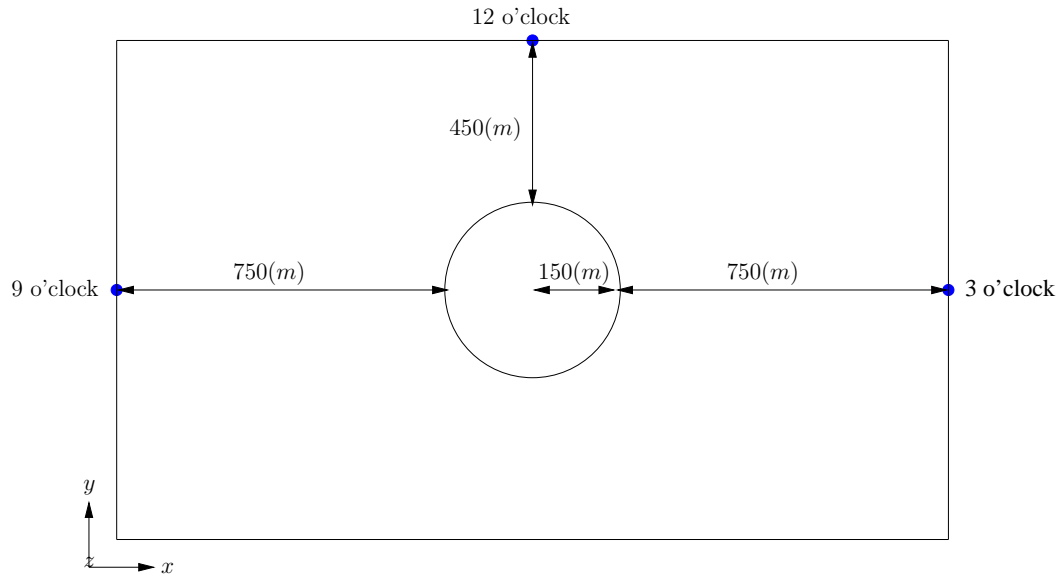


FIGURE 4.1. Domain size and wave probe positions to investigate phase velocities at truncated open boundary.

circumvent these cases, the phase velocity is numerically decided using the following rules:

$$C(t) = \begin{cases} 0 & \text{for } C(t - \Delta t) \leq 0, \text{ or when } \left| \frac{\partial \phi}{\partial t} \right| \text{ and } \left| \frac{\partial \phi}{\partial n} \right| \text{ are small} \\ C(t - \Delta t) & \text{for } 0 < C(t - \Delta t) < \frac{\Delta x}{\Delta t} \\ \frac{\Delta x}{\Delta t} & \text{for } C(t - \Delta t) \geq \frac{\Delta x}{\Delta t} \end{cases} \quad (4.9)$$

Even after applying these rules, numerical difficulties are not always avoided on the truncated open boundary.

Figure 4.1 shows the size of the calculation domain and wave probe positions. The

domain size is $1800 \times 1200 (m^2)$. The wave probe positions were set at the open boundary as 3 o'clock, 9 o'clock, and 12 o'clock respectively. The diffracted waves start to propagate at $t = \Delta t$ therefore one can estimate the arrival of the diffracted waves arrive at the open boundary.

During the probe, severe fluctuation of the phase velocity was detected. Figure 4.2 represents this phenomenon. All three graphs show time history of the phase velocity at the open boundary. The x axis represents the dimensionless time (t/T) and the y axis represents the phase velocity (m/sec). The simulation conditions are: $\omega = 0.6$ (rad/sec), period = 10.47 (sec), and wavelength = 171.16 (m). The top and the bottom graphs show that the diffracted waves arrived at the open boundary between the fourth and fifth cycles. The middle graph shows at the arrival of the waves between the second and the third cycles at the wave probe position at 12 o'clock. The top and the middle graphs show that the open boundary works in a reasonably acceptable manner during one dimensionless time. From the graphs we can conclude that the second to the fifth cycles are not severely affected by the reflected waves from the open boundary. The ramp function effects stop at the second cycle therefore we expect the data from the second to fifth cycles to contain a markedly decrease in the reflected wave effect.

Figure 4.3 shows undesirable reflected wave effects on the entire calculation domain. The incident wave propagates to the positive x direction therefore the y directional diffracted force should not be present. From the seventh cycle, the x directional diffracted force starts to diverge. The y directional force also began to increase noticeably from the seventh cycle.

We attempted various methods to avoid undesirable reflected waves. Methods used

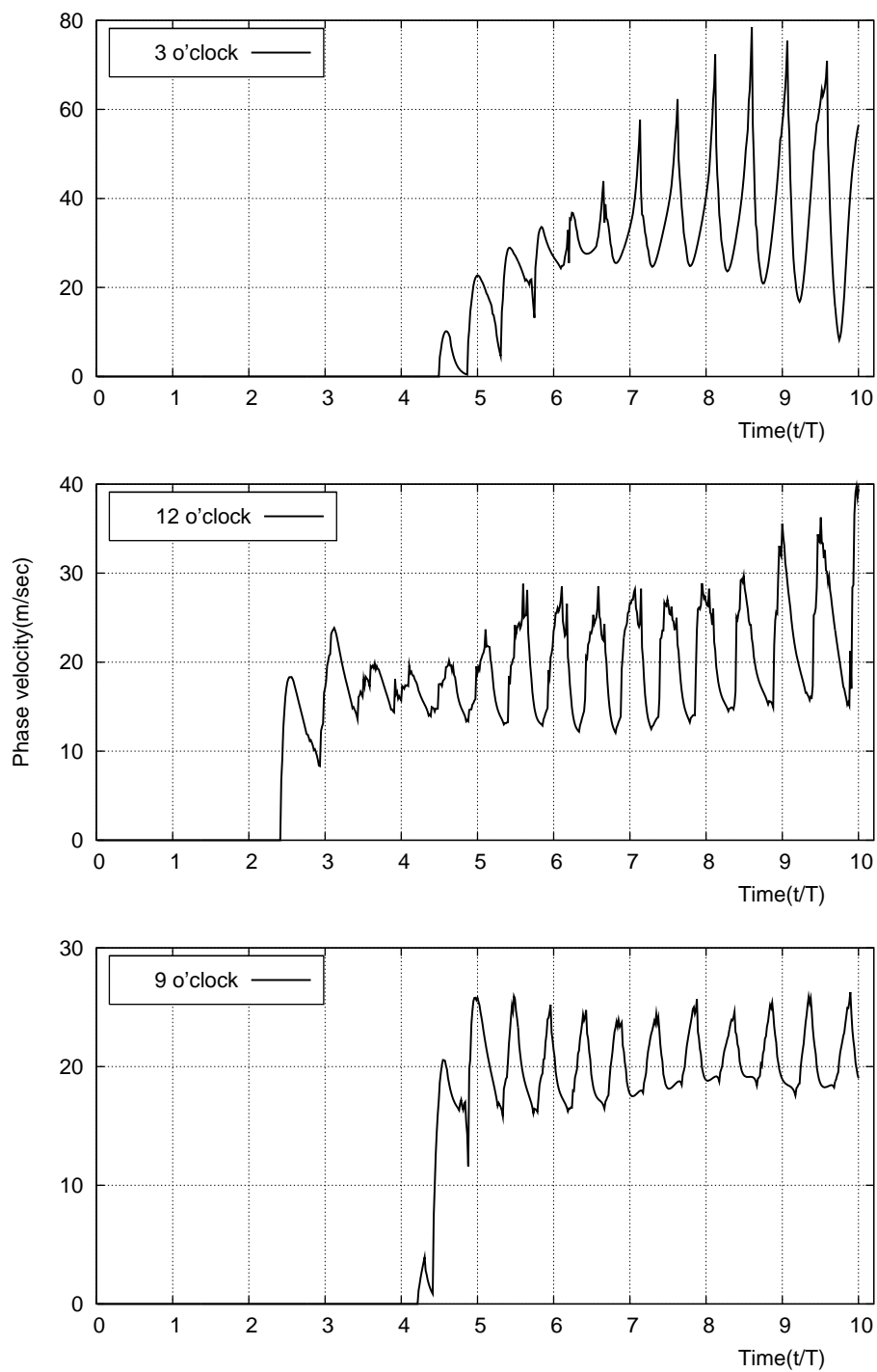


FIGURE 4.2. Phase velocity at open truncated boundary.

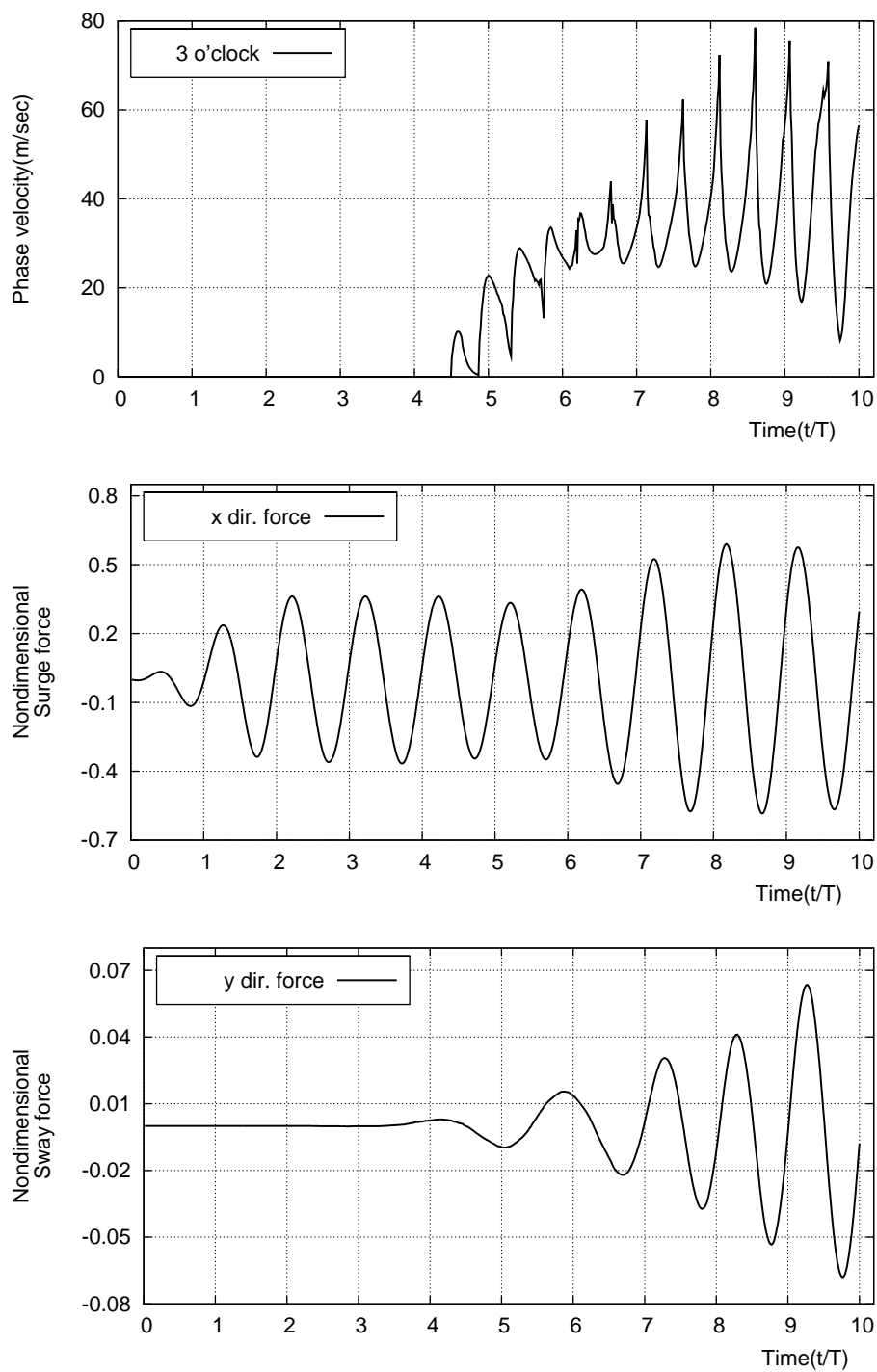


FIGURE 4.3. Relationship between phase velocity at open boundary and diffraction forces in surge and sway.

are discussed in the next three sections.

4.2 Maximum likelihood method

The maximum likelihood method(MLM) is introduced to get the desired information with a minimum data set. MLM has several advantages. MLM requires only a few numbers of the outcomes so that it can save the total simulation time especially in the case of time marching process. This method also helps avoid the undesirable accumulation of numerical errors. However, in order to use the MLM, the selected raw data must be uncontaminated.

The calculated data set with error is assumed to be

$$Y_i = X_{ij}a_j + e_i, \quad (4.10)$$

where $i = 1 \dots n$ represents the time steps and $j = 1, 2$ is the parameters to be estimated.

In the equation (4.10), Y_i is the measured or calculated data. $X_{ij}a_j$ is the linear harmonic response. e_i is the error. In this study, Y_i is the output of the linear system so that the incident wave frequency (ω) is known.

$$\begin{aligned} Y_i - e_i = A \cos(\omega t_i + \psi) &= X_{ij}a_j \\ &= Ae^{i\psi} = a_1 + ia_2. \end{aligned} \quad (4.11)$$

The matrix form of the equation (4.11) is given as

$$Y = Xa + e. \quad (4.12)$$

Maximum likelihood estimators are

$$\begin{aligned} \hat{A} &= \sqrt{a_1^2 + a_2^2}, \\ \hat{\psi} &= \arctan(-a_2/a_1), \\ a_j &= (a_1, a_2) = (X^T X)^{-1} X^T Y. \end{aligned} \quad (4.13)$$

Figure 4.4 shows an example of MLM in the hemisphere case. The incident wave frequency is $0.65(\text{rad}/\text{sec})$. The size of grid is $20 \times 60(m^2)$. The domain size is $460 \times 460(m^2)$. All three graphs show heave forces in diffracted wave cases. X -axis is the cycles that come from the real time divided by period. Y -axis is the force that is nondimensionalized as $\rho g A x_{cl}^2$. Modulation function is applied up to the second cycle. After modulation function effects were over, this force started to converge to the dimensionless value of 0.06. Between the fifth and the sixth cycle, the solution began to fluctuate. This phenomenon accounts for a typical truncated open boundary problem. Therefore, twelve data sets must be chosen between the fourth and the fifth cycle before this reflected wave starts to contaminate all the calculation domains as the middle graph showed. THOBEM and WAMIT results are compared in the bottom graph. The results showed good agreement between THOBEM and WAMIT.

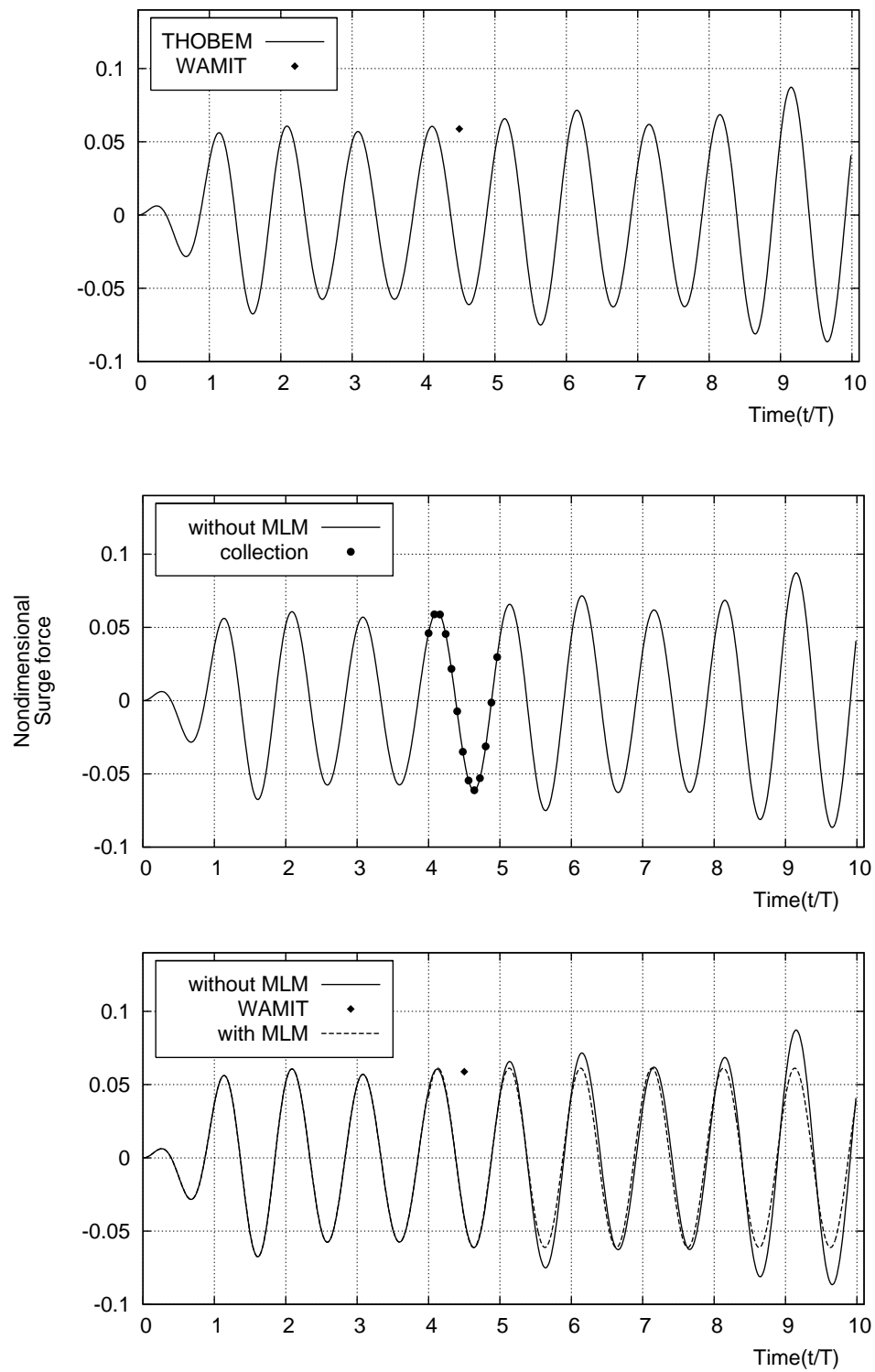


FIGURE 4.4. Examples of MLM.

4.3 Guidelines for elements generation

In preparing for the grid discretizations of numerical simulations, refined meshes are generally applied in regions with the rapid change in geometry or with the rapid variation of the solution. In the context of FPSOs, refined meshes are needed at the body near the bow and the stern where there are sharp edges and sudden changes in geometry. The free surface mesh along and adjacent to the body contour line (i.e. the waterline) and the body mesh adjacent to the free surface also need refined meshes. The guidelines are commonly used for the constant panel boundary element methods (Lee, Newman & Zhu 1996; Kim, Kring & Scлавounos 1997; Korsmeyer, Bingham & Newman 1999). They were applied for THOBEM simulations that were initially unsuccessful.

Upon deeper examination, it was found that improper grid discretization was a factor that contributed to the premature divergence in the time domain solution for an FPSO problem. Indeed, the time domain solution performed better when the uniform mesh discretization (i.e. constant sized elements) was employed. Use of the constant sized element throughout the computational domain is not a practical strategy since the size of the element is determined by the minimum local resolution requirement.

These problems can be solved by grouping the element size in the various domains. The size of each group is determined by the wave length. Along the body contour line the free surface mesh should have the inner domain. The size of the inner domain is one or two wavelengths wide. The inner domain should consist of several rings within which the panel size is approximately constant. A large panel size is used in the outer domain (outside the truncated open boundary). Mesh optimization requires balancing the panel sizes in the inner and outer domains along with the boundary

locations of the interior domain and the exterior open boundary.

The discretization scheme is necessary because higher order panels do not always work with distorted aspect ratios. Therefore, the constant size element with a properly curved element is required. In the beginning of the study, a circular domain was adopted to avoid the corner problem on an open boundary without a wall effect. This was initially expected to make the problem simpler. In comparison with the rectangular domain, the circular domain showed more difficulties in convergence. Nevertheless, the circular domain still has several merits. It can be extended to a bigger domain size with relatively fewer node points. In the case of a cylindrical or a hemispheric body shape, it is more convenient to make elements from the inner region of the free surface to the open boundary because of geometrical similarities. To solve these problems, one-way or two-way biased panels were integrated on the free surface boundary as shown in figures 4.5 and 4.6.

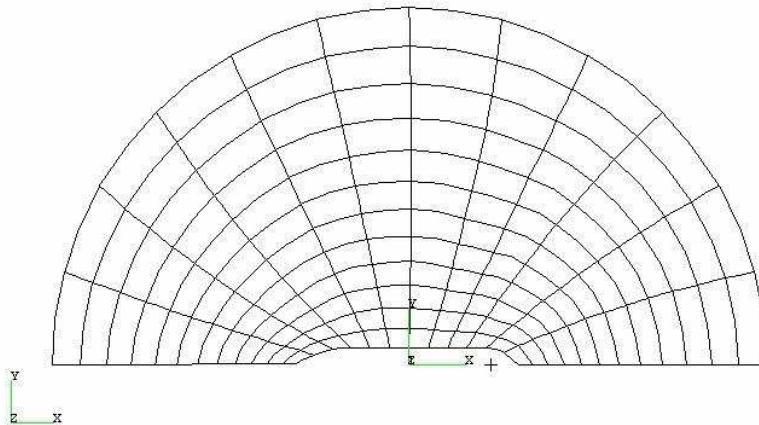


FIGURE 4.5. Circular domain for an FPSO with one-way biased elements.

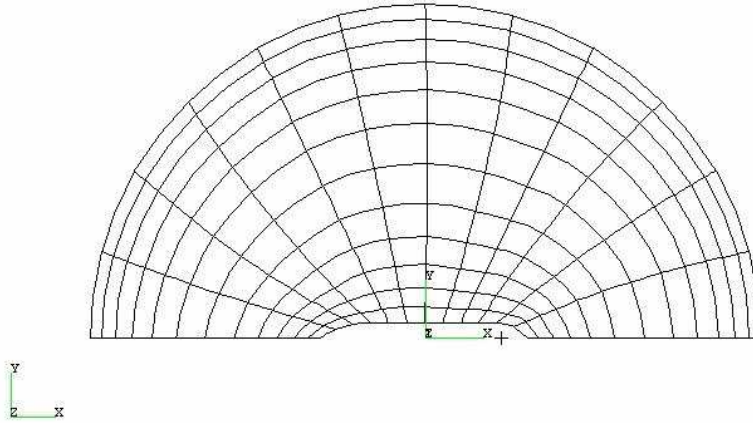


FIGURE 4.6. Circular domain for an FPSO with two-way biased elements.

Increasing the number of spokes seems to be a solution. However, this requires more elements with a longer simulation time and does not necessarily improve convergence. In some cases, convergence was achieved in unexpected ways. Figure 4.7 shows inner and outer regions for higher resolution close to the hemisphere. Figure 4.8 shows smaller elements along the open truncated boundary. The recommended guideline for a robust mesh generation is a rectangular domain shape with an inner region that prevents a change of the element shape from severe distortion.

4.4 Time stepping methods

At this point, a time independent boundary value problem becomes an initial value problem. Initial boundary value problems are one of the four approximation methods commonly used for ordinary differential equations to solve the free surface prob-

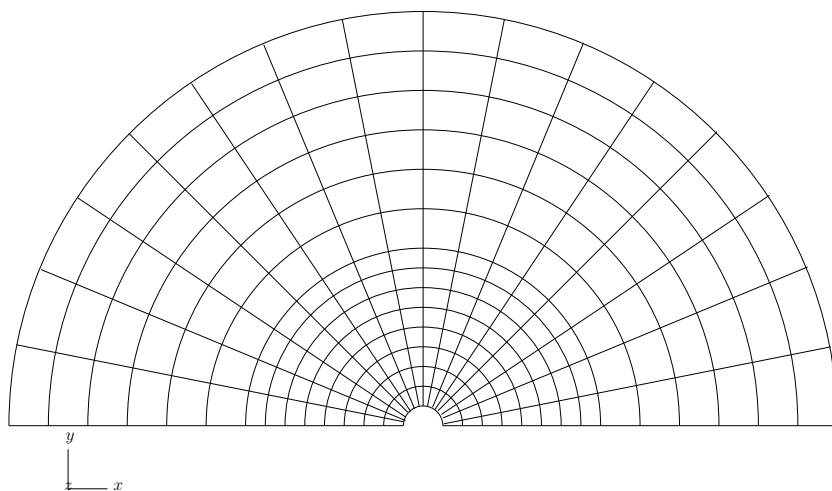


FIGURE 4.7. Circular domain for hemisphere with inner and outer regions.

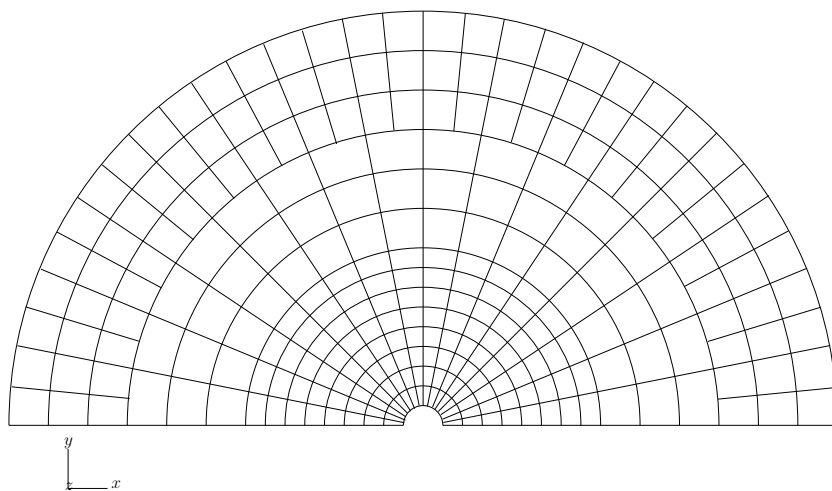


FIGURE 4.8. Circular domain for hemisphere with inner and outer regions, and smaller elements on the open boundary.

lem. These are: the Euler's method, the Runge-Kutta(R-K) method, the Predictor-Corrector(P-C) method, and the Hamming's method. The P-C method can be used separately: the Adams-Moulton (A-M) method and the Adams-Bashforth(A-B) method.

The fourth order R-K method for a free surface kinematic and dynamic boundary condition at each time step is denoted as

$$\eta^{\tau+1} = \eta^{\tau} + \frac{1}{6}\Delta t (\eta_1 + 2\eta_2 + 2\eta_3 + \eta_4) \quad (4.14)$$

and

$$\phi^{\tau+1} = \phi^{\tau} + \frac{1}{6}\Delta t (\phi_1 + 2\phi_2 + 2\phi_3 + \phi_4), \quad (4.15)$$

where $\eta^{\tau+1}$ and $\phi^{\tau+1}$ are the required values for the next time step. The η^{τ} and ϕ^{τ} are the given values at the time step and Δt is the time increment. The subscripts 1 to 4 in η and ϕ represent the evaluation stage of the four procedures in one time step. The R-K method is called a multi-step procedure since it needs four times as much calculation in comparison with the A-B-M method.

Dommermuth & Yue (1987) suggested a guidance for the mesh size and the time increment. They performed a Von Neumann stability analysis for the fourth order R-K method with linearized forms of free surface boundary conditions.

The Courant condition is

$$\Delta t^2 \leq \frac{8}{\pi} \frac{\Delta x}{g}, \quad (4.16)$$

where Δt is the time step size and Δx is the local grid spacing. Dommermuth & Yue

suggested fixing Δx first and then choosing the minimum time step size Δt .

4.4.1 Saw-tooth instability

The free surface configuration, after a time duration over a one-dimensionless time unit, began to develop some wiggles on the free surface in front of the sphere and spread out gradually in the longitudinal direction. Reduction of the time step to a minimum step size to increase the number of elements did not minimize the effect of a saw-toothed instability phenomena.

Longuet-Higgins & Cokelet (1976) first demonstrated the phenomena of a saw-tooth instability in their two-dimensional fully nonlinear time dependent wave simulations. They assumed that this instability occurred partly from the numerical cause and partly from the physical reason. Therefore, a smoothing technique was employed to suppress this instability. However, this technique may result in an underestimated solution. Miyata, Sato & Baba (1987) assumed that the possible cause was due to the panels in the region of higher gradients. The minimum element size cannot be controlled effectively for a given time step. A smaller time step is required avoiding the instability problem. Accordingly, the total simulation time may increase. This study intended to use this smoothing technique moderately in order to keep a portion of solution containing the physical meaning. Dommermuth & Yue (1987) recommended the proper size of time step and the panel size as shown in the equation (4.16). If these guidelines are applied, the saw-tooth instability still remains. The Chebyshev filters will be adopted to suppress it.

4.4.2 Chebyshev filtering scheme

The undesirable saw-tooth like a noise in wave elevations with high frequencies usually occurs as the total simulation time increases. This usually occurs when the time step size increases for the purpose of reducing the total simulation time. This instability may cause the failure of the simulation if it accumulates without control. This numerical instability is not well-understood. However, the time step and grid size are known as the two most important factors. To remove this instability, numerical filtering methods can be employed (Miyata, Sato & Baba 1987). However, excessive use of numerical filtering may affect the field solution, which is usually underestimated.

The Chebyshev filtering scheme was introduced by Longuet-Higgins & Cokelet (1976) to avoid a saw-toothed appearance in the wave profile. Bai, Kyoung & Kim (2003) also adopted it to improve their numerical stability in a shallow water problem.

The method is shown as follows: A function $f(x)$ defined at equally spaced points x_j ($j = 1, 2, 3, \dots$), which alternate points lie on a smooth curve, can be locally approximated by two polynomials as

$$\begin{aligned}
 h(x) &= (a_0 + a_1x + a_2x^2 + \dots + a_nx^n) \\
 &+ (-1)^j(b_0 + b_1x + b_2x^2 + \dots + b_{n-1}x^{n-1}), \quad (4.17)
 \end{aligned}$$

where $(a_0 + a_1x + a_2x^2 + \dots + a_nx^n)$ represent the smooth mean curve and the remainder is the quantity which oscillates.

This study used with $n = 1$ and $j = 2$.

$$\bar{f}_j = \frac{1}{4} (f_{j-1} + 2f_j + f_{j+1}). \quad (4.18)$$

When $n = 2$ and $j = 2$, this leads to the five point smoothing formula.

$$\bar{f}_j = \frac{1}{16} (-f_{j-2} + 4f_{j-1} + 10f_j + 4f_{j+1} - f_{j+2}). \quad (4.19)$$

When $n = 3$ and $j = 2$, this leads to the five point smoothing formula.

$$\bar{f}_j = \frac{1}{32} (-f_{j-3} + 9f_{j-1} + 16f_j + 9f_{j+1} - f_{j+3}). \quad (4.20)$$

Upon further investigation, there was no saw-tooth phenomenon found in the case studies with a proper size of element and time stepping.

4.5 Modulation function

Modulation function is adopted to avoid a sudden interruption in the calculation domain. This is called a ramp function. The idea of a modulation function is straightforward: Set a duration of a modulation function effect for the gradually developing scattered or diffracted potential. Then, observe how long the modulation function effect lasts.

There are no absolute rules to accelerate the body from rest to the final speed. For instance, Haussling & Coleman (1979) used

$$F_{mod}(t) = \begin{cases} 0, & \text{when } t = 0 \\ t, & \text{when } 0 < t < 1 \\ 1, & \text{when } t \geq 1 \end{cases}, \quad (4.21)$$

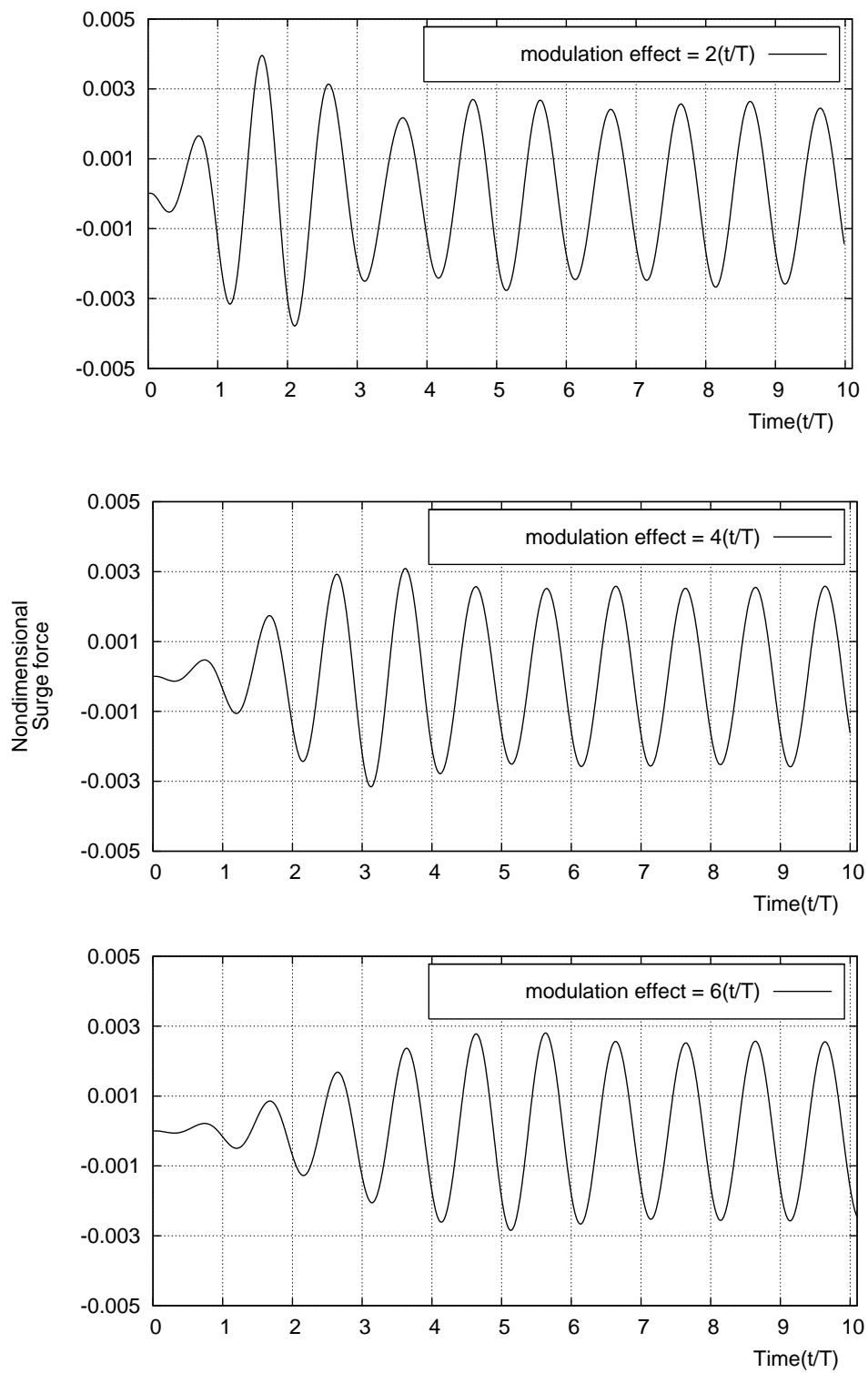
where F_{mod} is modulated values. Ohring (1981) used an abrupt starting speed as $u(t) = 1$. Mizumura (1985) used a smooth acceleration function by setting $u(t) = \tanh 3t$. This rule was chosen to accelerate the body uniformly from its rest to the final speed.

The equation (4.22) was used for the present study.

$$F_{mod}(t) = \begin{cases} \frac{1}{2} \left[1 - \cos \left(\frac{\pi t}{T_{mod}} \right) \right] & \text{when } t \leq T_{mod} \\ 1 & \text{when } t > T_{mod} \end{cases}, \quad (4.22)$$

where T_{mod} is the duration of the modulation effect.

Figure 4.9 shows the modulation function effect. All three graphs show a nondimensional surge force. The top graph shows that the modulation function worked until the second cycle. Between the second and third cycle, there are overestimated values and there needs to be a longer application of modulation function. The middle graph shows that the modulation function worked until the fourth cycle, then it starts to converge from the fifth cycle. The bottom graph shows the modulation effect until the sixth cycle. After the modulation effect is over, the solution is converged. Applying a longer modulation function requires more simulation time. Therefore, a properly chosen duration is necessary for the modulation functions.

FIGURE 4.9. Comparison of modulation function effect until $t/T = 2, 4,$ and 6 .

4.6 Overview of THOBEM, WAMIT, and TiMIT

In the Chapter IV, numerical simulations are performed by THOBEM, WAMIT and TiMIT. Although these programs are based on potential theory, each has its distinctive qualities. THOBEM uses a higher order element whereas the other methods use a constant panel. THOBEM and TiMIT are time domain simulation programs and WAMIT is a frequency domain program. The constant current force can be solved using THOBEM and TiMIT. WAMIT is a BEM program to solve a boundary value problem for the interaction of water-waves with prescribed bodies at infinite- and finite-water depth. TiMIT was developed based on the WAMIT algorithm. To treat time domain simulation, TiMIT was adopted by an impulse response function.

There are several limitations to these programs. These limitations are due to the potential theory and the unknown position of the boundaries (i.e. position of the free surface).

4.6.1 The limitations

The limitations are as follows:

- i) Viscous effects of the fluid cannot be handled because of its potential flow.
- ii) Small wave amplitude compared to the wave length is due to the nonlinear boundary value problem with a perturbation series solution.
- iii) For diffraction problems, a body stays at its mean position. When a body moves, its motion is in the same order as the wave amplitude.

4.6.2 Process in general

THOBEM, WAMIT, and TiMIT are all based on the boundary element method. The similarities of the process are as follows:

- i) The time harmonic solution corresponding to the first- and second-terms of the series expansion are solved for a given steady state incident wave field.
- ii) The incident wave field is assumed to be represented by a superposition of the fundamental first-order solutions of particular frequency components in the absence of the body.
- iii) The boundary value problem is recasted into integral equations using the wave source potential as a Green function.
- iv) The integral equation is then solved by a panel method for the unknown velocity potential or the source strength on the body surface.

4.6.3 The differences

These processes are actually quite similar to each other. However, the main differences are as follows:

- i) The Green function in WAMIT

The Green function $G(x; \xi)$ is the velocity potential at the point x because a point source with the strength -4π is located at the point ξ .

$$G(x; \xi) = \frac{1}{r} + \frac{1}{r'} + \frac{2\nu}{\pi} \int_0^\infty dk \frac{e^{k(z+\zeta)}}{k - \nu} J_0(kR). \quad (4.23)$$

ii) Similarly, the Green function in TiMIT is

$$G(x; \xi, t) = \frac{1}{r} + \frac{1}{r'} + 2 \int_0^\infty dk \left[1 - \cos(\sqrt{gkt}) \right] e^{k(z+\zeta)} J_0(kR). \quad (4.24)$$

iii) The Green function in THOBEM is

$$G(x; \xi) = \frac{1}{r} + \frac{1}{r'}, \quad (4.25)$$

where

$$r^2 = (x - \xi)^2 + (y - \eta)^2 (z - \zeta)^2 \quad (4.26)$$

and

$$r^2 = (x - \xi)^2 + (y - \eta)^2 (z + \zeta)^2. \quad (4.27)$$

J_0 is the Bessel function of zero order and $\nu = \omega^2/g$ is the wavenumber.

In the equation (4.24),

$$R = \sqrt{(x - \xi + U|t - \tau|)^2 + (y - \eta)^2}. \quad (4.28)$$

In the equation (4.23),

$$R = \sqrt{(x - \xi)^2 + (y - \eta)^2}. \quad (4.29)$$

The exciting force components are expressed by means of convolution integrals

$$F_j(t) = \int_{-\infty}^{\infty} d\tau K_{jD}(t - \tau, \beta) \zeta(\tau) \quad \text{when } j = 1, 2, \dots, 6, \quad (4.30)$$

where kernel $K_{jD}(t, \beta)$ is the diffraction impulse response function. In order to make this clearer, please refer to Appendix D for more details on convolution integrals.

Table 4.1 shows the differences among these programs.

	THOBEM	WAMIT 5.4	TiMIT
Panel	higher order	constant	constant
Simulation domain	time	frequency	time
Current force	capable	incapable	capable
License	Texas A&M	MIT	MIT
Source code	Fortran 77, 90/95	Fortran 90	Fortran 77, 90/95
Commercial provider	no	yes	no

TABLE 4.1 Comparison of the simulation programs: THOBEM, WAMIT ver. 5.4, and TiMIT.

4.7 Simulation results

A hemisphere was chosen for the preliminary simulation since it does not have any sharp edges. Based on the hemisphere case study, we collected mor information for the time domain simulation. There still remain the numerical issues previoully mentioned such as solution divergence, saw-tooth instability, and the reflection at the

open truncated boundary. However, we could overcome these numerical difficulties in sections 4.1 - 4.5.

4.7.1 A case study for convergence test with various time grid sizes

A convergence test was performed. A convergence test cannot be performed only on the element size of the body surface in the WAMIT case. THOBEM has even more complicated factors as below:

- i) the time grid size
- ii) the duration of the modulation function
- iii) the free surface domain size
- iv) the free surface element size

Sizes of elements are the parameters on the body and the open truncated boundary. However, these two are not the only major factors that cause convergence. Since both elements are also highly related to free surface elements, we did not intend to provide a convergence test for the body elements. The data set of the time history was obtained from a time marching scheme. This data set was not regenerated from the frequency domain using fast Fourier transform (FFT). Therefore, this case study was needed to run a supplementary test for convergence with the various sizes of the time grid.

The simulation was performed up to seven cycles under the following conditions: The domain size is $1360 \times 1280 (m^2)$. The incident wave frequency is $0.6 (rad/sec)$. The

distance between node points is 40 (m). The duration of the modulation function effect was set to the second cycle.

Figures 4.10 - 4.13 show x directional diffracted wave forces with various frequencies. The size of the time step was defined as a wave period divided by the number of time steps shown as a t -step in the graphs.

Figure 4.10 shows time steps from 20 to 50 in segments of 10. The time step 20 case started to diverge from the fourth cycle. Heavy fluctuation was shown between the fourth and the fifth cycles. Beyond the fifth cycle, it showed divergence. The time step 30 case showed divergence after the sixth cycle. Time step 40 and 50 cases in figure 4.10 and time step 60 and 70 in figure 4.11 show similarly diverged phenomenon. These simulations cannot be performed after the seventh cycle because divergence occurs between the sixth and the seventh cycles.

The x directional force started to converge from the time step 80. Figures 4.12 and 4.13 show convergence tests for time steps from 100 to 160. Most simulations were performed in as many as 150 time steps and successfully performed up to 20 cycles without any numerical difficulties.

4.7.2 Diffraction study

The diffraction study was performed in order to get the first order wave forces and moment. The dimension of the simulation model is based on the Gulf of Mexico FPSO(GoM FPSO). Table 4.2 shows the dimension of the FPSO simulation model.

Figure 4.14 shows a perspective view of an FPSO in the rectangular domain. The bow is to the negative x -axis direction. The free surface elements near the FPSO are

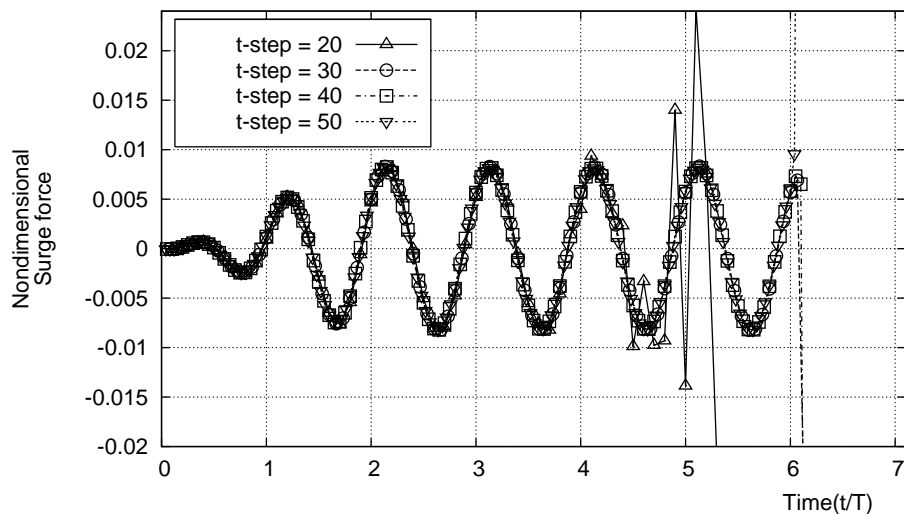


FIGURE 4.10. Convergence test for time steps per nondimensional time 20, 30, 40, and 50.

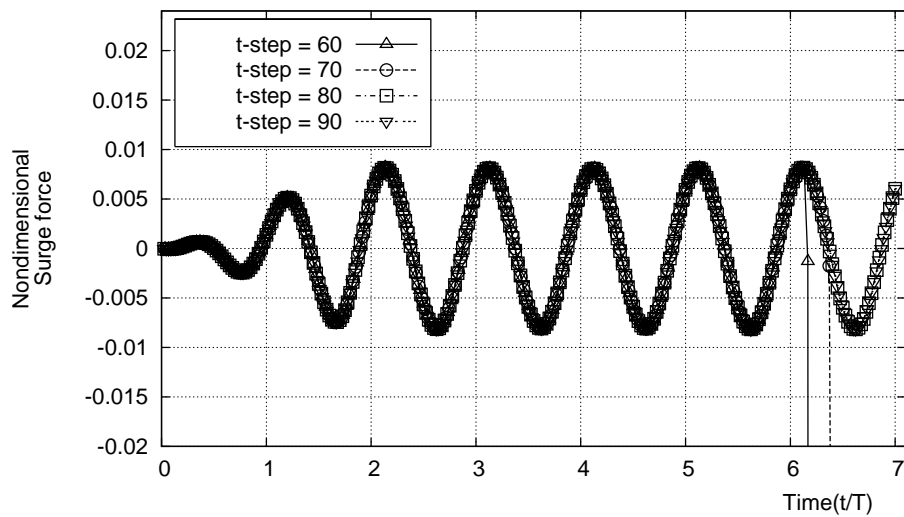


FIGURE 4.11. Convergence test for time steps per nondimensional time 60, 70, 80, and 90.

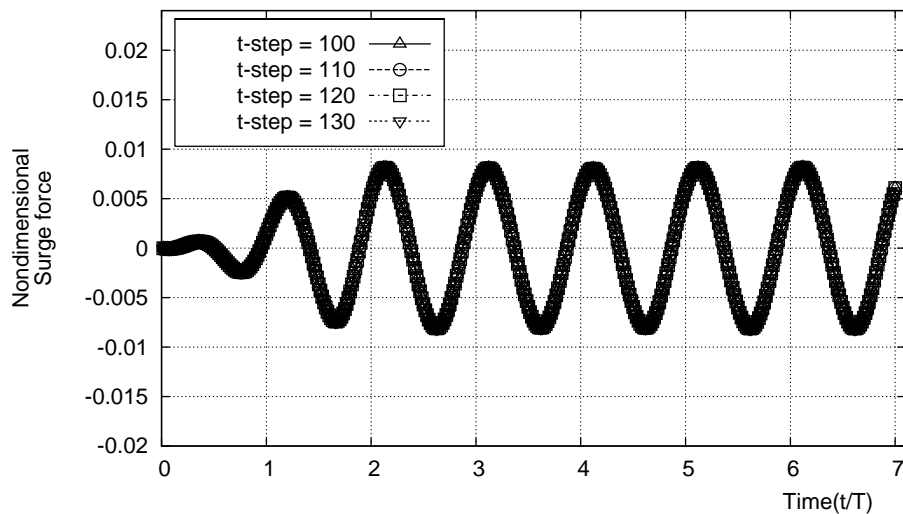


FIGURE 4.12. Convergence test for time steps per nondimensional time 100, 110, 120, and 130.

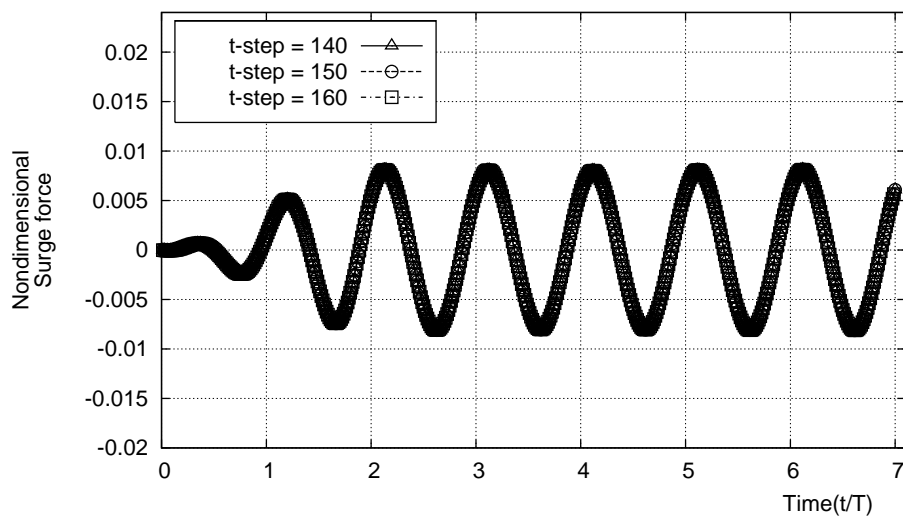


FIGURE 4.13. Convergence test for time steps per nondimensional time 140, 150, and 160.

Designation	Quantity	Symbol
Vessel size	200	kDWT
Length between perpendiculars	310	m
Breadth	47.17	m
Depth	28.04	m
Draft	15.12	m
Block coefficient	0.85	

TABLE 4.2 Dimensions of the GoM FPSO.

selected particularly in order to avoid a sudden change of the element shape. The open boundary is truncated at $680(m)$ from the origin.

Figure 4.15 shows the time history of the wave forces and moments of the GoM FPSO. The first and second graphs are the first order forces to the x - and z -axis respectively. Due to the modulation function effect up to the second cycle, the THOBEM results show a transient mode. The third graph shows overestimated values after modulation function effect stops. They start to converge from the third cycle. WAMIT can provide the time history of the first order quantities with the magnitude and the relative phase angle. The time history for WAMIT is generated as a post process.

Figure 4.16 shows the comparison results of THOBEM and WAMIT. All three graphs show the first order forces and moment from the diffracted waves. The y -axis represents nondimensional values. Force is normalized by $\rho g A X_{cl}^2$ and moment is normalized by $\rho g A X_{cl}^3$. X_{cl} is the characteristic length of body and A is the incident wave amplitude.

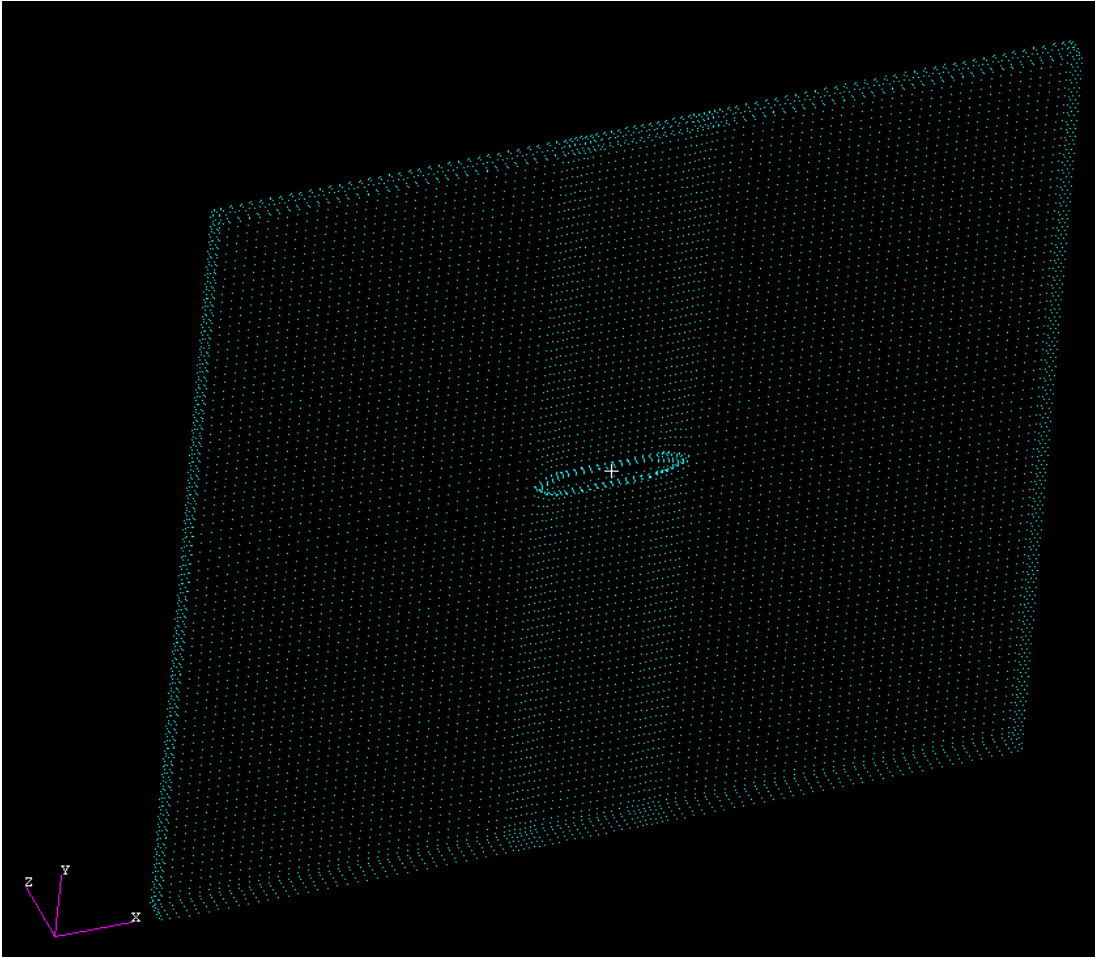


FIGURE 4.14. Perspective view of an FPSO in the rectangular domain.

THOBEM results are evenly deployed from 0.6 to 0.8 (rad/sec) in 9 cases. WAMIT results are also evenly deployed in the same frequency range in 41 cases similar to THOBEM's. We compared the results to see whether any irregular frequency problems occurred. The WAMIT results show smooth variation in this frequency range. The top graph resulted in good agreement from 0.6 to 0.675.

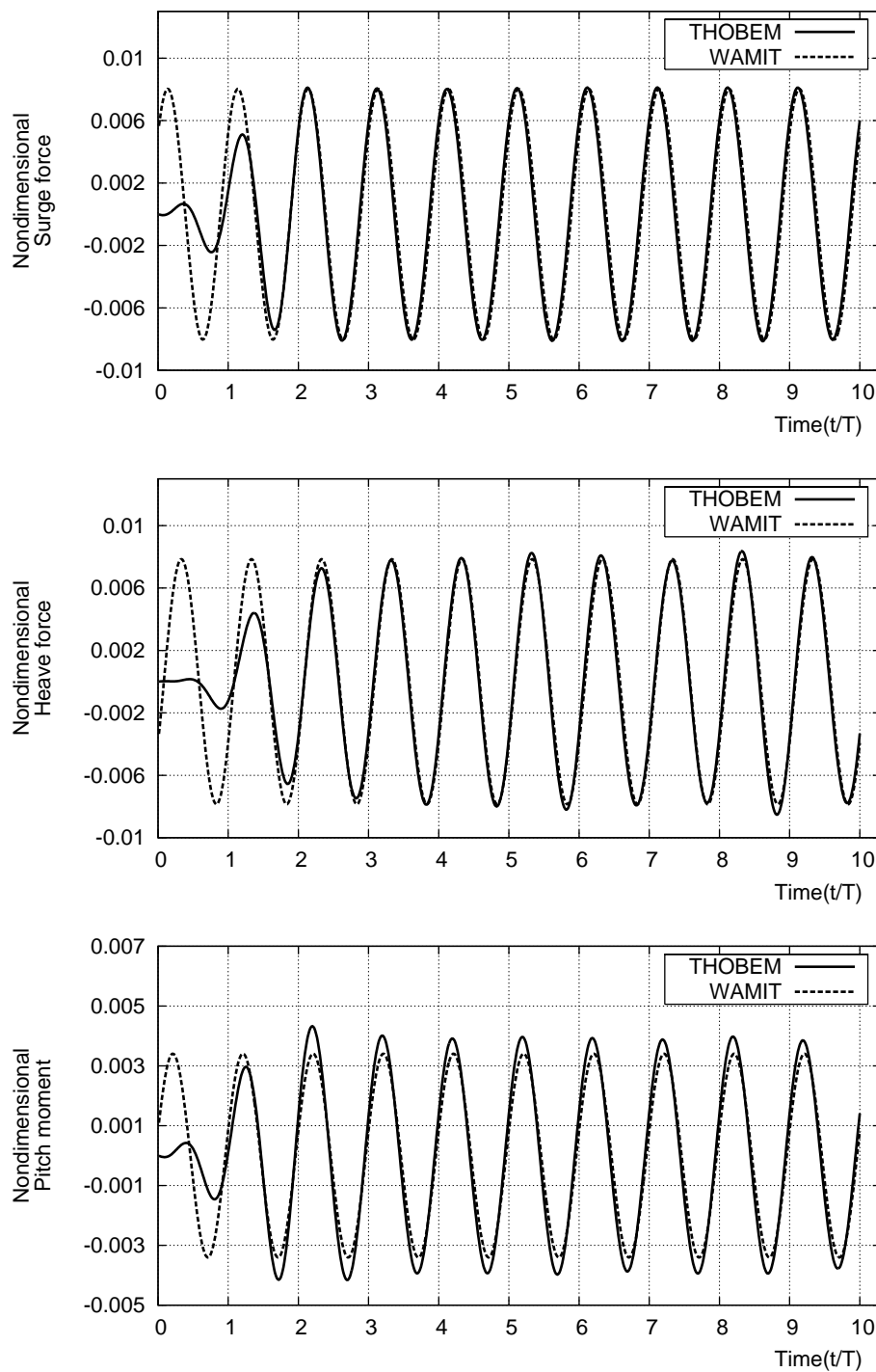


FIGURE 4.15. Comparison of THOBEM and WAMIT in time history of wave forces and moment.

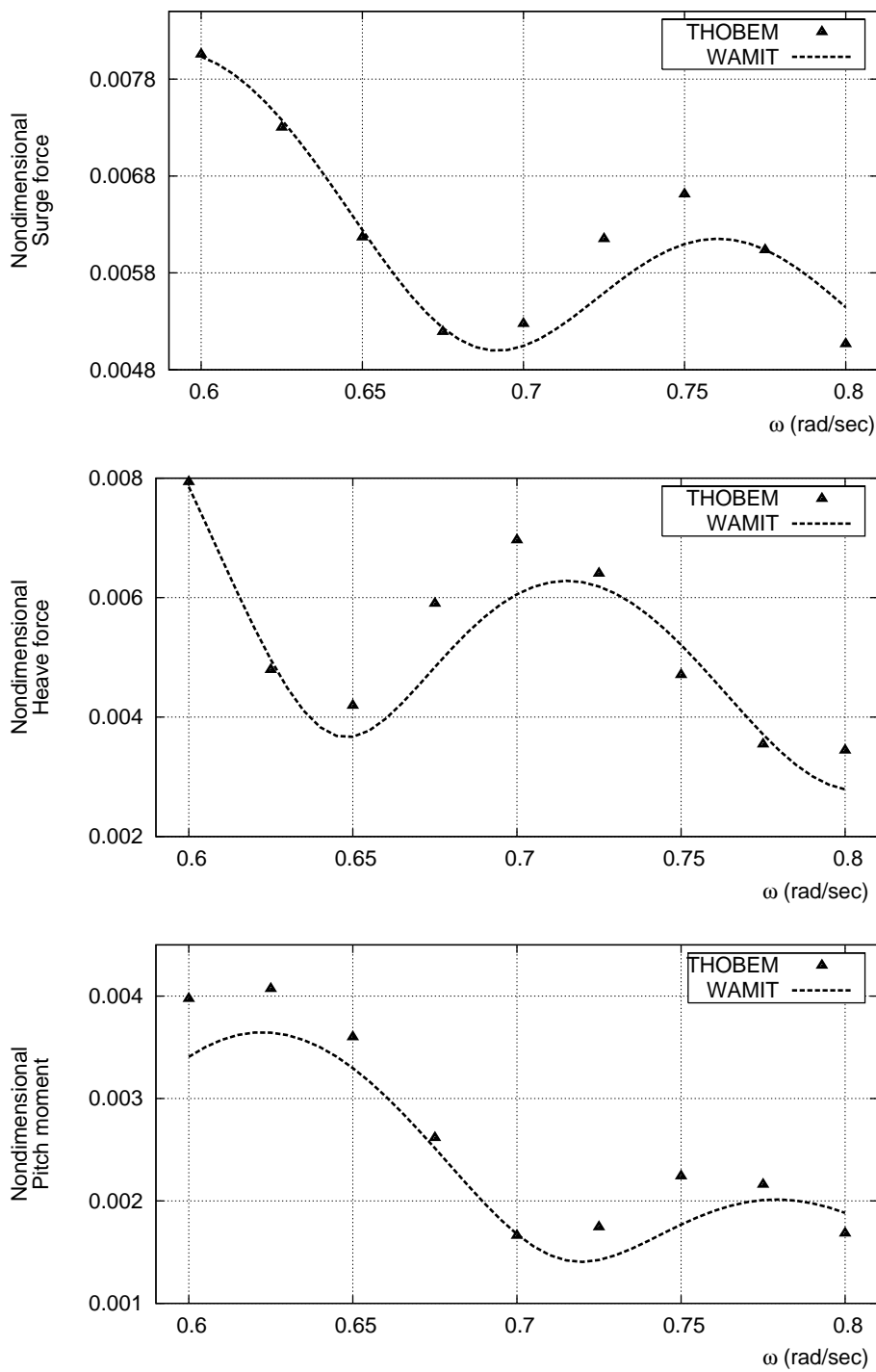


FIGURE 4.16. Comparison of THOBEM and WAMIT of the first order forces and moment in various frequencies.

4.7.3 Mean drift force

Mean drift force was investigated in diffraction case study. Mean drift force can be split into four components. Pinkster (1978) split up the drift force into four components:

$$\begin{aligned}
 \bar{F}_I^{(2)} &= \frac{1}{2}\rho g \int_{W_o} \left(\eta_R^{(1)}\right)^2 \vec{n} dW \\
 \bar{F}_{II}^{(2)} &= -\frac{1}{2}\rho \int_{S_B} (\nabla\phi^{(1)} \cdot \nabla\phi^{(1)}) \vec{n} dS \\
 \bar{F}_{III}^{(2)} &= -\rho \int_{S_B} (\vec{\alpha} \cdot \nabla) \left(\frac{\partial\phi^{(1)}}{\partial t} - U \frac{\partial\phi^{(1)}}{\partial x} + \nabla\phi^{(1)} \cdot \nabla\bar{\phi} \right) \vec{n} dS \\
 \bar{F}_{IV}^{(2)} &= \Omega^{(1)} \times \vec{F}^{(1)} + \vec{F}_{HS}^{(2)}
 \end{aligned} \tag{4.31}$$

The first components come from the relative wave amplitude square. The second components come from Bernoulli's quadratic term. These two terms are not related to current effect and body motions. A diffraction case with a zero Froude number case needs the first and the second components.

Figure 4.17 shows the comparison between THOBEM and WAMIT results. WAMIT provides total mean drift forces so that the results are not compared component by component. Figure 4.18 shows the first and the second components in THOBEM.

Some numerical errors can be included in the results of both WAMIT and THOBEM. We investigated where these differences came. The straits forward approach is to

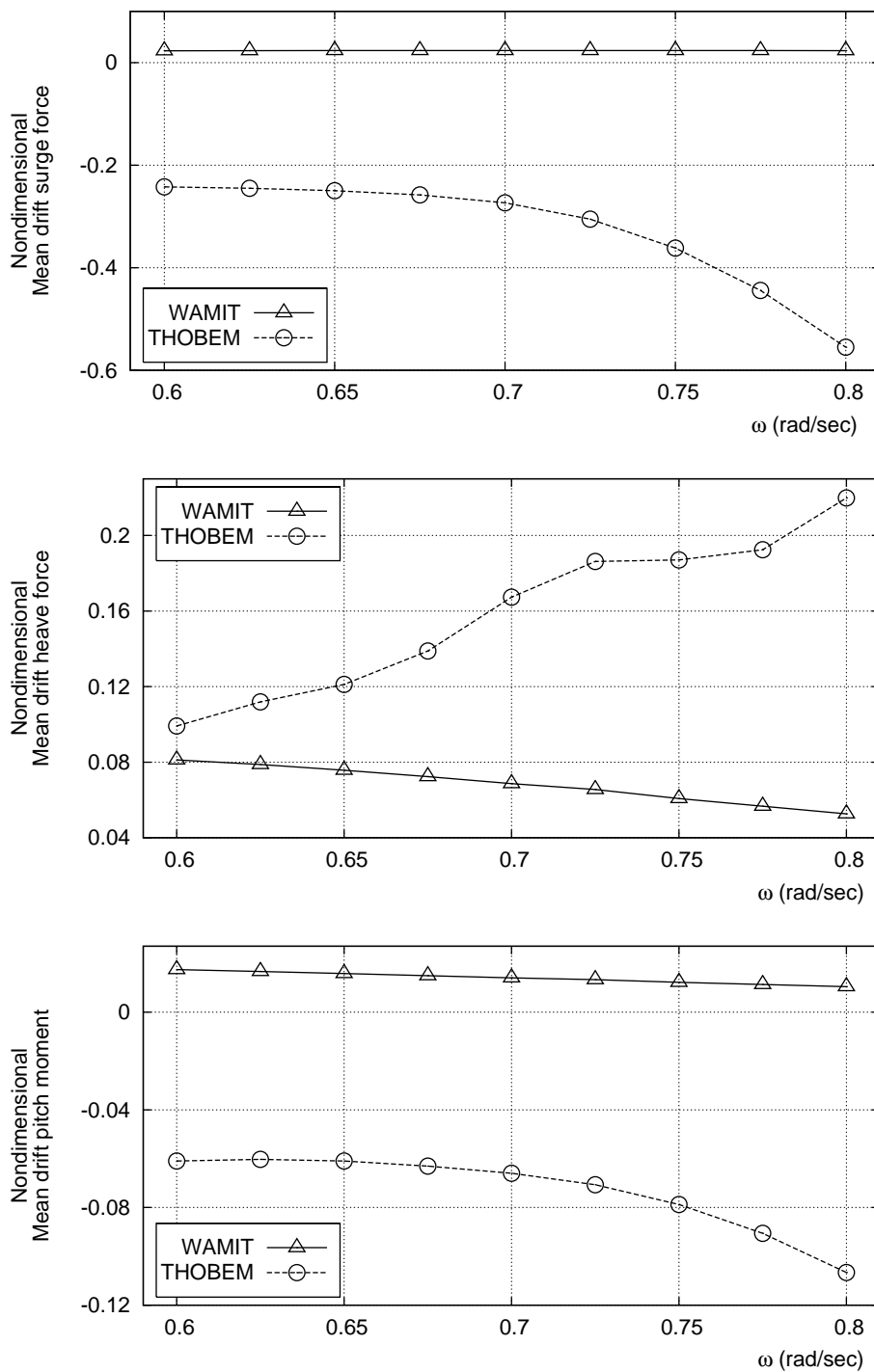


FIGURE 4.17. Comparison of THOBEM and WAMIT results for mean drift forces and moment with diffracted waves.

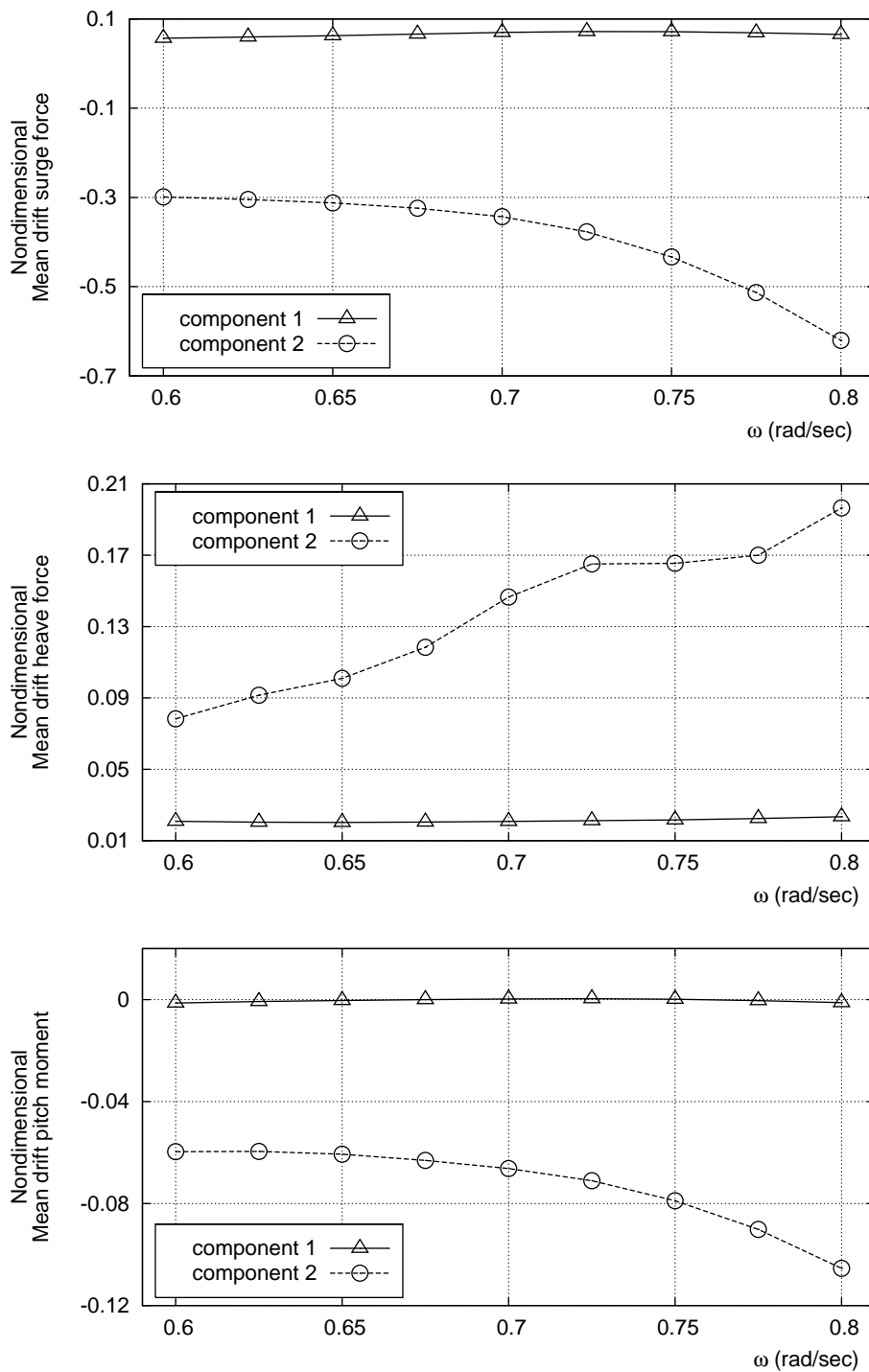


FIGURE 4.18. The first and second component of the mean drift forces and moment in THOBEM with diffracted waves.

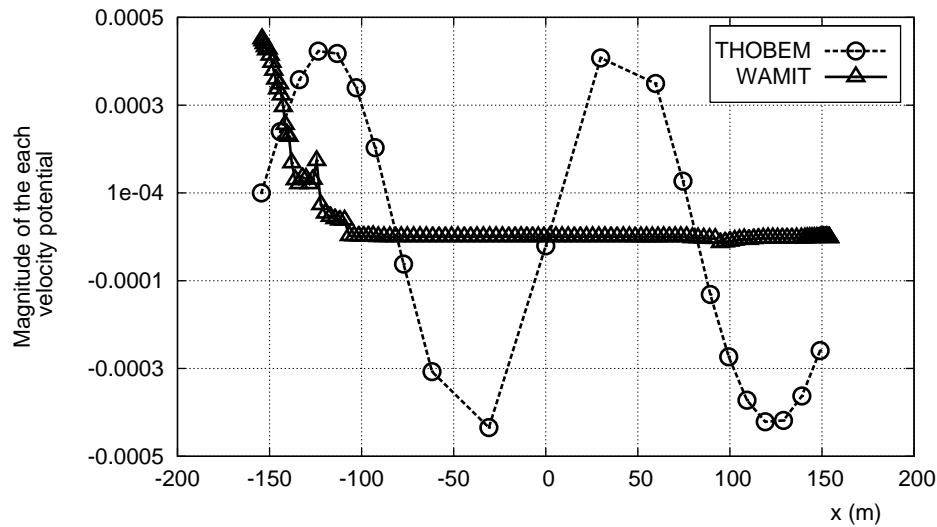


FIGURE 4.19. Comparison of THOBEM and WAMIT of the velocity potential.

compare velocity potentials at each node point. The problem this approach is WAMIT and THOBEM model is not the identical model. WAMIT is used constant panels and THOBEM is used higher order elements. Therefore, strategy of the investigation is of comparing between group of panel in WAMIT and group of element in THOBEM.

WAMIT can provide velocities with patricidal derivatives of the velocity potential as real and imaginary part. This is comparing of the mean drift force so that these are time independent variables. As long as we can extract proper information of the each panel or elements, we can compare for the WAMIT and THOBEM.

Figure 4.19 shows comparison of THOBEM and WAMIT result. X-axis represents x-coordinates of the node point. Y-axis is for the $1/2 \rho(\nabla\phi)^2$. According to the WAMIT result, dominant factor of the mean drift force is the potentials in the bow. Most of the node points did not effect at the result of the mean drift force. THOBEM result shows that the dominant factors indicated around bow, mid-section, and stern

case	data collection		number of data set	modulation function
	start	end		
1	3	4	150	2
2	4	5	150	3
3	4	5	150	2
4	4	5	100	2
5	8	9	150	7

TABLE 4.3 Parametric study for radiated wave.

4.7.4 Radiation study

A radiation problem was probed to get an added mass and the damping coefficient. The FPSO was forced to oscillate under a given amplitude and frequency in calm water. A wave was generated and propagated from the FPSO to the open boundary. This is called a radiated wave.

We did not expect to get any transient mode effect built up shown in figures 4.22 - 4.25. For this reason we performed a parametric case study. Table 4.3 shows parameters for the simulation. Cases 1 and 2 have the same sized time step. Data collection points are set to a period of one cycle later the modulation function effect stops. The modulation function effect stopped at the second and the third cycles respectively. Added mass and damping coefficients were obtained between the third cycle and the fourth cycle in case 1.

Figures 4.20 and 4.21 show the time history of the first order radiated wave forces

and moment when the FPSO oscillates in surge and in heave respectively. These simulations used the parameters of case 5 in table 4.3. The top graph is surge force. The middle graph is heave force. The bottom graph is pitch moment. The forces are normalized as $\rho g X_{cl}^2 A$ and the moments are normalized as $\rho g X_{cl}^3 A$. X_{cl} is the characteristic length of body and A is the amplitude of the forced motion. All six graphs show the forces and moment gradually developing and converging immediately after the modulation function effects stop. Most parametric cases turned out with similar features to convergence. The heave case simulations were performed up to the twelfth cycle without any numerical difficulties.

Figure 4.22 shows comparison results of added mass and damping coefficients to the x direction when THOBEM and WAMIT are in surge. Both of them are normalized by $\rho \forall$ and $\rho \omega \forall$ respectively, where ρ is the water density, \forall is the volume of FPSO, and ω is the forced oscillation frequency of the FPSO.

The top graph shows added mass. It shows better agreement in frequency ranges between 0.6 and 0.7(rad/sec) than the frequency range between 0.7 and 0.8. The frequency ranges between 0.7 and 0.8 (rad/sec) show slightly underestimated values. This decreasing trend is similar to the WAMIT results.

Figure 4.23 shows a comparison of the results of added mass and damping coefficients in z direction between THOBEM and WAMIT in surge. When an FPSO is forced to oscillate in x -axis, the added mass and damping coefficient in z direction have very small values in comparison with the x direction case. Therefore, figure 4.23 shows smaller values than figure 4.22. Added mass emerged out overestimated from the oscillation frequency of 0.6(rad/sec) to 0.65(rad/sec).

Figure 4.24 shows comparison results of added mass and damping coefficients in x

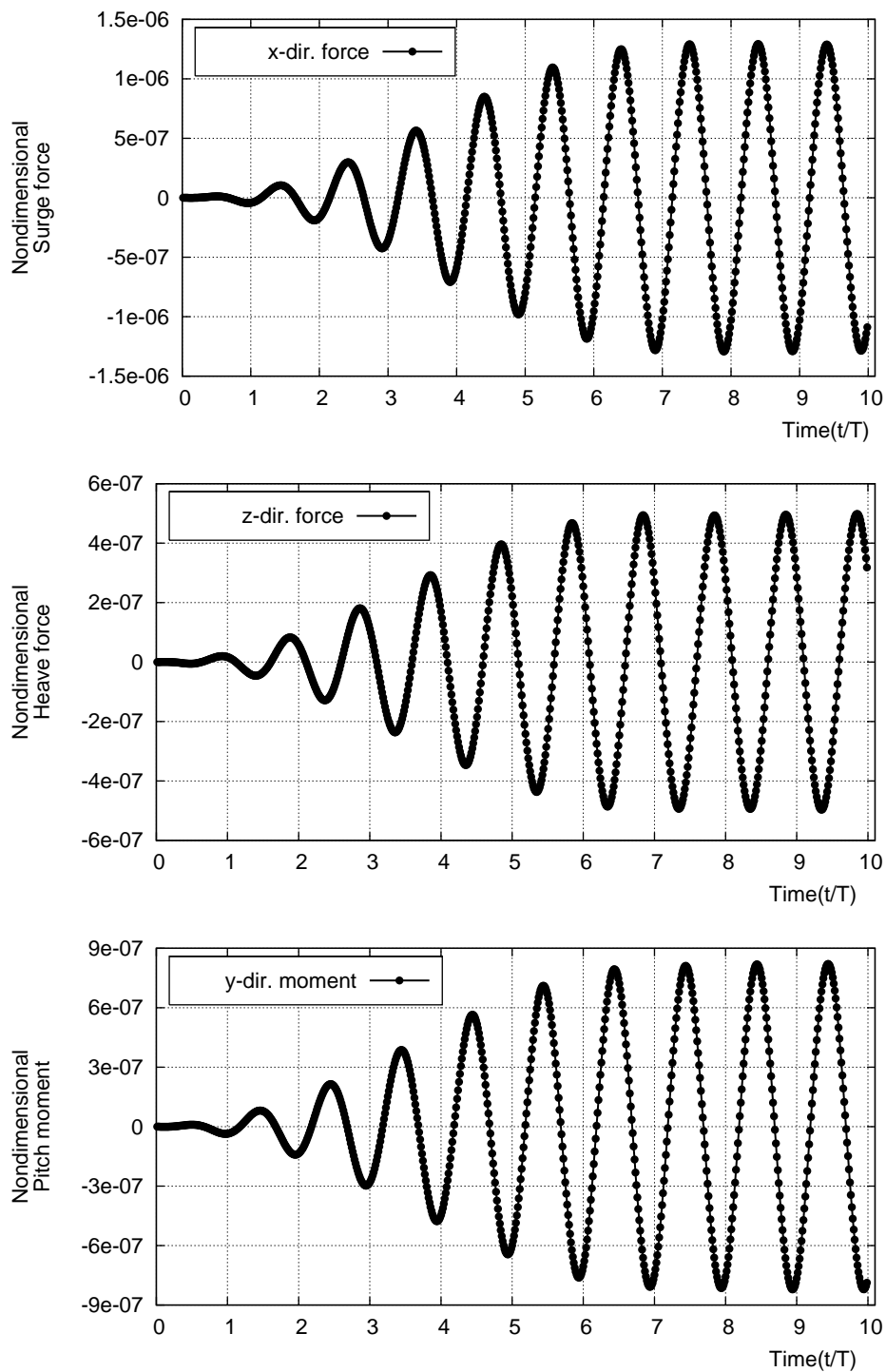


FIGURE 4.20. Time history of forces and moment from radiated wave in surge.

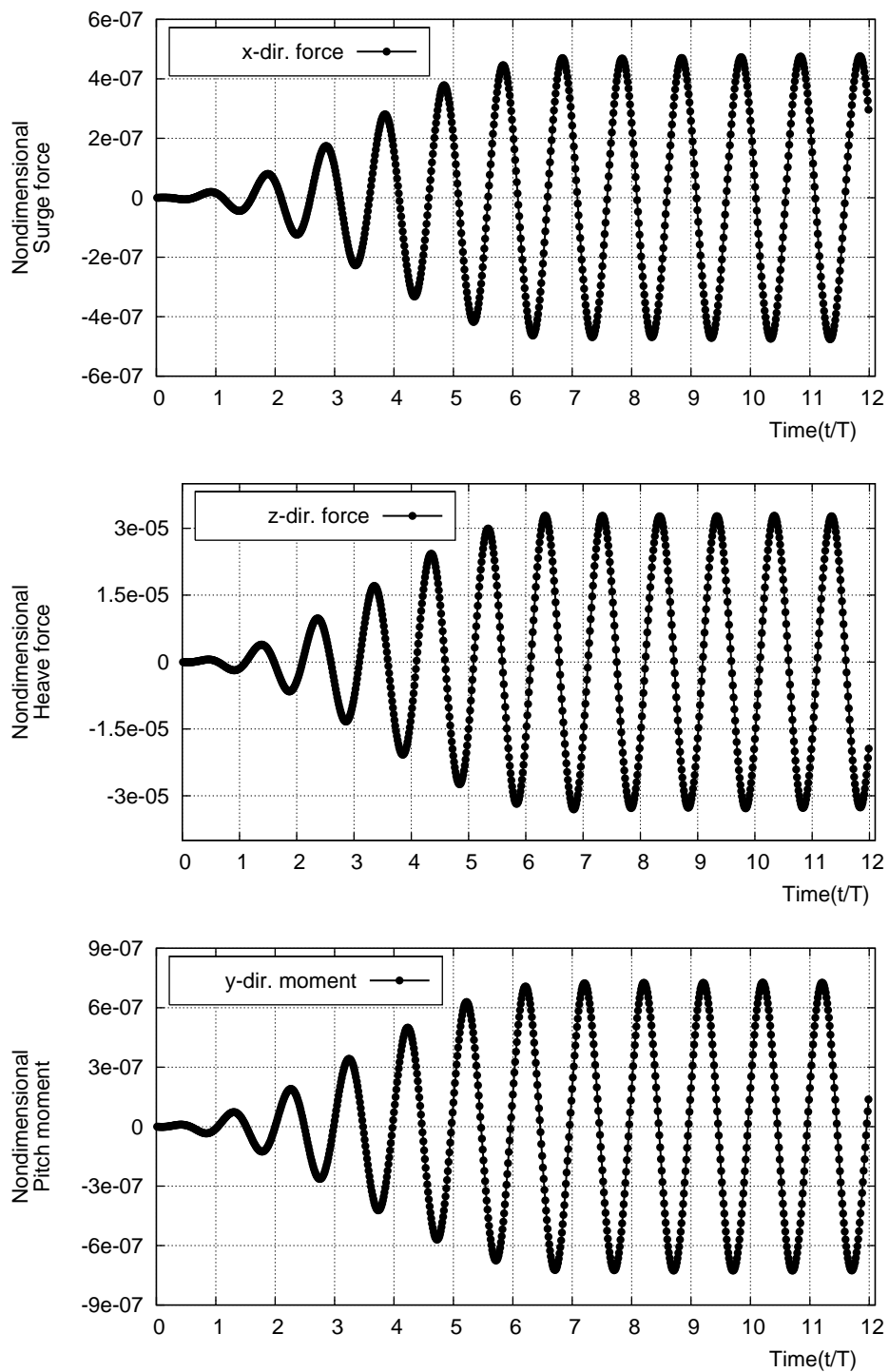


FIGURE 4.21. Time history of forces and moment from radiated wave in heave.

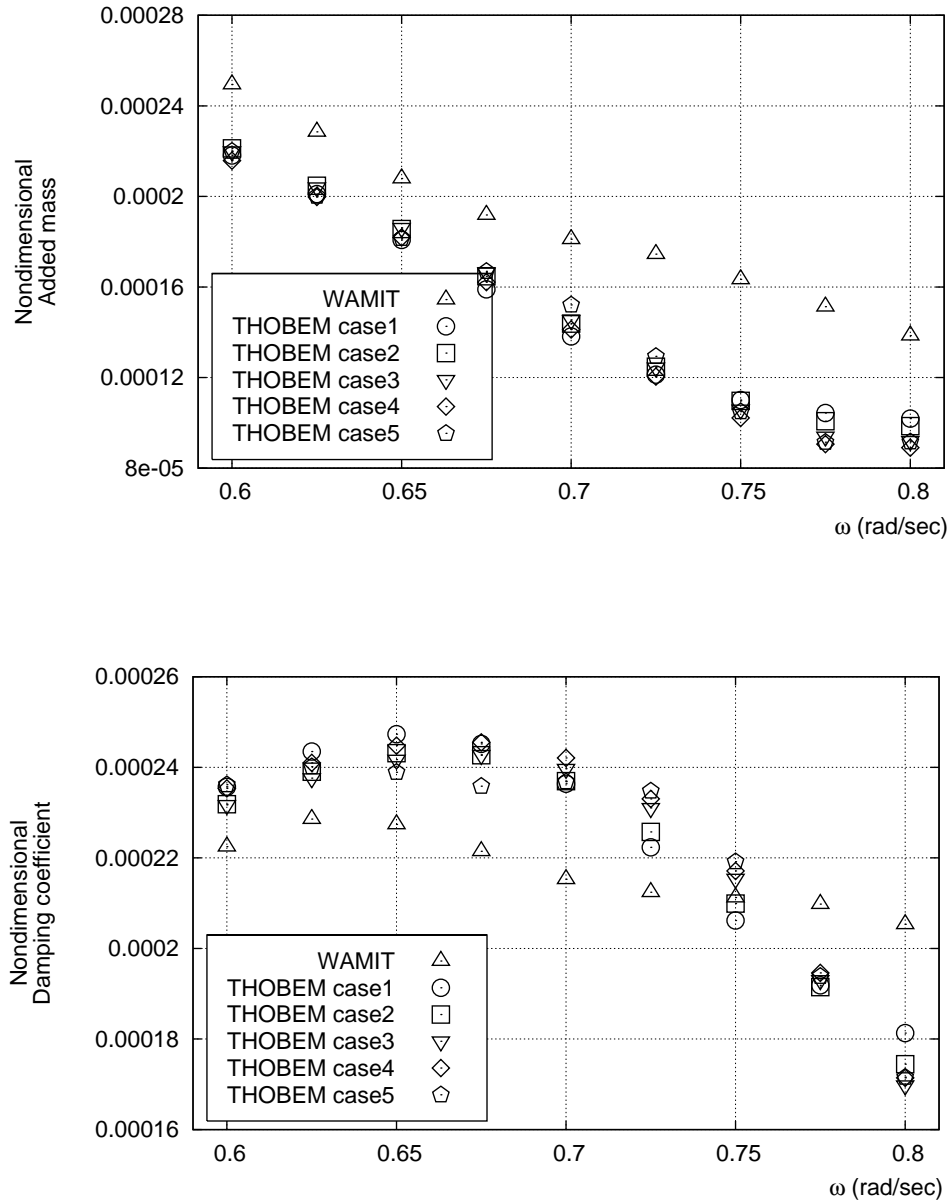


FIGURE 4.22. Added mass and damping coefficients in x direction when body oscillates in surge.

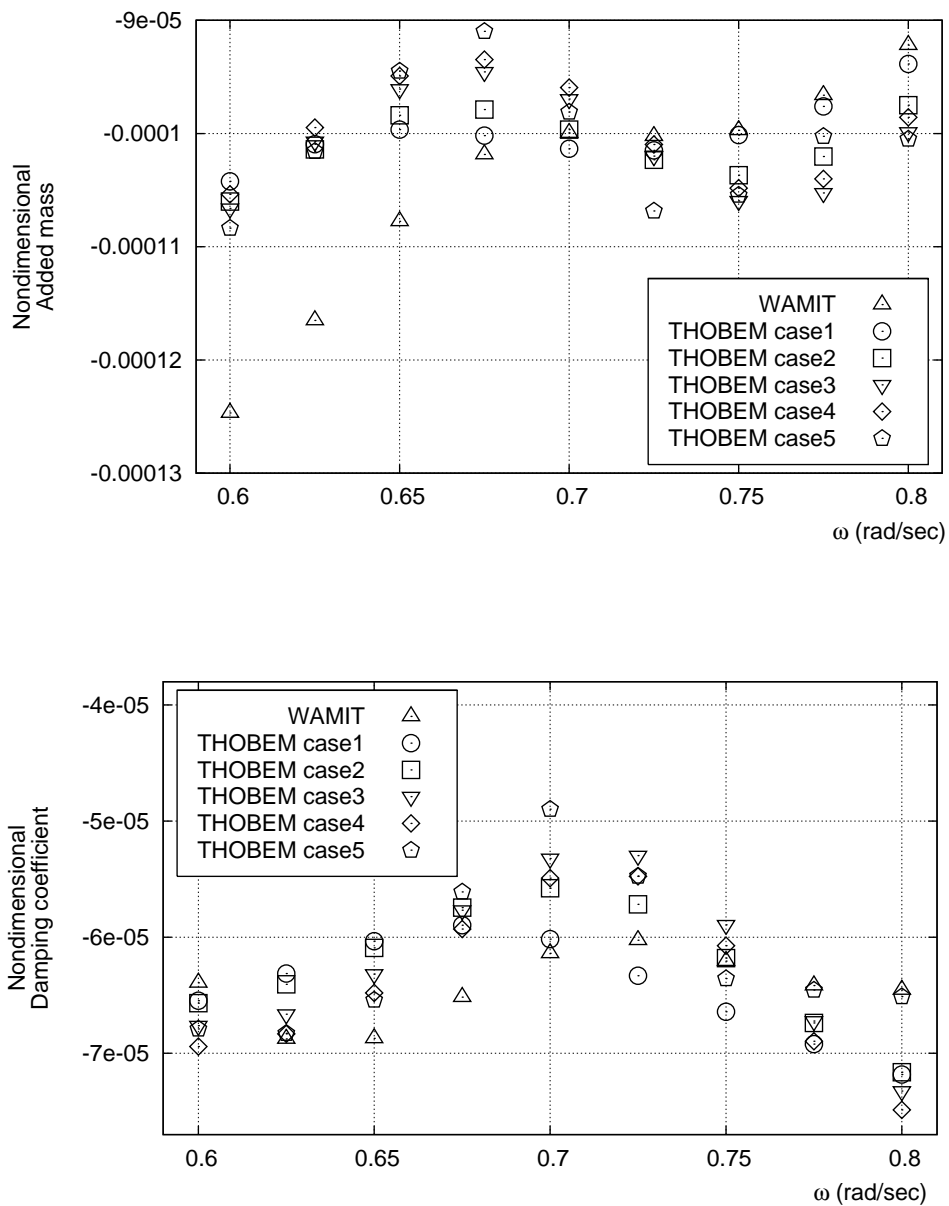


FIGURE 4.23. Added mass and damping coefficients in z direction when body oscillates in surge.

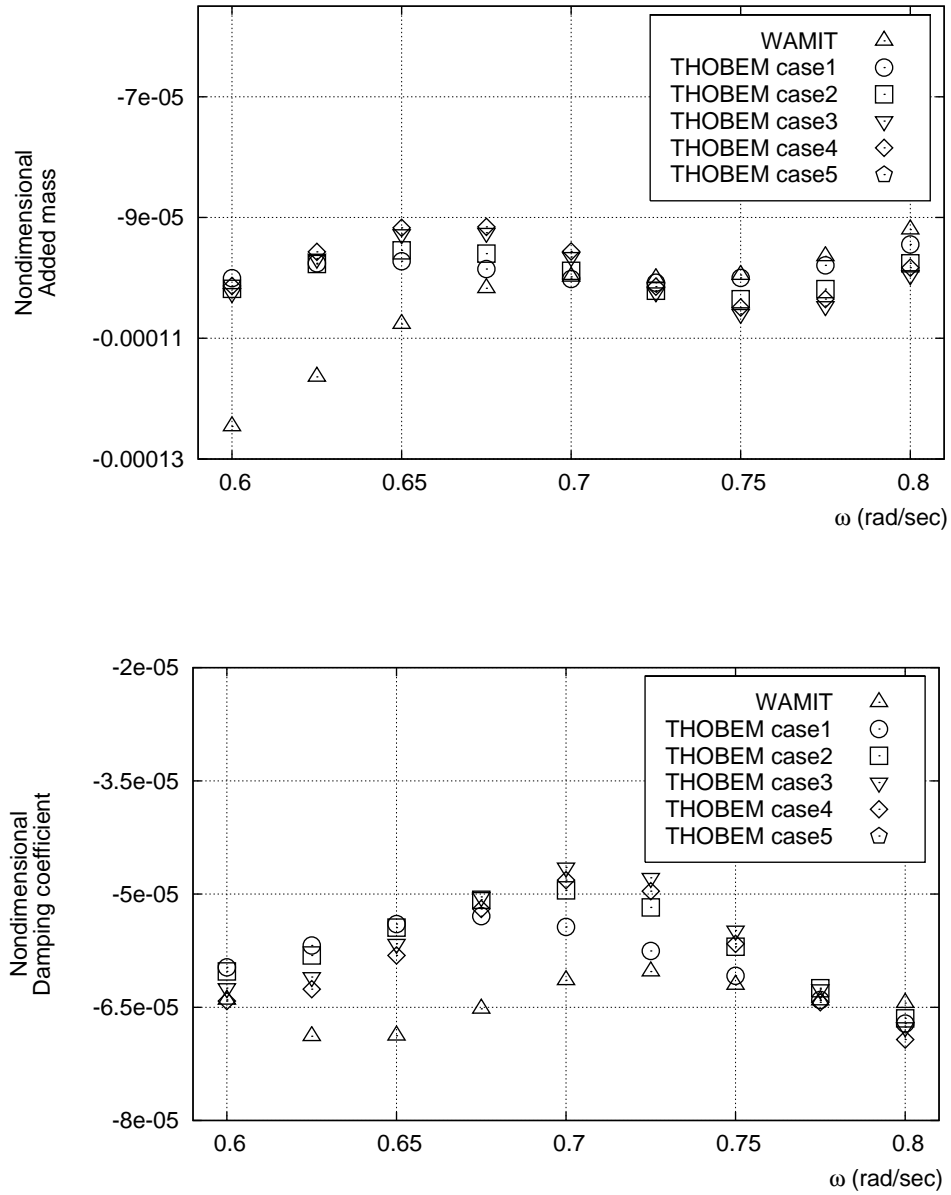


FIGURE 4.24. Added mass and damping coefficients in x direction when body oscillates in heave.

direction between THOBEM and WAMIT in heave. When $t = 0$, the FPSO is in the calm water without any motion. When $t = \Delta t$, the FPSO starts to oscillate by the forced motion amplitude ($A=0.1$) and frequency ($\omega=0.6$ to 0.8) in z direction. In the heave oscillation, the x directional added mass and damping coefficient were smaller values than z directionals'. The added mass coefficients were overestimated in the forced oscillation frequency ranges between 0.6 and 0.65 (rad/sec). The rest show good agreement. The bottom graph shows damping coefficients with good agreement.

Figure 4.25 shows a comparison of the results of the added mass and damping coefficients in z direction between THOBEM and WAMIT in heave. The top graph shows the differences of the added mass coefficients in the forced oscillation frequency range from 0.6 to 0.65 (rad/sec). The THOBEM results show better agreement in the higher frequency range.

4.7.5 Current effect study

Current effect studied both with diffracted and with radiated waves in various frequencies. Figure 4.26 shows two cases of the current effect with a diffracted wave. Figure 4.26 (a) shows an adverse current case. Incident wave propagates to the positive x -axis and the current travels to negative x -axis. This is the same as the head sea. Figure 4.26 (b) shows a collinear current case. Incident wave propagates to the same direction of the adverse case and the current travels in the same direction of the incident wave.

Before performing the simulation, we can predict the current effect. Table 4.4 shows this predictions. For adverse current, encounter frequency (ω_e) will be smaller than incident wave frequency (ω). Surge force will be smaller than without current cases

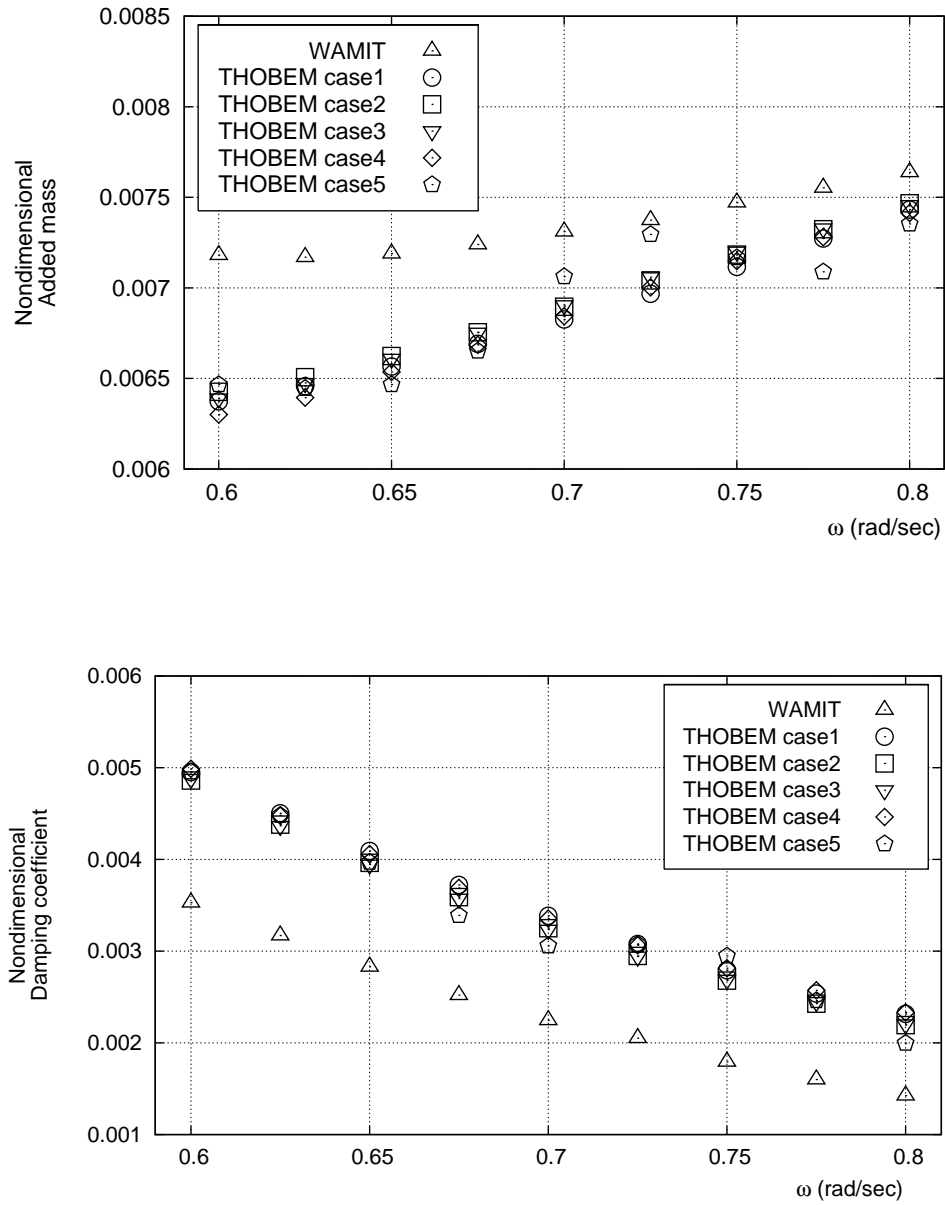


FIGURE 4.25. Added mass and damping coefficients in z direction when body oscillates in heave.

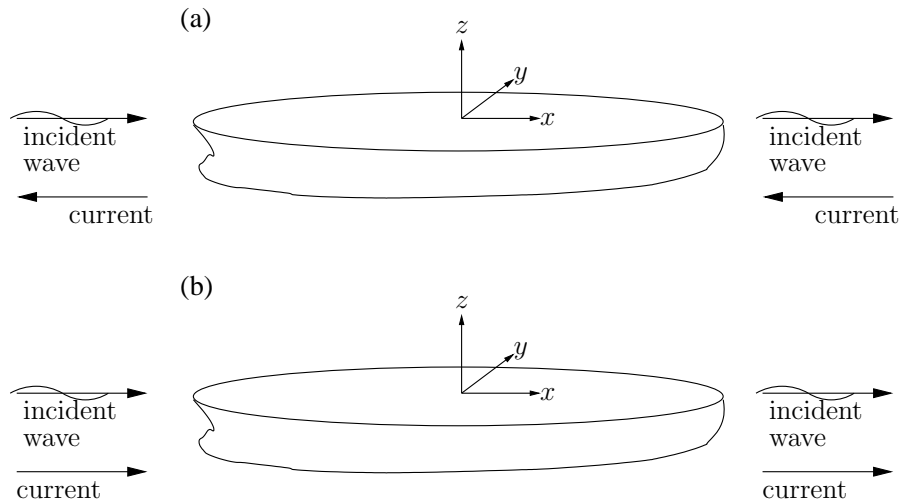


FIGURE 4.26. Current effect with diffracted waves for (a) head sea(adverse current) effect (b) following sea(collinear current) effect.

force. Heave force will not affect much from the current effect.

Figure 4.27 shows time history of the first order diffracted wave forces and moment with and without current. The top graph is surge force. The middle graph is heave force. The bottom graph is pitch moment. The forces are normalized as $\rho g X_{cl}^2 A$ and the moments are normalized as $\rho g X_{cl}^3 A$. X_{cl} is the characteristic length of body and A is the incident wave amplitude. The non-dimensional time used as t/T . This t/T varies with encounter frequency to show more clearly the effect of the current. All three graphs show the forces and moment gradually developing and converging immediately after the modulation function effects stop at the second cycle. Froude numbers were used -0.01 for collinear current and +0.01 for adverse current as parameter for the current effect. As we predicted in table 4.4, the magnitudes of surge force shows obviously collinear, zero, adverse current in order. Heave force and pitch moment show not much differences.

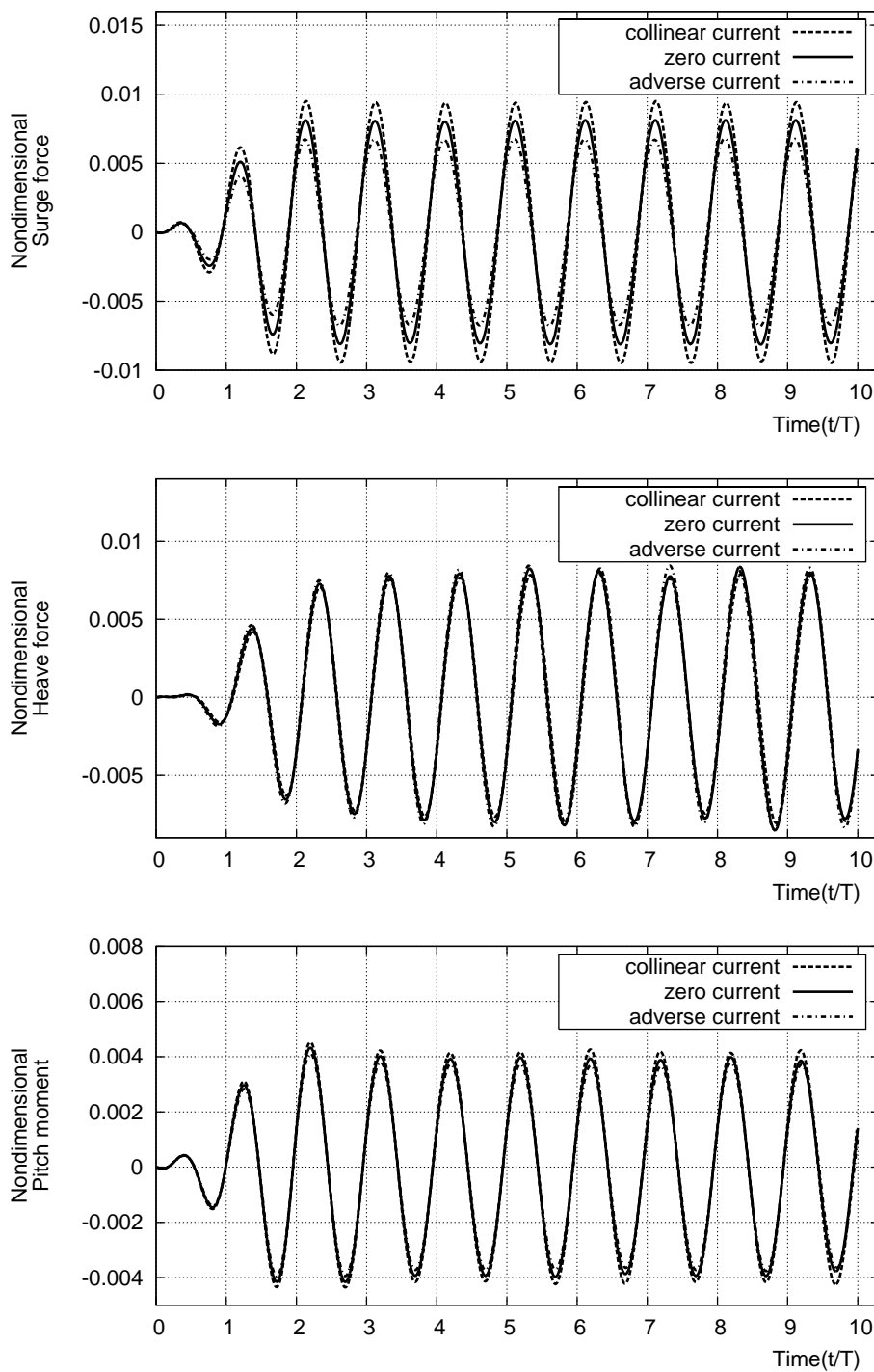


FIGURE 4.27. Time history of forces and moment for diffracted waves

($\omega = 0.6(\text{rad}/\text{sec})$) with current effect ($F_n = \mp 0.01$).

head sea (adverse current)		following sea (collinear current)
$F_n > 0$		$F_n < 0$
$\omega > \omega_e$		$\omega < \omega_e$
F_x	<	F_x
F_z	\approx	F_z
M_y	<	M_y

TABLE 4.4 Expectations of the current effect with diffracted waves.

Figure 4.28 shows time history of the first order diffracted wave forces and moment with and without current as same manner in figure 4.27. Froude numbers were used -0.03 for collinear current and +0.03 for adverse current as parameter for the current effect.

Top graph shows the surge force gradually developing and converging immediately after the modulation function effects stop at the second cycle. The middle graph shows the heave needs one more cycle to converge after the modulation function effects stop. The bottom graph shows the pitch moment a little overestimated for collinear current case after the modulation function effects stop. This is not significant effect for the entire time domain simulation result. However, we may take more care for converging with current effect especially, collinear current.

Figure 4.29 shows comparison adverse and collinear current effects with various Froude number. Two graphs show the surge forces with current effect. Top graph shows adverse current effect. This effect show the linearly decreasing surge force due to the

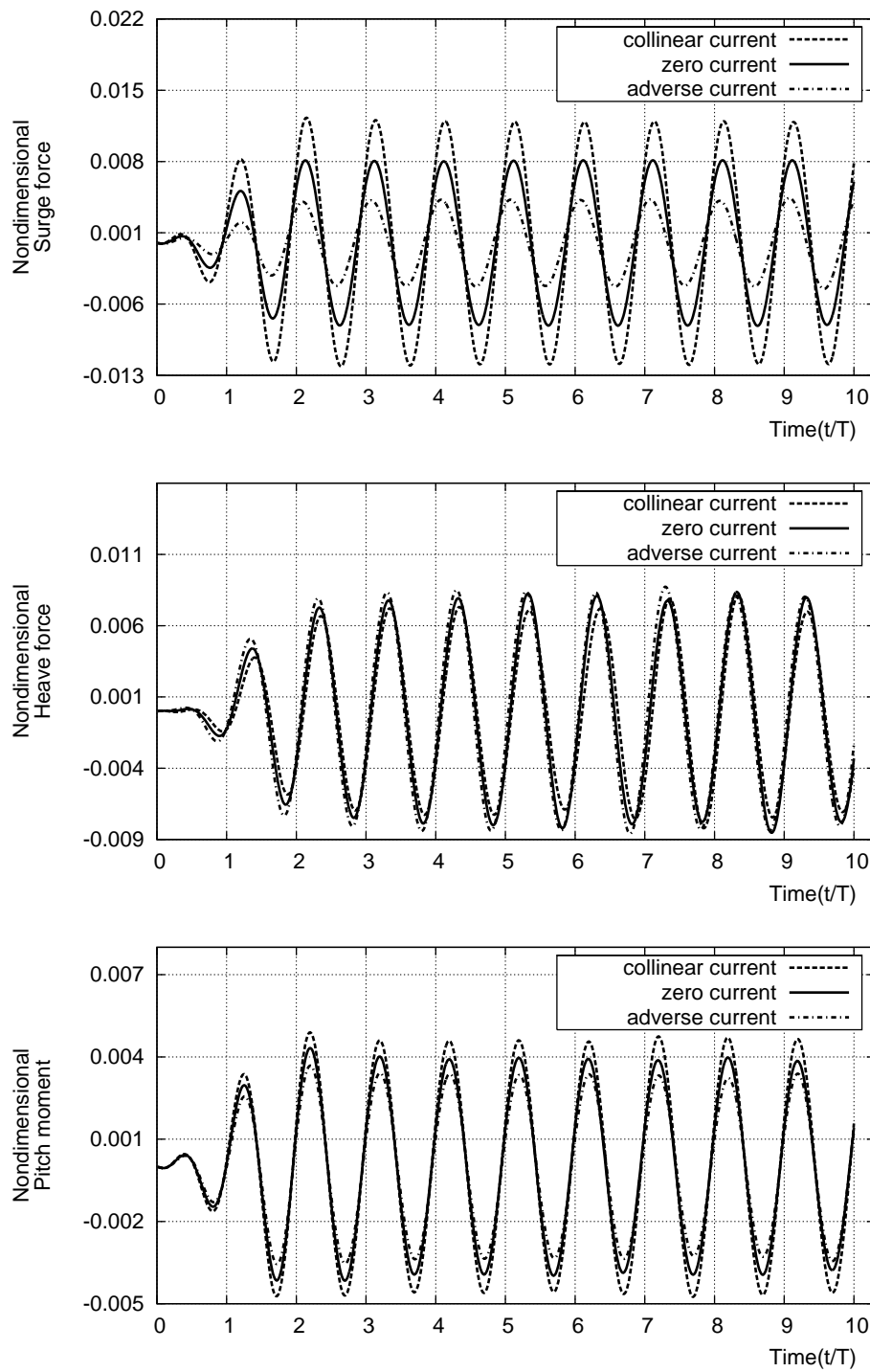


FIGURE 4.28. Time history of forces and moment for diffracted waves

($\omega = 0.6(\text{rad}/\text{sec})$) with current effect ($F_n = \mp 0.03$).

increasing Froude number. Bottom graph shows collinear current effect. This effect shows the linearly increasing surge force due to the increasing Froude number.

Figures 4.30 and 4.31 show the surge force for diffracted waves in various frequencies with adverse current effect. Top graphs shows magnitude of forces with incident wave frequencies. Bottom graph shows magnitude of forces with encounter frequencies. Top graphs show more clearly the differences of the forces. Bottom graphs show more clearly the trend of the varying forces due to the current effect. The frequency range between 0.6 and 0.625 and between 0.725 and 0.775 show agreement with table 4.4.

Figures 4.32 and 4.33 show in the same manner in Figure 4.30 with collinear current effect. We predicted collinear current effect makes larger forces at negative Froude number case. In the table 4.4, we have an prediction of the current effect base on engineers instinct. However, Accordingly figures 4.30 and 4.31 show it can not be simply predicted.

Current effect studied on radiated waves at various frequencies. Figure 4.34 shows two cases of the current effect with a radiated wave. Figure 4.34 (a) shows when an FPSO is under forced oscillations in surge. Incident wave propagates to the positive x -axis at stern and to the negative x -axis at bow. The current travels to negative x -axis at the positive Froude number. Therefore, the collinear current effect was shown at bow and the adverse current effect was shown at stern. Figure 4.34 (b) shows when an FPSO moves in heave oscillation. The current travels to positive x -axis at the negative Froude number. the adverse current effect was shown at bow and the collinear current effect was shown at stern. Opposite current headings were also studied as shown in figure 4.34. There is no significant difference in the outcomes so

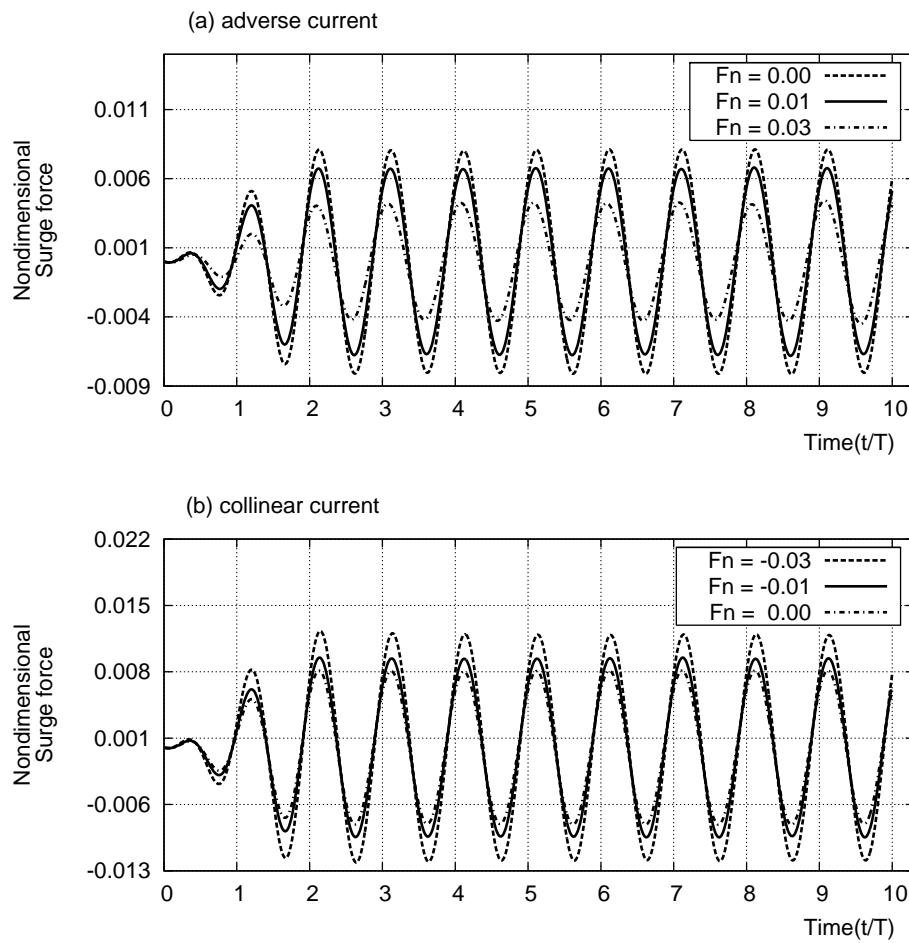


FIGURE 4.29. Time history of forces and moment for diffracted waves ($\omega = 0.6(\text{rad}/\text{sec})$) with (a) adverse and (b) collinear current effect.

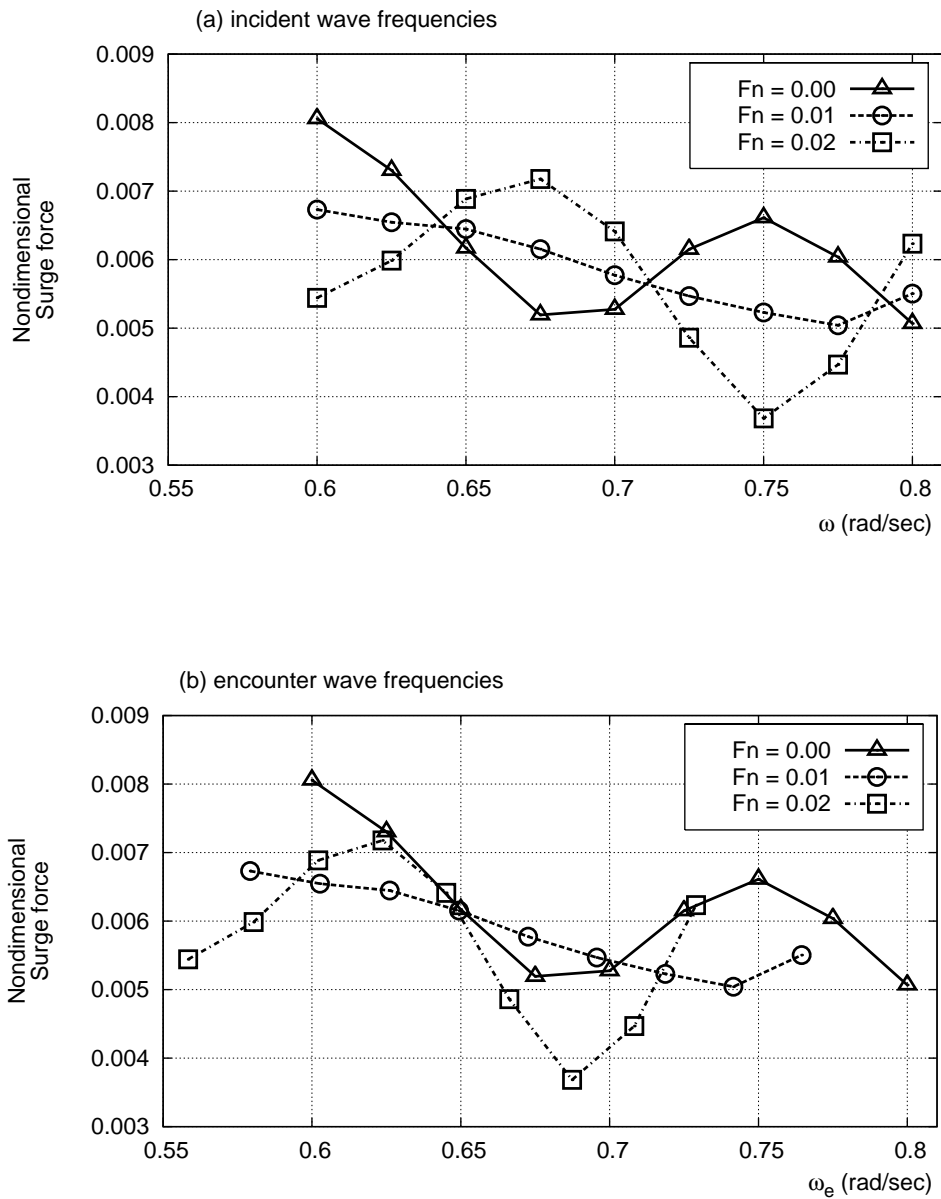


FIGURE 4.30. Surge forces for diffracted waves in various frequencies with head sea (adverse current) effect.

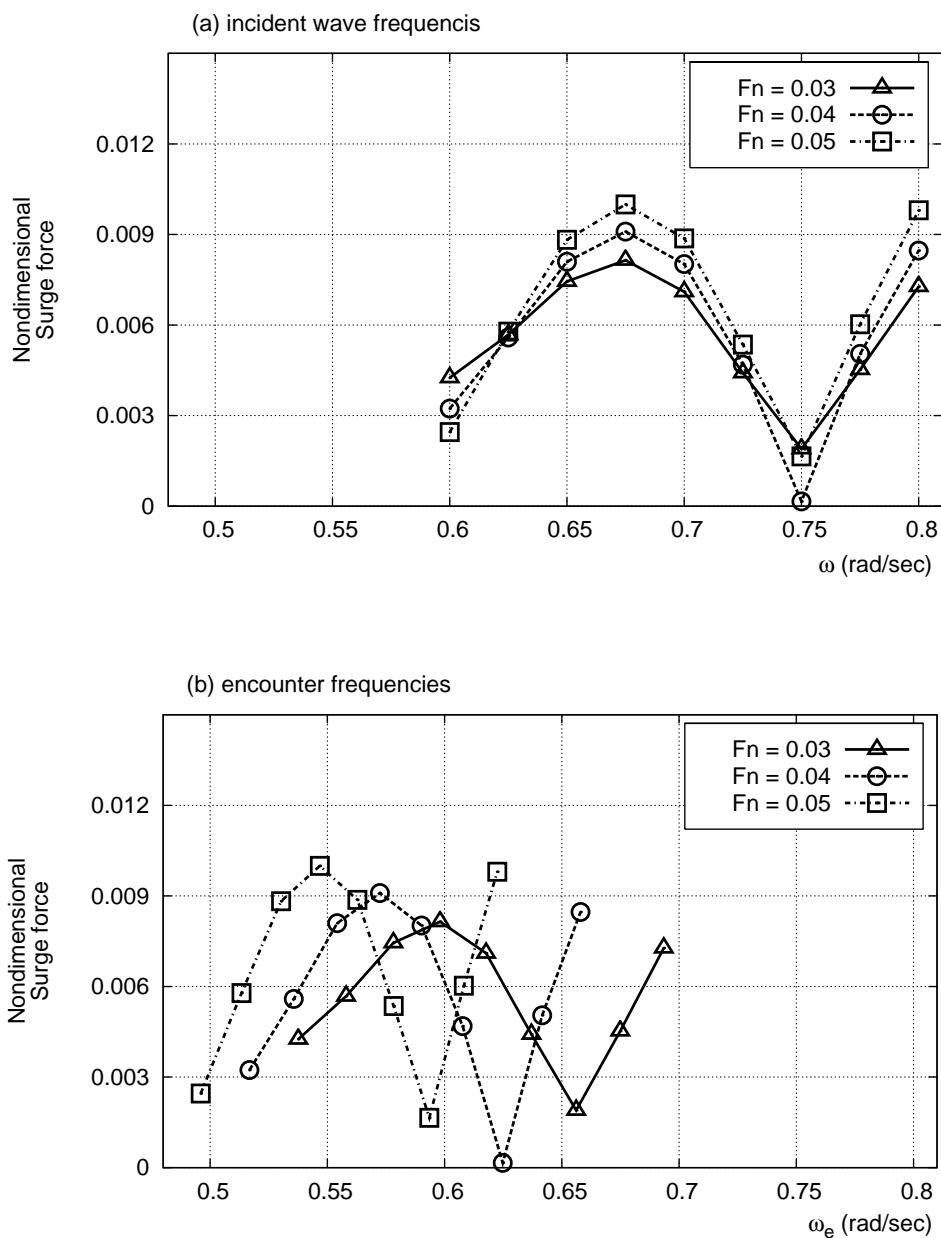


FIGURE 4.31. Surge forces for diffracted waves in various frequencies with head sea (adverse current) effect.

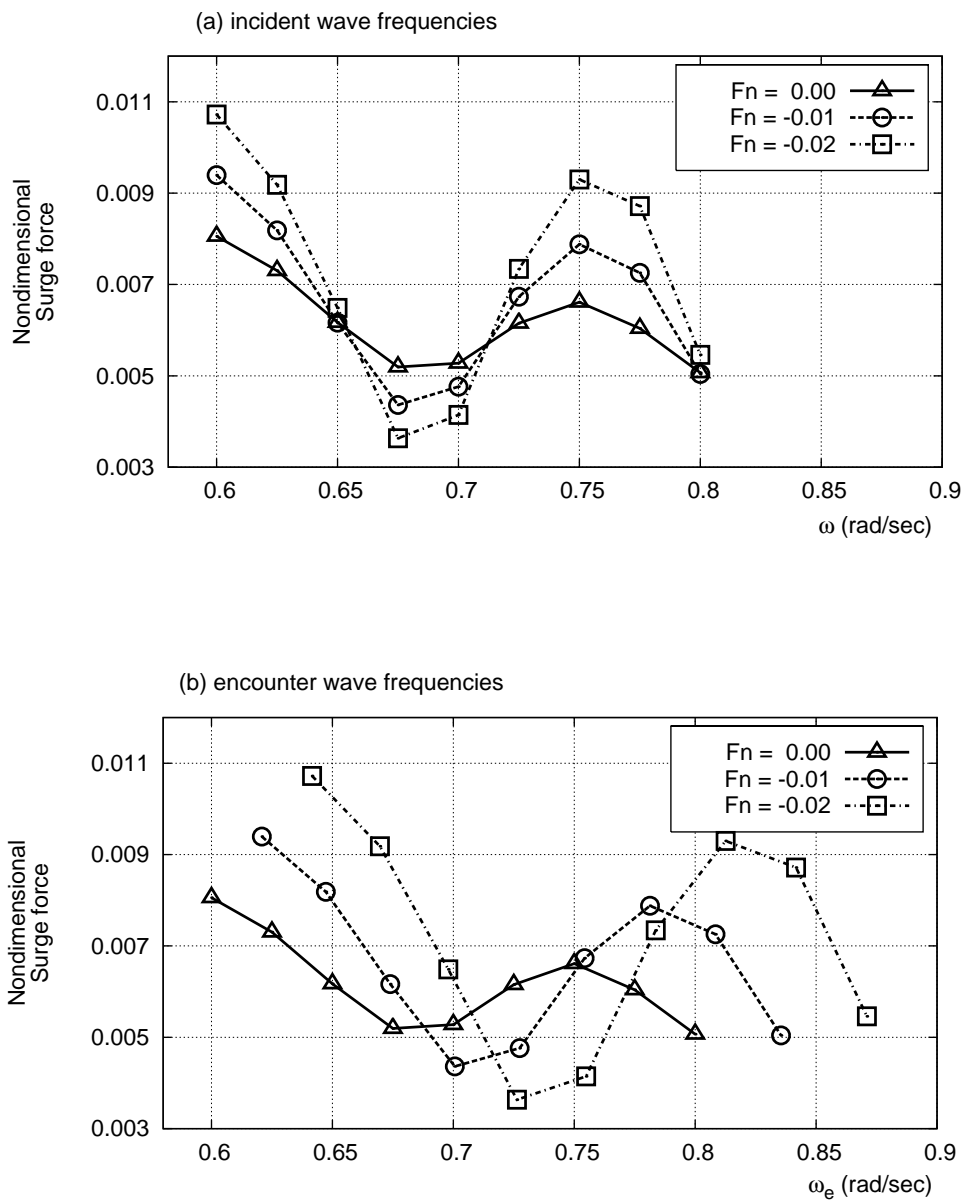


FIGURE 4.32. Surge forces for diffracted waves in various frequencies with following sea (collinear current) effect.

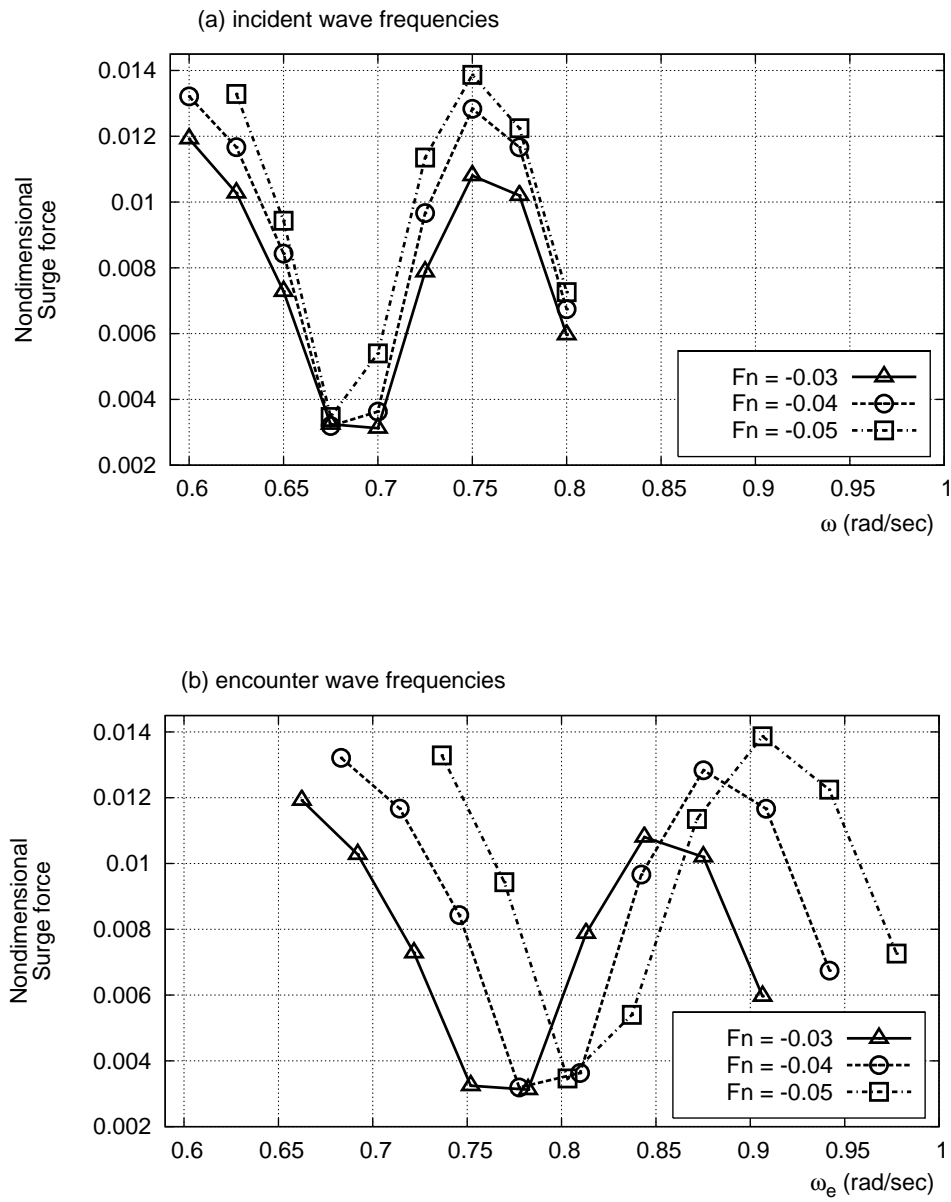


FIGURE 4.33. Surge forces for diffracted waves in various frequencies with following sea (collinear current) effect.

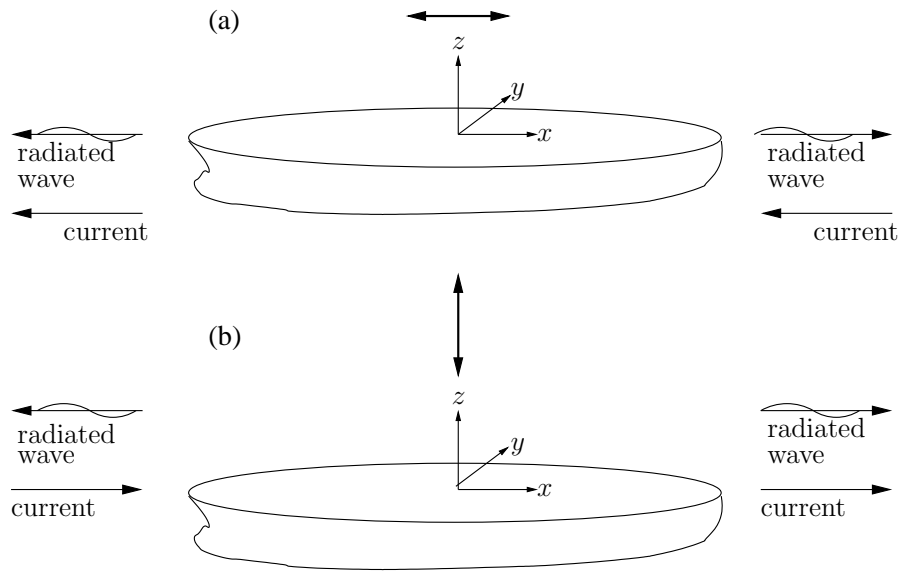


FIGURE 4.34. Current effect with radiated waves in (a) surge with the positive Froude number and (b) heave with the negative Froude number.

that we only provided current headings shown in figure 4.34.

Figures 4.35 - 4.38 show nondimensional added mass and damping coefficient when an FPSO is under forced oscillation in surge. These added mass increased with Froude number. The Froude numbers are 0.01, 0.02, 0.03, and 0.04. Due to the current effect, figure 4.35 shows larger added mass than the zero current case.

Figures 4.39 - 4.42 show nondimensional added mass and damping coefficient when an FPSO is under forced oscillation in heave. Due to the current effect, added mass in surge shows more significant values than the zero current case.

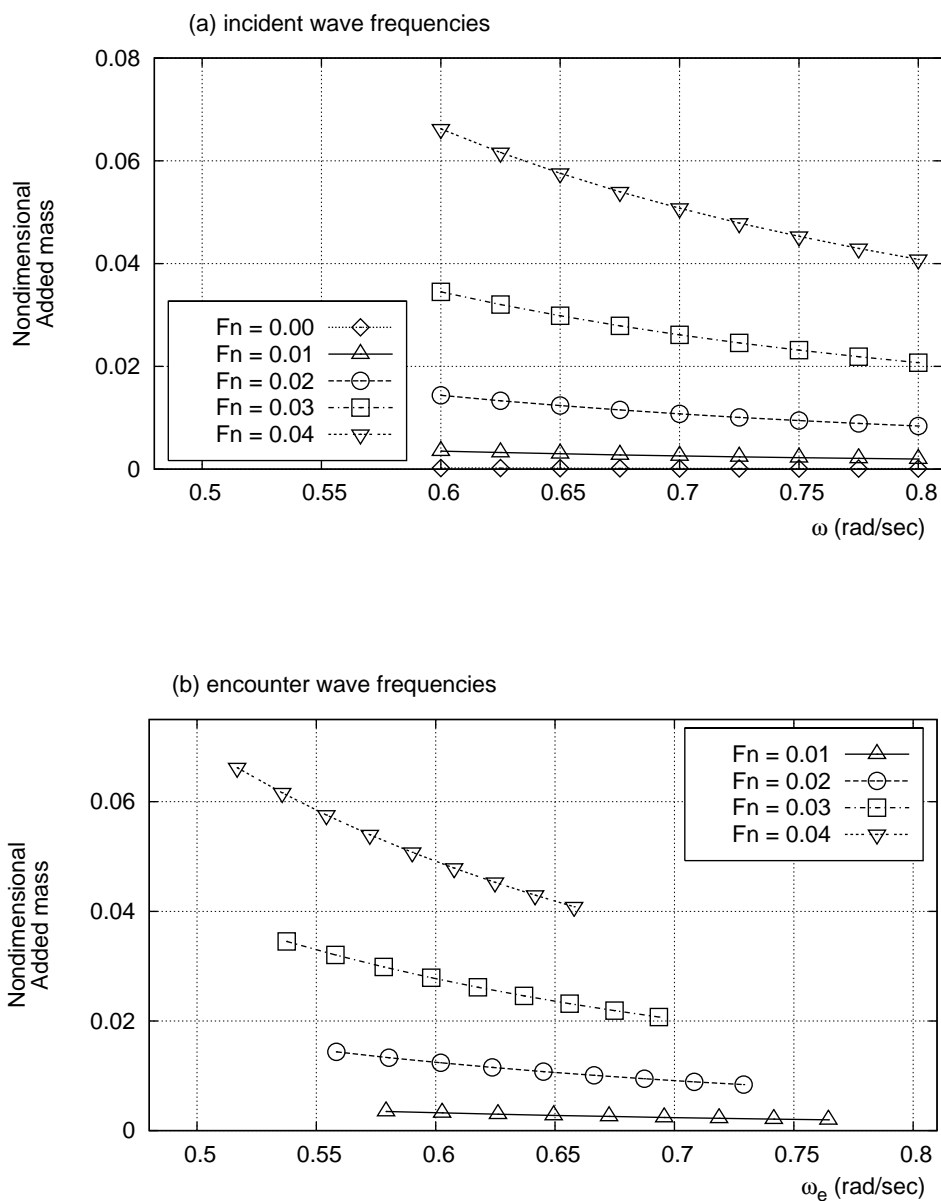


FIGURE 4.35. Added mass in surge with radiated waves at various frequencies for (a) incident wave frequencies and (b) encounter frequencies when the FPSO oscillates in surge.

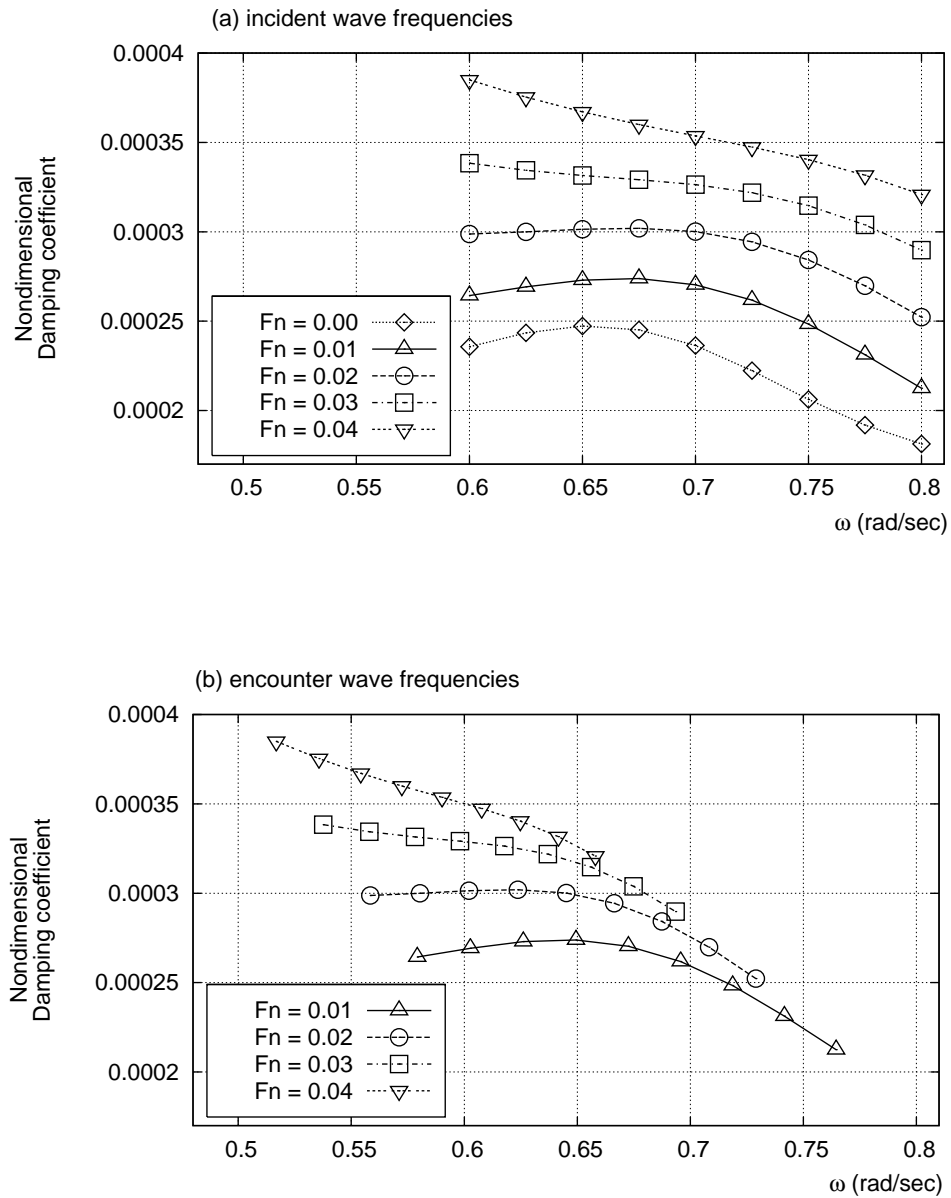


FIGURE 4.36. Damping coefficient in surge with radiated waves in various frequencies for (a) incident wave frequencies and (b) encounter frequencies when the FPSO oscillates in surge.

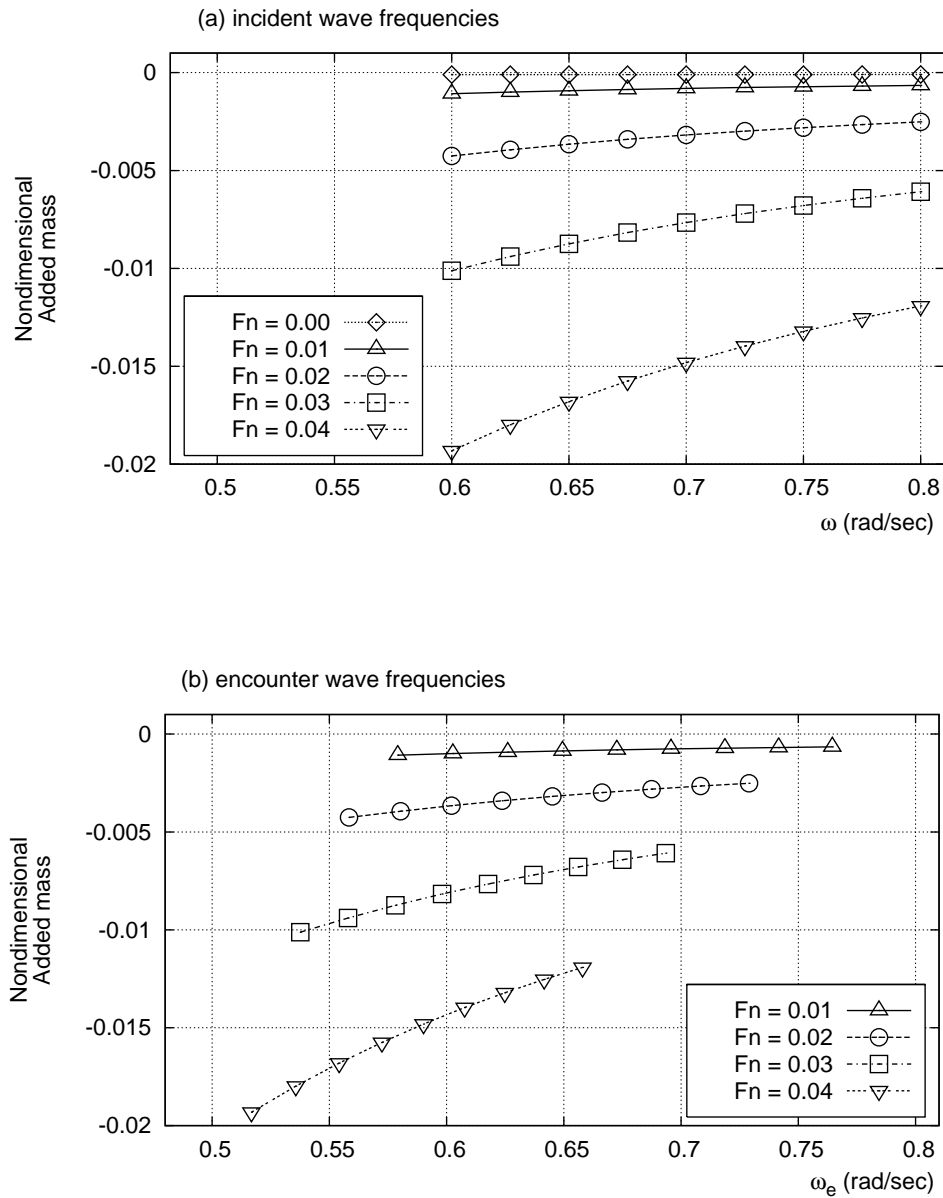


FIGURE 4.37. Added mass in heave with radiated waves at various frequencies for (a) incident wave frequencies and (b) encounter frequencies when the FPSO oscillates in surge.

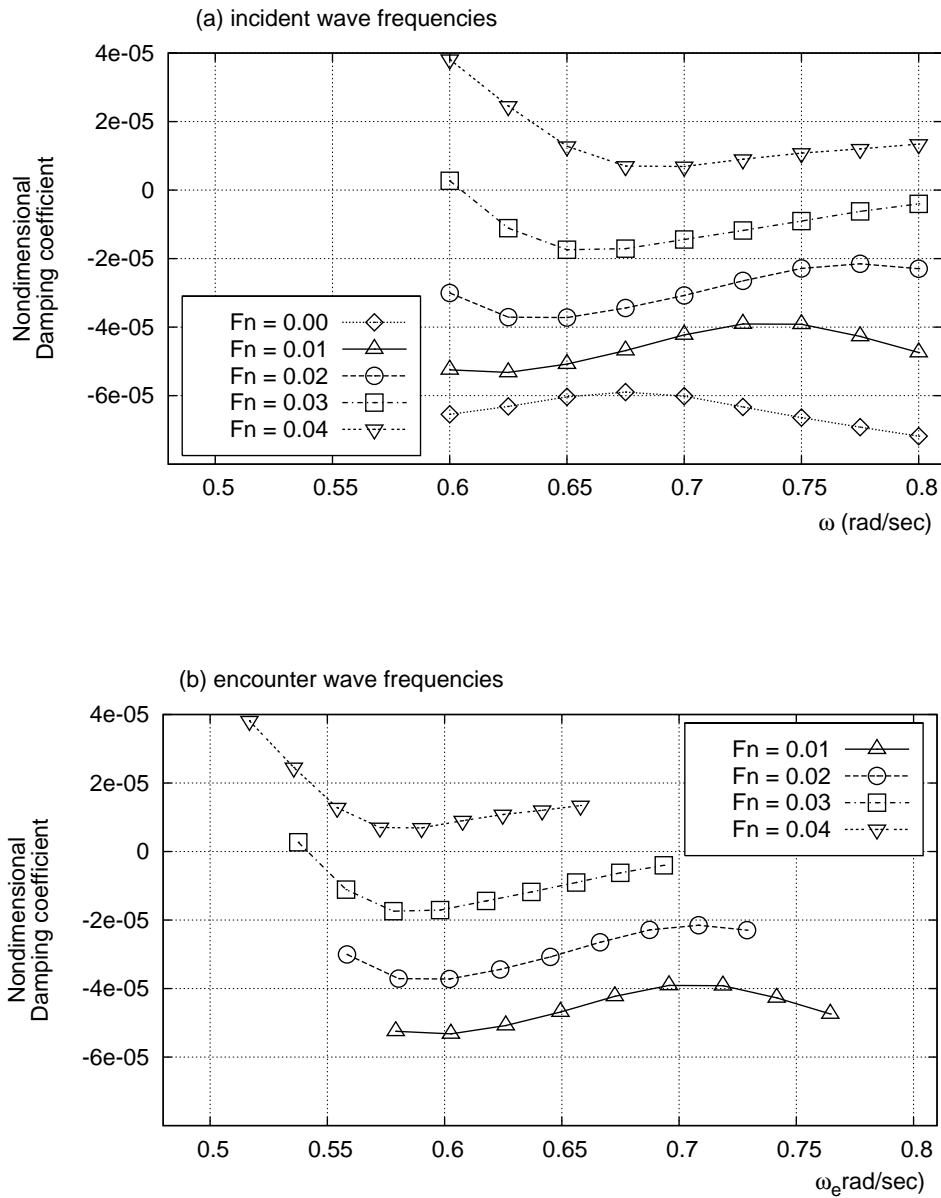


FIGURE 4.38. Damping coefficient in heave with radiated waves in various frequencies for (a) incident wave frequencies and (b) encounter frequencies when the FPSO oscillates in surge.

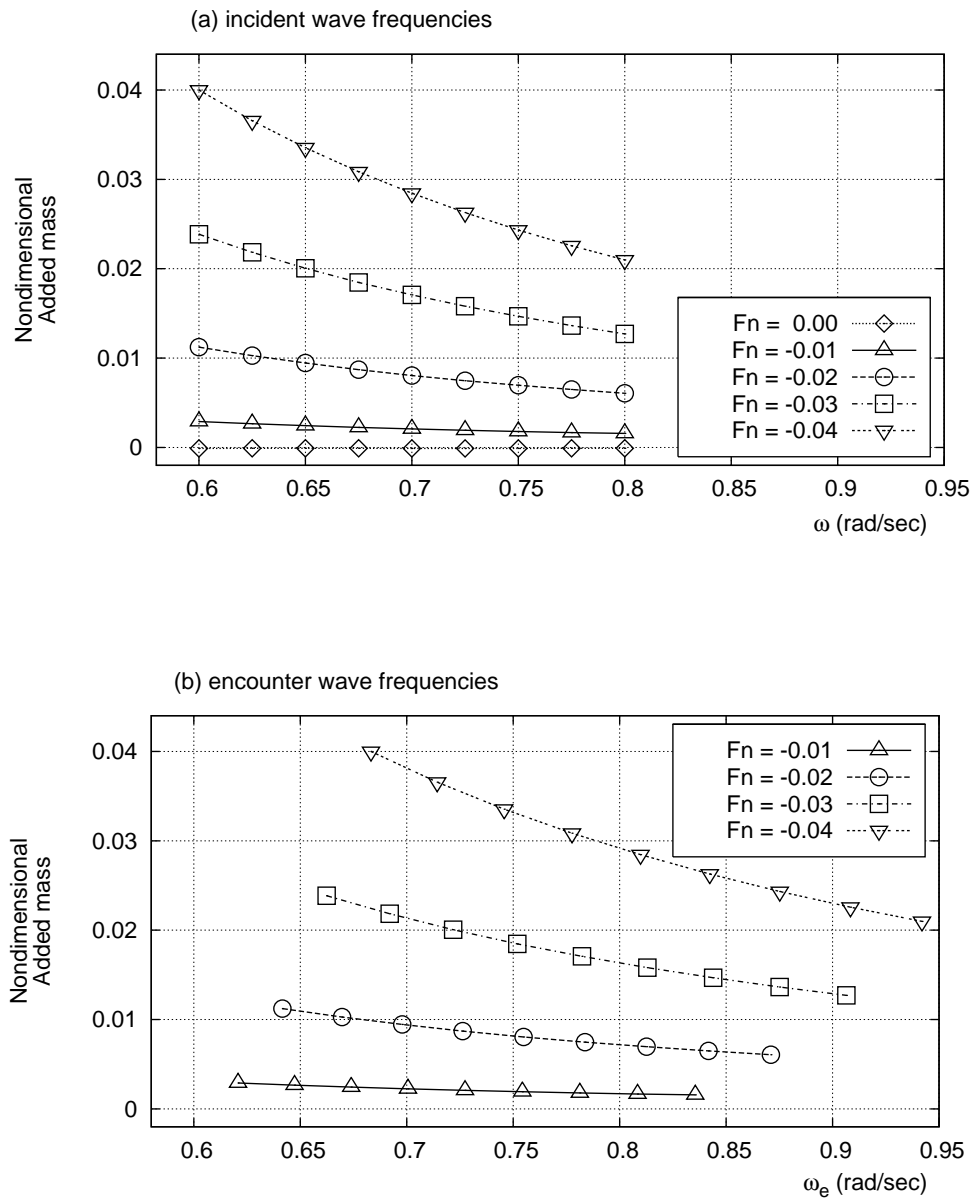


FIGURE 4.39. Added mass in surge with radiated waves at various frequencies for (a) incident wave frequencies and (b) encounter frequencies when the FPSO oscillates in heave.

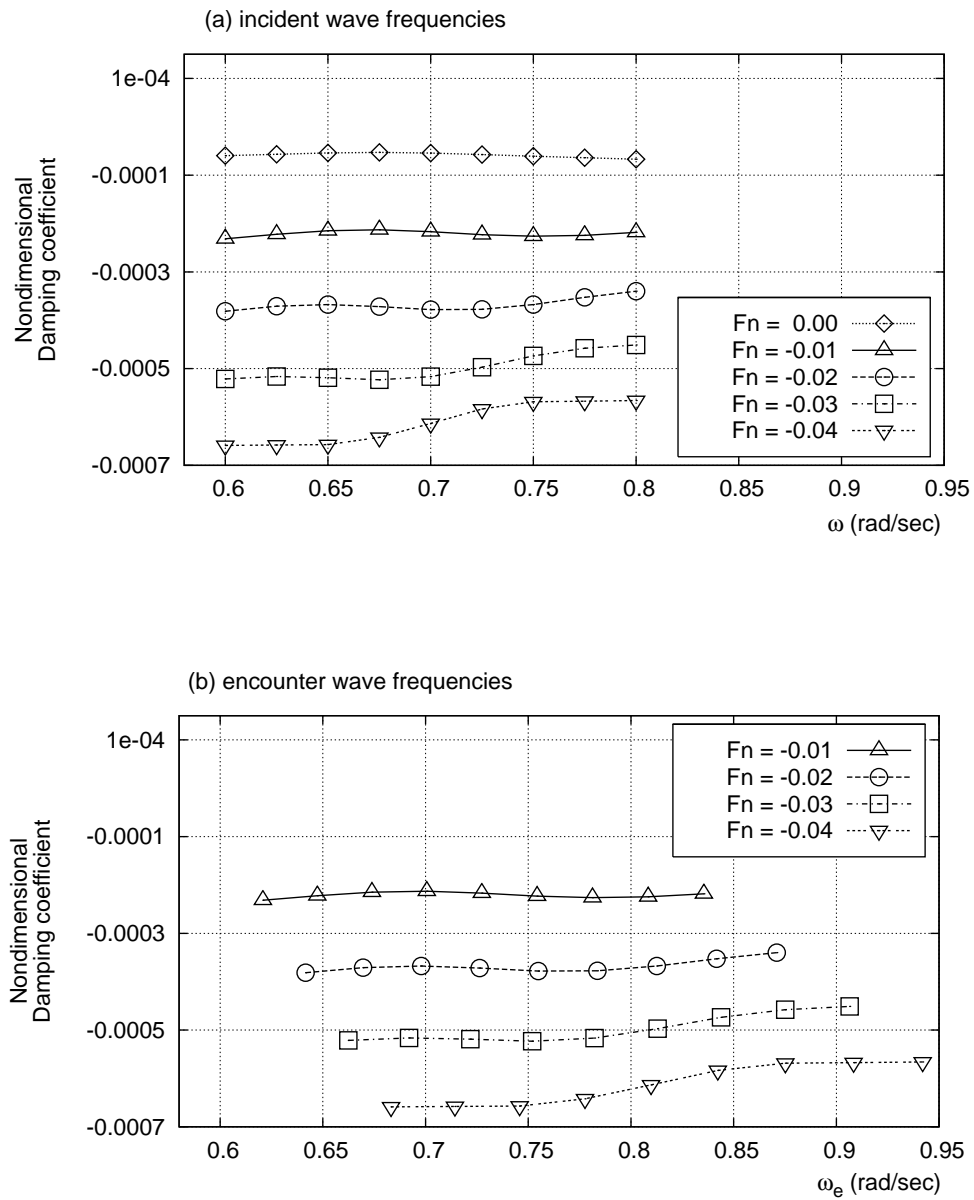


FIGURE 4.40. Damping coefficient in surge with radiated waves in various frequencies for (a) incident wave frequencies and (b) encounter frequencies when the FPSO oscillates in heave.

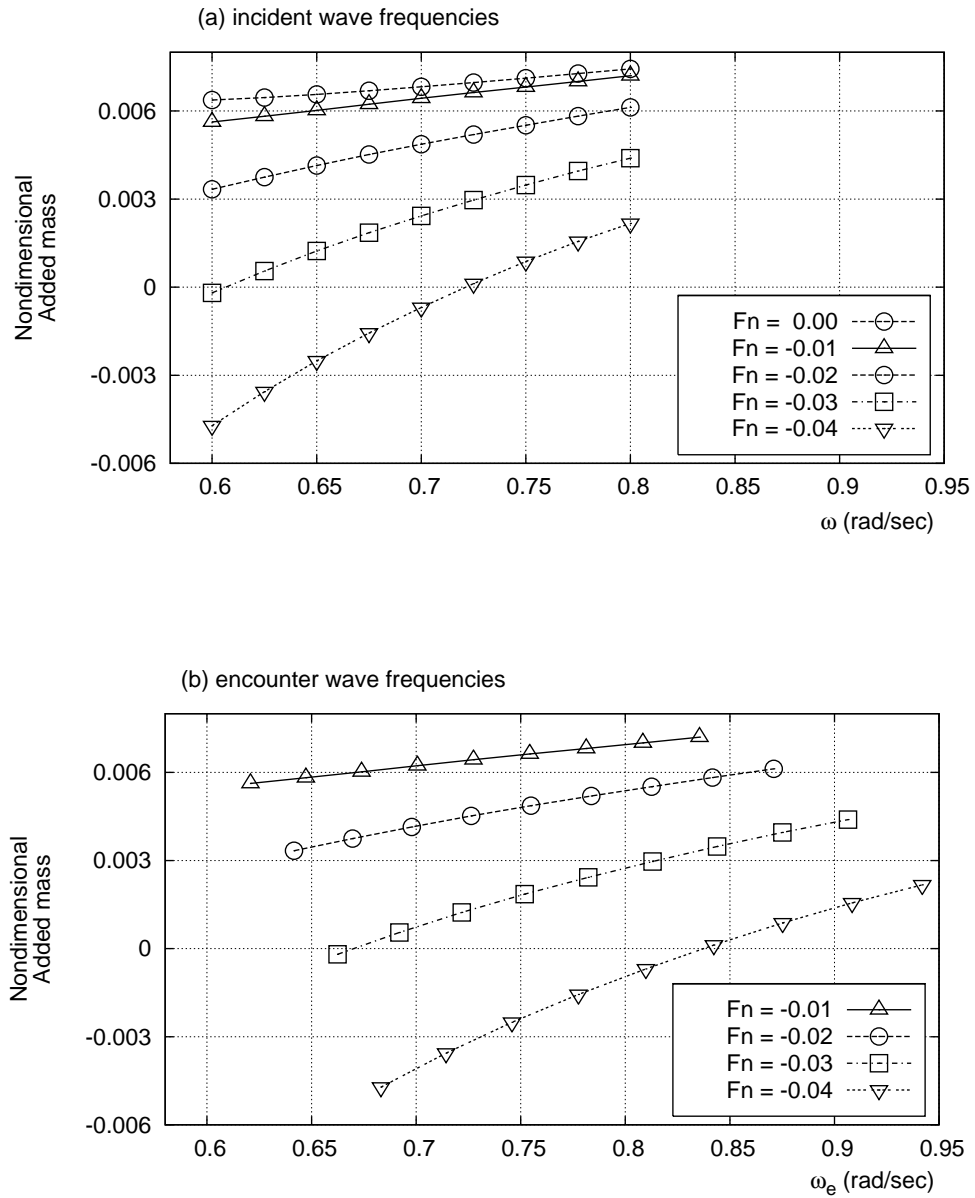


FIGURE 4.41. Added mass in heave with radiated waves at various frequencies for (a) incident wave frequencies and (b) encounter frequencies when the FPSO oscillates in heave.

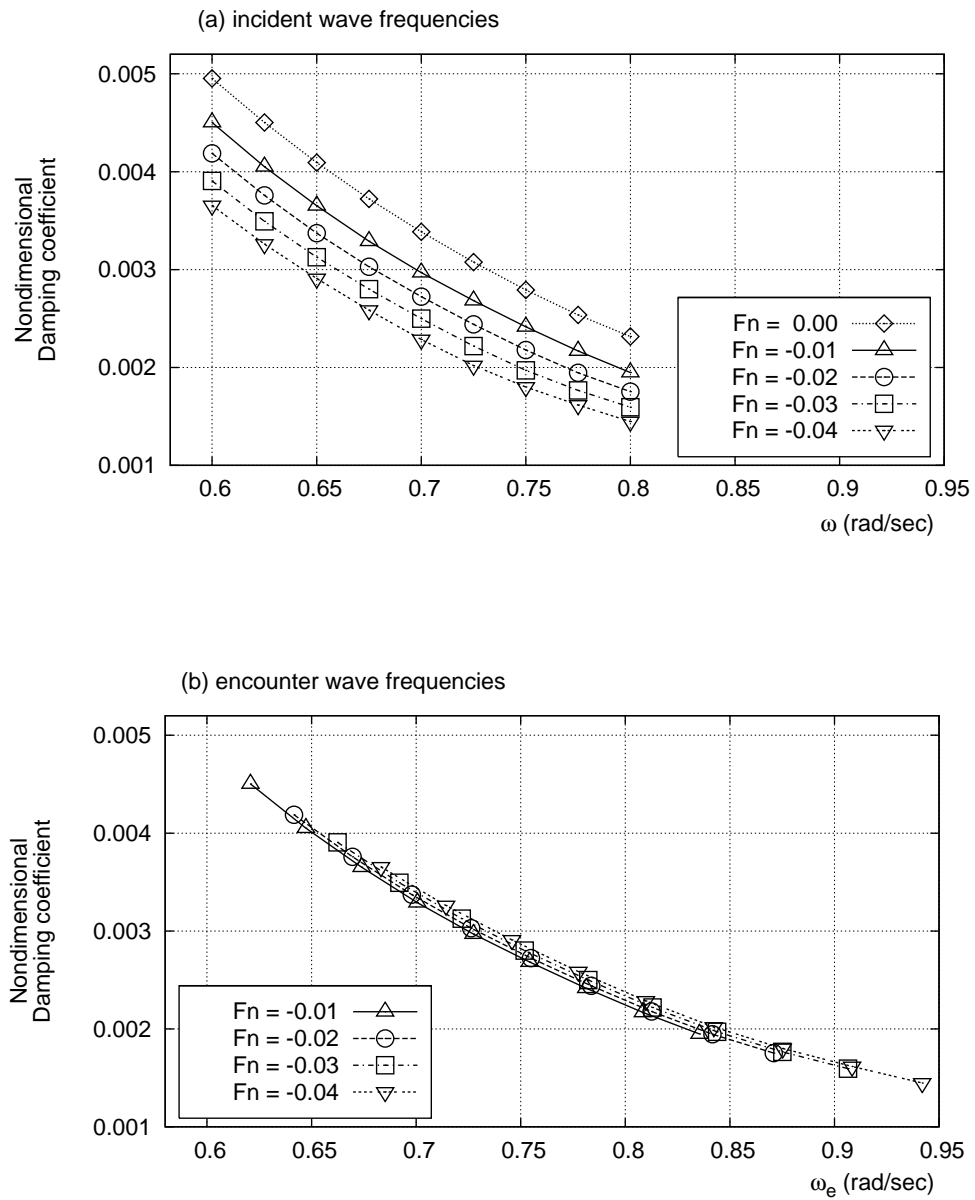


FIGURE 4.42. Damping coefficient in surge with radiated waves in various frequencies for (a) incident wave frequencies and (b) encounter frequencies when the FPSO oscillates in heave.

4.7.6 The influence of the current on wave length

So far all of the radiation and the diffraction case studies were investigated under the condition of both wave and current paralleled to the x -axis. Therefore, we can assume that the y -axis component is equal to zero.

$$U_1 = U(x), \quad U_2 = 0, \quad \text{and} \quad \vec{k} = (k, 0) \quad (4.32)$$

Consider a current travelling along the x -axis with the constant velocity U . We can define the encounter frequency

$$\omega_e = kU + \omega = k_o U_o + \omega_o, \quad (4.33)$$

where $()_o$ is reference point. ω_e is often referred to the encounter frequency since dividing it by 2π gives the number of waves encountered by the ship per unit time. ω_e is constant.

When the equation (4.33) is divided by k ,

$$\frac{kU}{k} + \frac{\omega}{k} = \frac{k_o U_o}{k} + \frac{\omega_o}{k}. \quad (4.34)$$

Then multiply by k_o/ω_o is $1/C_o$

$$\left(\frac{1}{C_o}\right) (U + C) = \left(\frac{k_o}{k} U_o + \frac{\omega_o}{k}\right) \left(\frac{k_o}{\omega_o}\right). \quad (4.35)$$

Again multiply by k/k_o is

$$\left(\frac{k}{k_o}\right) \left(\frac{U}{C_o} + \frac{C}{C_o}\right) = \left(\frac{k_o^2}{k\omega_o} U_o + \frac{k_o}{k}\right) \left(\frac{k}{k_o}\right) \quad (4.36)$$

or

$$\left(\frac{k}{k_o}\right) \left(\frac{U}{C_o} + \frac{C}{C_o}\right) = \frac{k_o}{\omega_o} U_o + 1. \quad (4.37)$$

Therefore,

$$\left(\frac{k}{k_0}\right) \left(\frac{U}{C_o} + \frac{C}{C_o}\right) = \frac{U_o}{C_o} + 1. \quad (4.38)$$

The phase velocities C and C_o are defined as

$$\begin{aligned} C^2 &= \left(\frac{\omega}{k}\right)^2 = \frac{g}{k} \tanh k\bar{h} \\ C_o^2 &= \left(\frac{\omega_o}{k_o}\right)^2 = \frac{g}{k_o} \tanh k_o\bar{h}_o, \end{aligned} \quad (4.39)$$

where \bar{h} and \bar{h}_o are local mean water depths.

From equation (4.39)

$$\frac{C^2}{C_o^2} = \frac{k_o}{k} \frac{\tanh k\bar{h}}{\tanh k_o\bar{h}_o} \quad (4.40)$$

and

$$\frac{C^2}{C_o^2} = \frac{k_o}{k} \frac{\tanh k\bar{h}}{\tanh k_o\bar{h}_o} = \left(\frac{U/C_o + C/C_o}{U_o/C_o + 1}\right) \left(\frac{\tanh k\bar{h}}{\tanh k_o\bar{h}_o}\right). \quad (4.41)$$

For deep water,

$$\frac{C}{C_o} = \frac{1}{2} \left[1 + \left(1 + 4\frac{U}{C_o} \right)^{1/2} \right]. \quad (4.42)$$

Equation (4.42) shows that phase velocity and wave length increase in the collinear current case ($U > 0$). In the adverse current ($U < 0$) case, phase velocity and wave length decrease. Figure 4.43 shows change of the wave length when the current travels along the x -axis. When the FPSO is under forced oscillation in heave, adverse current effect shows in the upstream when the Froude number is -0.03. In this adverse case, wave length decreases in the downstream.

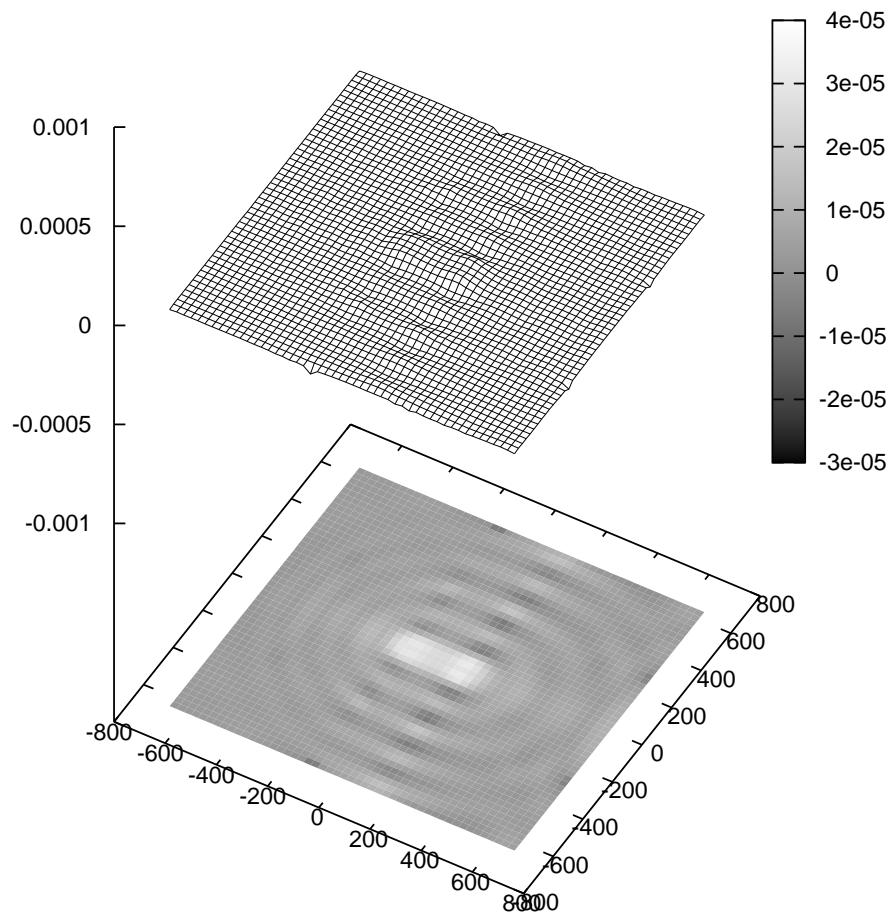


FIGURE 4.43. Change of wave length due to collinear and adverse current effects.

4.7.7 The influence of the current on wave elevation

The influence of the current on wave elevation can be determined by the conservation of wave energy,

$$\nabla \cdot \left[(U + C_g) \frac{E}{\omega} \right] = 0, \quad (4.43)$$

where $U + C_g$ is the local absolute group velocity.

$$\begin{aligned} (U + C_g) \frac{E}{\omega} &= \text{const} \\ (U_o + C_{g_o}) \frac{E_o}{\omega_o} &= \text{const}, \end{aligned} \quad (4.44)$$

where $E = 1/2\rho g A^2$.

$$\begin{aligned} (U + C_g) \frac{E}{\omega} &= (U_o + C_{g_o}) \frac{E_o}{\omega_o} \\ (U + C_g) \frac{A^2}{\omega} &= (U_o + C_{g_o}) \frac{A_o^2}{\omega_o} \\ \frac{A^2}{A_o^2} &= \left(\frac{\omega}{\omega_o} \right) \left(\frac{U_o + C_{g_o}}{U + C_g} \right) \end{aligned} \quad (4.45)$$

For deep water, $C_g \rightarrow 1/2C$ and $\omega \rightarrow g/C$ so that the current effect on wave elevation is

$$\begin{aligned} \frac{A^2}{A_o^2} &= \left(\frac{C_o}{C} \right) \left(\frac{U_o + \frac{1}{2}C_o}{U + \frac{1}{2}C} \right) \\ &= \left(\frac{C_o}{C} \right) \left(\frac{\frac{U_o}{C_o} + \frac{1}{2}}{\frac{U}{C_o} + \frac{1}{2}} \right). \end{aligned} \quad (4.46)$$

To eliminate C/C_o , let $Z = \frac{C}{C_o} = \frac{1}{2} \left[1 + \left(1 + 4 \frac{U}{C_o} \right)^{1/2} \right]$

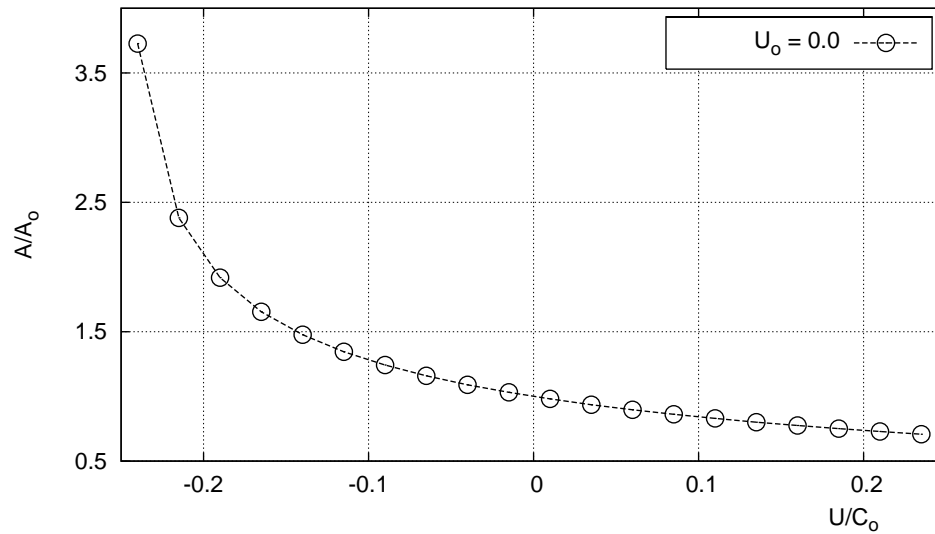


FIGURE 4.44. Change of wave amplitude due to collinear and adverse current effects.

so that

$$\frac{A^2}{A_o^2} = \left(\frac{\frac{1}{2} + \frac{U_o}{C_o}}{\frac{U}{C_o} + \frac{1}{2}Z} \right) \left(\frac{1}{Z} \right). \quad (4.47)$$

When current speed U is reached at $-1/2C$ ($= -1/4C_o$), the wave amplitude becomes infinite.

Equation (4.47) plots in figure 4.44. Figure 4.44 displays that wave amplitude increases adverse current ($U < 0$). In the collinear current case ($U > 0$), wave amplitude decreases. Our numerical results also show this trend in the table 4.5. Set two wave probe positions in the upstream $(-340, 275, 0)$ and the downstream $(340, 275, 0)$. Froude numbers are -0.03, 0.00, and 0.03. Wave frequency is 0.6(rad/sec). When the FPSO is under forced oscillation in heave, the adverse current effect shows in the



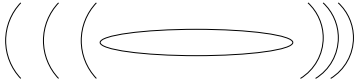
Froude number	wave amplitud		change of wavelength
	upstream	downstream	
-0.03	0.016	0.015	
0.00	0.014	0.016	
0.03	0.013	0.018	

TABLE 4.5 Change of wave amplitudes due to collinear and adverse current effect in the upstream and downstream.

upstream when the Froude number is -0.03. In this adverse case, wave amplitude increases from 0.014 to 0.016. When the Froude number is 0.03, the collinear current effect shows in the upstream. In this collinear case, wave amplitude decreases from 0.014 to 0.012.

4.7.8 Current effect with headings

Figure 4.45 shows the combinations of the various waves and current headings for the head sea (adverse current) cases. Figure 4.45 (a) shows incident wave approach from far-field to the starboard side of the FPSO. Current headed from far-field to the port side of the FPSO. Case studies were done on heading angles of the incident waves at degrees of -5, -10, -15, and -30. Current heading angles are 175, 170, 165, 150 degree angles. Figure 4.45 (b) shows the current headings from far-field to the port side of the FPSO at 175, 170, 165, and 150 degrees. The incident waves were headed to the bow at a zero degree angle. Figure 4.45 (c) shows the incident wave and current headings from far-field to the port side of the FPSO. The incident wave headings are 5, 10, 15, and 30 degree angles. The current headings are 175, 170, 165, and 150 degree angles.

Figure 4.46 shows the combinations of the different waves and current headings for following sea (collinear current) cases. Figure 4.46 (a) shows the current and incident wave approach from far-field to the starboard side of the FPSO. Case studies were done on heading angles of the incident waves and current at -5, -10, -15, and -30 degrees. Figure 4.46 (b) shows the current heading from far-field to the starboard side of the FPSO at -5, -10, -15, and -30 degrees. The incident waves were headed to the bow at a zero degree angle. Figure 4.46 (c) shows the current heading from far-field to the starboard side of the FPSO. The current headings are -5, -10, -15, and -30 degree angles. The incident waves were headed from far-field to the port side of the FPSO. The incident wave headings are 5, 10, 15, and 30 degree angles.

Figures 4.47 - 4.52 show the forces and moments for diffracted waves with a head sea (adverse current) effect. Incident waves approached from far-field to the starboard

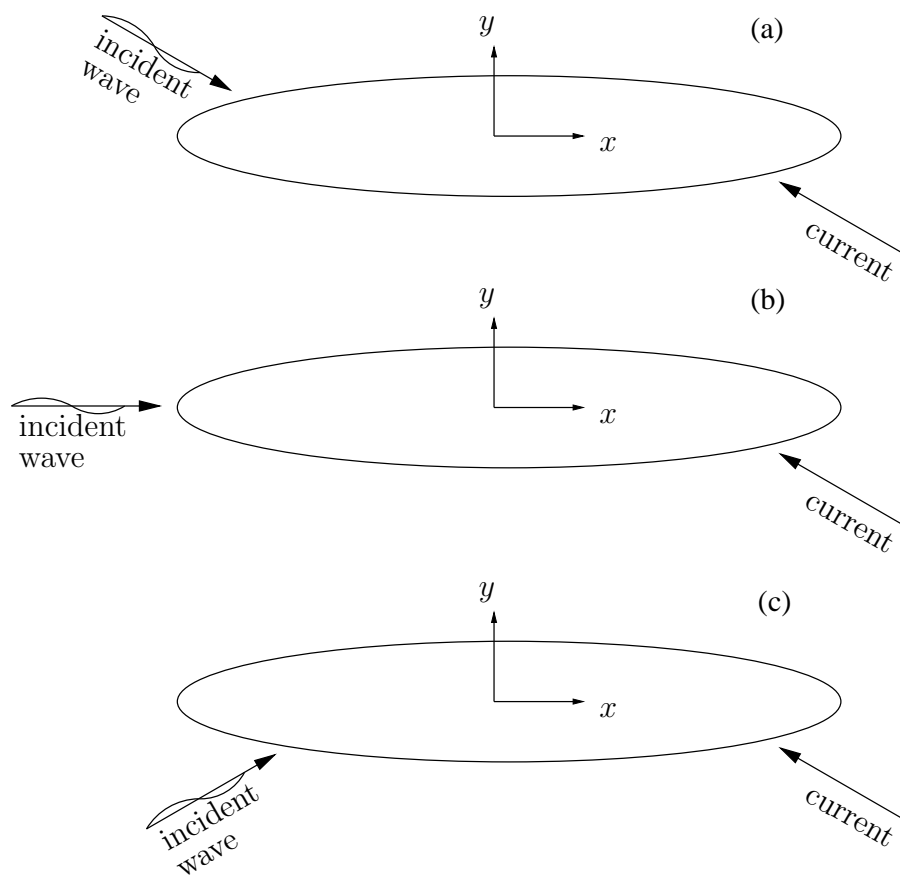


FIGURE 4.45. Current effect with diffracted waves in various headings for head sea (adverse current) cases.

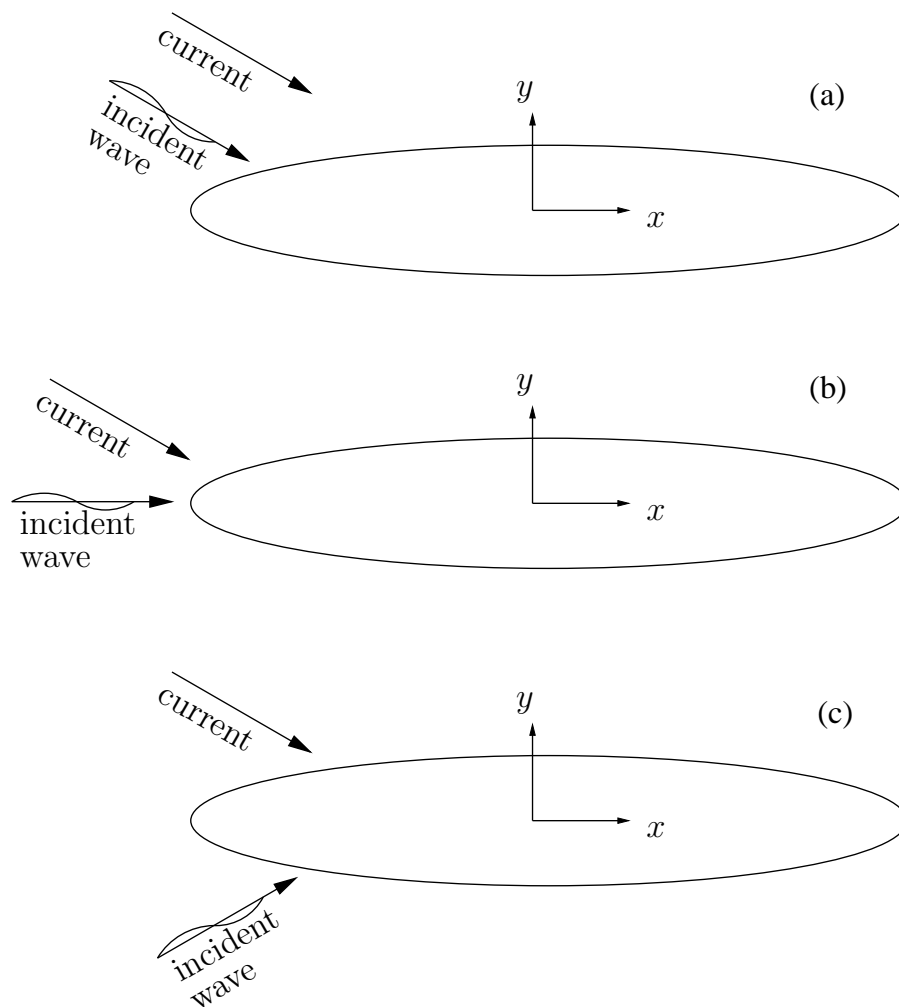


FIGURE 4.46. Current effect with diffracted waves in various headings for following sea (collinear current) cases.

side of the FPSO with a -5 degree heading angle. Current approaches from far-field to the port side of the FPSO with a 175 degree angle as shown in figure 4.45 (a). Figure 4.47 shows the surge forces with various Froude numbers. Figure 4.30 shows the transient mode of surge forces at the Froude numbers of 0.00 and 0.01. Figures 4.30 and 4.31 show a similar trend without the transient mode in surge forces at the Froude numbers of 0.02, 0.03, 0.04, and 0.05. Accordingly, common Froude numbers were chosen as 0.02, 0.03, and 0.04. This trend implies that higher Froude numbers produce stronger forces and moments. Figure 4.48 shows sway forces. Higher Froude numbers produce greater sway forces. Figure 4.49 shows heave forces. Heave did not show variance as much as surge and sway forces. Figures 4.50 and 4.51 show the roll and pitch moment respectively. Heave force, roll moment, and pitch moment were less variant than surge force, sway force, and yaw moment. Figure 4.52 shows yaw moment with various Froude numbers. The results demonstrate that higher Froude numbers display larger yaw moment.

Figures 4.53 - 4.55 show surge, sway force, and yaw moment. These three forces and moments are highly affected by the directional waves and current headings. Surge forces have a transient trend at relatively small heading angles. In these cases, incident wave heading angles are -5, 10, and -15 and current heading angles are 175, 170, and 165. These small heading angles do not considerably affect surge forces. When the incident wave heading angle is -30 degrees and the current heading angle is 150, the trend of surge force is different than the smaller heading angles in figure 4.54. When an FPSO is exposed to the relatively large headings of the current or waves, the trend of surge force is similar to that of sway force. This interesting phenomenon is assumed to be caused by the FPSOs geometric properties. Sway forces show that larger Froude numbers make greater sway forces. Figure 4.55 shows yaw moments in

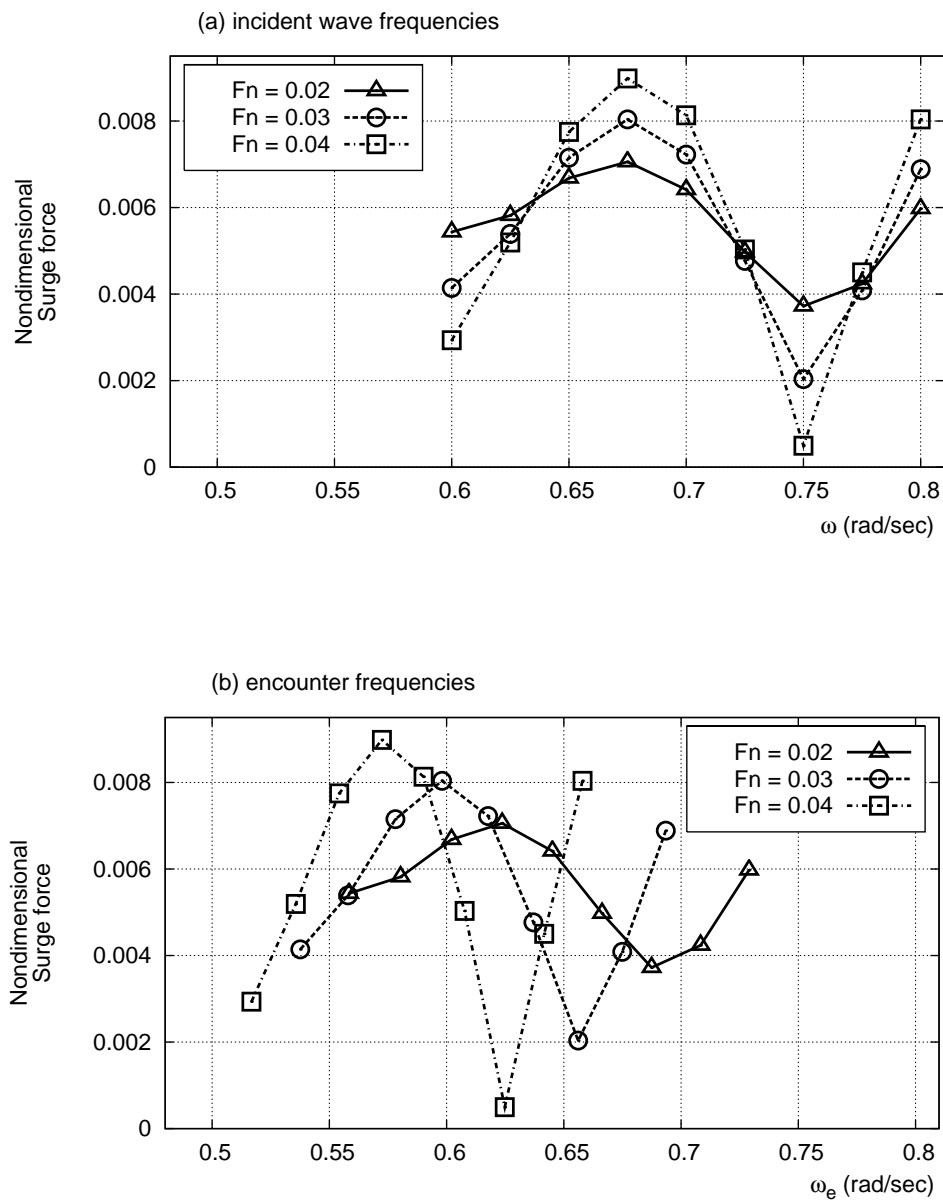


FIGURE 4.47. Surge forces with diffracted waves in various frequencies for head sea (adverse current) effect. Wave and current heading angles are -5 and 175 degrees respectively.

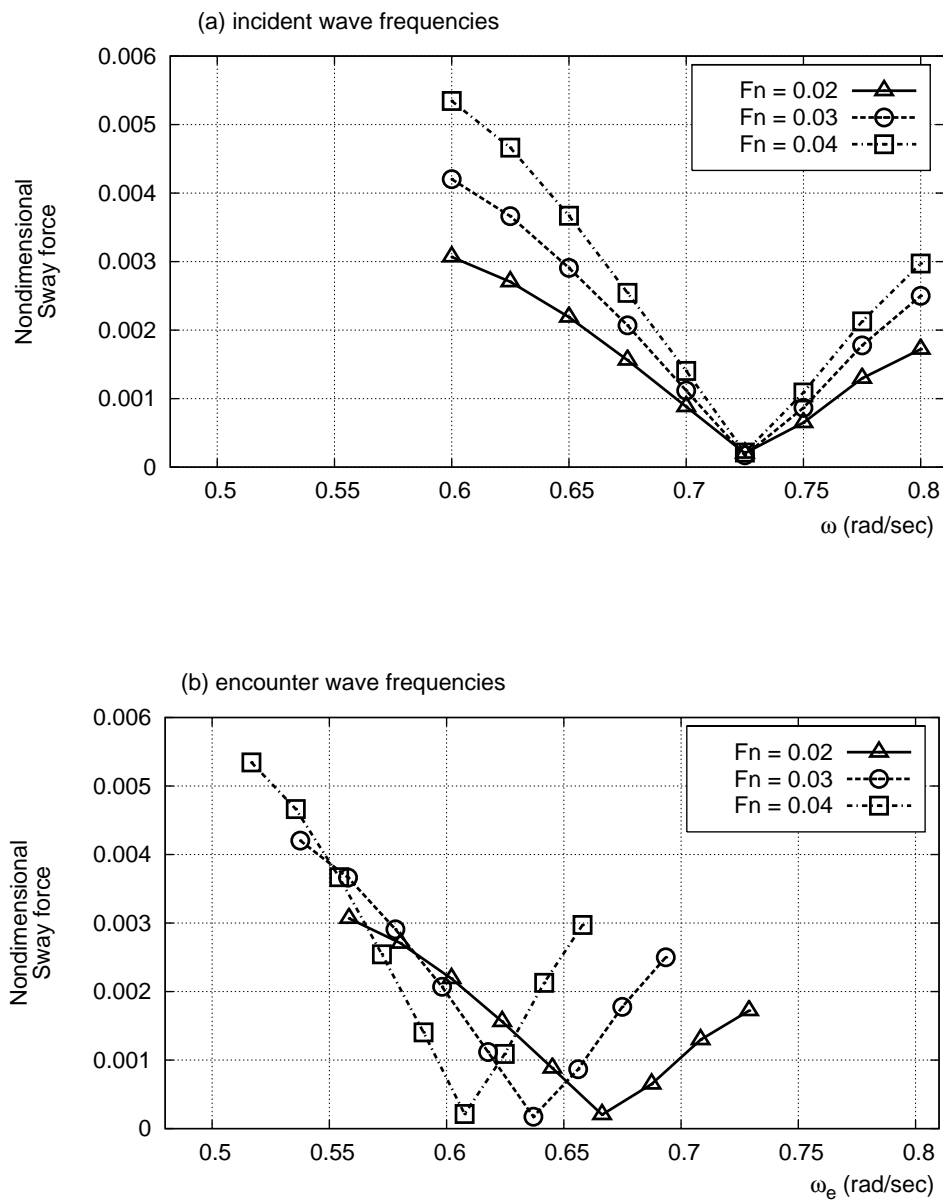


FIGURE 4.48. Sway forces with diffracted waves in various frequencies for head sea (adverse current) effect. Wave and current heading angles are -5 and 175 degrees respectively.

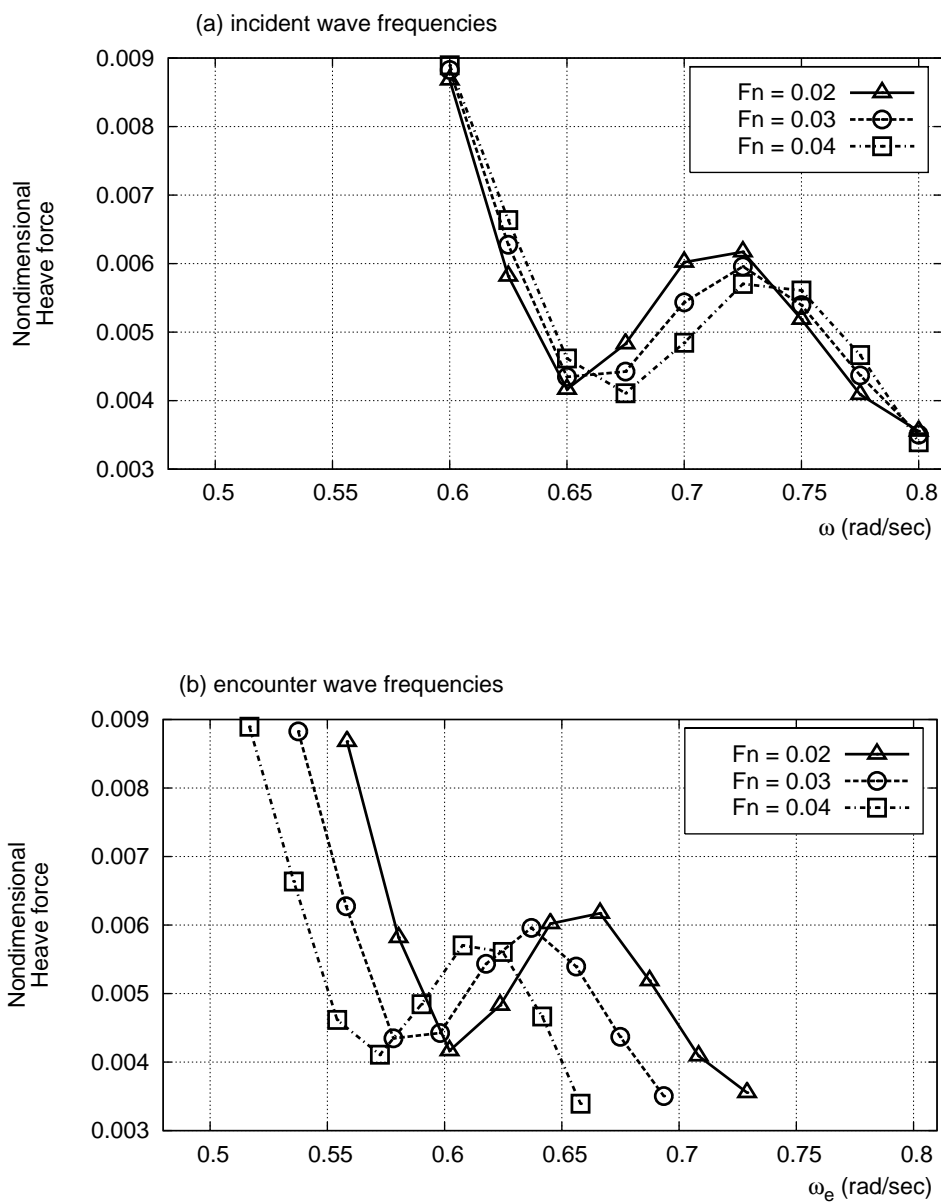


FIGURE 4.49. Heave forces with diffracted waves in various frequencies for head sea (adverse current) effect. Wave and current heading angles are -5 and 175 degrees respectively.

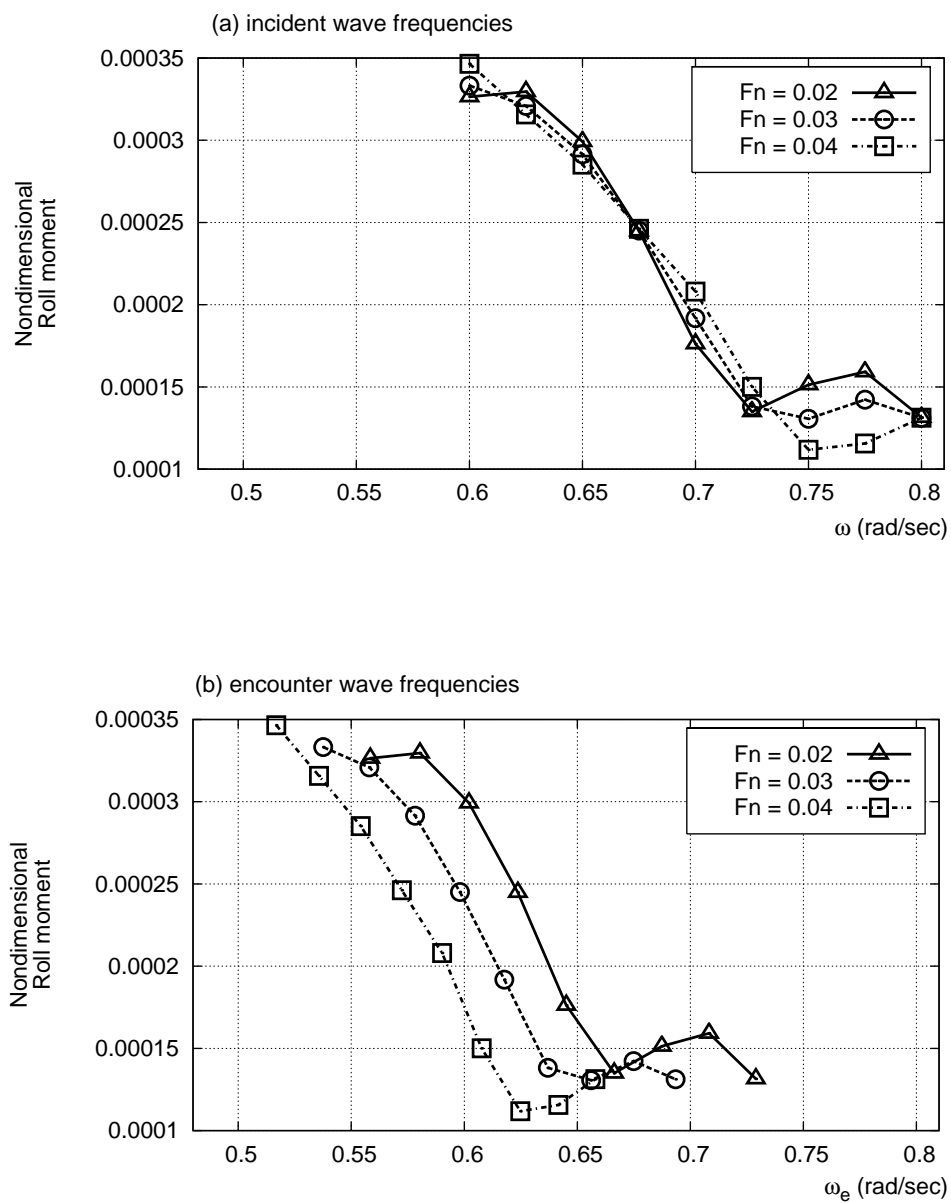


FIGURE 4.50. Roll moments with diffracted waves in various frequencies for head sea (adverse current) effect. Wave and current heading angles are -5 and 175 degrees respectively.

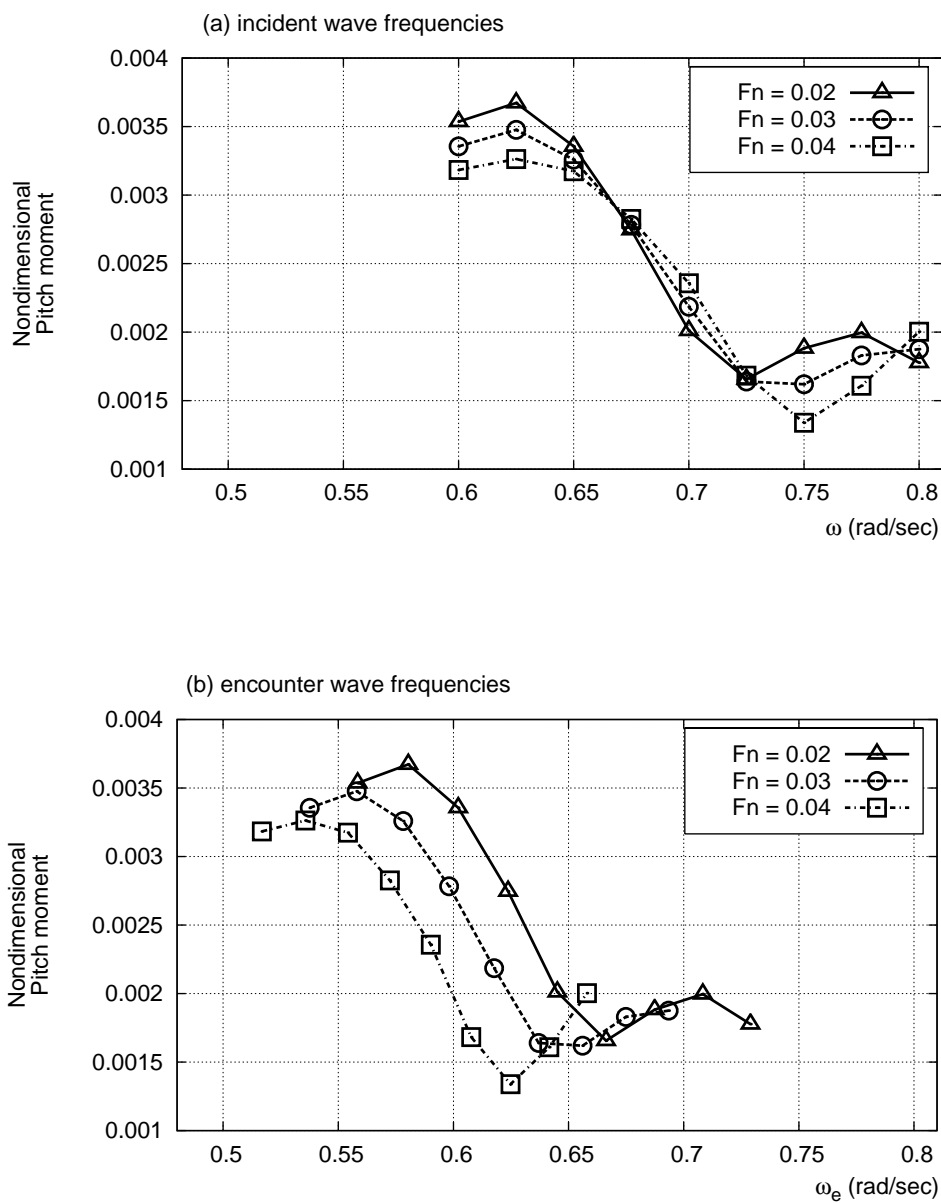


FIGURE 4.51. Pitch moments with diffracted waves in various frequencies for head sea (adverse current) effect. Wave and current heading angles are -5 and 175 degrees respectively.

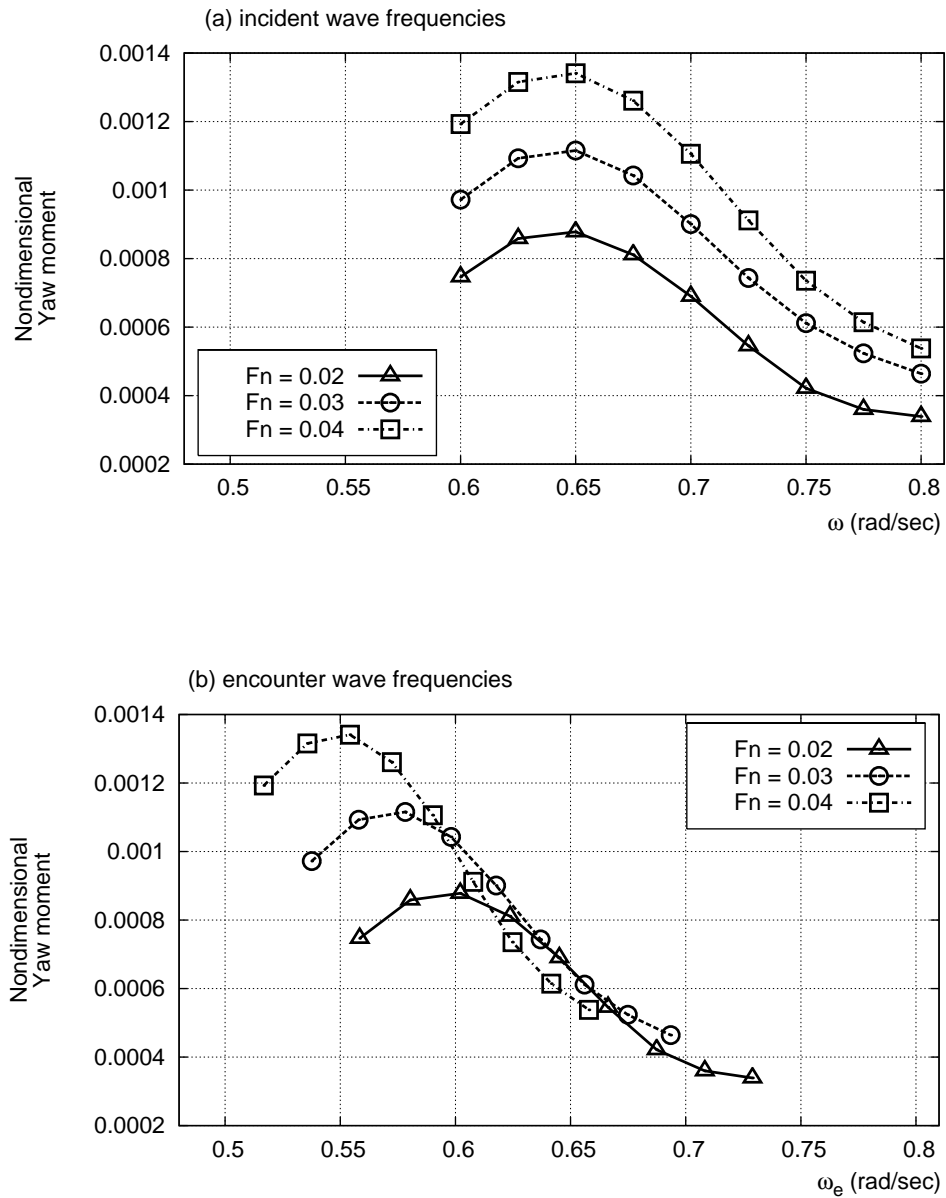


FIGURE 4.52. Yaw moments with diffracted waves in various frequencies for head sea (adverse current) effect. Wave and current heading angles are -5 and 175 degrees respectively.

the various Froude numbers.

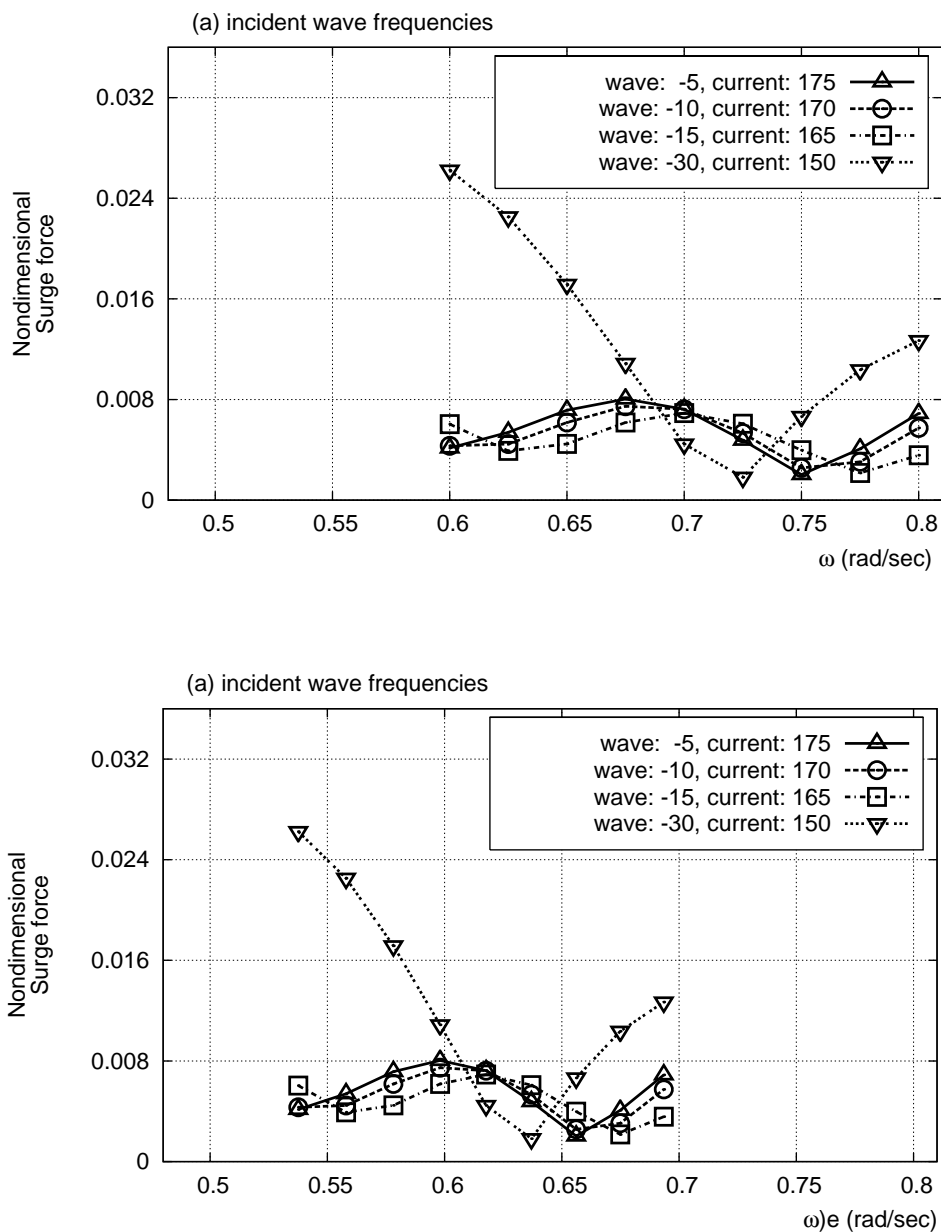


FIGURE 4.53. Surge forces with diffracted waves in various frequencies for head sea (adverse current) effect at Froude number is 0.03. Wave heading angles are -5, -10, -15, and -30. Current heading angles are 175, 170, 165, 150 degrees.

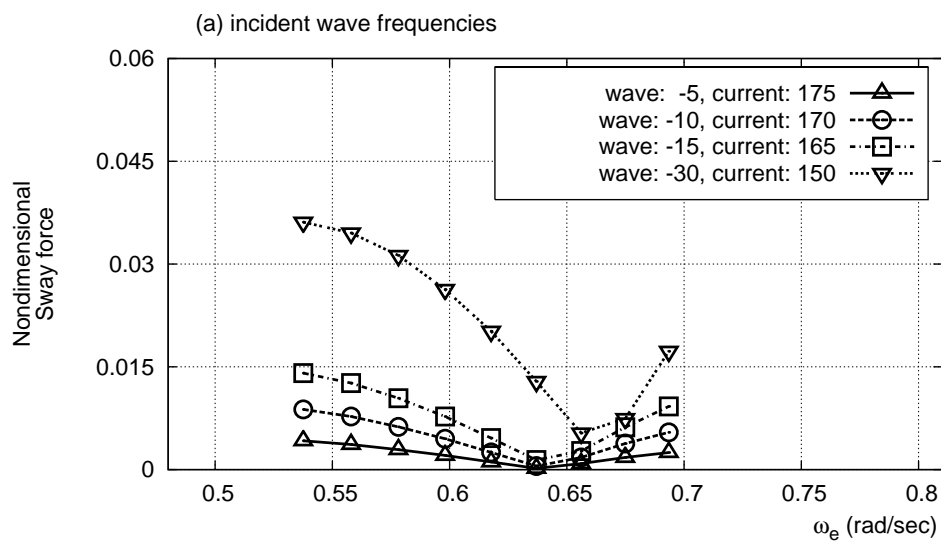
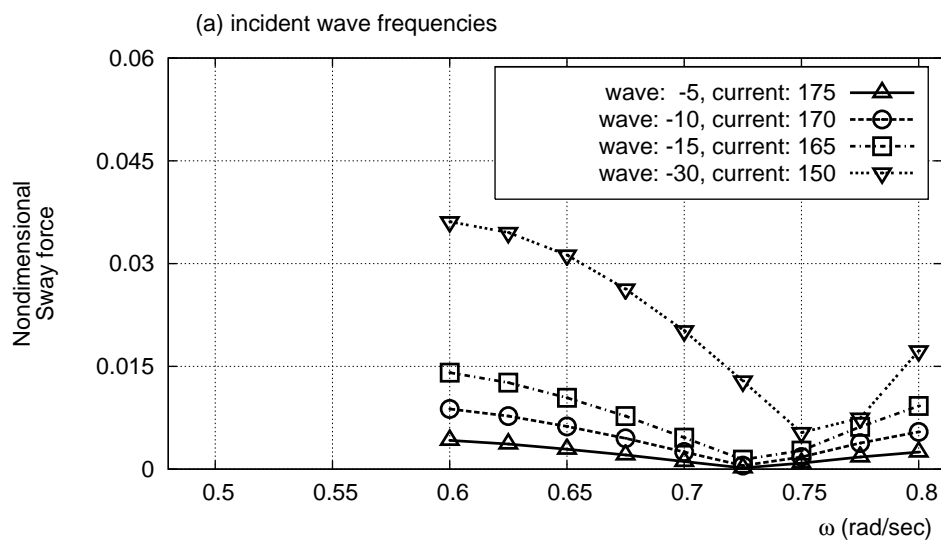


FIGURE 4.54. Sway forces with diffracted waves in various frequencies for head sea (adverse current) effect at Froude number is 0.03. Wave heading angles are -5, -10, -15, and -30. Current heading angles are 175, 170, 165, 150 degrees.

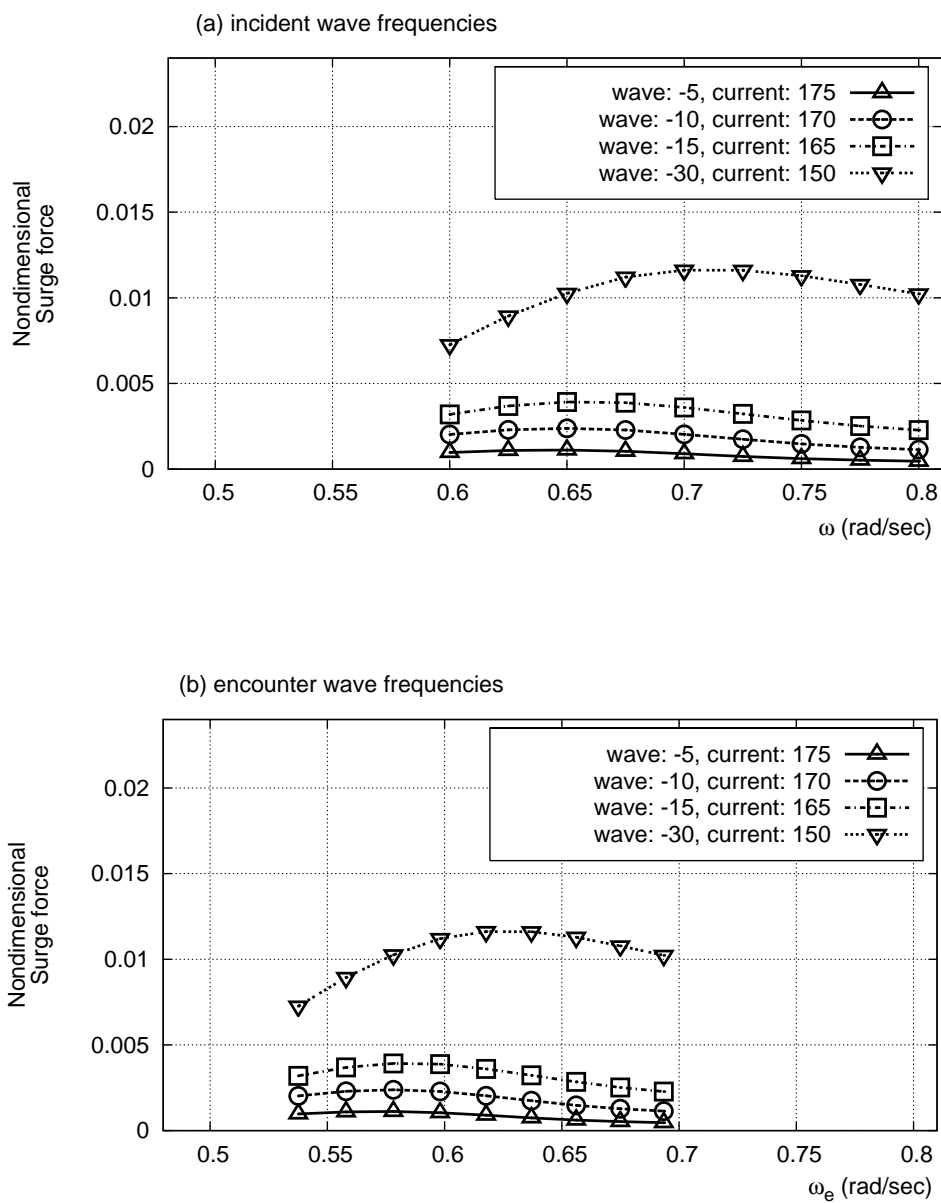


FIGURE 4.55. Yaw moments with diffracted waves in various frequencies for head sea (adverse current) effect at Froude number is 0.03. Wave heading angles are -5, -10, -15, and -30. Current heading angles are 175, 170, 165, 150 degrees.

CHAPTER V

SUMMARY AND CONCLUSIONS

In order to understand the behavior of an FPSO, we used several numerical simulation programs in this study. The programs we used were developed based on boundary element theory. We found some possibilities for handling FPSO behavior through numerical simulations. This study also suggests an accurate way of helping and guiding the prior steps of the FPSO model scale experiments.

5.1 Conclusions

A time domain simulation for an FPSO with diffracted and radiated problems has been accomplished by using a higher order boundary element method (HOBEM) in the time domain. We found that there were some numerical difficulties in obtaining a converged solution through THOBEM simulations. To avoid this problem, several numerical methods were applied for the simulation: Element creation, modulation function, MLM, Chebyshev filtering, and the determination of the proper domain size.

It is essential for the current case to use the double body potential as an approximation of the steady potential. The accuracy of the results for the FPSO depend strongly upon that of the double body potential. The reason for this is that the grid on the hull is too coarse to represent the stationary velocity field precisely. The final outcome may lack accuracy in the case of forward speed. This can be overcome by using finer grids, or preferably using a higher order panel method in the calculation of the double

body potential.

When integrating the equation in the time domain, time step size is an essential factor to obtain a converged solution. The predictor-corrector(P-C) method worked fine with proper size of the time grid (or time stepping). In comparing the results obtained using P-C method with the second and the fourth order solutions, the results were almost identical. Accordingly, the various time stepping methods were excluded from the case study.

There are several strengths of this study. First, this time domain simulation can provide an approximated solution that can be acceptable in a time domain simulation. This time domain simulation is basically different from the simulation obtained from the frequency domain solution. Second, this study can visualize the simulation better and more intuitively in terms of understanding the physical phenomena. Third, this time domain procedure can be applied along the other time history data without any difficulties. For example, a radiation problem was solved by the oscillation of a body, as a model test.

However, some weaknesses lie on the convergence of the simulation in the solution. Due to a higher order element, we cannot put a severely dense element in all calculation domains. The BEM has a singularity problem when the source point and the field point start very closely. They tend to show an unrealistic influential strength on each of the nodes. Previous studies have not discussed this singularity problem at all because most case studies were performed only by using a simple body. Apparently, this simple body required no dense element in the higher order element method. This would be the next critical issue to be solved in the study as it has remained unsolved in previous research.

5.2 Future works

Future research is needed to include a large movement in the horizontal plane for an FPSO. The large movement is one of the most interesting phenomena in an FPSO response. For inclusion of a large movement, pre-process along with mesh generation should be automated so that a particular time step can move an FPSO with a large horizontal response. In addition, parallel job sequence control should be adopted to use computational resources efficiently.

Future studies are needed to explore the possibility of the shallow water effect. Since this study was performed without a bottom boundary, it may require consideration of the shallow water effect when considering the FPSOs' operational depth. Although the first order linear wave problem was taken into account, the Orlandi condition showed some reflections on the open boundary. Further information is needed to supplement findings of the study and efforts are needed to develop more efficient and sophisticated numerical techniques in terms of time and accuracy of the simulation.

REFERENCES

- ABUL-AZM, A. G. & WILLIAMS, A. N. 1988 Second-order diffraction loads on truncated cylinders. *Journal of Waterway, Port, Coastal & Ocean Engineering* **114** (4), 436–454.
- BAI, K. J., KYOUNG, J. H. & KIM, J. W. 2003 Numerical computations for a nonlinear free-surface problem in shallow water. *Journal of Offshore Mechanics and Arctic Engineering* **125**, 33–40.
- BECK, R. F. & KING, B. 1989 Time-domain analysis of wave exciting forces on floating bodies at zero forward speed. *Applied Ocean Research* **11** (1), 19–25.
- BECK, R. F. & LIAPIS, S. J. 1987 Transient motion of floating bodies at zero forward speed. *Journal of Ship Research* **31**, 164–176.
- BEER, G. 2001 *Programming the boundary element method, an introduction for engineers*. West Sussex, England: Wiley.
- BOO, S. Y. 1993 Application of higher-order boundary element method to steady ship wave problem and time-domain simulation of nonlinear gravity waves. PhD Dissertation, Texas A&M University, College Station, Texas.
- BORESI, A. P., CHONG, K. P. & SAIGAL, S. 2003 *Approximate solution methods in engineering mechanics*, 2nd edn. Hoboken, New Jersey: John Wiley & Sons, Inc.
- BREBBIA, C. A. & DOMINGUEZ, J. 1977 Boundary element methods for potential problems. *Applied Mathematical Modelling* **1** (7), 372–378.

- BREBBIA, C. A. & DOMINGUEZ, J. 1989 *Boundary elements: an introductory course*, 1st edn. Southampton, UK: Computational mechanics Publications.
- BREBBIA, C. A. & PARTRIDGE, P. W., ed. 1992 *Boundary elements in fluid dynamics*. Southampton, UK: Computational Mechanics Publications.
- CELEBI 1997 Computational of transient fully nonlinear free surface waves and wave-body interactions. PhD Dissertation, Texas A&M University, College Station, Texas.
- CHANG, M. S. 1977 Computation of three-dimensional ship-motions with forward speed. In *Proceedings of the Second International Conference on Numerical Ship Hydrodynamics*, pp. 124–135. University of California, Berkeley.
- COINTE, R. 1989 Nonlinear simulation of transient free surface flows. In *Proceedings of the Fifth International Conference on Numerical Ship Hydrodynamics*. Hiroshima, Japan.
- DOMMERMUTH, D. G. & YUE, D. K. P. 1987 Numerical simulation of nonlinear axisymmetric flows with a free surface. *Journal of Fluid Mechanics* **178**, 195–219.
- EATOCK-TAYLOR, R. & HUNG, S. M. 1987 Second order diffraction forces on a vertical cylinder in regular waves. *Applied Ocean Research* **9** (1), 19–30.
- FALTINSEN, O. M. 1990 *Sea loads on ships and offshore structures*. New York: Cambridge University Press.
- FINKELSTEIN, A. 1957 The initial value problem for transient water waves. *Communications on Pure and Applied Mathematics* **10**, 511–522.
- FROUDE, W. 1868 *Observations and suggestions on the subject of determining by experiment the resistance of ships*. London, England: Institute of Naval Architects.

- GUEVEL, P. & BOUGIS, J. 1982 Ship-motions with forward speed in infinite depth. *International Shipbuilding Progress* **29**, 117–130.
- HAUSSLING, H. J. & COLEMAN, R. M. 1979 Nonlinear water waves generated by an accelerated circular cylinder. *Journal of Fluid Mechanics* **92**, 767–781.
- HESS, J. L. & SMITH, A. M. O. 1964 Calculation of nonlifting potential flow about arbitrary three-dimensional bodies. *Journal of Ship Research* **8** (3), 22–44.
- HSIN, C. Y., KERWIN, J. E. & NEWMAN, J. N. 1993 A higher-order panel method based on b-splines. In *Proceedings of the Sixth International Conference on Numerical Ship Hydrodynamics*, pp. 133–151. The National Academy of Sciences.
- HUGHES, G. 1954 Friction an form resistance in turbulent flow and a proposed formulation for use in model and ship correlation. In *Transaction of the Institution of Naval Architects* **96**, pp. 314–376.
- HUNTER, P. & PULLAN, A. 2003 Fem/bem notes. Department of Engineering Science, The University of Auckland, New Zealand.
- INGLIS, R. B. & PRICE, W. G. 1982 A three dimensional ship motion theory. comparison between theoretical predictions and experimental data of the hydrodynamic coefficients with forward speed. In *Transactions of the Royal Institute of Naval Architecture* **124**, pp. 141–157.
- ISAACSON, M. & CHEUNG, K. F. 1992 Time-domain solution for wave-current interactions with a two-dimensional body. *Applied Ocean Research* **15**, 39–52.
- JAGANNATHAN, S. 1988 Non-linear free surface flows and an application of the orlanski boundary condition. *International Journal for Numerical Methods in Fluids* **8**, 1051–1070.

- JASWON, M. A. 1963 Integral equation methods in potential theory. part i. In *Proceedings of the Royal Society of London, Series A, Mathematical and Physical Sciences* **275**, pp. 33–46.
- KIM, B. & SHIN, Y. S. 2003 A nurbs panel method for three-dimensional radiation and diffraction problems. *Journal of Ship Research* **47** (2), 177–186.
- KIM, Y., KRING, D. C. & SCLAVOUNOS, P. D. 1997 Linear and nonlinear interactions of surface waves with bodies by a three-dimensional rankine panel method. *Applied Ocean Research* **19**, 235–249.
- KORSMEYER, F. T., BINGHAM, H. B. & NEWMAN, J. N. 1999 *TiMIT: A panel-method program for transient wave-body interactions*. Research Laboratory of Electronics, MIT, Cambridge, Massachusetts.
- KORSMEYER, F. T., LEE, C. H., NEWMAN, J. N. & SCLAVOUNOS, P. D. 1988 The analysis of wave effects on tension-leg platforms. In *Proceedings of the Seventh International Conference on Offshore Mechanics and Arctic Engineering*, pp. 1–14. Houston, Texas.
- LEE, C. H., MANIAR, H., NEWMAN, J. N. & ZHU, X. 1997 Computations of wave loads using a b-spline panel method. In *Twenty-First Symposium on Naval Hydrodynamics*, pp. 75–92.
- LEE, C. H., NEWMAN, J. N. & ZHU, X. 1996 An extended boundary integral equation method for the removal of irregular frequency effects. *International Journal for Numerical Methods in Fluids* **23**, 637–660.

- LIU, Y. H. 1988 Analysis of fluid structure interaction by using higher-order boundary elements in potential problems and its application in coupling vibrations of bending and torsion of ships. PhD Dissertation, Shanghai Jiao Tong University.
- LIU, Y. H., KIM, C. H. & LU, X. S. 1991 Comparison of higher-order boundary element and constant panel methods for hydrodynamic loadings. In *International Journal of Offshore and Polar Engineering Conference ISOPE* **1**, pp. 476–483.
- LIU, Y. H., KIM, M. H. & KIM, C. H. 1995 The computation of second-order mean and double-frequency wave loads on compliant tlp by hoberm. *Journal of Offshore and Polar Engineering* **5**, 111–119.
- LONGUET-HIGGINS, M. S. & COKELET, E. D. 1976 The deformation of steep surface waves on water. In *Proceedings of Royal Society* **A350**, pp. 1–26. London, England.
- MICHELL, J. H. 1898 The wave resistance of ship. *Philosophical Magazine* **5** (272), 106–123.
- MIYATA, H., SATO, T. & BABA, N. 1987 Difference solution of a viscous flow with free surface wave about an advancing ship. *Journal of Computational Physics* **72**, 393–421.
- MIZUMURA, K. 1985 Nonlinear water waves developed by an accelerated circular cylinder. In *Boundary Elements VII: Proceedings of the Seventh International Conference* (ed. C. A. Brebbia), pp. 9.49–9.59.
- MOLIN, B. 1979 Second-order diffraction loads upon three-dimensional bodies. *Applied Ocean Research* **1** (4), 197–202.

- NAKOS, D. & SCLAVOUNOS, P. 1991 Ship motions by a three-dimensional Rankine panel method. In *Eighteenth Symposium on Naval Hydrodynamics*, pp. 21–40. Washington, D.C.: National Academy Press.
- NEWMAN, J. N. 1978 The theory of ship motions. *Advances in Applied Mechanics* **18**, 221–280.
- NOBLESSE, F. & YANG, C. 2004a A simple Green function for diffraction-radiation of time-harmonic waves with forward speed. *Ship Technology Research* **51**, 35–52.
- NOBLESSE, F. & YANG, C. 2004b Weakly singular boundary-integral representations of free-surface flow about ships or offshore structures. *Journal of Ship Research* **48**, 31–44.
- OGILVIE, T. F. 1964 Recent progress toward the understanding and prediction of ship motions. In *Proceedings of the Fifth Symposium on Naval Hydrodynamics*, pp. 3–79. Bergen, Norway.
- OHRING, S. 1981 Three-dimensional ship wave generation using an efficient finite difference scheme with double model linearization. *Journal of Computational Physics* **41**, 8–114.
- OLIVEIRA, F.S.B.F. 2000 Improvement on open boundaries on a time dependent numerical model of wave propagation in the nearshore region. *Ocean Engineering* **28**, 95–115.
- ORLANSKI, I. 1976 A simple boundary condition for unbounded hyperbolic flows. *Journal of Computational Physics* **21**, 251–269.
- PENNWELL, PETROLEUM GROUP 1998 *Floating production technology at use in variety of projects* **1**, Tulsa, Oklahoma: Pennwell Publishing Company.

- PINKSTER, J. A. 1978 Wave feed-forward as a means to improve dynamic positioning. In *Proceedings of the Offshore Technology Conference* **3057**, Houston, Texas.
- QIU, W. 2001 A panel-free method for time-domain analysis of floating bodies in waves. PhD Dissertation, Dalhousie University, Halifax, Nova Scotia, Canada.
- QIU, W., PENG, H. & HSIUNG, C. C. 2003 A panel-free method for time-domain analysis. In *Twenty-Fourth Symposium on Naval Hydrodynamics*, pp. 963–976.
- RAHMAN, M. 1984 Wave diffraction by large offshore structures: an exact second-order theory. *Applied Ocean Research* **6** (2), 90–100.
- RAHMAN, M. 1987 A design method of predicting second-order wave diffraction caused by large offshore structures. *Ocean Engineering* **14** (1), 1–18.
- STOKER, J. J. 1957 *Water waves: the mathematical theory with applications*. New York: Interscience Publishers.
- SYMM, G. T. 1963 Integral equation methods in potential theory. part ii. In *Proceedings of the Royal Society of London, Series A, Mathematical and Physical Sciences* **275**, pp. 23–32.
- TENG, B. & EATOCK-TAYLOR, R. 1995 Application of a higher-order boundary element method in the calculation of wave run-up in a weak current. *International Journal of Offshore and Polar Engineering* **5**, 219–224.
- VADA, T. 1987 A numerical solution of the second-order wave-diffraction problem for a submerged cylinder of arbitrary shape. *Applied Ocean Research* **9** (1), 19–30.
- WEHAUSEN, J. V. 1967 Initial value problem for the motion in an undulating sea of a body with fixed equilibrium position. *Journal of Engineering Mathematics* **1**, 1–19.

- WEHAUSEN, J. V. 1971 The motion of floating bodies. *Annual Reviews of Fluid Mechanics* **3**, 237–268.
- WICHERS, J. E. W. & HUIJSMANS, R. M. H. 1984 On the low-frequency damping forces acting on offshore moored vessels. In *Proceedings of the Offshore Technology Conference* **4831**, pp. 315–324. Houston, Texas.
- WILLIAMS, A. N. & ABUL-AZM, A. G. 1990 A comparison of complete and approximate solution for second-order diffraction loads on arrays of vertical circular cylinders. *Ocean Engineering* **15** (5), 427–445.
- WU, G. X. & EATOCK-TAYLOR, R. 1987 A Green's function form for ship motions at forward speed. *Shipbuild Program* **34**, 189–196.
- WU, G. X. & EATOCK-TAYLOR, R. 1990 The second order diffraction force on a horizontal cylinder in finite water depth. *Applied Ocean Research* **12** (3), 106–111.
- YANG, C., LOHNER, R. & NOBLESSE, F. 2004 Comparison of classical and simple free-surface green functions. *International Journal of Offshore and Polar Engineering* **14** (4), 257–264.
- ZHAO, R., FLATINSEN, O. M., KROKSTAD, J. R. & AANESLAND 1988 Wave current interaction effects on large volume structures. In *Proceedings of the Behavior of Offshore Structures, BOSS'88*, pp. 623–638, Trondheim, Norway.

APPENDIX A

GREEN'S IDENTITIES

- The vector derivative identities are

$$\nabla \cdot (\psi \nabla \phi) = \psi \nabla^2 \phi + (\nabla \psi) \cdot (\nabla \phi) \quad (\text{A.1})$$

and

$$\nabla \cdot (\phi \nabla \psi) = \phi \nabla^2 \psi + (\nabla \phi) \cdot (\nabla \psi), \quad (\text{A.2})$$

where ∇ is the divergence. $\nabla \cdot$ is the gradient. ∇^2 is the Laplacian. $\mathbf{a} \cdot \mathbf{b}$ is the dot product.

From the divergence theorem,

$$\int_V (\nabla \cdot \mathbf{F}) dV = \int_S \mathbf{F} \cdot d\mathbf{a}. \quad (\text{A.3})$$

- Green's first identity is obtained from substituting (A.2) to (A.3).

$$\int_S \phi (\nabla \psi) \cdot d\mathbf{a} = \int_V \{ \phi \nabla^2 \psi + (\nabla \phi) \cdot (\nabla \psi) \} dV. \quad (\text{A.4})$$

- Green's second identity is arranged by subtracting (A.2) from (A.1).

$$\nabla \cdot (\phi \nabla \psi - \psi \nabla \phi) = \phi \nabla^2 \psi - \psi \nabla^2 \phi. \quad (\text{A.5})$$

From the divergence theorem (A.3),

$$\int_V (\phi \nabla^2 \psi - \psi \nabla^2 \phi) dV = \int_S (\phi \nabla \psi - \psi \nabla \phi) \cdot d\mathbf{a}. \quad (\text{A.6})$$

REFERENCES:

KAPLAN, W. 1991 *Advanced Calculus*, 4th edn. MA: Addison-Wesley

Cited in the WEISSTEIN, E. W. "Green's Identities." From MathWorld—A Wolfram Web Resource. <http://mathworld.wolfram.com/GreensIdentities.html>

APPENDIX B

OPEN SOURCE NUMERICAL LIBRARY

SLATEC is a fortran library of over 1400 routines for numerical tasks. Some of the subjects that SLATEC covered are: Arithmetic, error analysis, elementary and special functions, linear algebra, interpolation, nonlinear equations, optimization, differentiation, integration, differential and integral equations, integral transforms, statistics, probability, and data handling. SLATEC Common Mathematical Library, Version 4.1, was developed in July 1993. It is a comprehensive software library containing over 1400 general purpose mathematical and statistical routines written in Fortran 77.

APPENDIX C

LINUX CLUSTER

A clustering is considered to maximize limited computational resources. A clustering is a group of tightly coupled computers that work together. There are two categories in Linux clustering: shared memory and unshared memory. Shared memory is called a tight cluster. A shared memory cluster covers multi CPUs in one motherboard or multi core CPUs. In an unshared memory cluster, one is more likely to load a balancing technique. When a thread occurs, the sequence of a job gets coppered and then allocated to each in CPUs. Figure C.1 shows the sequence of the simulation job in this study. Higher order boduary elements were generated at K2 super computer in Texas A&M University supercomputing center or desktop pc in Offshore Technology Research Center. The next step is for matrix inversion. After that time domain simulation stats at the clusters.

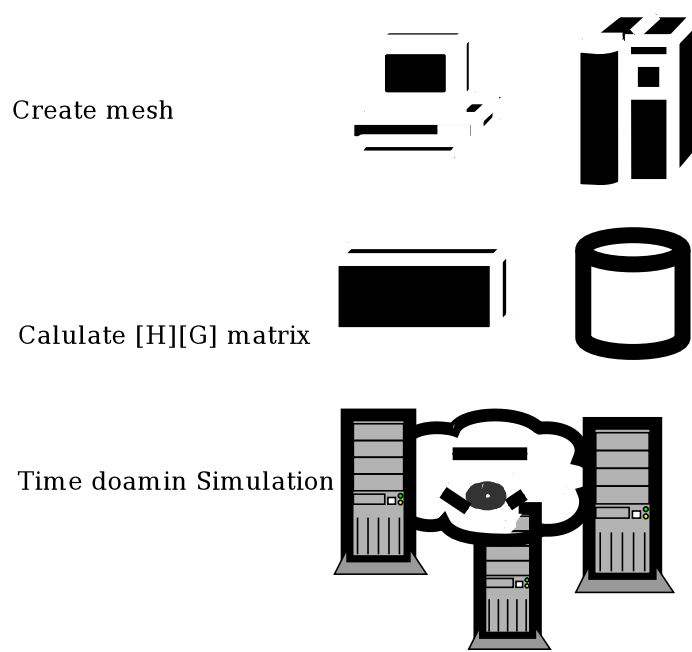


FIGURE C.1. Sequence of the process for numerical calculation

APPENDIX D

CONVOLUTION

Fourier Transform can transform a convolution into a multiplication. The convolution of two time functions $f(t)$ and $h(t)$ is defined mathematically as:

$$g(t) = \int_{-\infty}^{\infty} f(\tau)h(t - \tau)d\tau. \quad (\text{D.1})$$

$$g(t) = f(t) * h(t), \quad (\text{D.2})$$

where the asterisk means “convolved with”.

The physical meaning is as follows:

- $f(t)$ represents an input signal of the system
- $h(t)$ represents an impulse response of the system
- $g(t)$ represents an output of the system

Examples

- $f(t)$ is a time signal.
 $h(t)$ is a impulse response.
- Assume each point of $f(t)$ is an impulse(delta function) weighted by $f(t)$ at each point.

- Each impulse excites an impulse response.
- The scaling of impulse response is proportional to the level of $f(t)$ and the time origin of impulse response coincides with the impulse.
- Each scaled impulse response is delayed by the appropriate time interval from the time of excitation up to the time of measurement.
- $g(t)$ consists of the sum of these scaled impulse responses.

$$g(t_0) = \sum_{n=-\infty}^{\infty} g_n(t_0) = \sum_{n=-\infty}^{\infty} f(t_n)h(t_0 - t_n). \quad (\text{D.3})$$

More generally, the response at time t is

$$g(t) = \sum_{n=-\infty}^{\infty} f(t_n)h(t - t_n). \quad (\text{D.4})$$

When $\Delta t \rightarrow 0$, equation (D.4) will be equation (D.1)

APPENDIX E

CONVOLUTION WITH A DELTA FUNCTION

Consider response function is a unit delta function with time delay τ_o .

$$h(t) = \delta(t - \tau_o) \quad (\text{E.1})$$

Description of the system.

- The response of the system is $h(s)$ as a unit delta function.
- Each discrete impulse $f(t_n)$ generates a single impulse in response delayed by τ_o
- The overall effect is to delay the whole signal by τ_o , but otherwise to leave it unchanged.
- If the delta function is weighted with a scaling factor, then the entire response is also weighted by that scaling factor.
- In general it can be stated that the effect of convolving a function with a delta function is to shift its origin to the delta function.

Covolution of Spectral Functions

- $F(f) \star H(f) = \int_{-\infty}^{\infty} F(\phi)H(f - \phi)d\phi$
- Caution:
 $F(f)$ and $H(f)$ are complex variables.
 - multiplication of amplitudes

- addition of phases
- integration represents a complex or vector addition.

APPENDIX F

WAVES AND CURRENT HEADING EFFECTS

Wave and current oblique heading effects show a very interesting phenomenon for an FPSOs behavior. As mentioned in the section 4.7.8, we considered adverse and collinear current effects at various degree heading angles. Appendix E provides the remaining of the data that did not mentioned in the section 4.7.8.

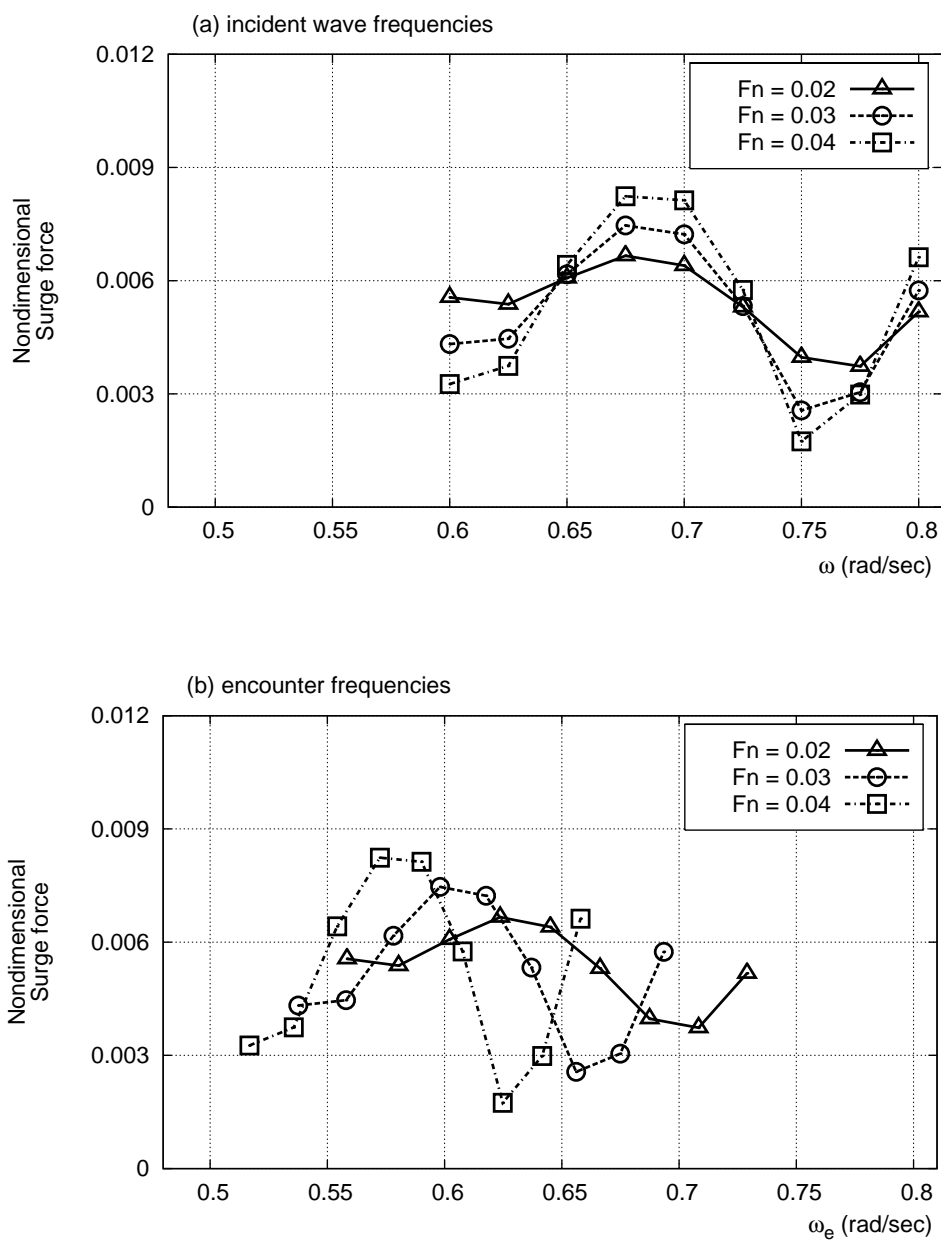


FIGURE F.1. Surge forces for diffracted waves in various frequencies with head sea (adverse current) effect. Wave and current heading angles are -10 and 170 degrees respectively.

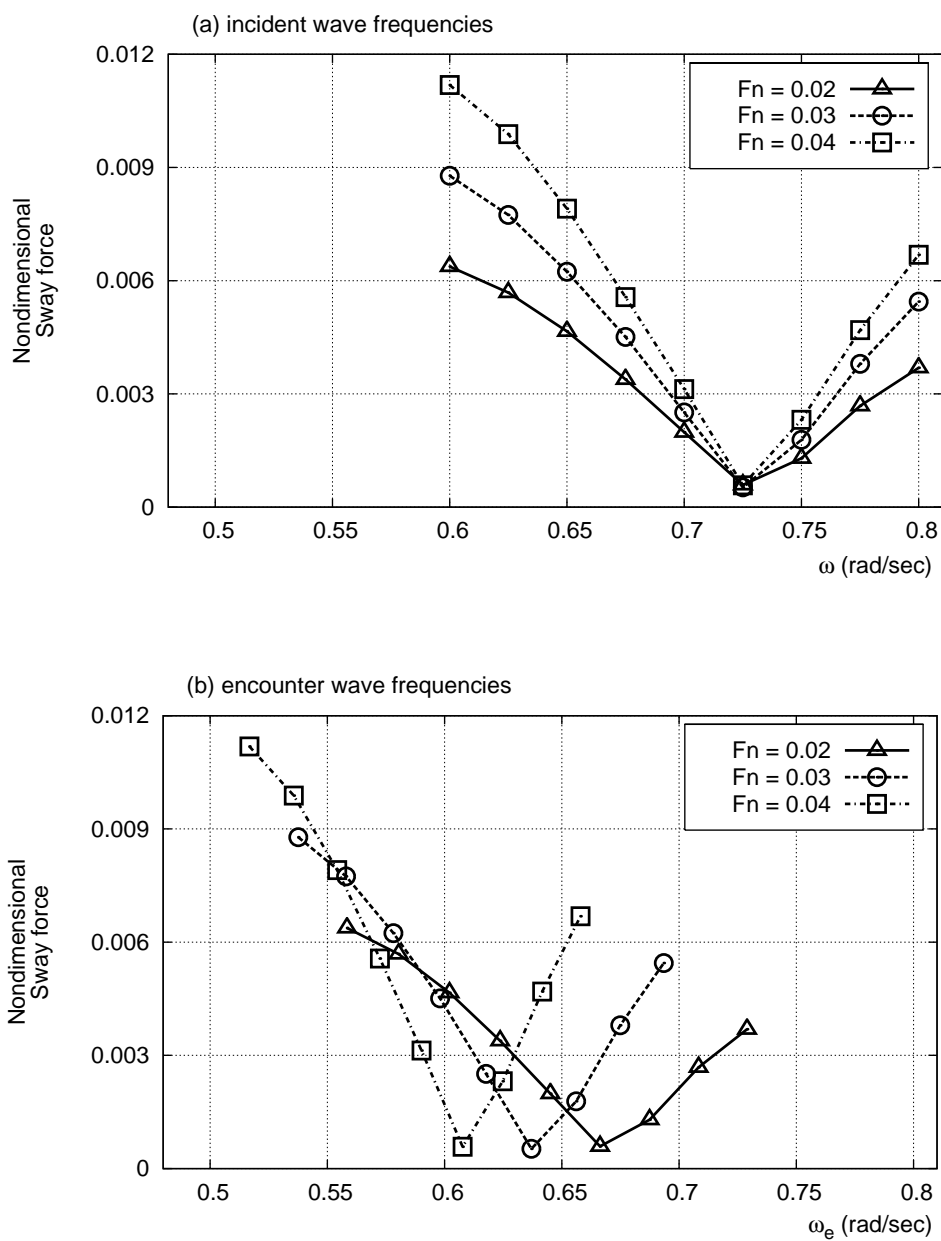


FIGURE F.2. Sway forces for diffracted waves in various frequencies with head sea (adverse current) effect. Wave and current heading angles are -10 and 170 degrees respectively.

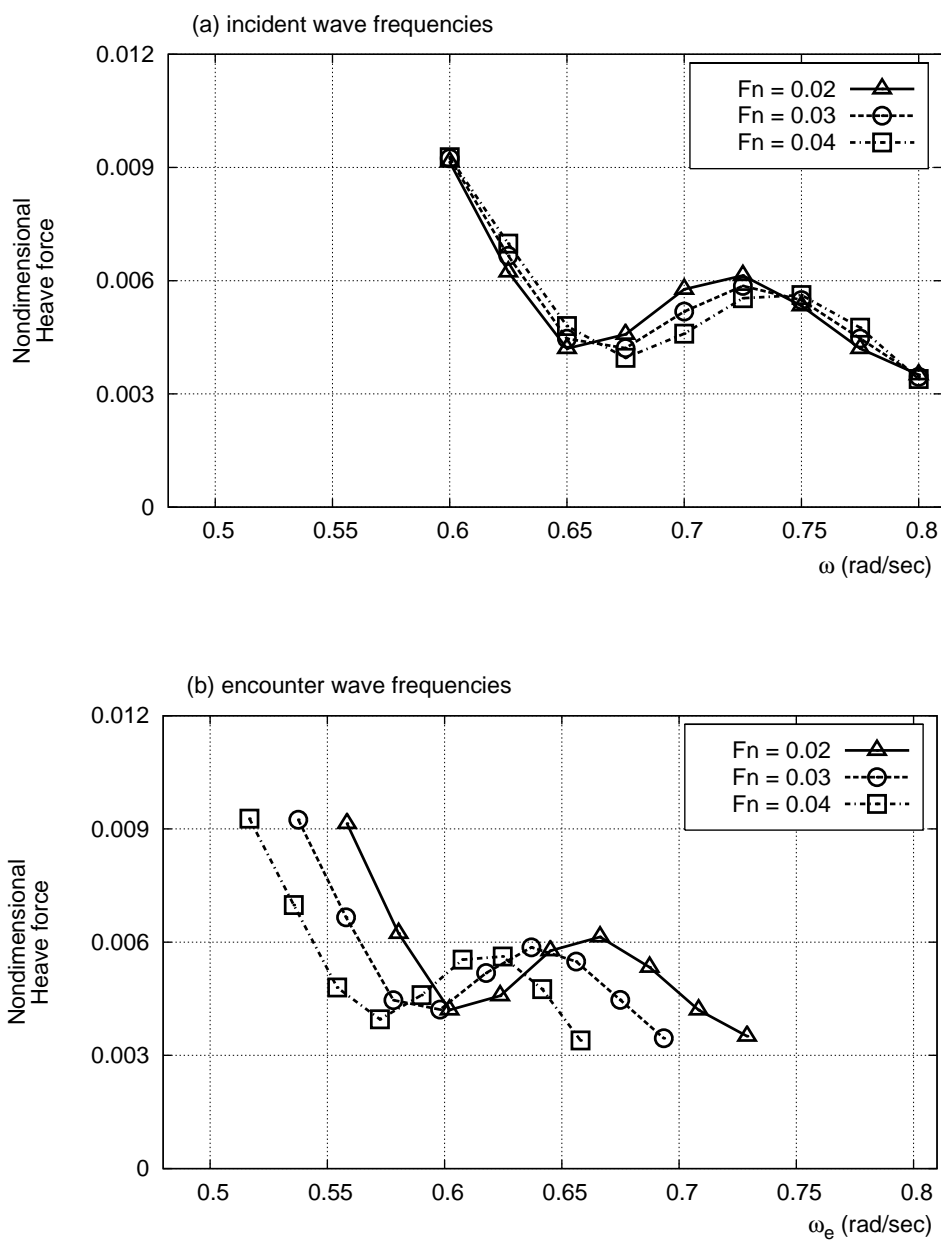


FIGURE F.3. Heave forces for diffracted waves in various frequencies with head sea (adverse current) effect. Wave and current heading angles are -10 and 170 degrees respectively.

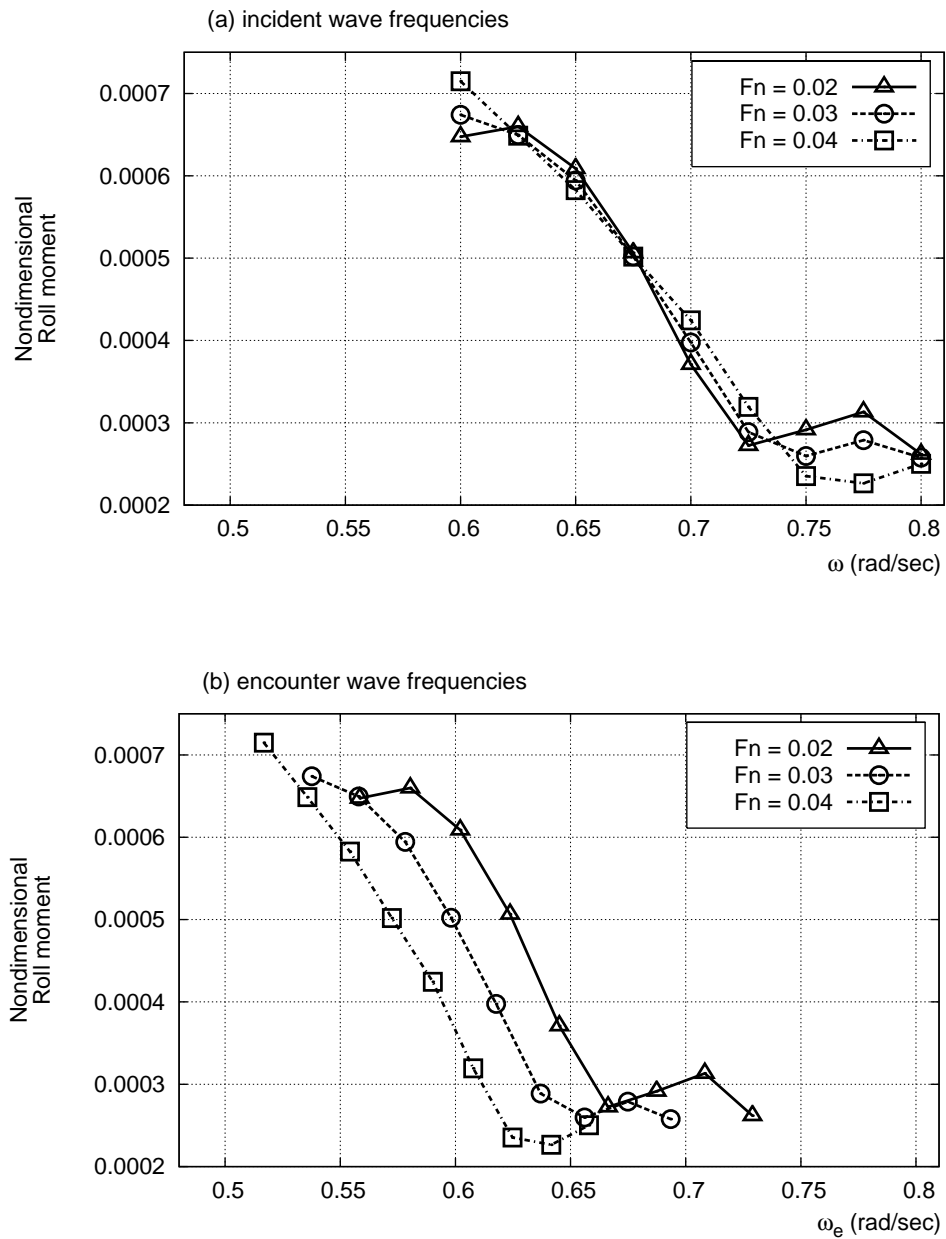


FIGURE F.4. Roll moments for diffracted waves in various frequencies with head sea (adverse current) effect. Wave and current heading angles are -10 and 170 degrees respectively.

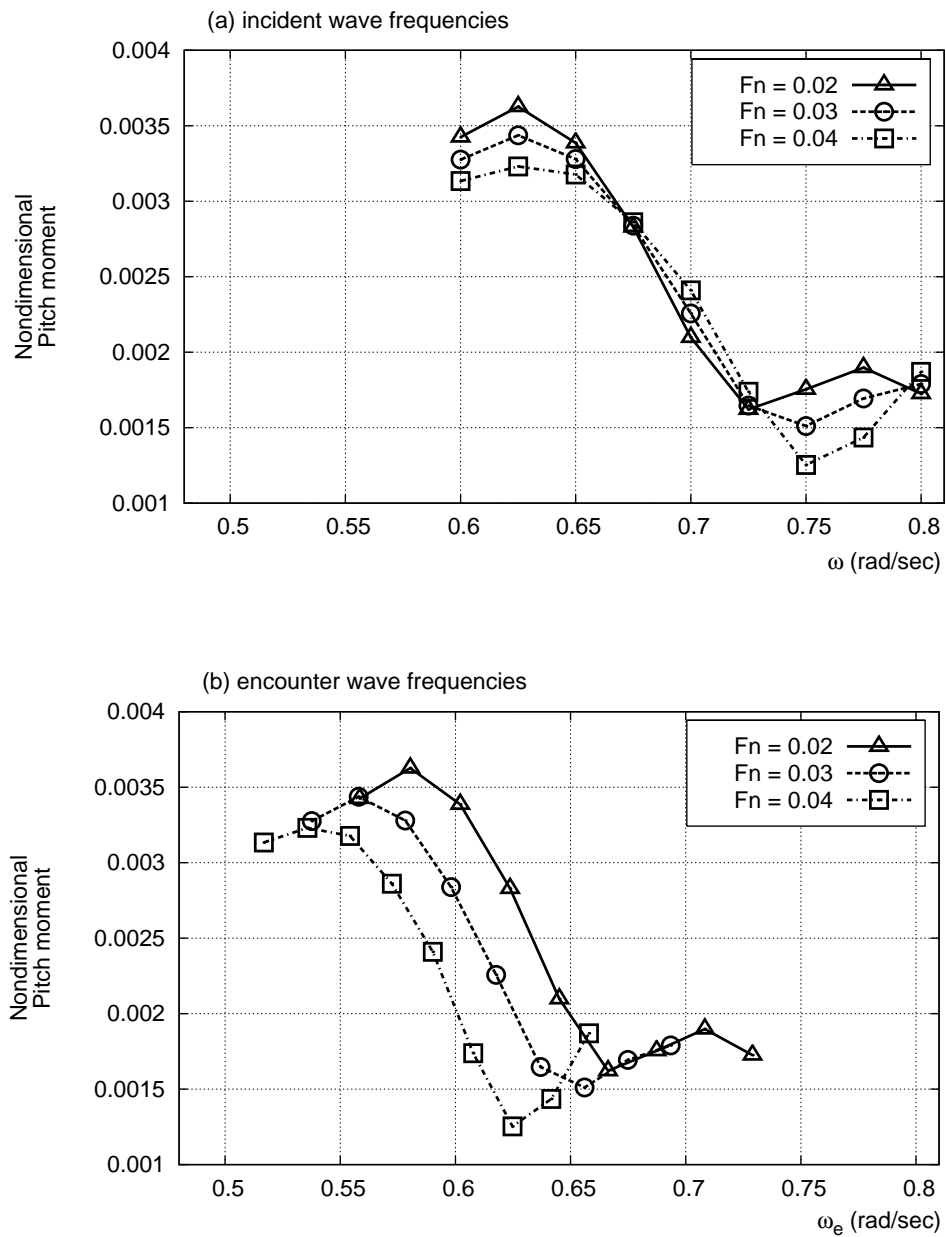


FIGURE F.5. Pitch moments for diffracted waves in various frequencies with head sea (adverse current) effect. Wave and current heading angles are -10 and 170 degrees respectively.

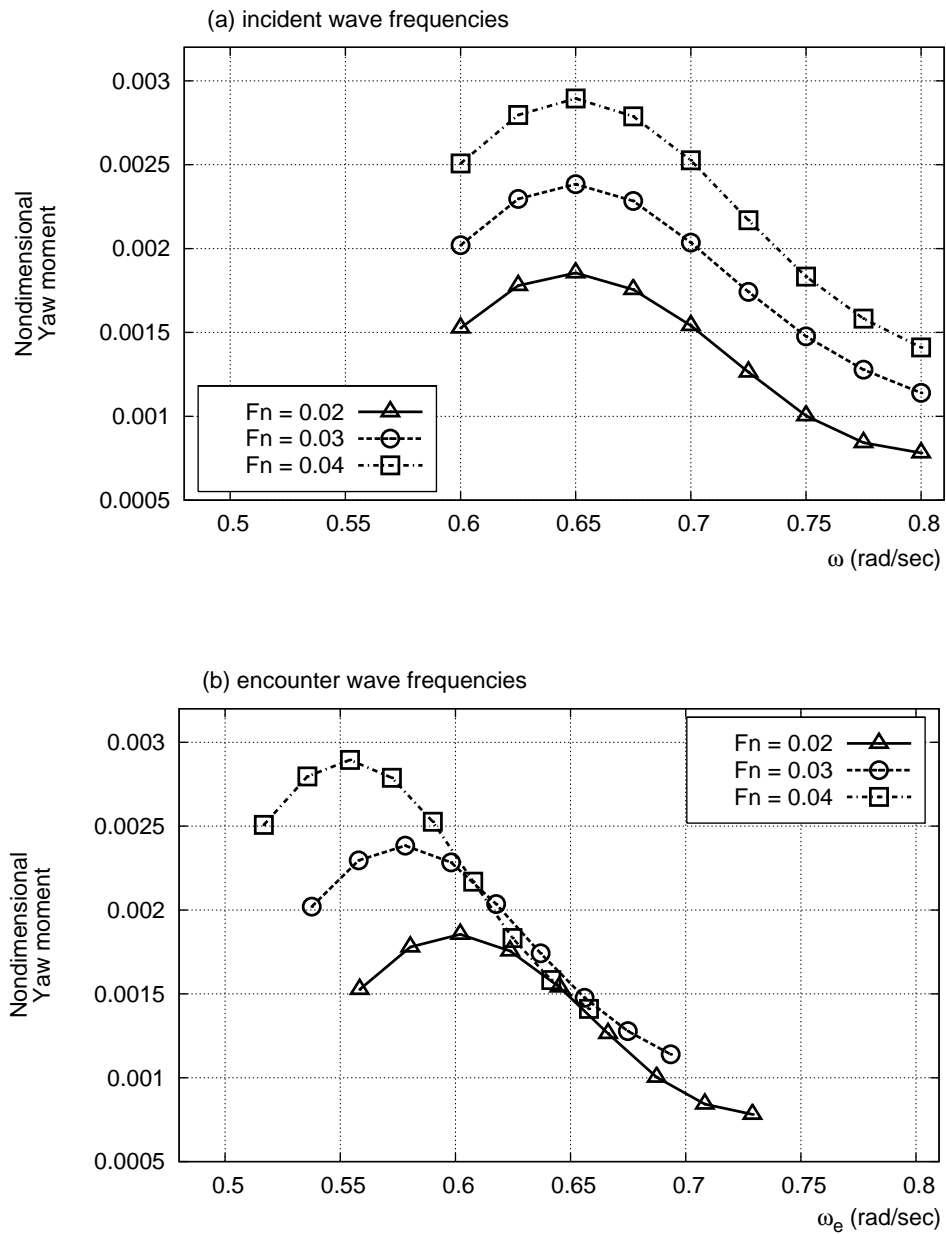


FIGURE F.6. Yaw moments for diffracted waves in various frequencies with head sea (adverse current) effect. Wave and current heading angles are -10 and 170 degrees respectively.

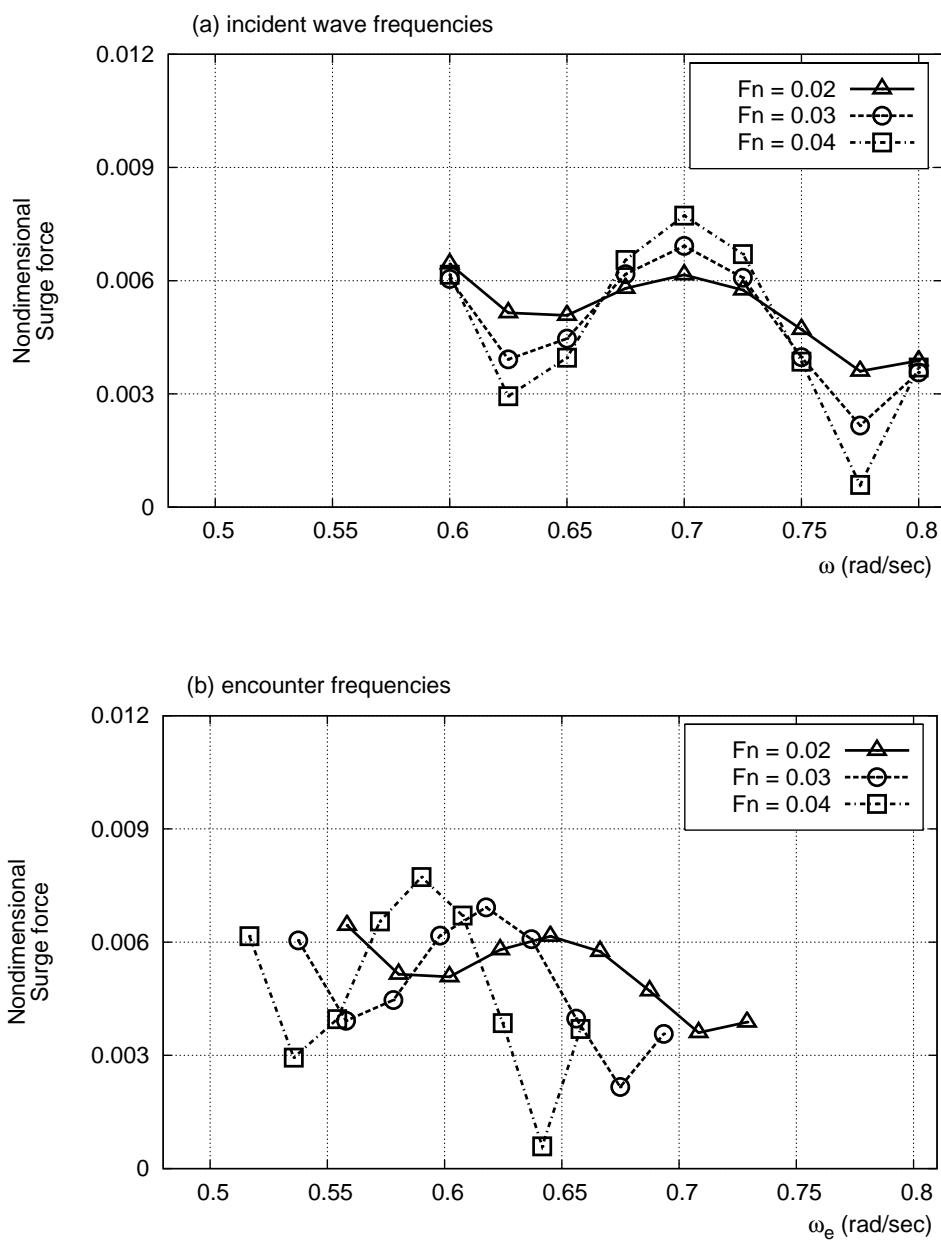


FIGURE F.7. Surge forces for diffracted waves in various frequencies with head sea (adverse current) effect. Wave and current heading angles are -15 and 165 degrees respectively.

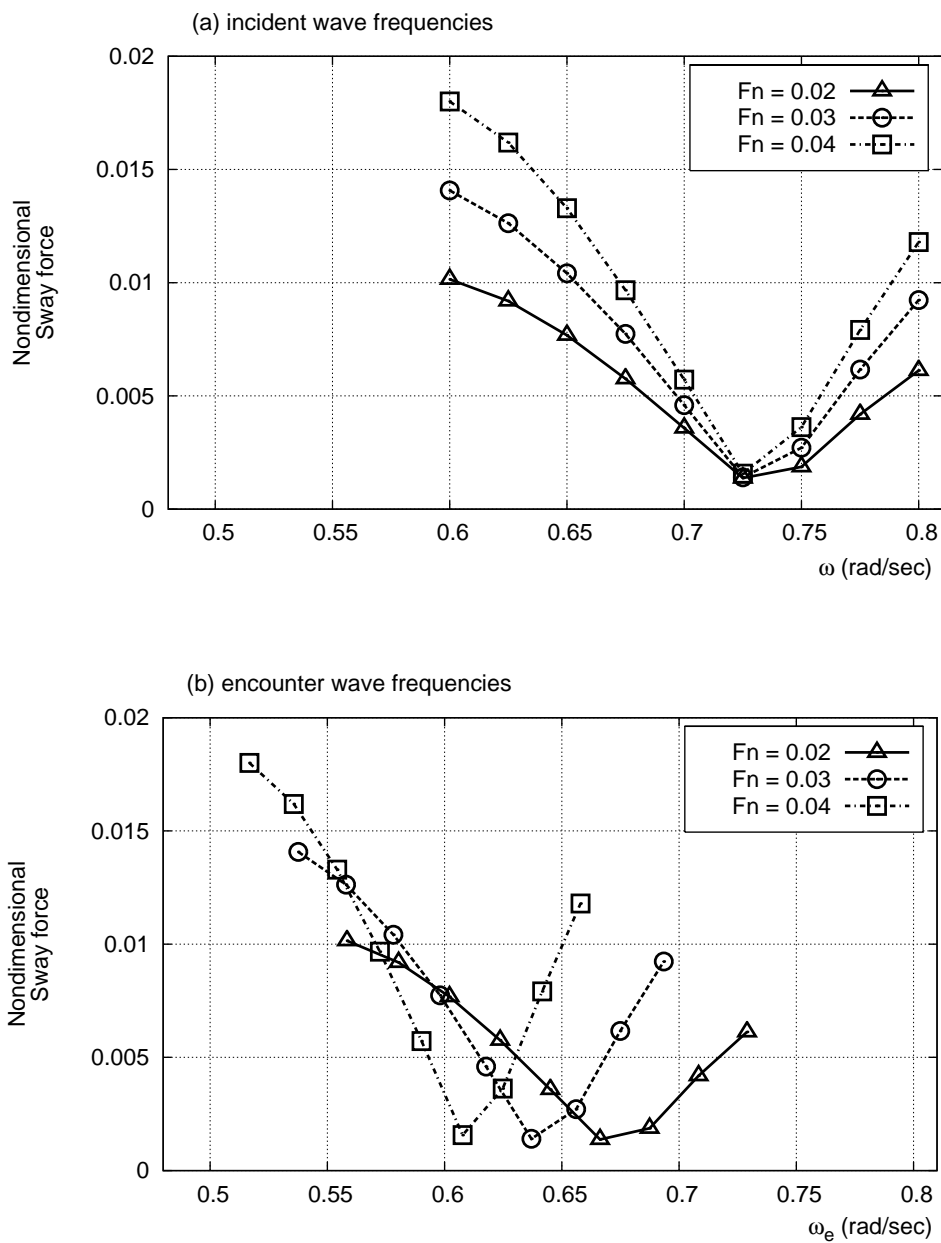


FIGURE F.8. Sway forces for diffracted waves in various frequencies with head sea (adverse current) effect. Wave and current heading angles are -15 and 165 degrees respectively.

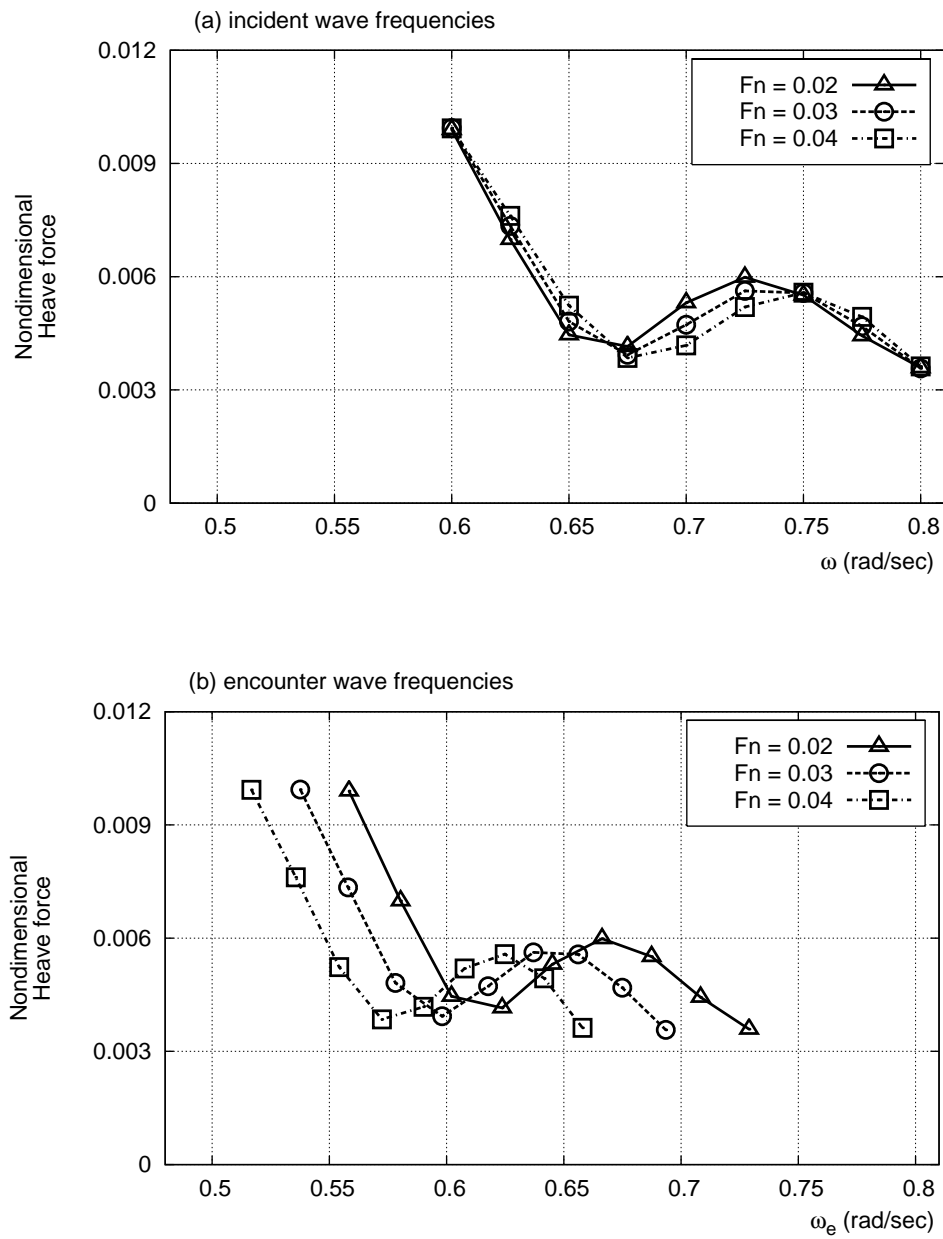


FIGURE F.9. Heave forces for diffracted waves in various frequencies with head sea (adverse current) effect. Wave and current heading angles are -15 and 165 degrees respectively.

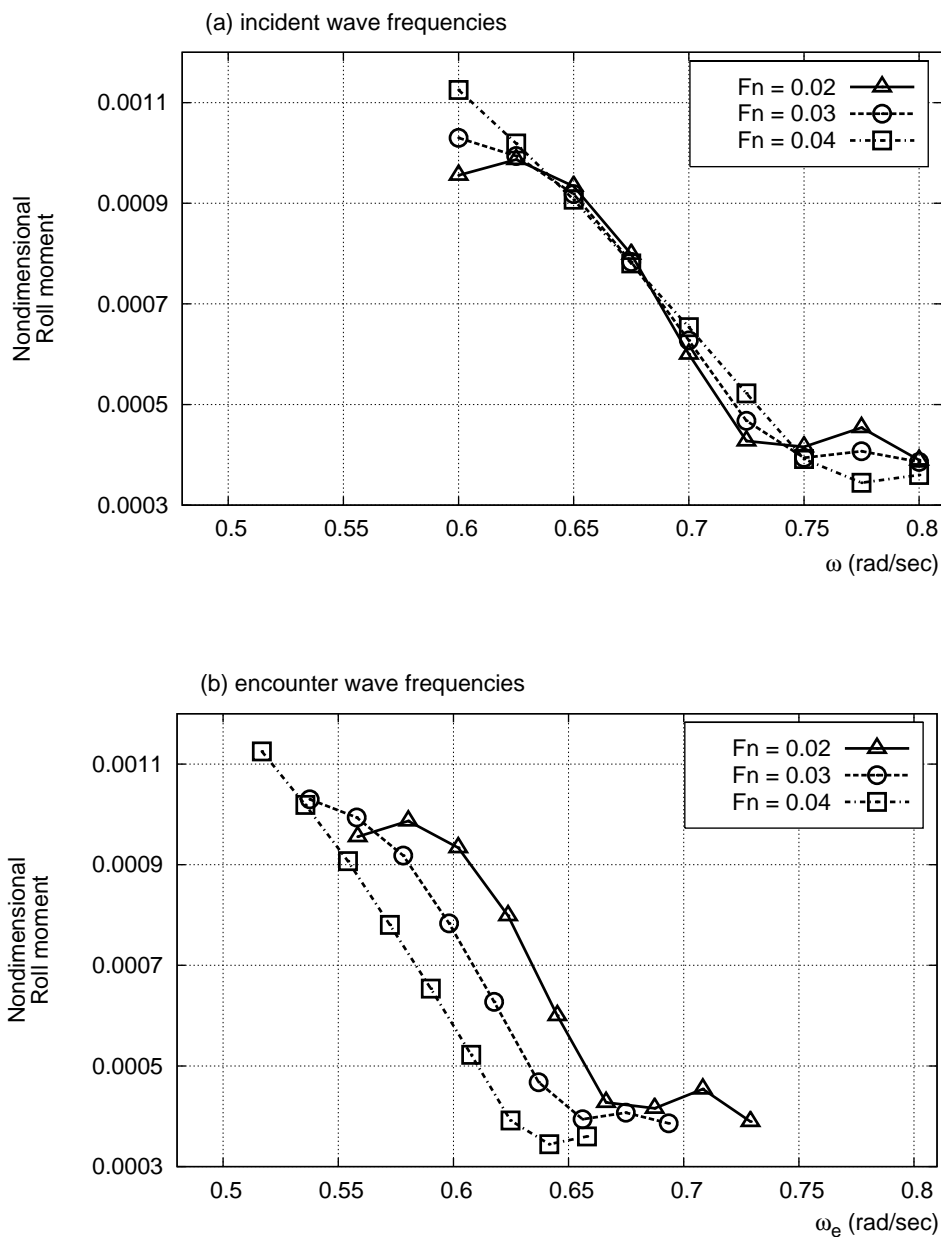


FIGURE F.10. Roll moments for diffracted waves in various frequencies with head sea (adverse current) effect. Wave and current heading angles are -15 and 165 degrees respectively.

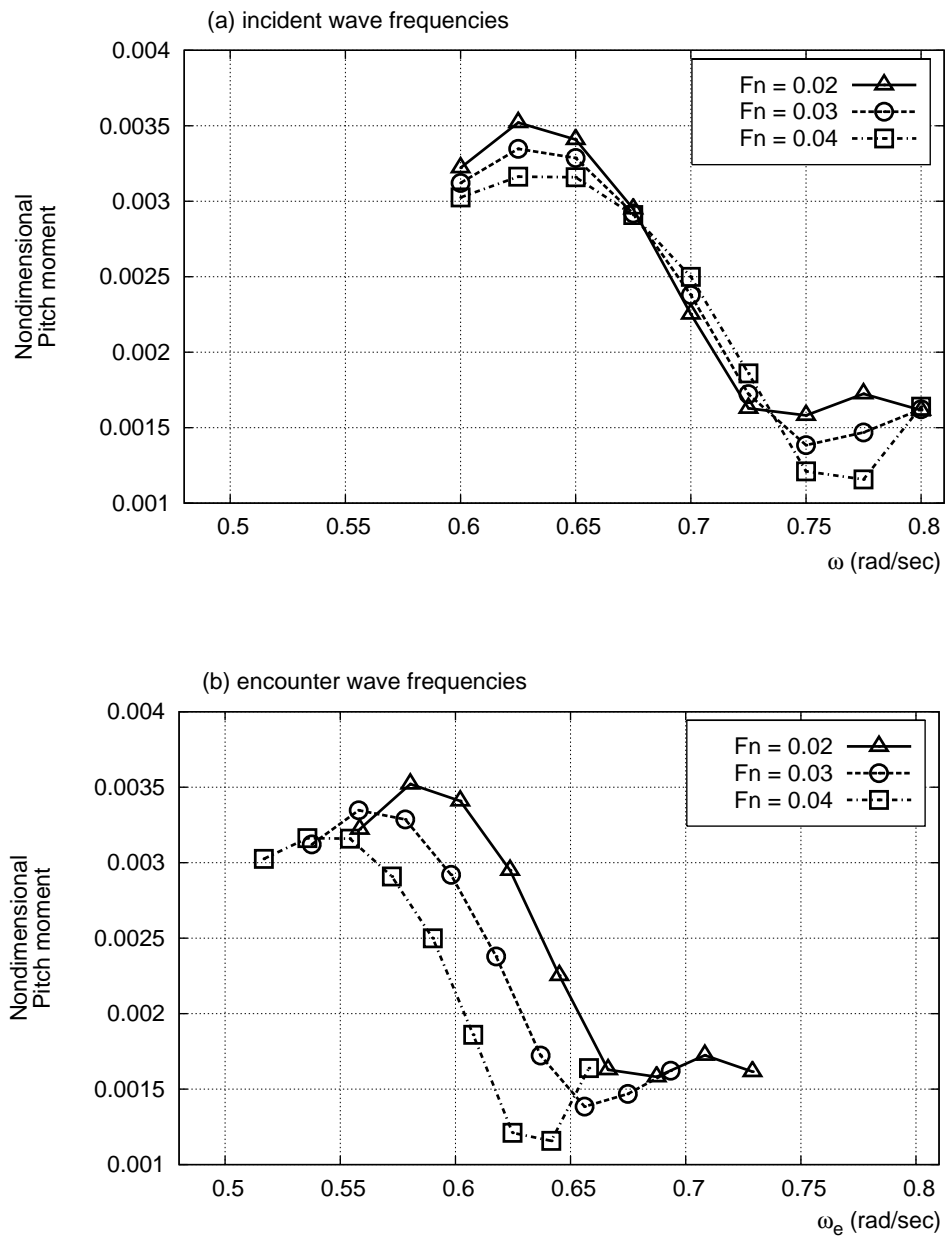


FIGURE F.11. Pitch moments for diffracted waves in various frequencies with head sea (adverse current) effect. Wave and current heading angles are -15 and 165 degrees respectively.

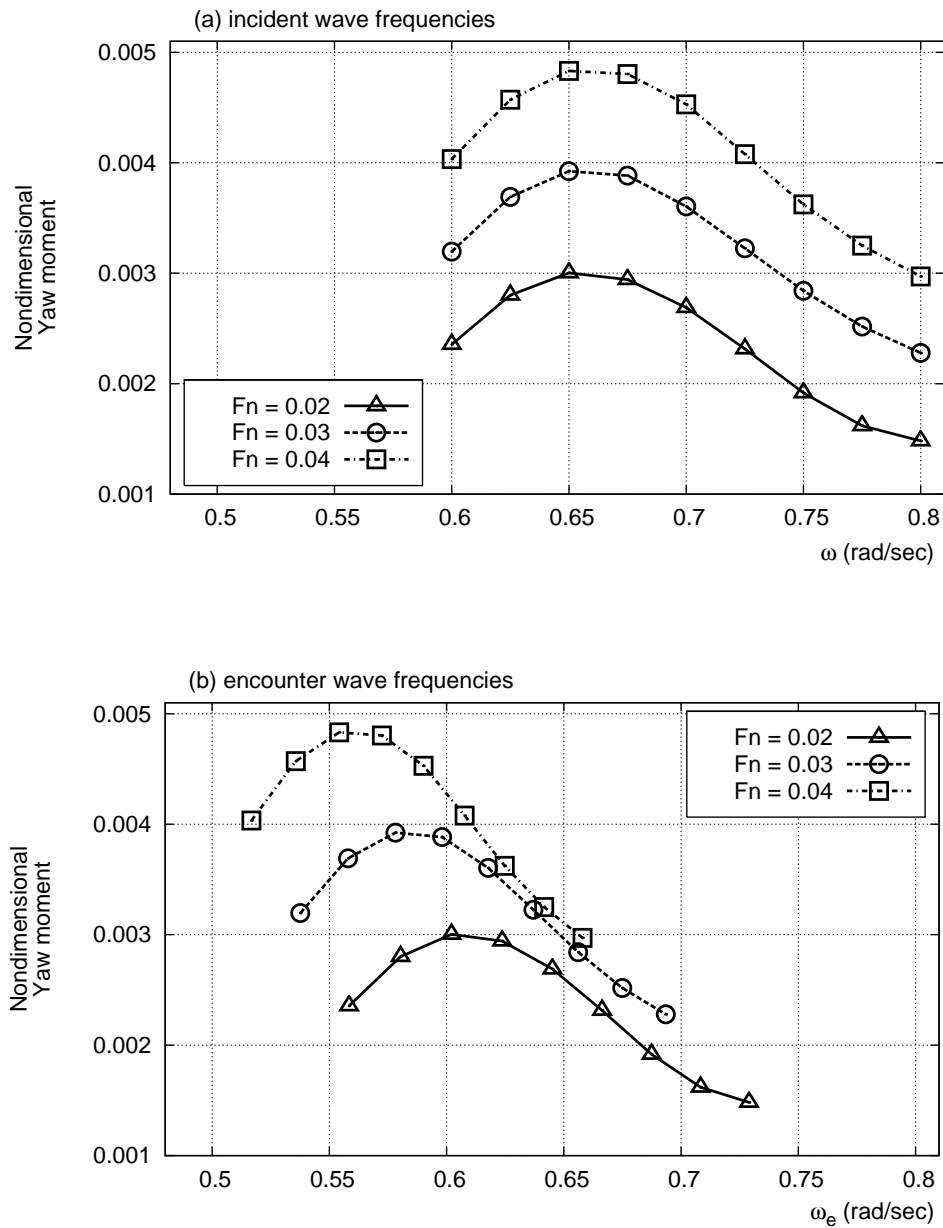


FIGURE F.12. Yaw moments for diffracted waves in various frequencies with head sea (adverse current) effect. Wave and current heading angles are -15 and 165 degrees respectively.

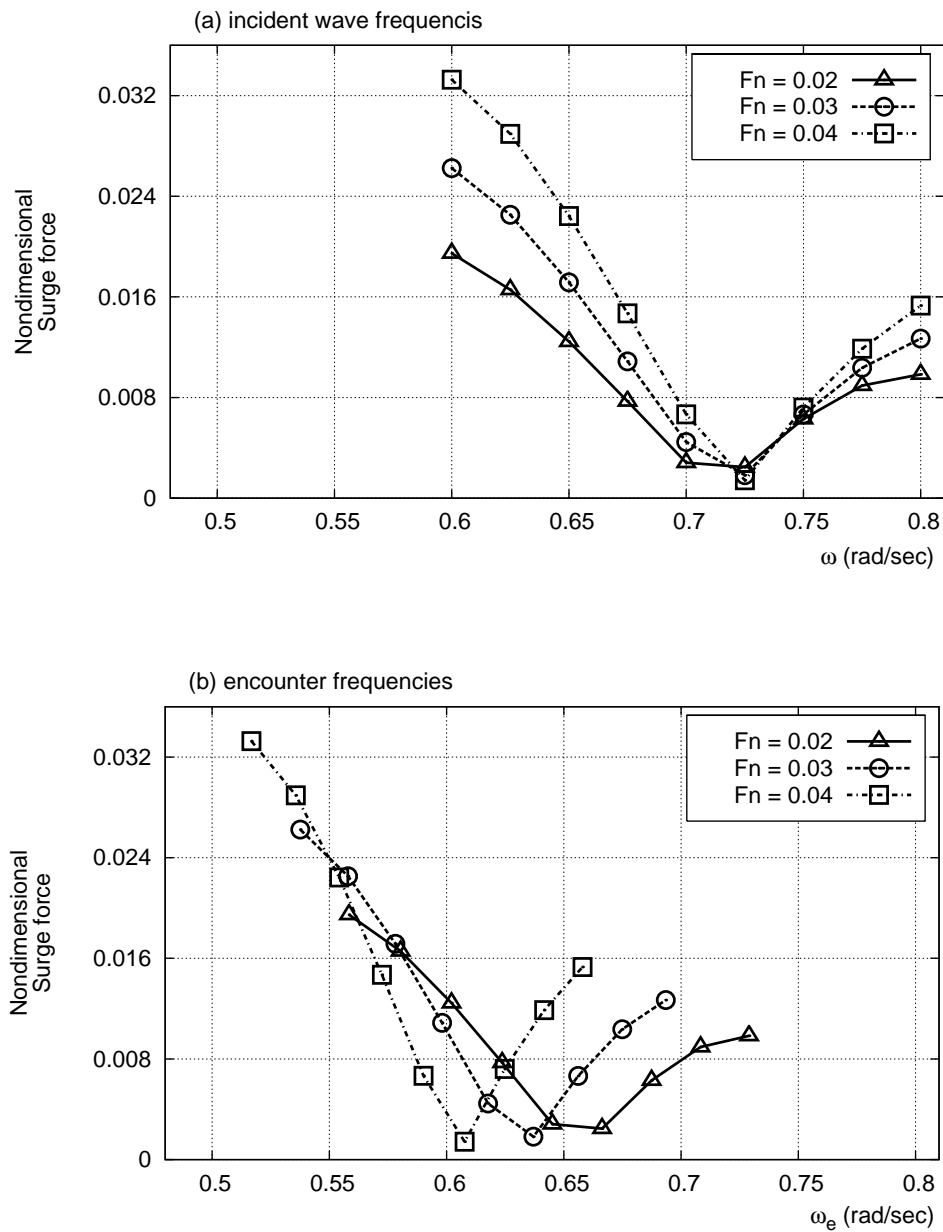


FIGURE F.13. Surge forces for diffracted waves in various frequencies with head sea (adverse current) effect. Wave and current heading angles are -30 and 150 degrees respectively.

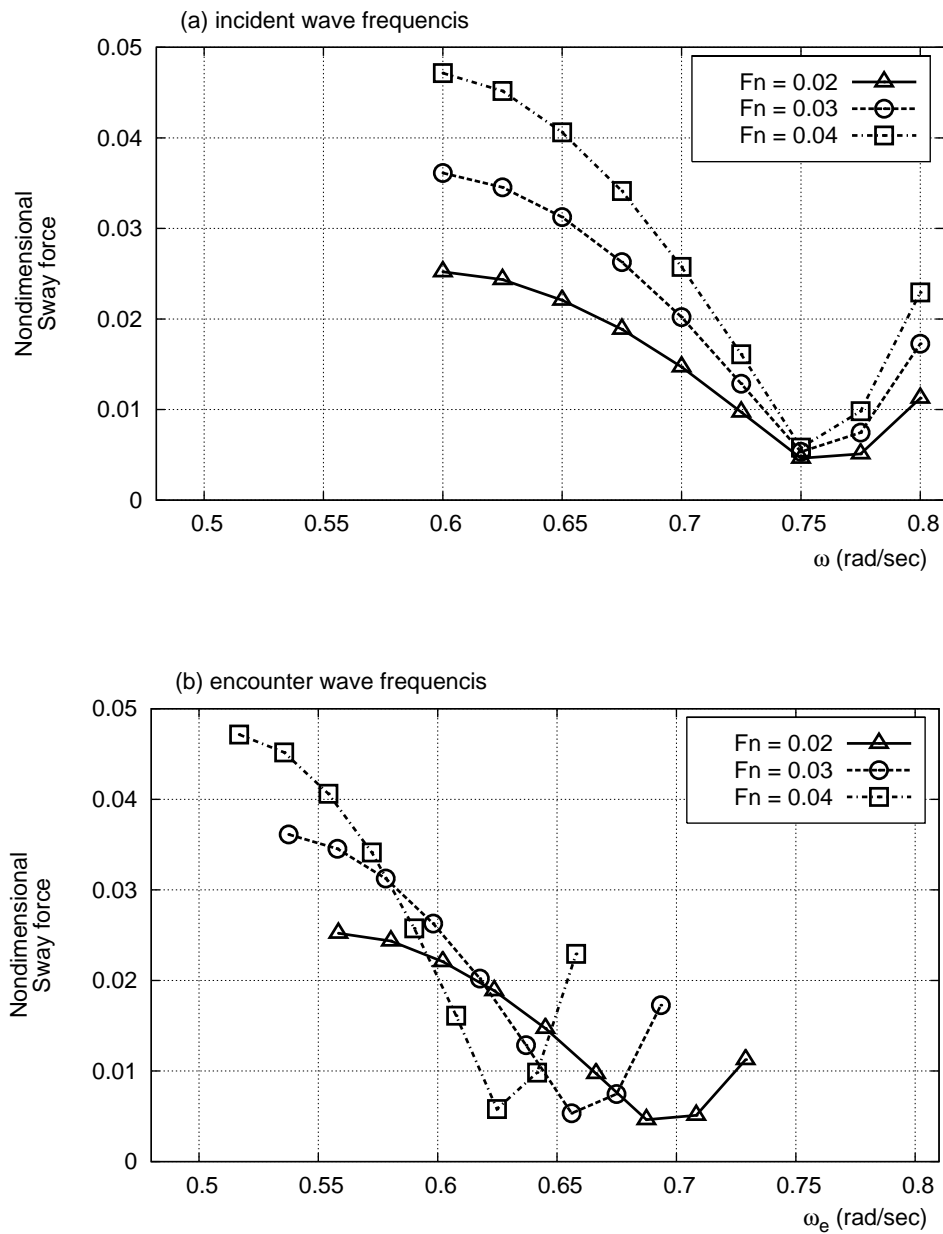


FIGURE F.14. Sway forces for diffracted waves in various frequencies with head sea (adverse current) effect. Wave and current heading angles are -30 and 150 degrees respectively.

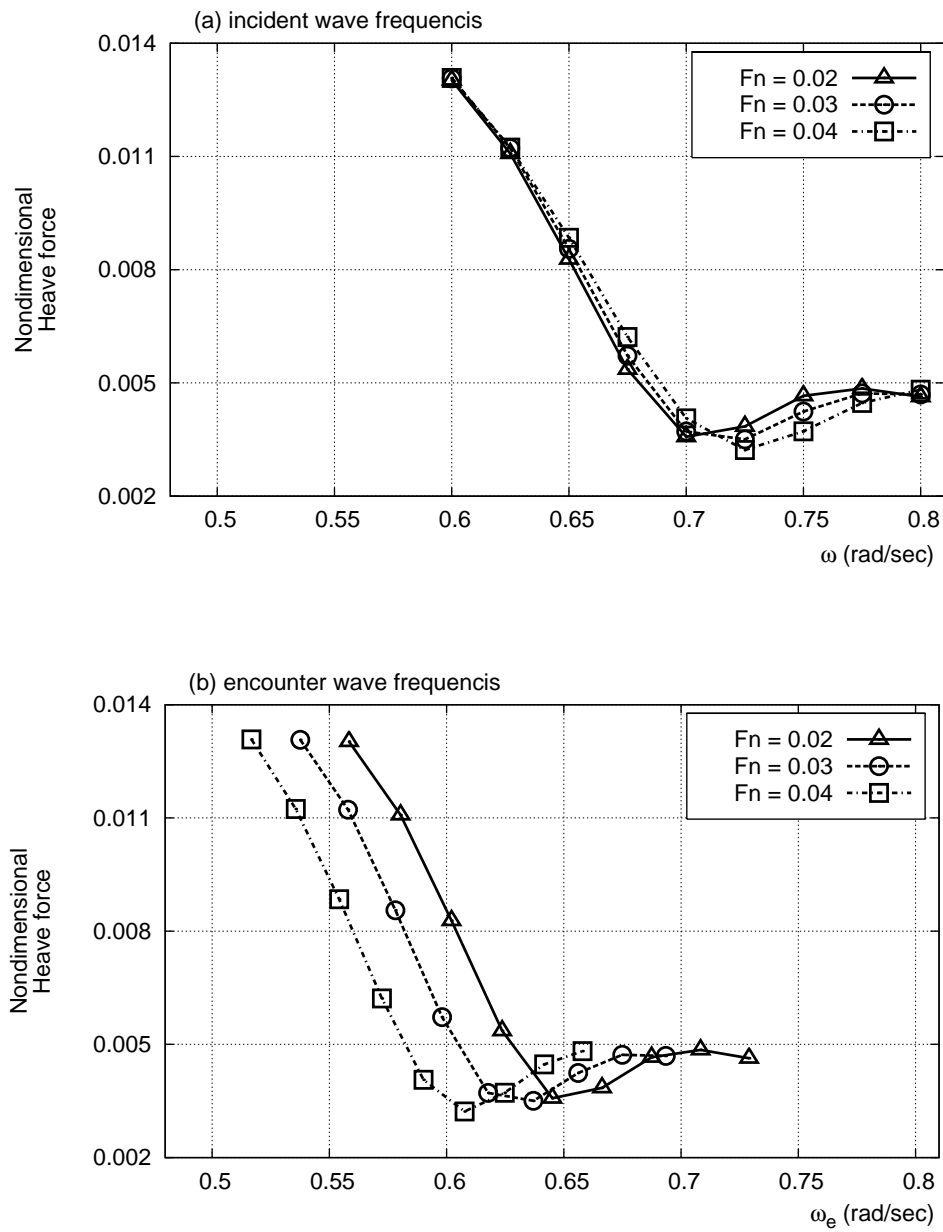


FIGURE F.15. Heave forces for diffracted waves in various frequencies with head sea (adverse current) effect. Wave and current heading angles are -30 and 150 degrees respectively.

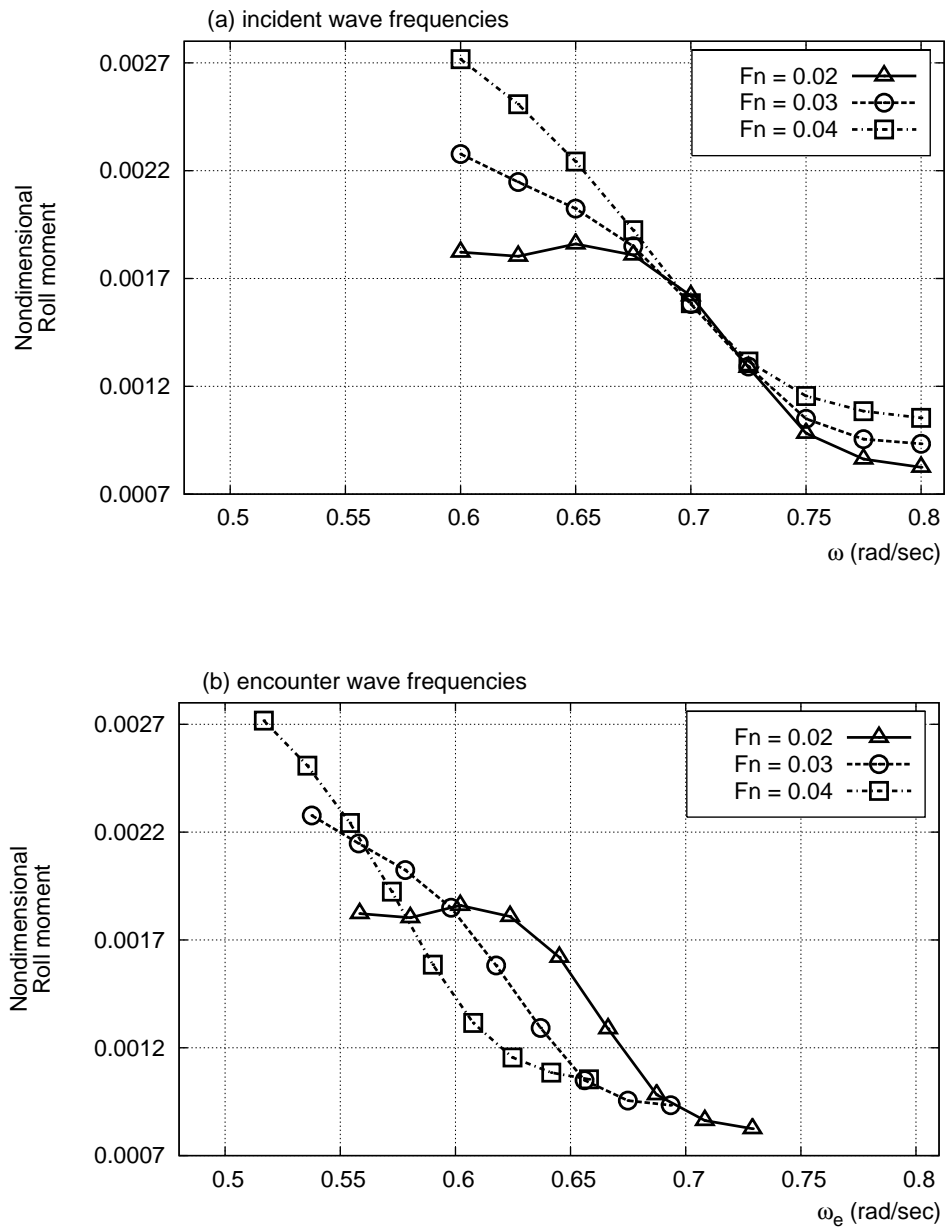


FIGURE F.16. Roll moments for diffracted waves in various frequencies with head sea (adverse current) effect. Wave and current heading angles are -30 and 150 degrees respectively.

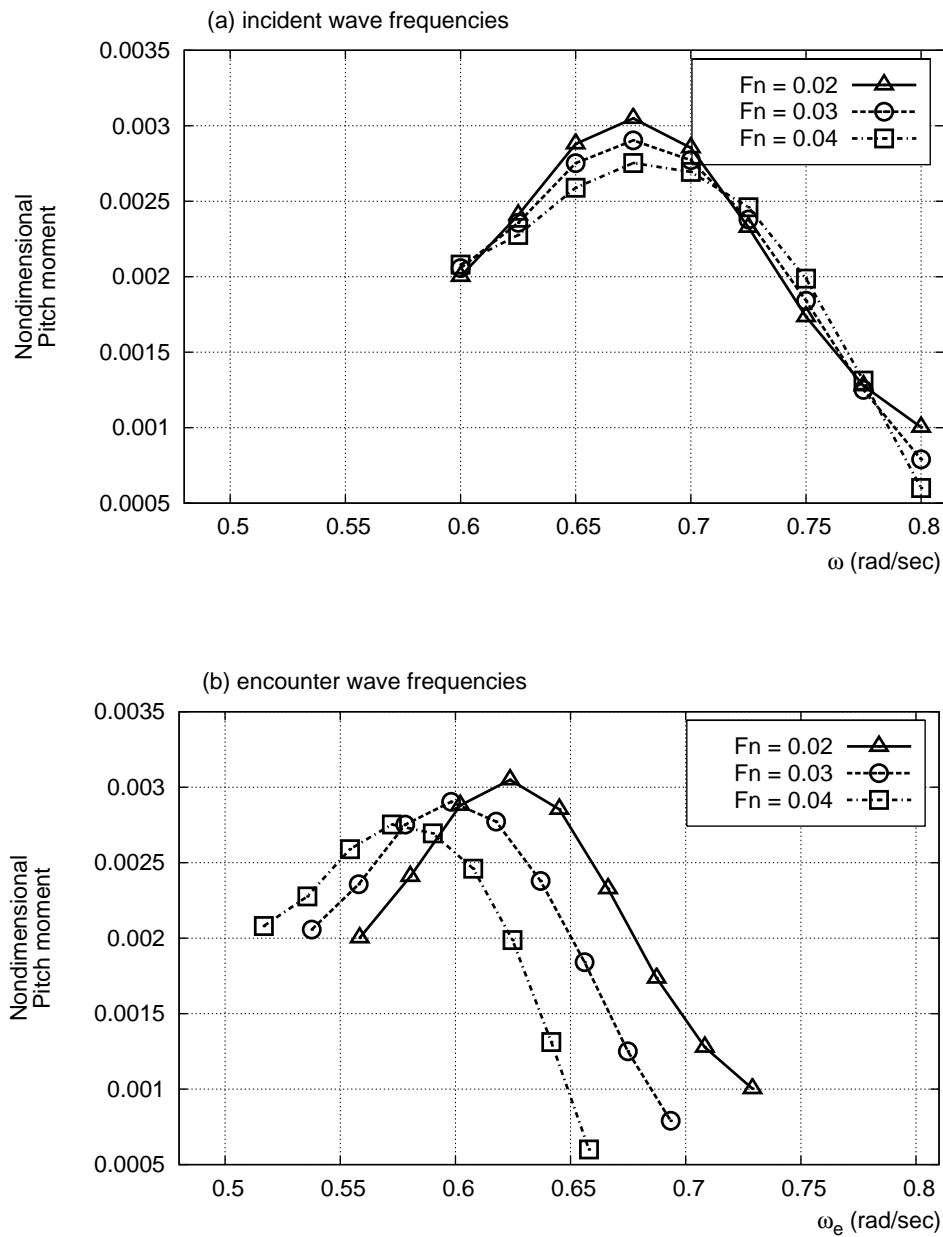


FIGURE F.17. Pitch moments for diffracted waves in various frequencies with head sea (adverse current) effect. Wave and current heading angles are -30 and 150 degrees respectively.

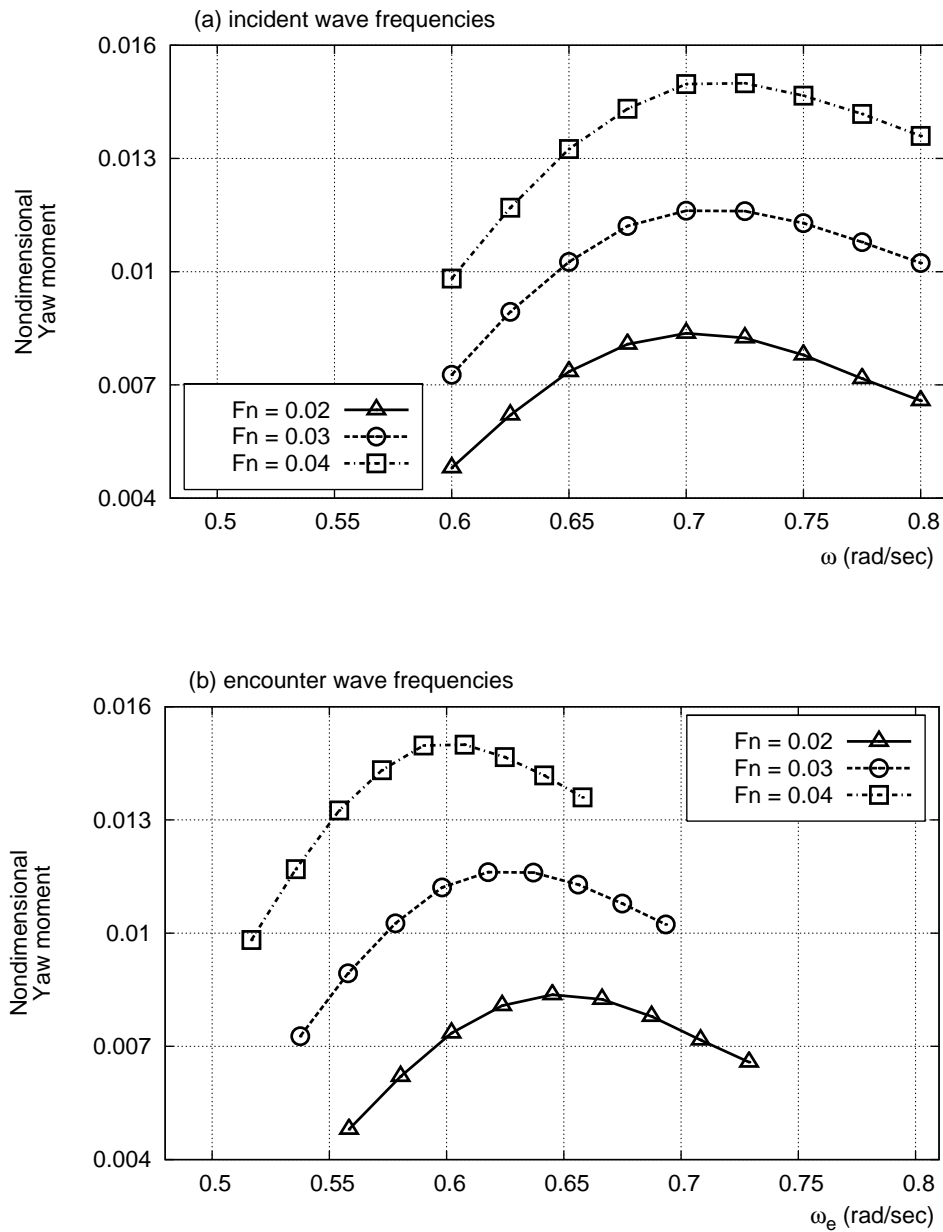


FIGURE F.18. Yaw moments for diffracted waves in various frequencies with head sea (adverse current) effect. Wave and current heading angles are -30 and 150 degrees respectively.

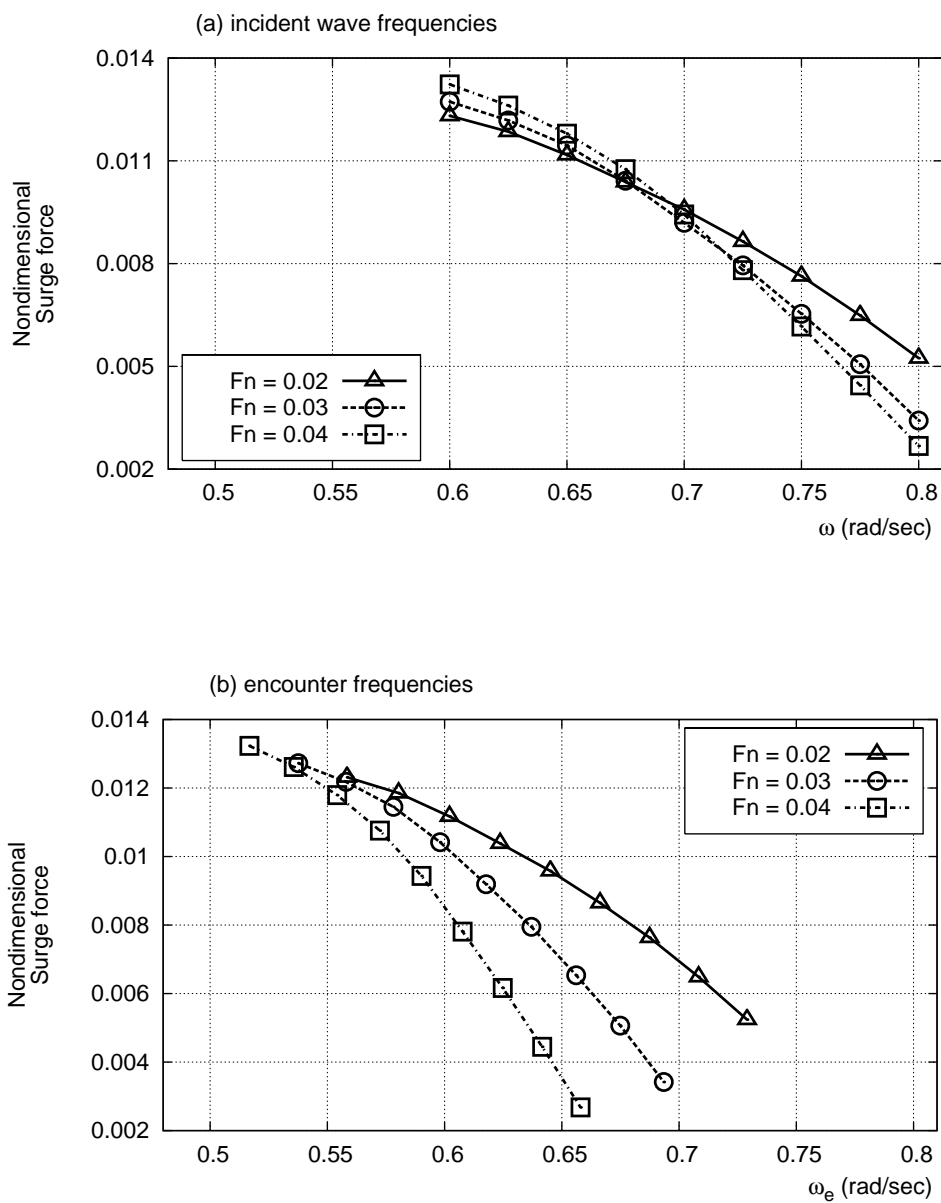


FIGURE F.19. Surge forces for diffracted waves in various frequencies with head sea (adverse current) effect. Wave and current heading angles are zero and 175 degrees respectively.

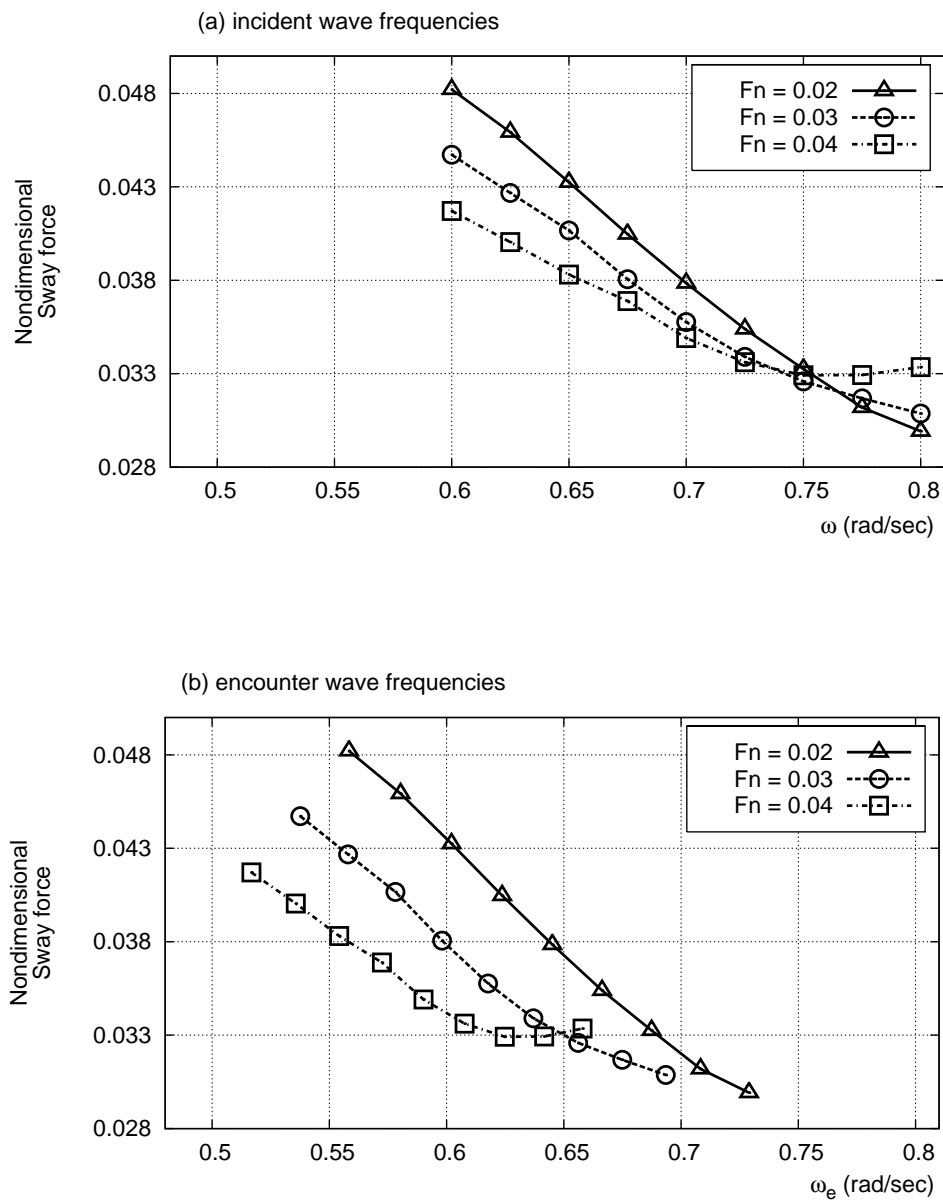


FIGURE F.20. Sway forces for diffracted waves in various frequencies with head sea (adverse current) effect. Wave and current heading angles are zero and 175 degrees respectively.

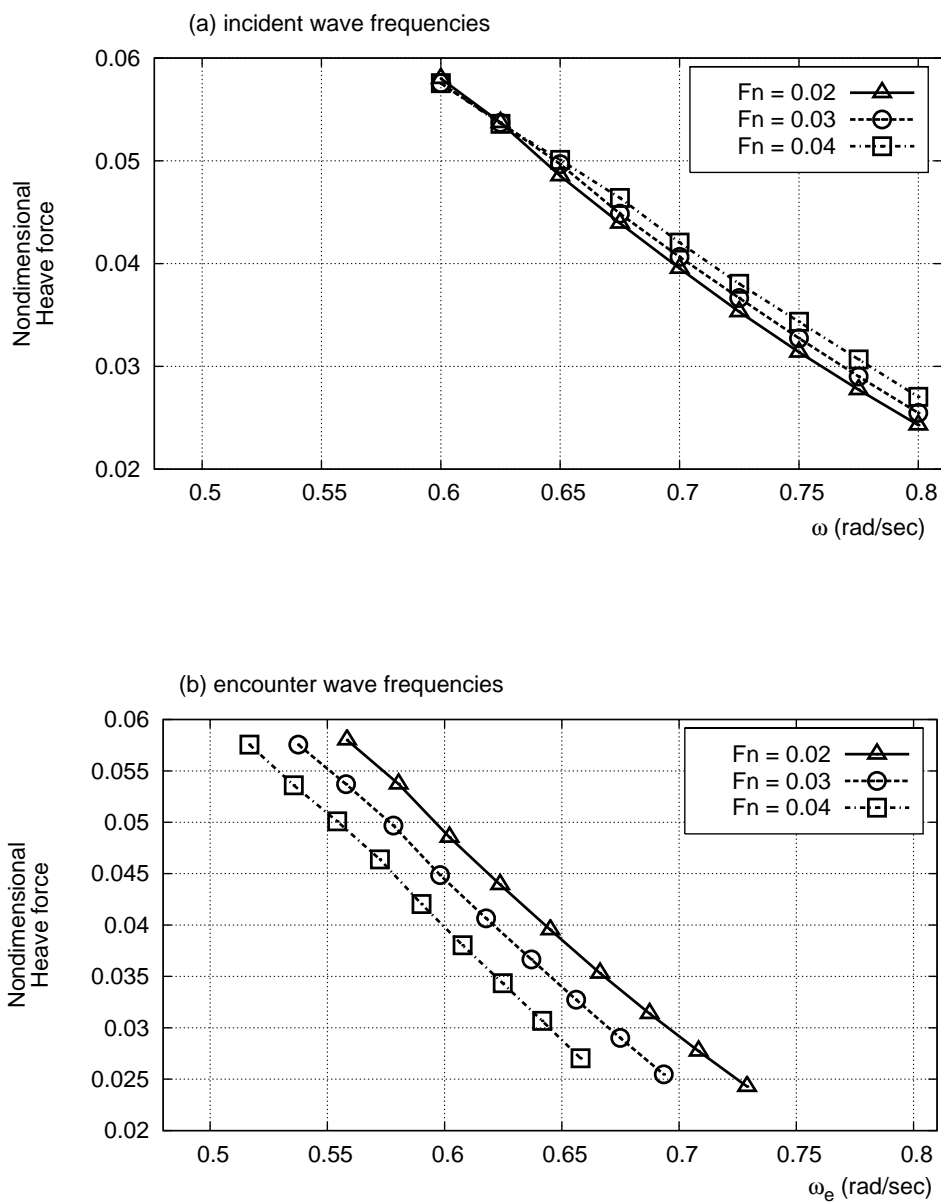


FIGURE F.21. Heave forces for diffracted waves in various frequencies with head sea (adverse current) effect. Wave and current heading angles are zero and 175 degrees respectively.

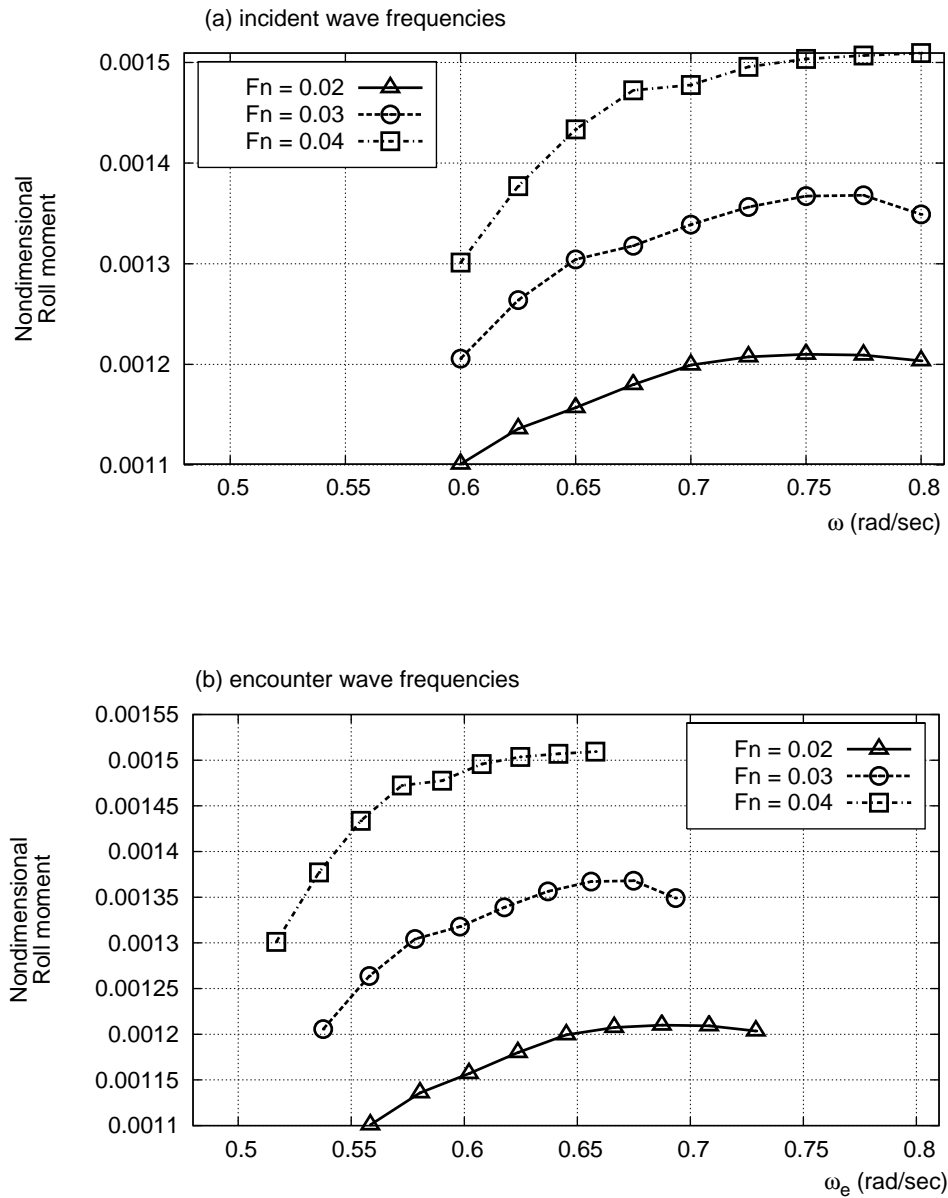


FIGURE F.22. Roll moments for diffracted waves in various frequencies with head sea (adverse current) effect. Wave and current heading angles are zero and 175 degrees respectively.

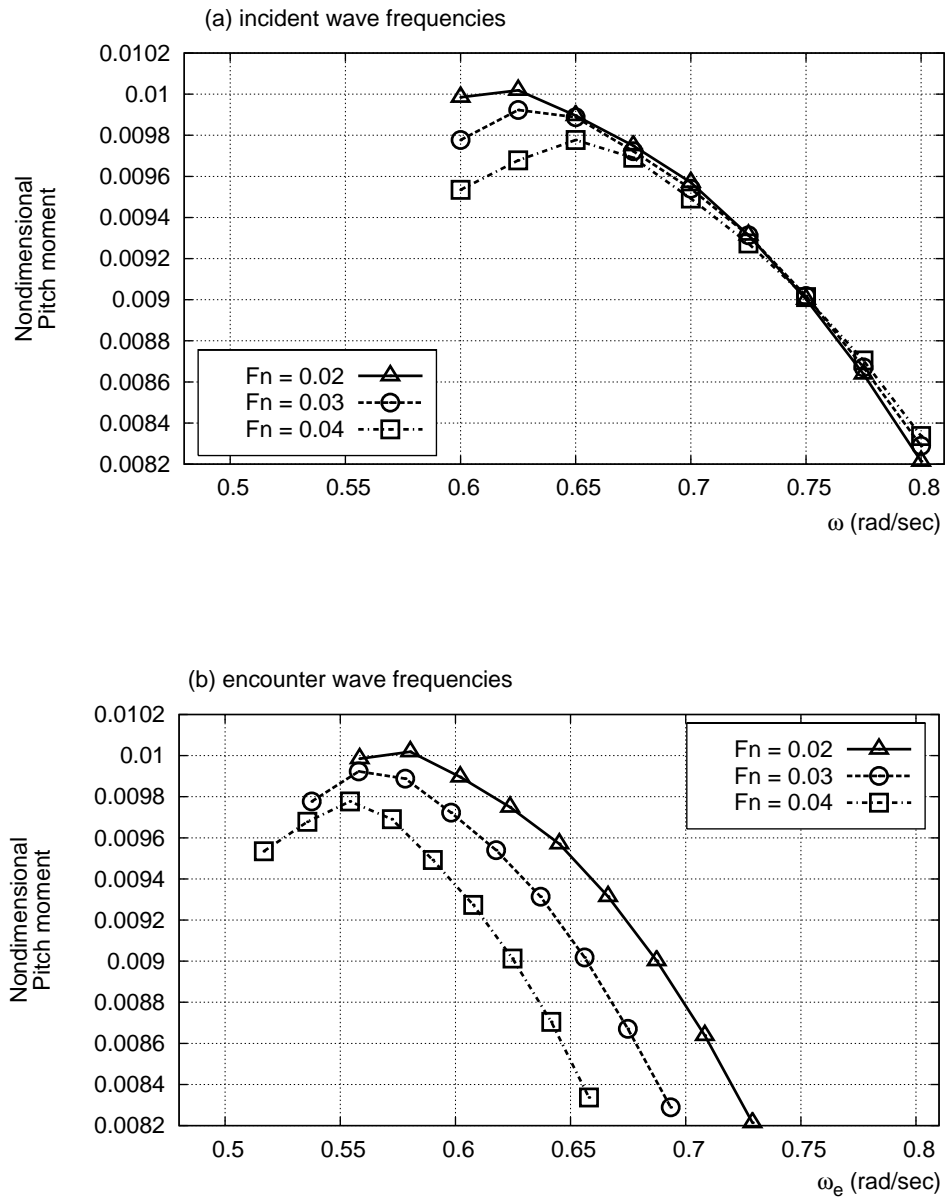


FIGURE F.23. Pitch moments for diffracted waves in various frequencies with head sea (adverse current) effect. Wave and current heading angles are zero and 175 degrees respectively.

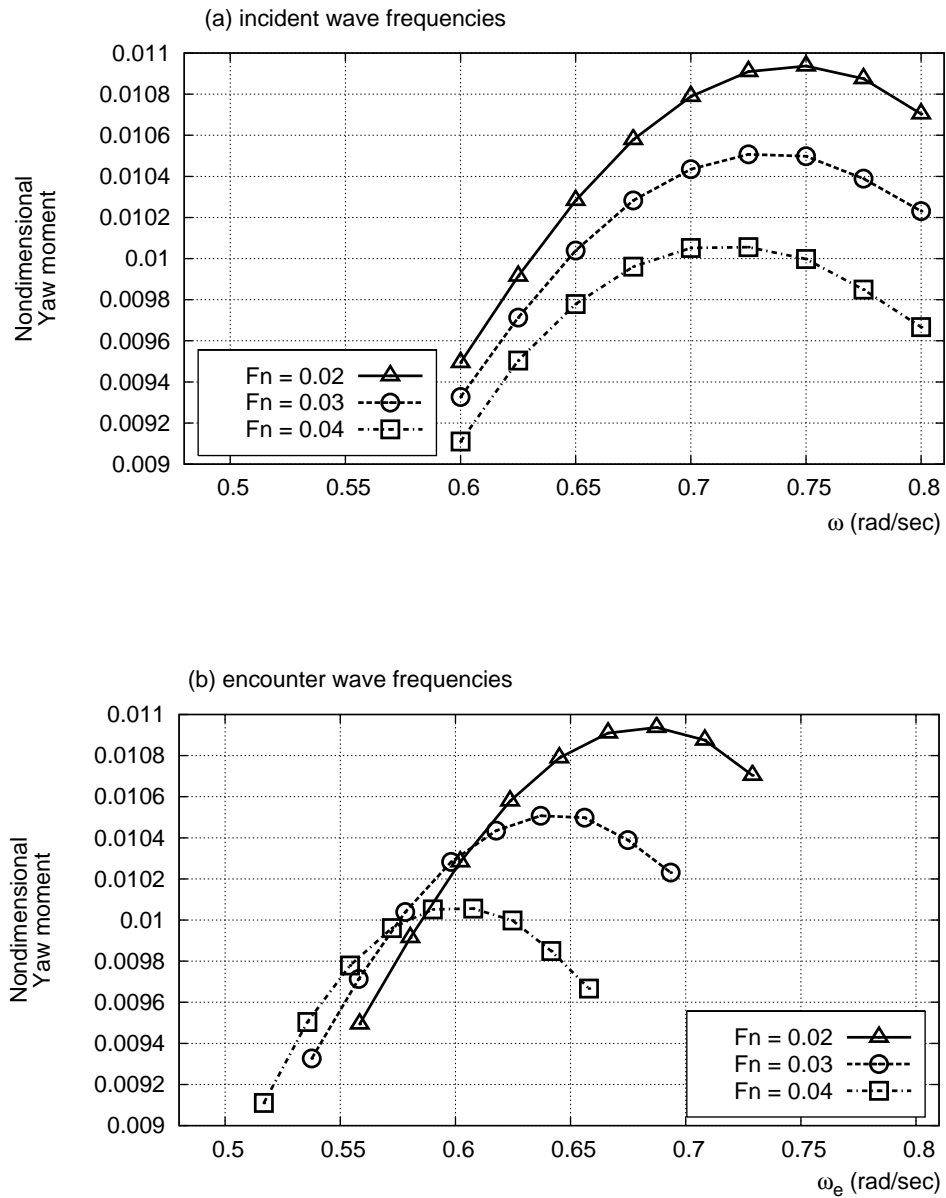


FIGURE F.24. Yaw moments for diffracted waves in various frequencies with head sea (adverse current) effect. Wave and current heading angles are zero and 175 degrees respectively.

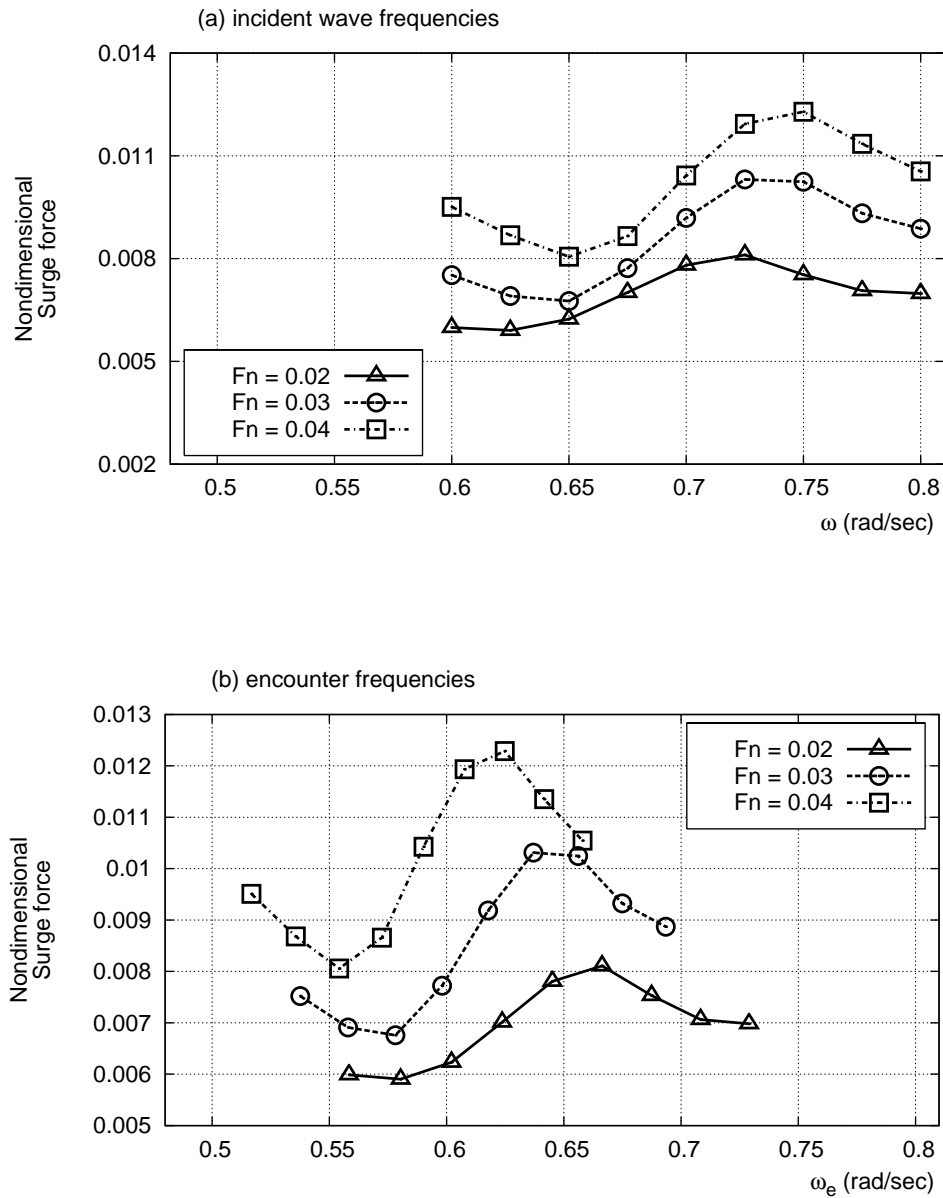


FIGURE F.25. Surge forces for diffracted waves in various frequencies with head sea (adverse current) effect. Wave and current heading angles are zero and 170 degrees respectively.

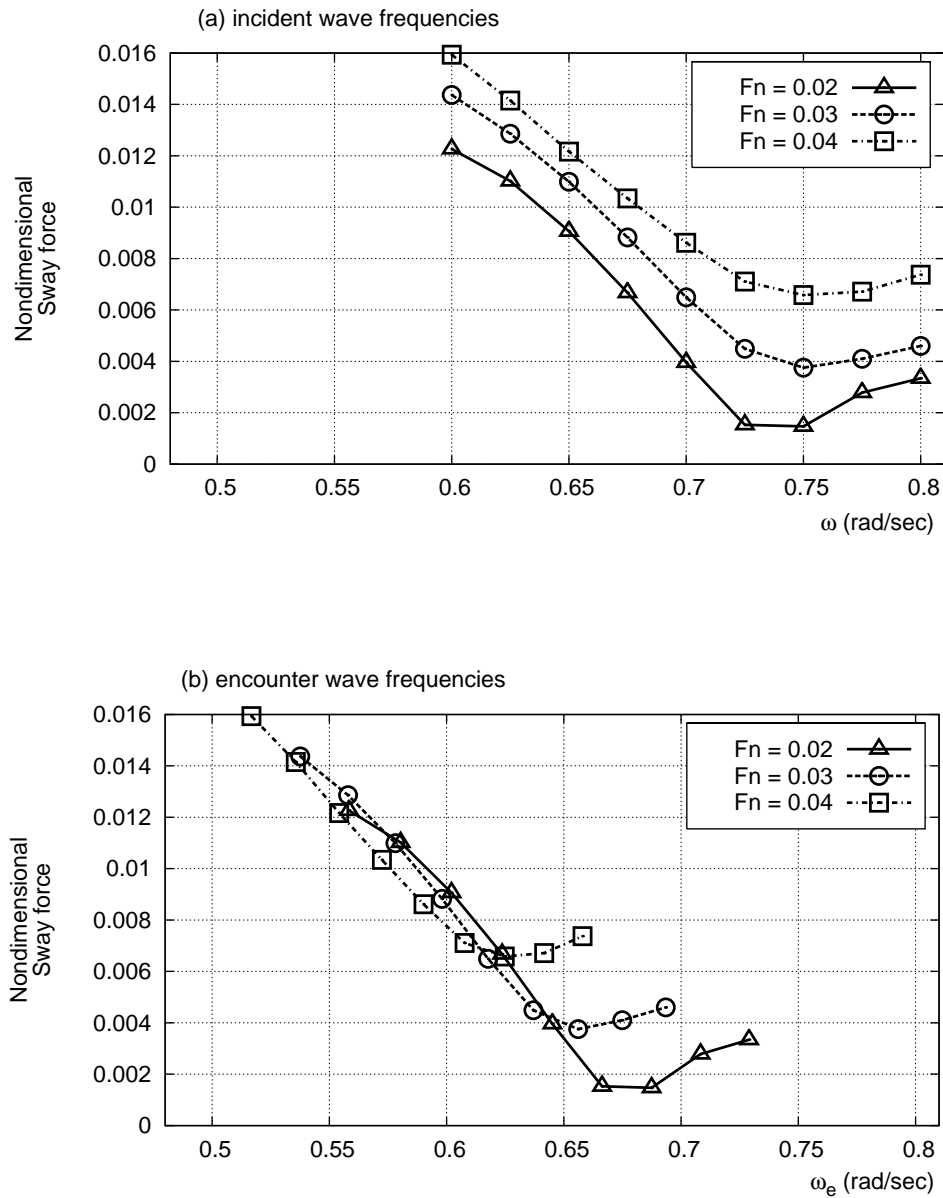


FIGURE F.26. Sway forces for diffracted waves in various frequencies with head sea (adverse current) effect. Wave and current heading angles are zero and 170 degrees respectively.

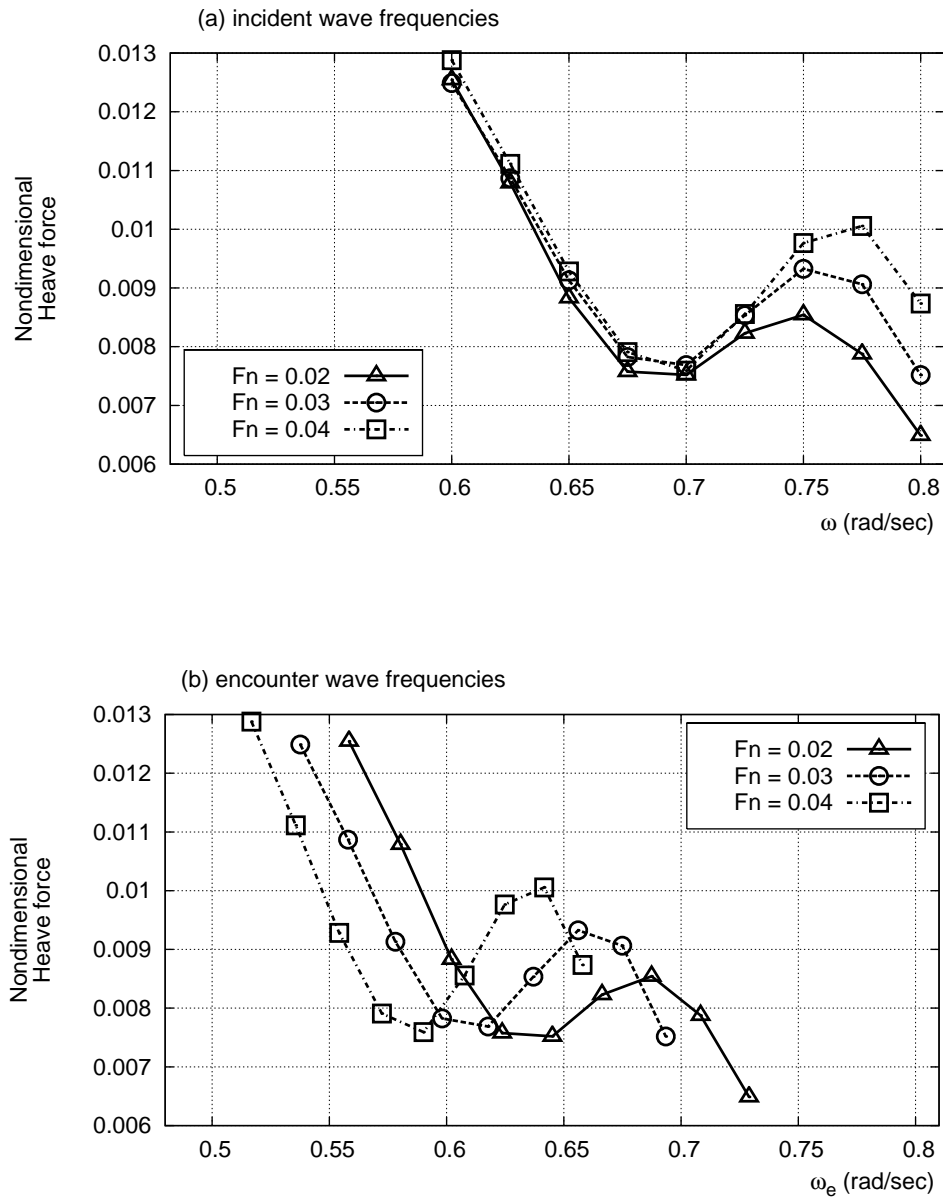


FIGURE F.27. Heave forces for diffracted waves in various frequencies with head sea (adverse current) effect. Wave and current heading angles are zero and 170 degrees respectively.

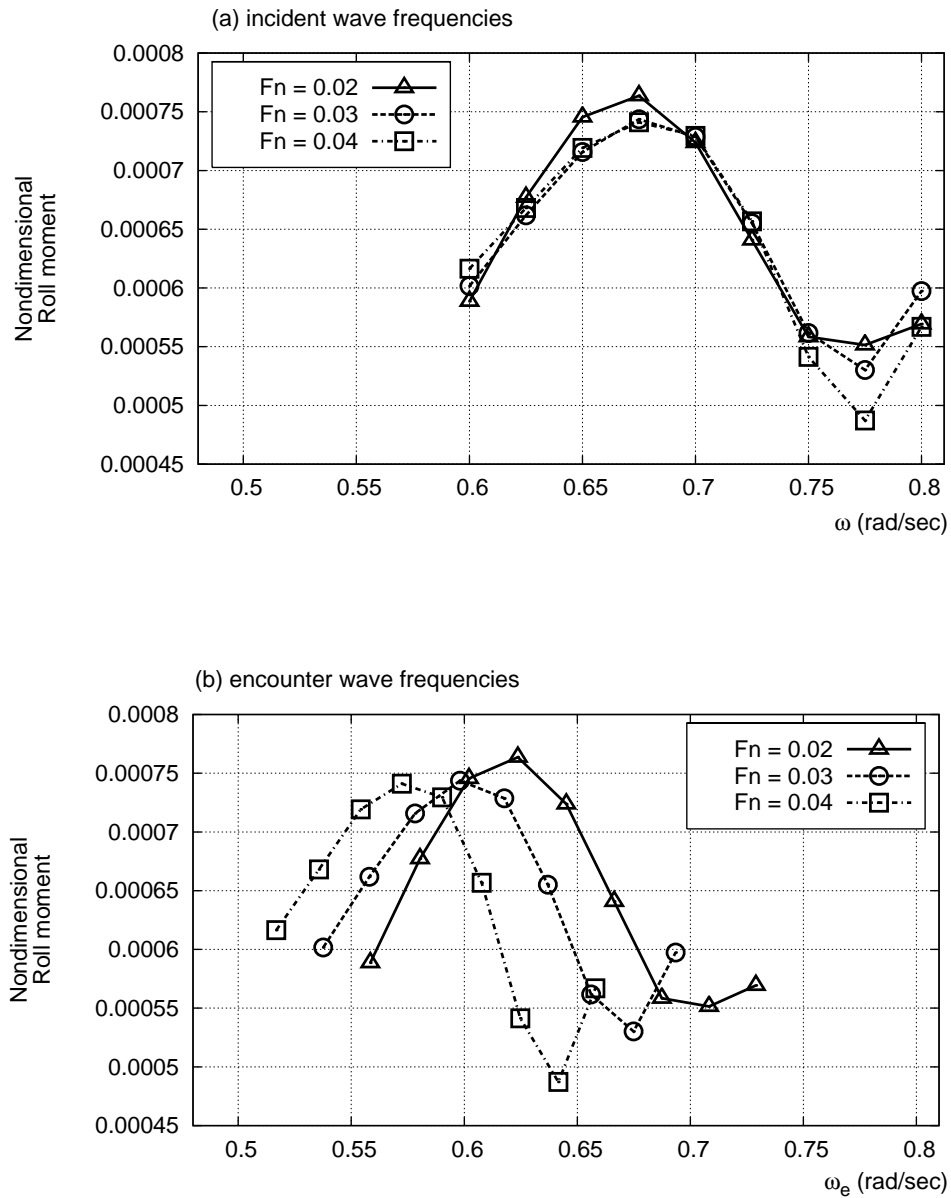


FIGURE F.28. Roll moments for diffracted waves in various frequencies with head sea (adverse current) effect. Wave and current heading angles are zero and 170 degrees respectively.

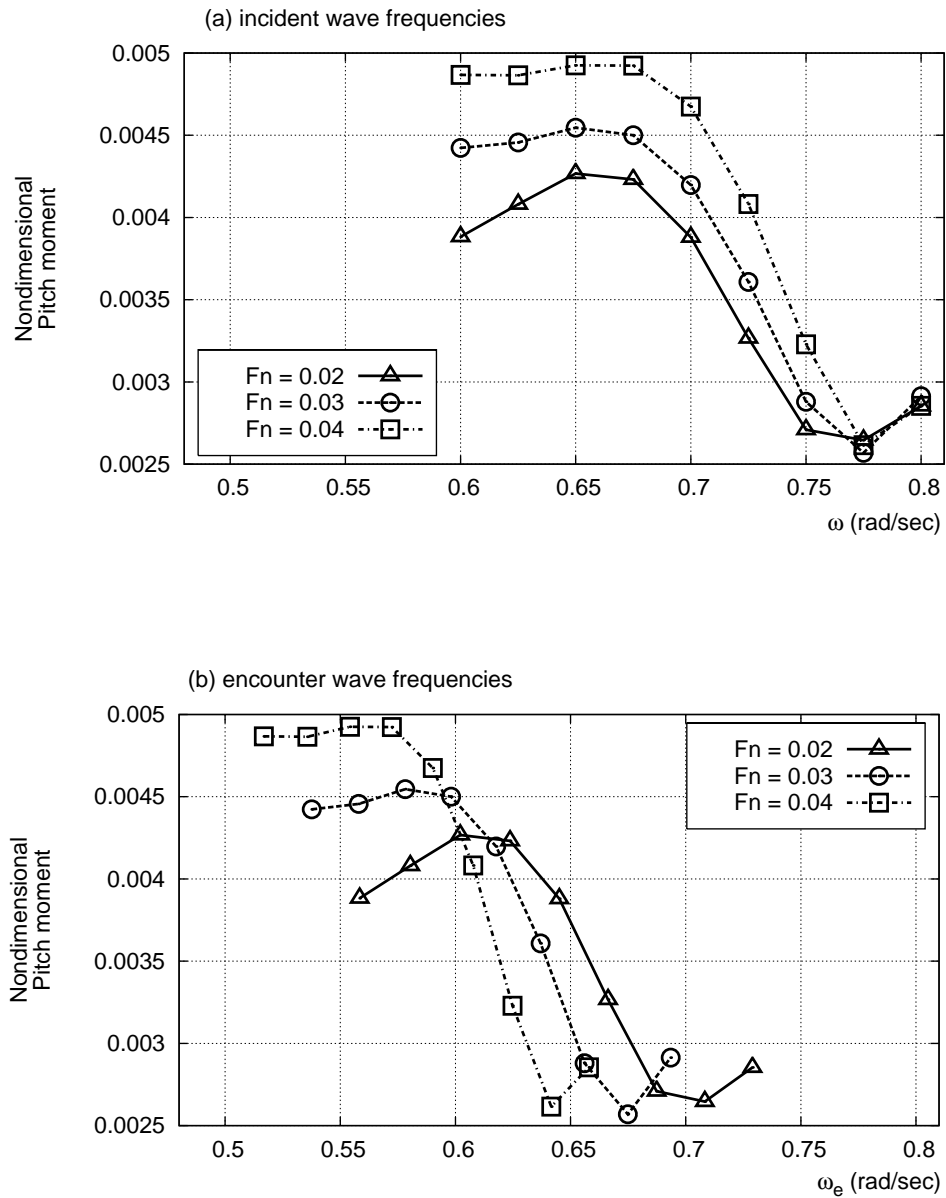


FIGURE F.29. Pitch moments for diffracted waves in various frequencies with head sea (adverse current) effect. Wave and current heading angles are zero and 170 degrees respectively.

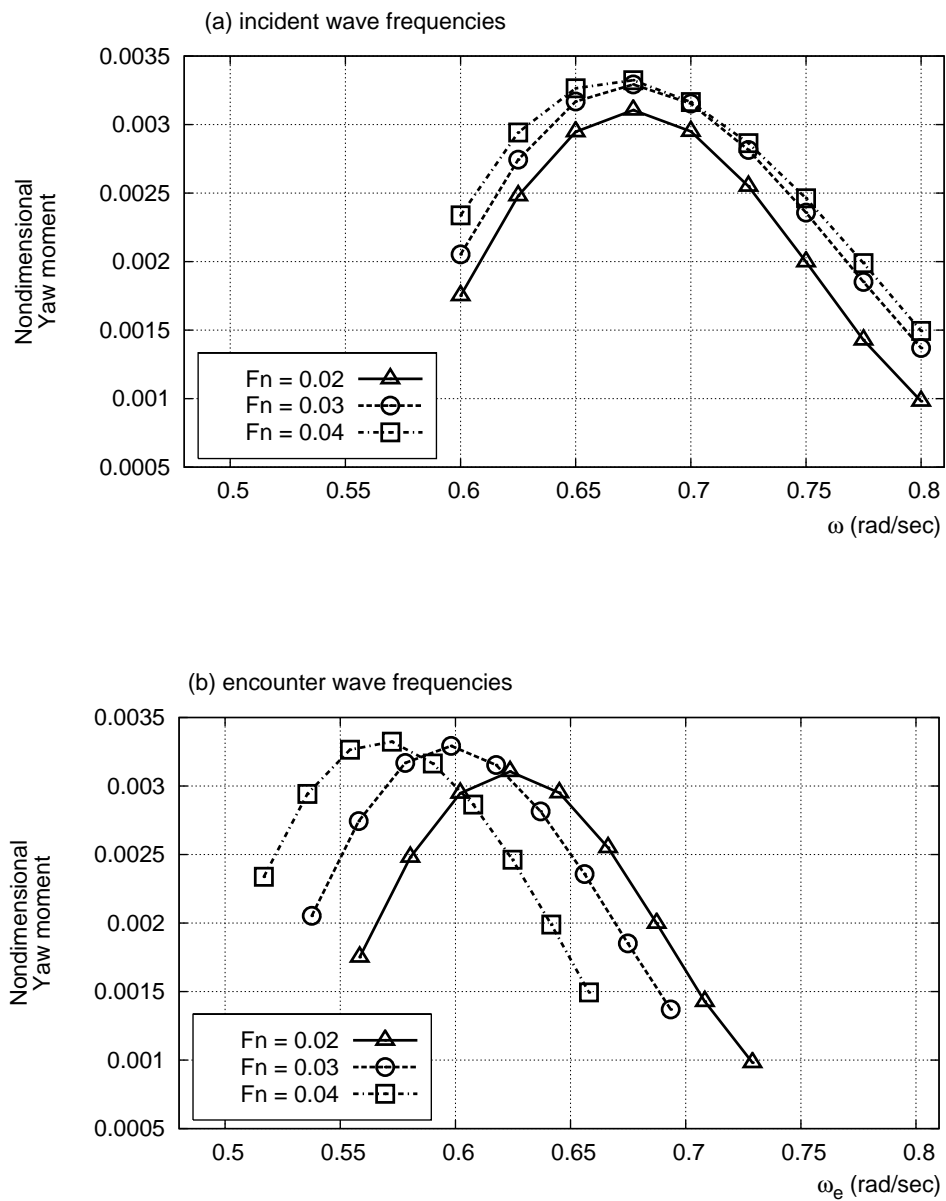


FIGURE F.30. Yaw moments for diffracted waves in various frequencies with head sea (adverse current) effect. Wave and current heading angles are zero and 170 degrees respectively.

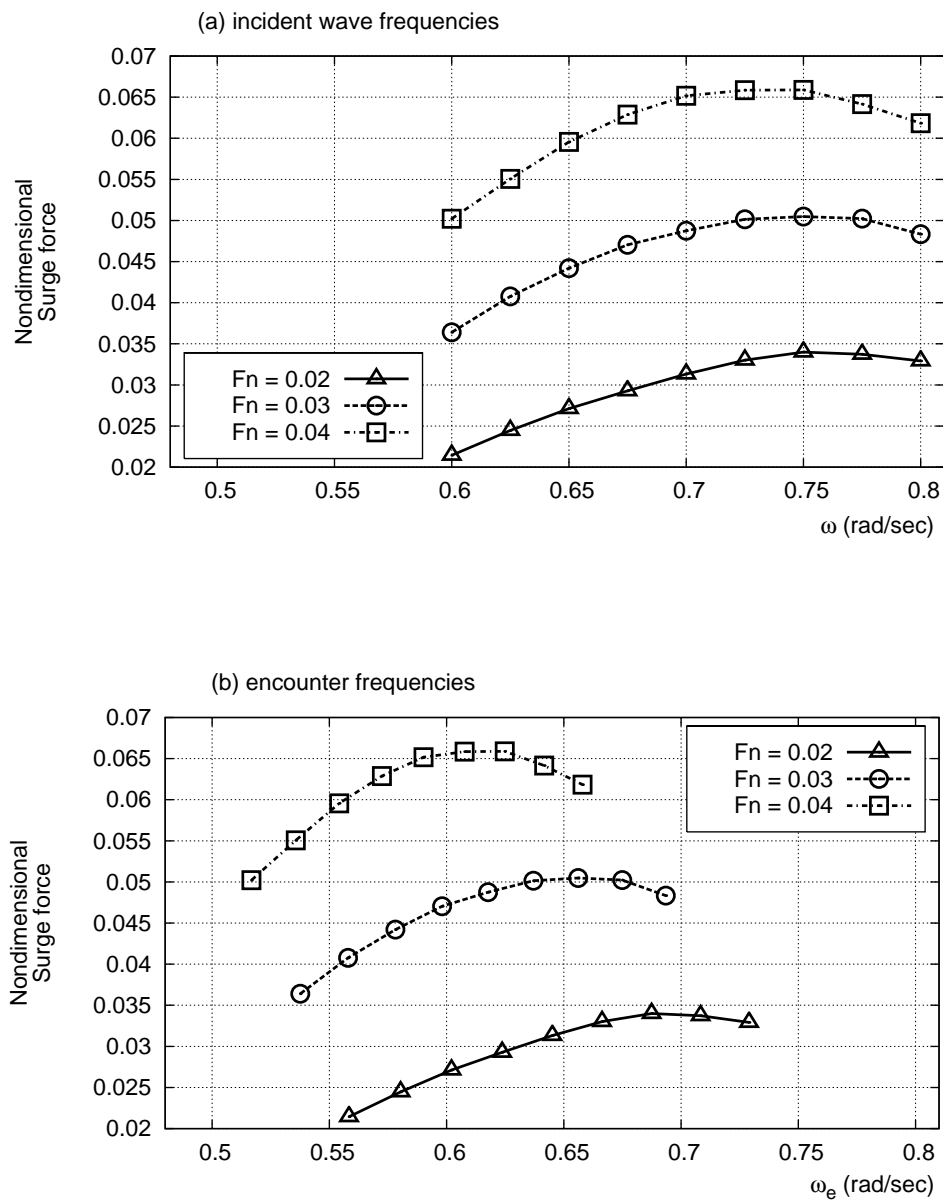


FIGURE F.31. Surge forces for diffracted waves in various frequencies with head sea (adverse current) effect. Wave and current heading angles are zero and 150 degrees respectively.

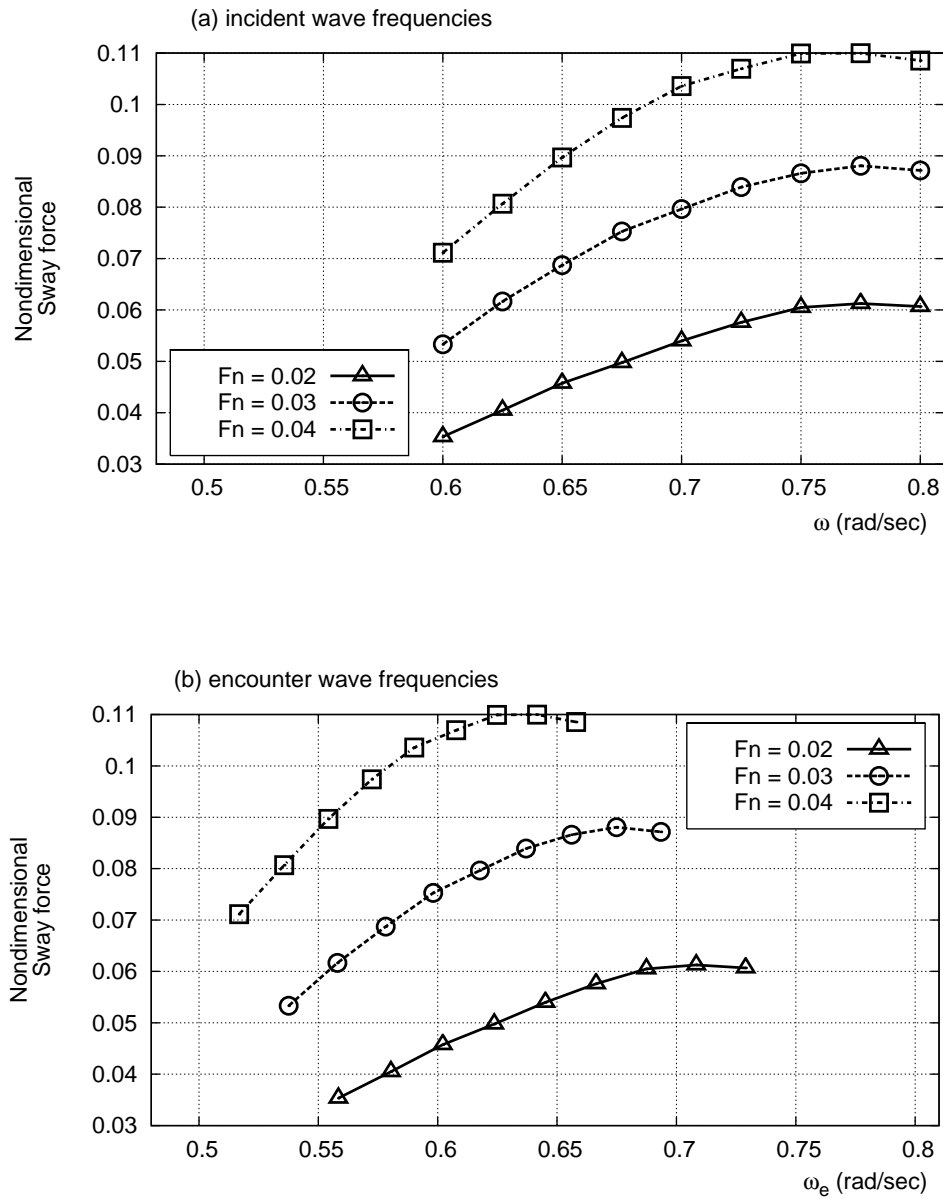


FIGURE F.32. Sway forces for diffracted waves in various frequencies with head sea (adverse current) effect. Wave and current heading angles are zero and 150 degrees respectively.

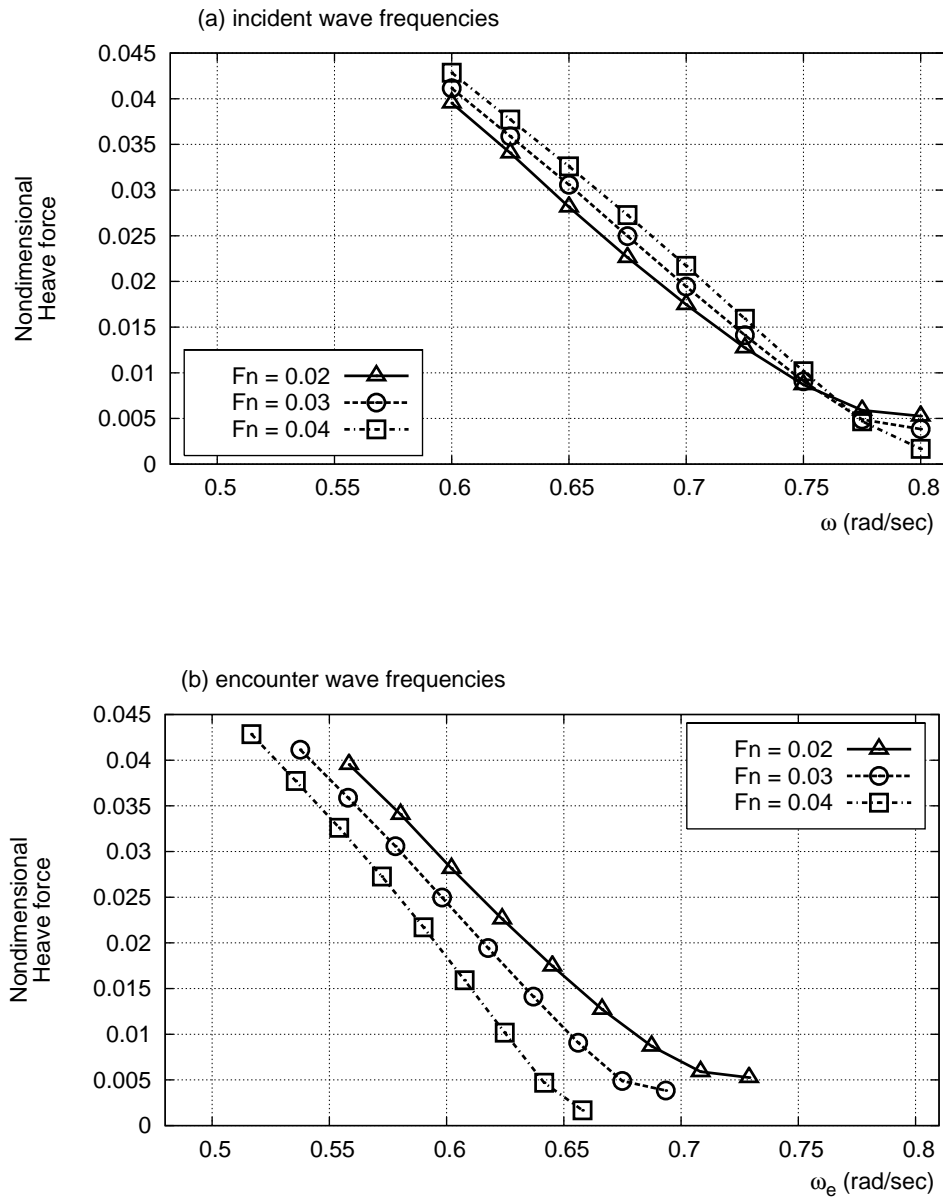


FIGURE F.33. Heave forces for diffracted waves in various frequencies with head sea (adverse current) effect. Wave and current heading angles are zero and 150 degrees respectively.

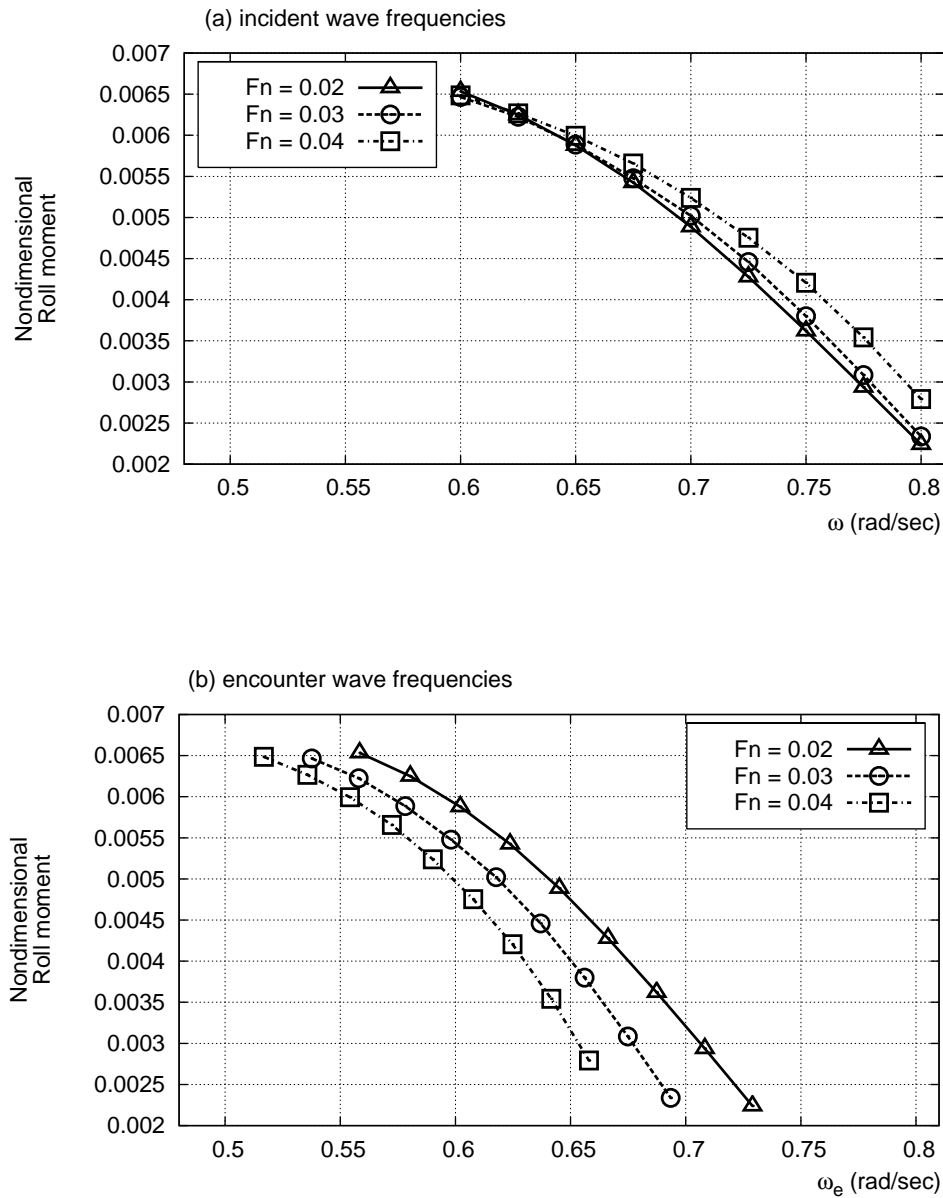


FIGURE F.34. Roll moments for diffracted waves in various frequencies with head sea (adverse current) effect. Wave and current heading angles are zero and 150 degrees respectively.

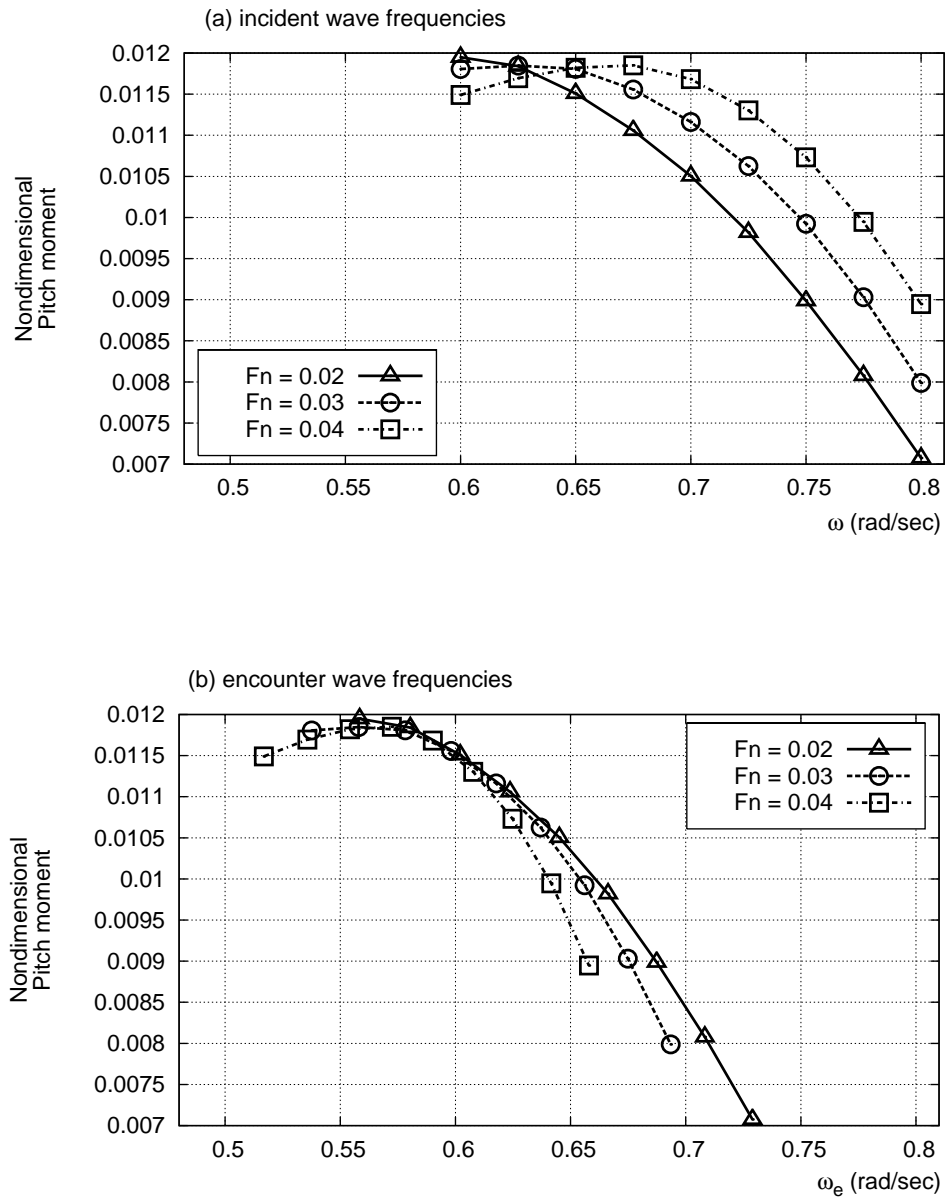


FIGURE F.35. Pitch moments for diffracted waves in various frequencies with head sea (adverse current) effect. Wave and current heading angles are zero and 150 degrees respectively.

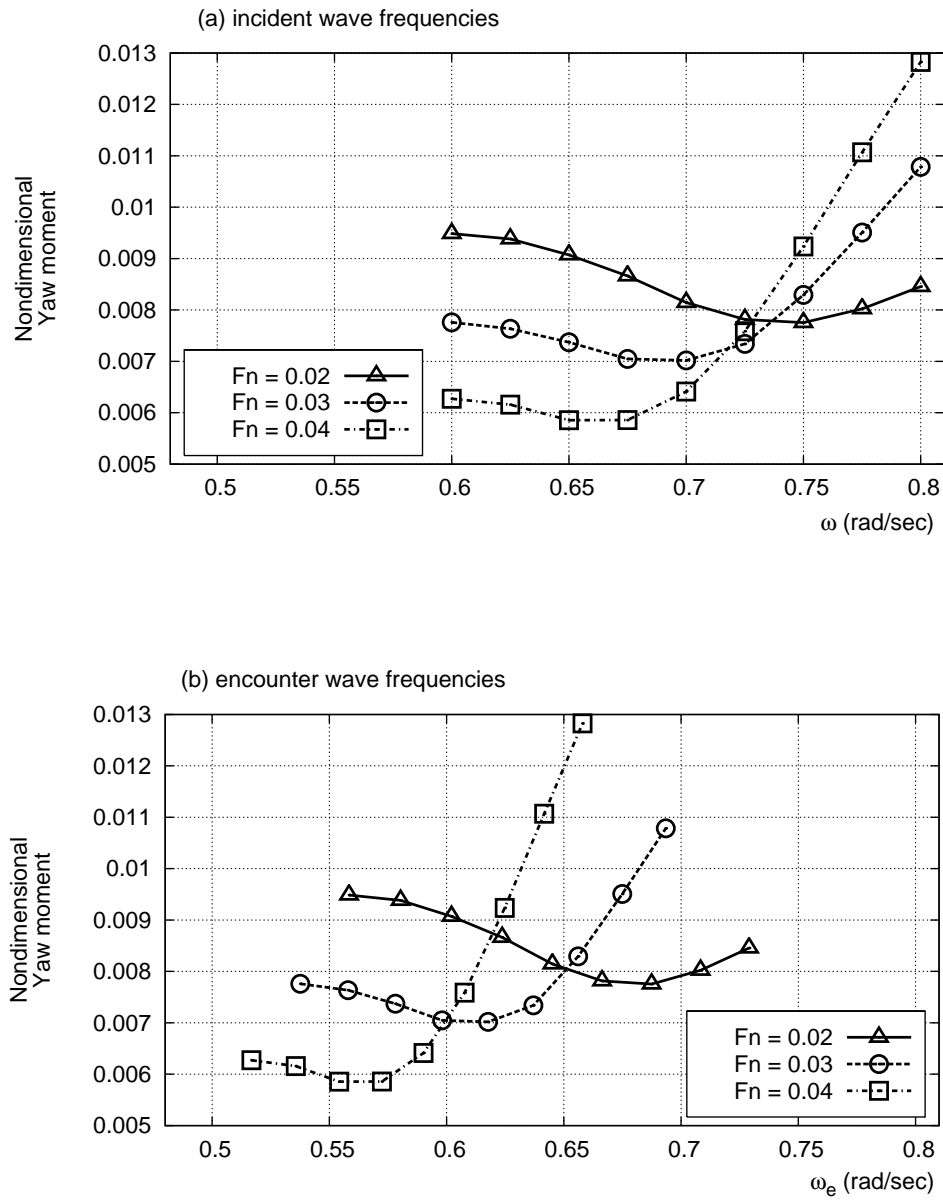


FIGURE F.36. Yaw moments for diffracted waves in various frequencies with head sea (adverse current) effect. Wave and current heading angles are zero and 150 degrees respectively.

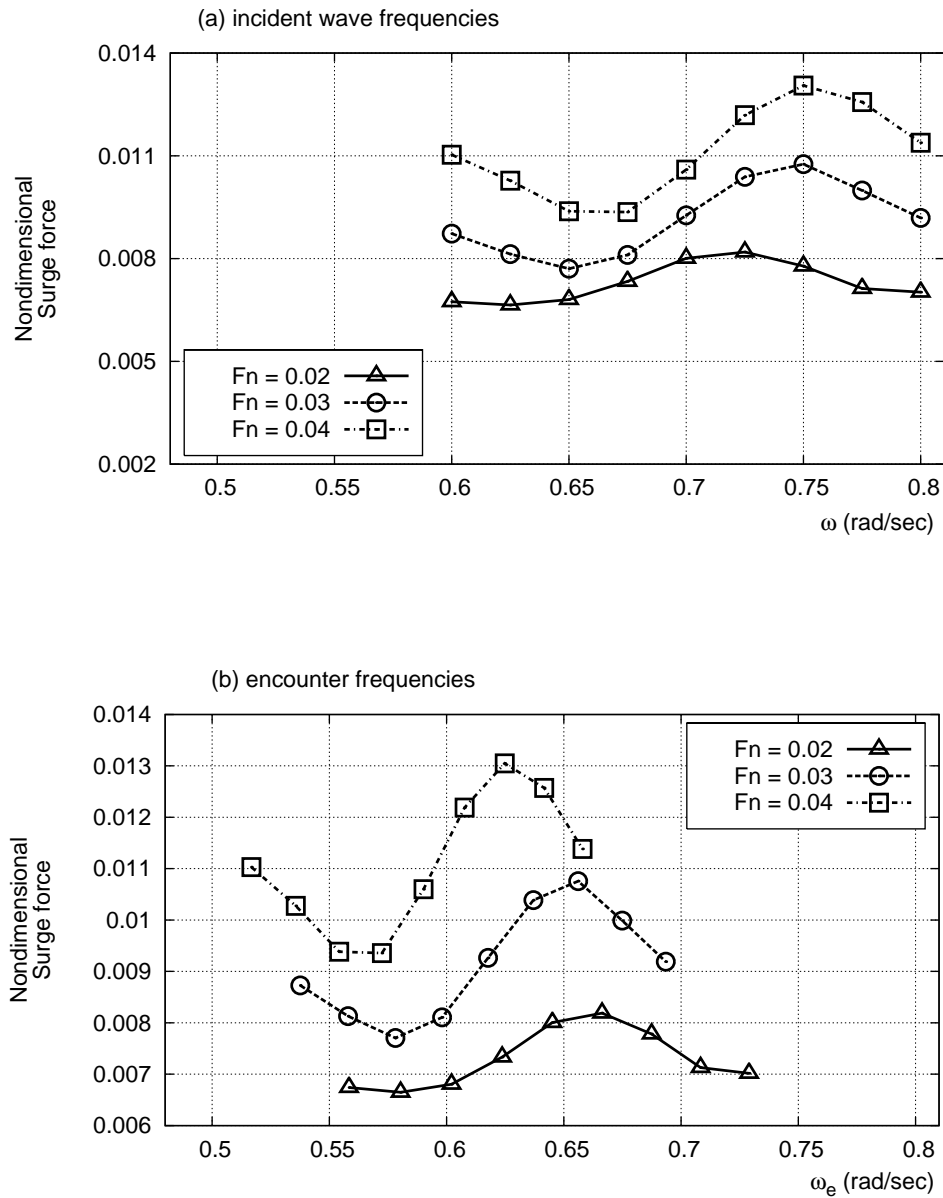


FIGURE F.37. Surge forces for diffracted waves in various frequencies with head sea (adverse current) effect. Waves heading angles and current heading angles are 5 and 175 degrees respectively.

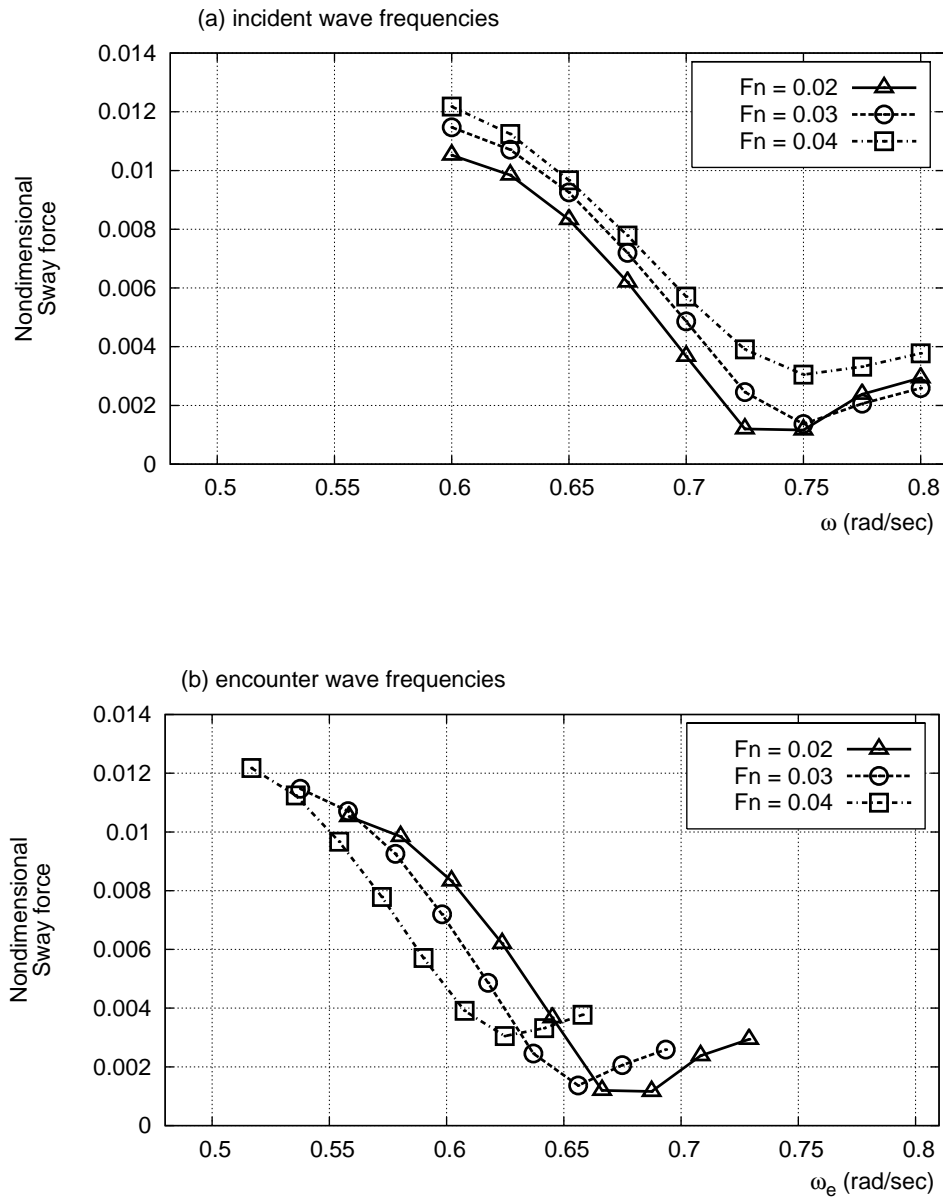


FIGURE F.38. Sway forces for diffracted waves in various frequencies with head sea (adverse current) effect. Wave and current heading angles are 5 and 175 degrees respectively.

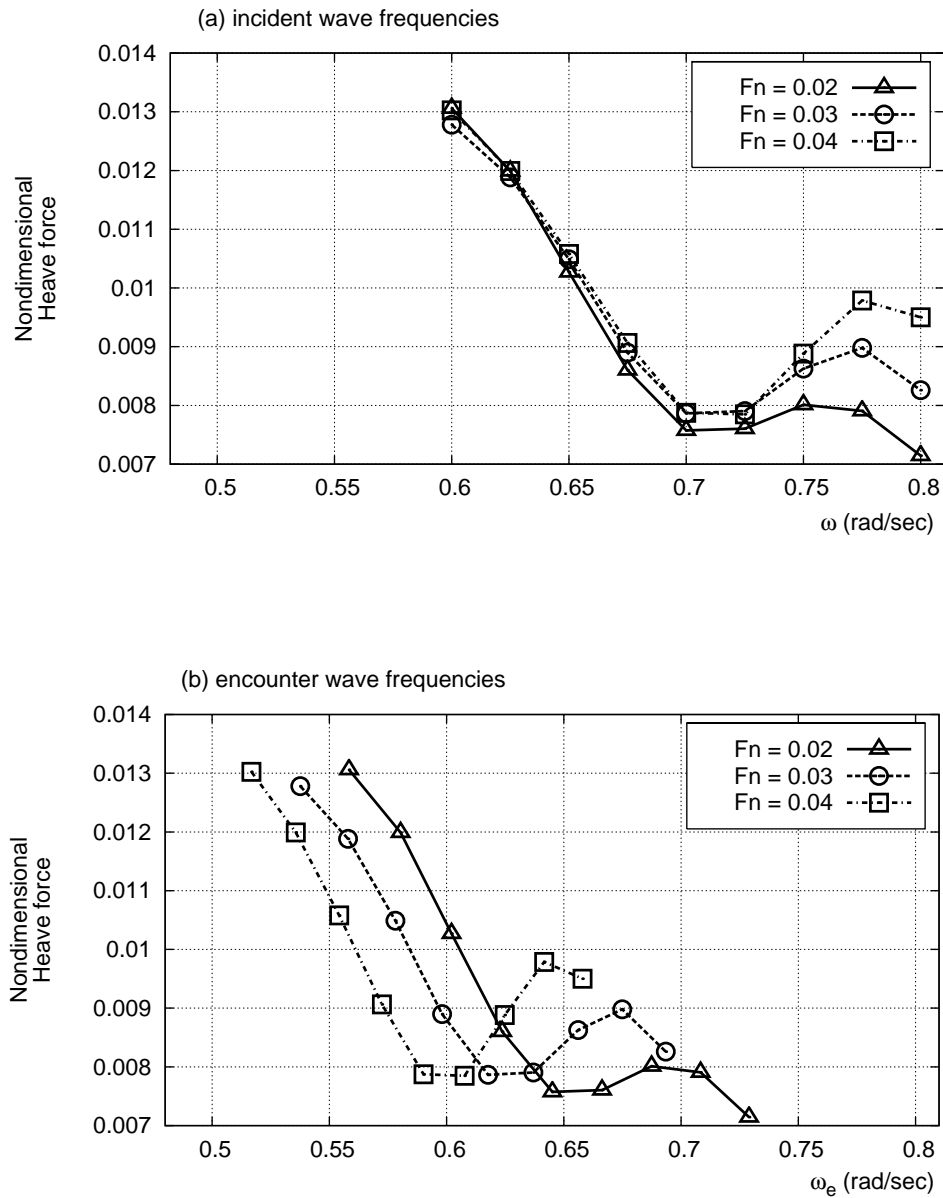


FIGURE F.39. Heave forces for diffracted waves in various frequencies with head sea (adverse current) effect. Wave and current heading angles are 5 and 175 degrees respectively.

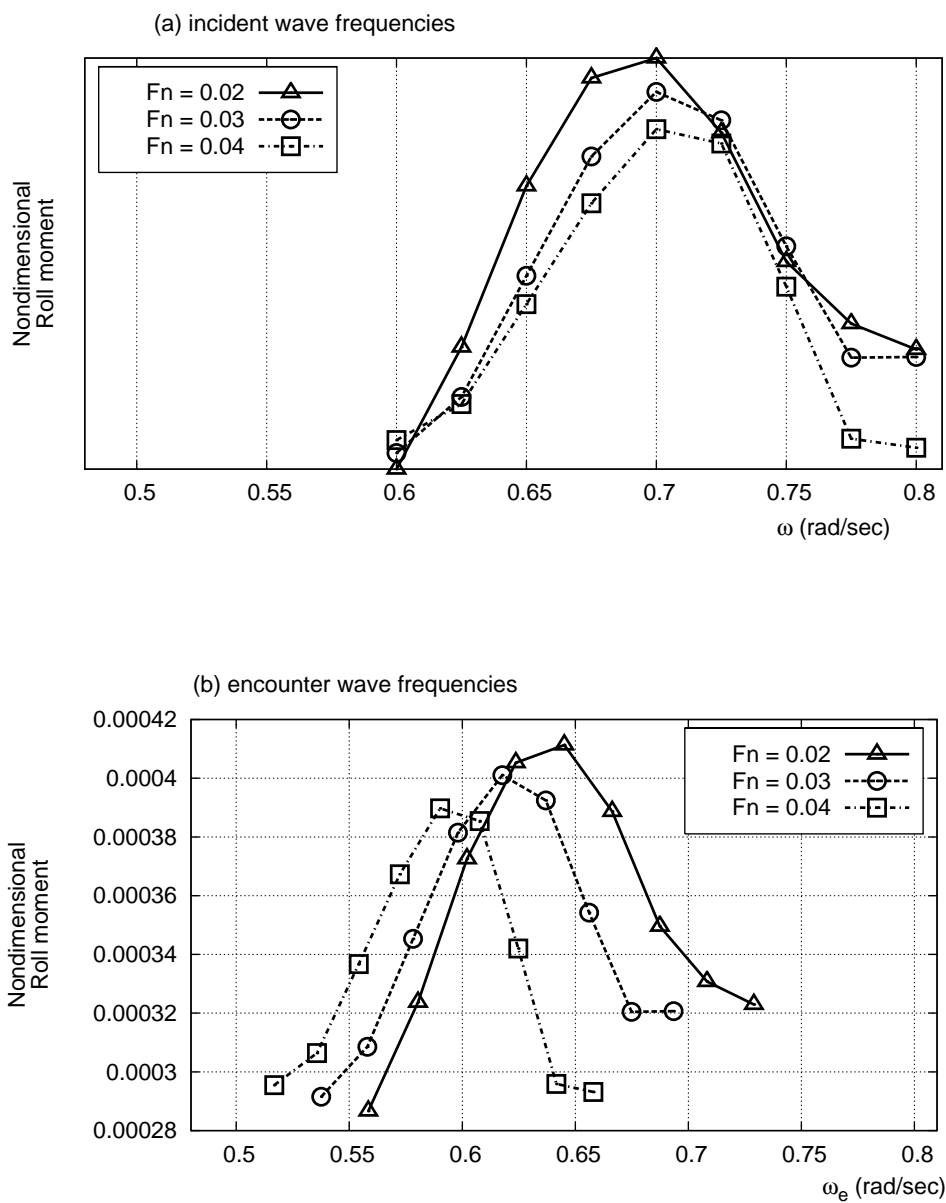


FIGURE F.40. Roll moments for diffracted waves in various frequencies with head sea (adverse current) effect. Wave and current heading angles are 5 and 175 degrees respectively.

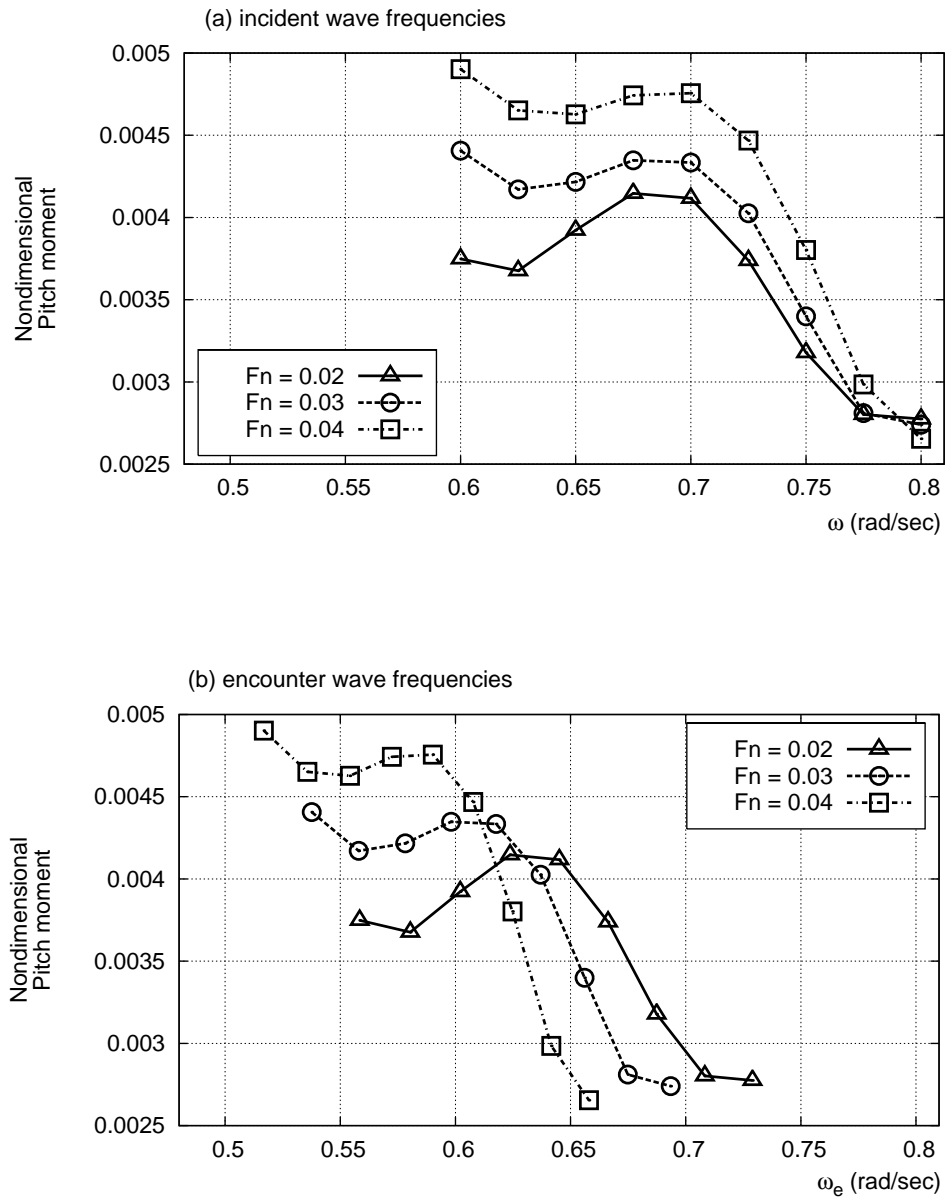


FIGURE F.41. Pitch moments for diffracted waves in various frequencies with head sea (adverse current) effect. Wave and current heading angles are 5 and 175 degrees respectively.

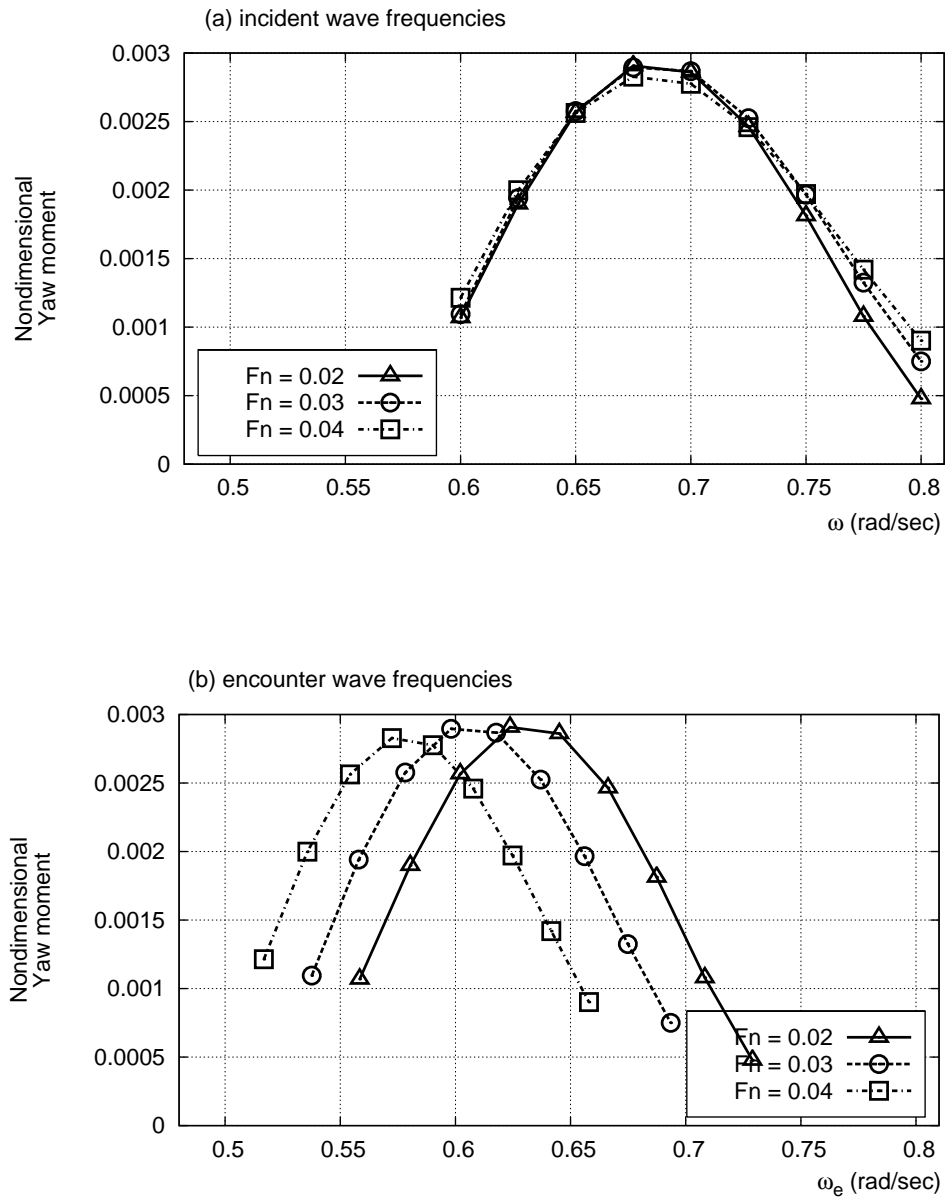


FIGURE F.42. Yaw moments for diffracted waves in various frequencies with head sea (adverse current) effect. Wave and current heading angles are 5 and 175 degrees respectively.

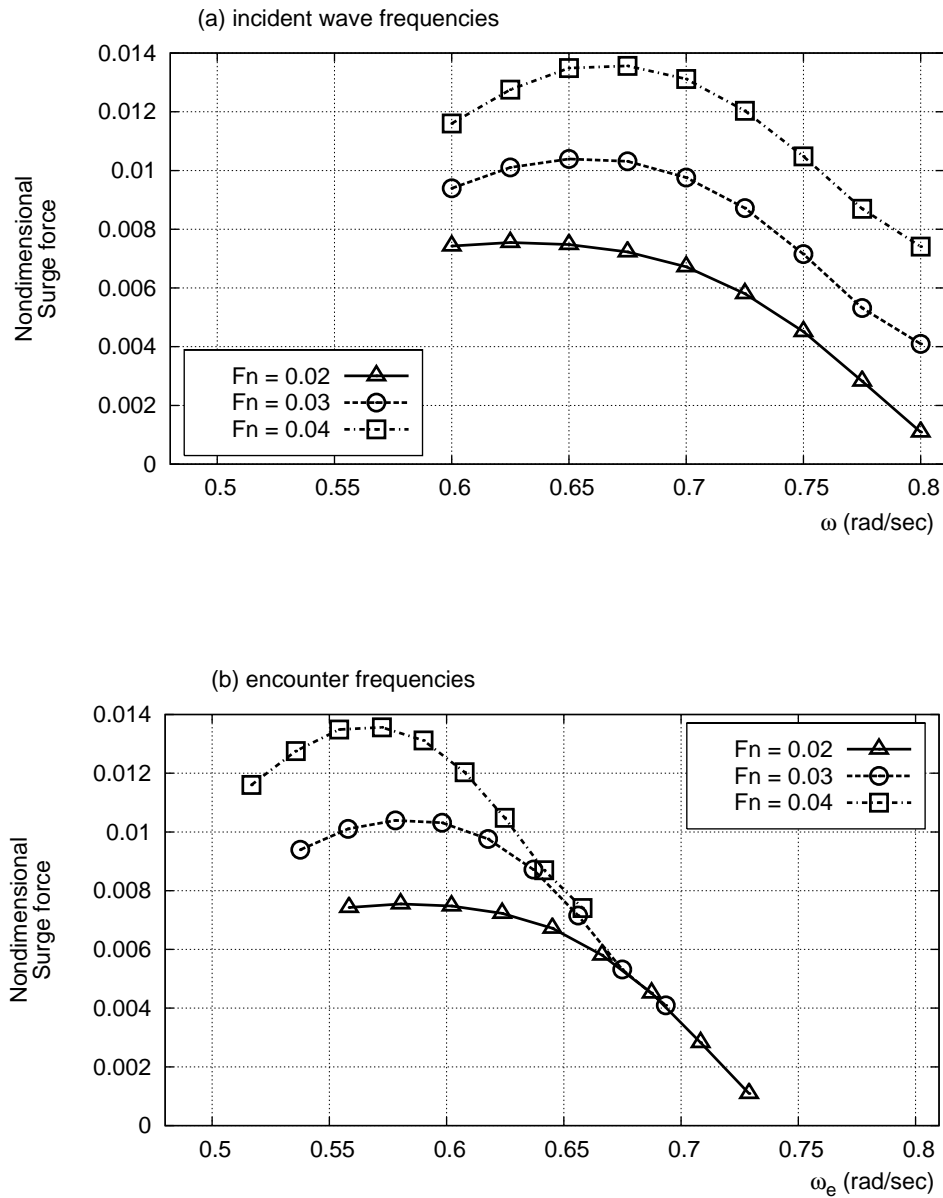


FIGURE F.43. Surge forces for diffracted waves in various frequencies with head sea (adverse current) effect. Waves heading angles and current heading angles are 10 and 170 degrees respectively.

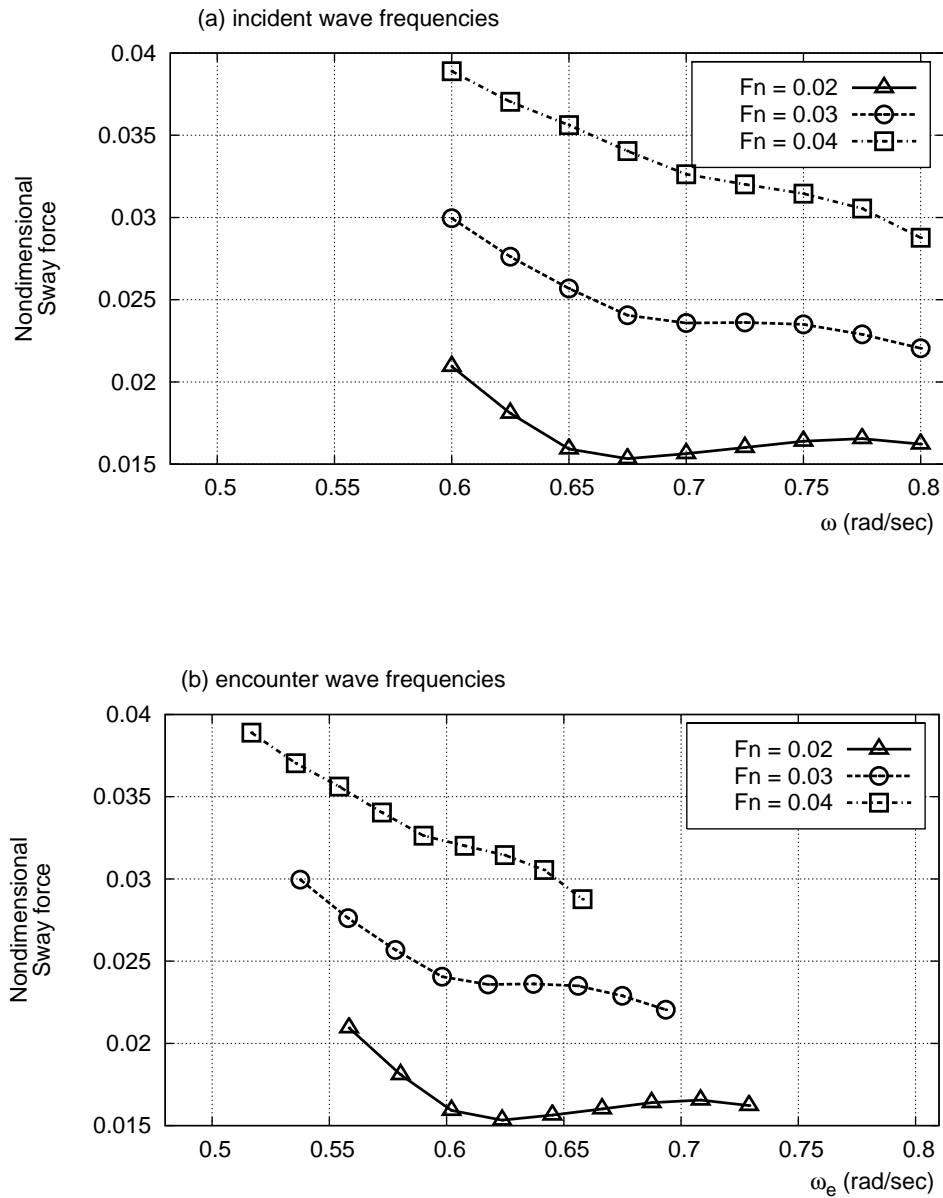


FIGURE F.44. Sway forces for diffracted waves in various frequencies with head sea (adverse current) effect. Wave and current heading angles are 10 and 170 degrees respectively.

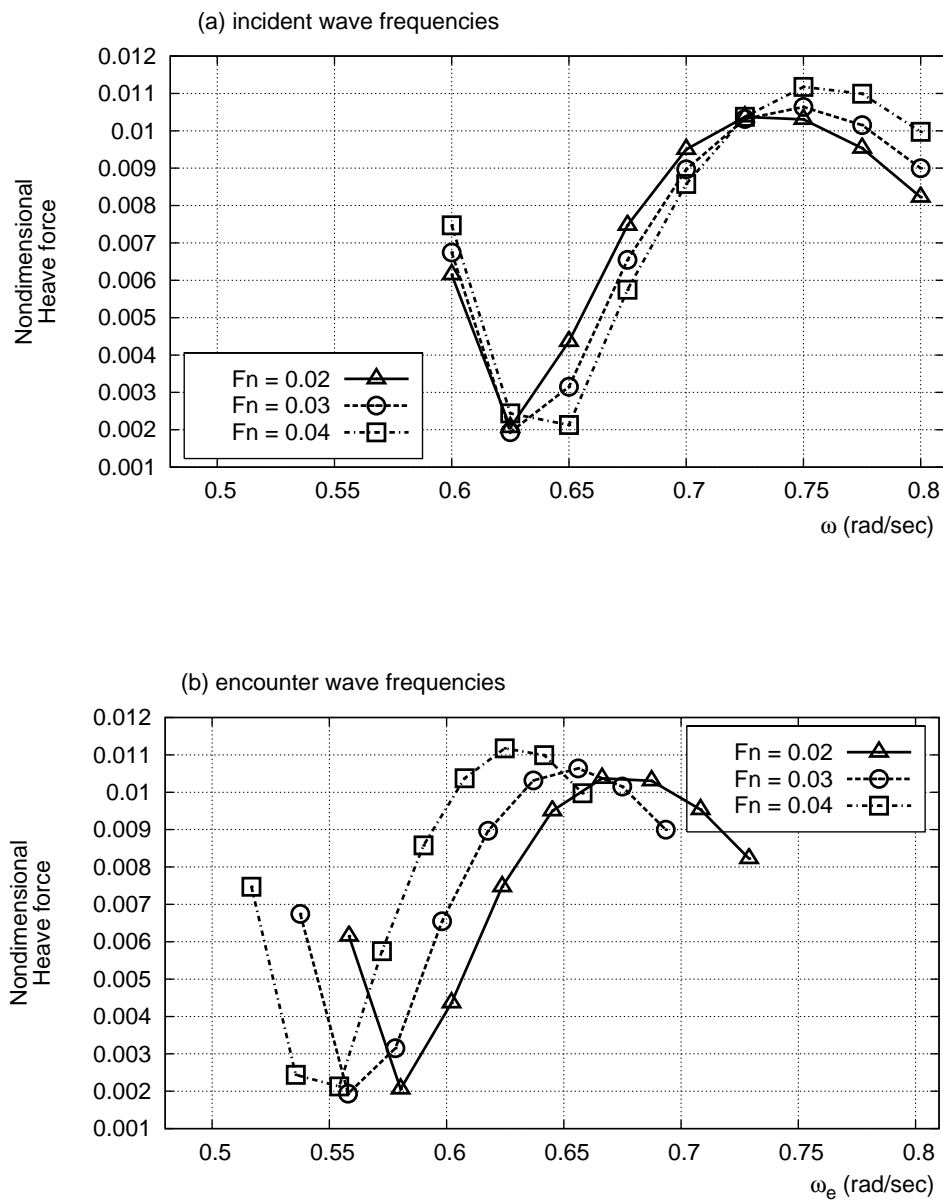


FIGURE F.45. Heave forces for diffracted waves in various frequencies with head sea (adverse current) effect. Wave and current heading angles are 10 and 170 degrees respectively.

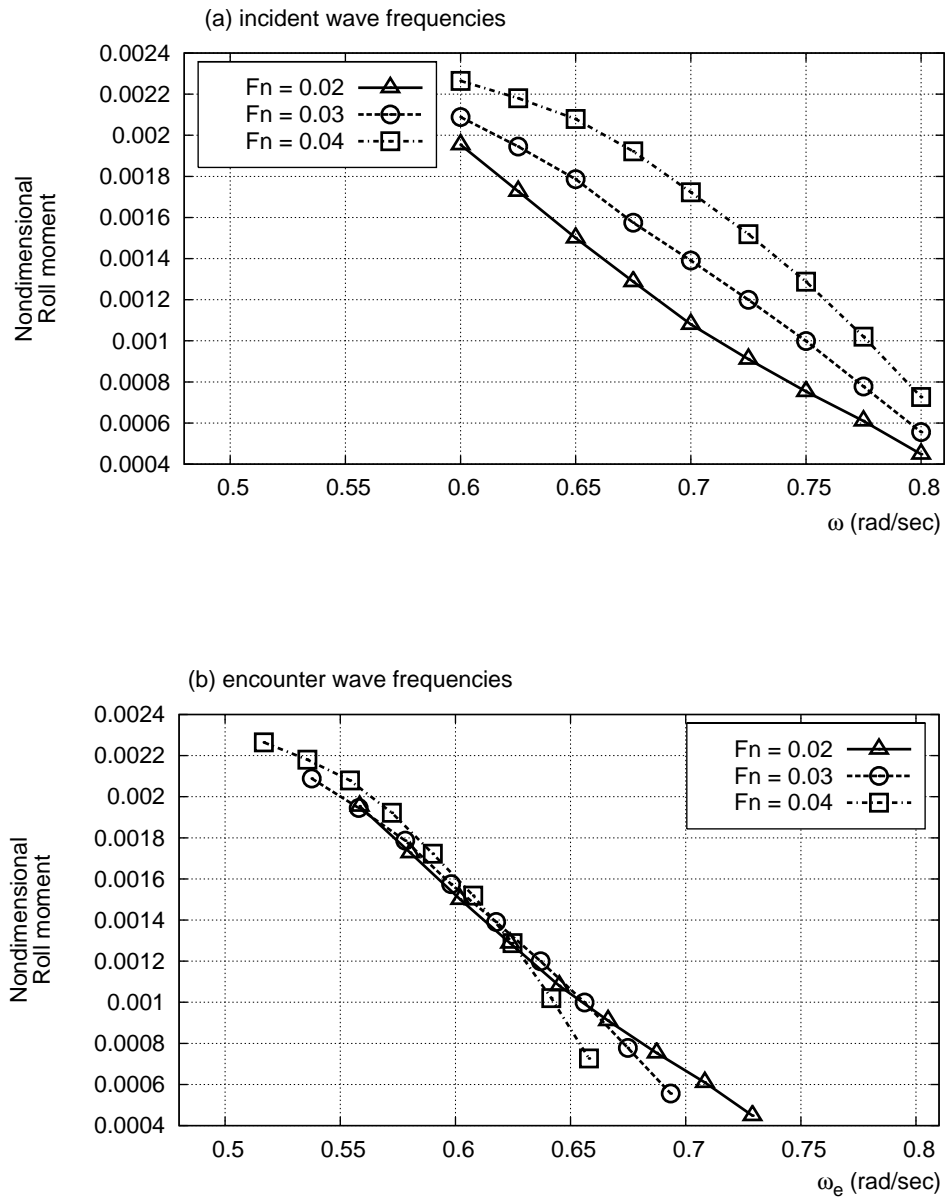


FIGURE F.46. Roll moments for diffracted waves in various frequencies with head sea (adverse current) effect. Wave and current heading angles are 10 and 170 degrees respectively.

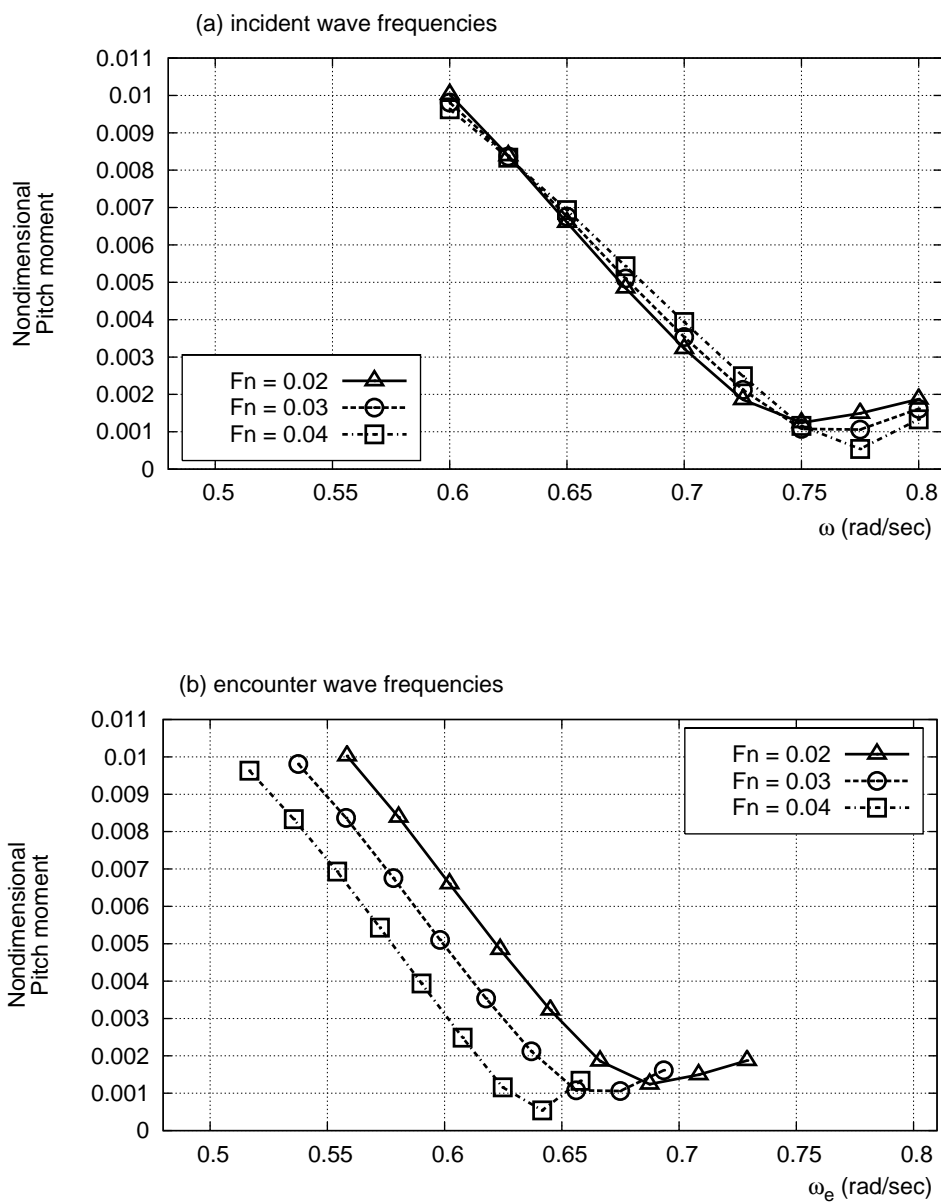


FIGURE F.47. Pitch moments for diffracted waves in various frequencies with head sea (adverse current) effect. Wave and current heading angles are 10 and 170 degrees respectively.

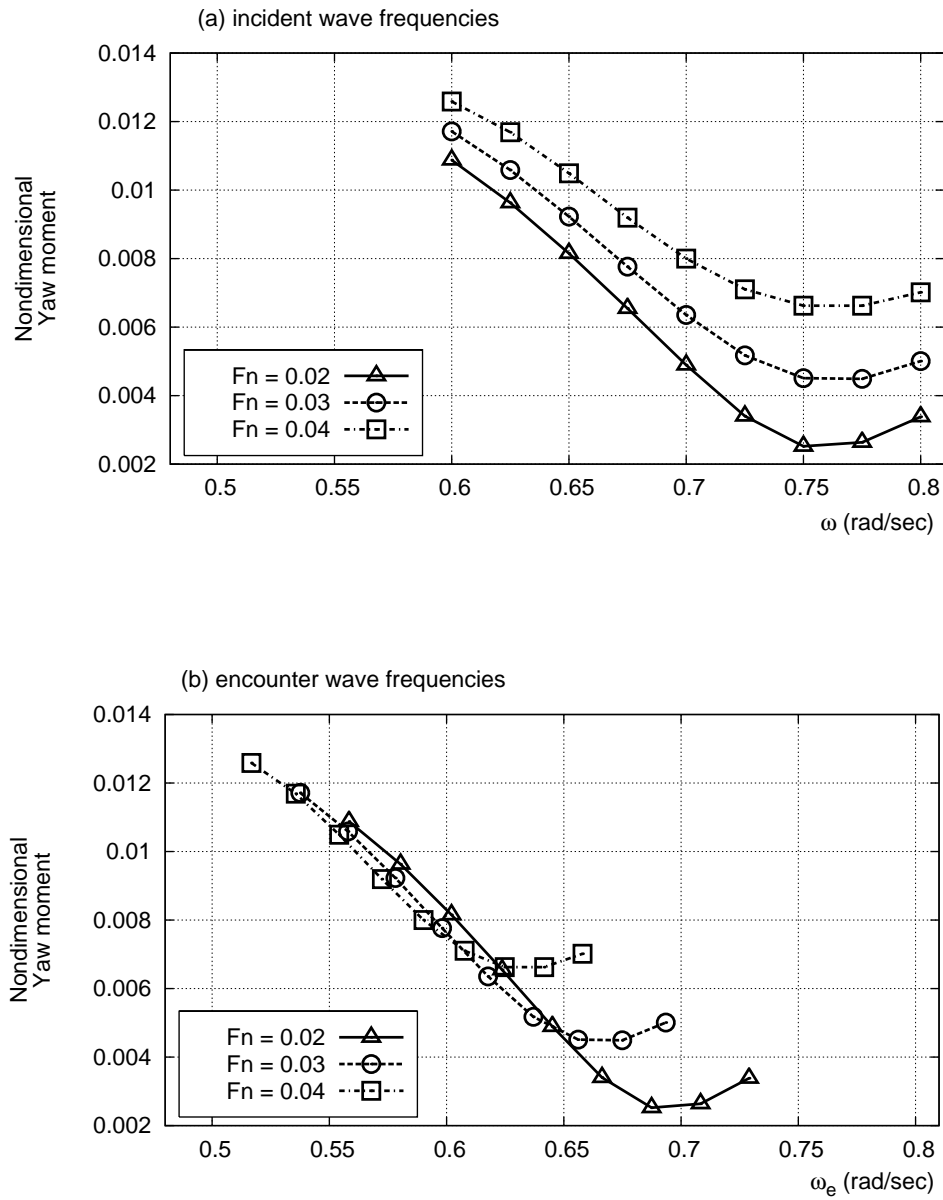


FIGURE F.48. Yaw moments for diffracted waves in various frequencies with head sea (adverse current) effect. Wave and current heading angles are 10 and 170 degrees respectively.

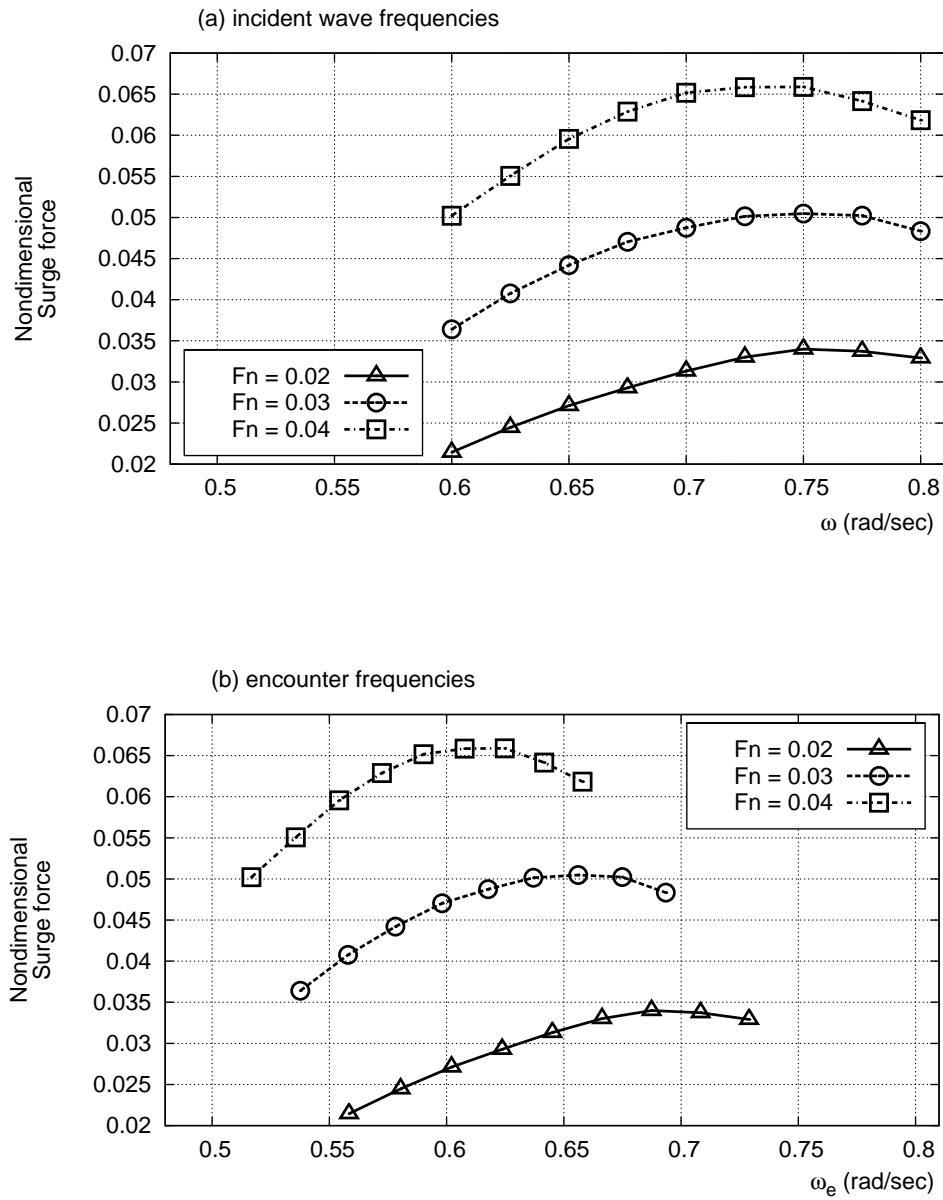


FIGURE F.49. Surge forces for diffracted waves in various frequencies with head sea (adverse current) effect. Waves heading angles and current heading angles are 30 and 150 degrees respectively.

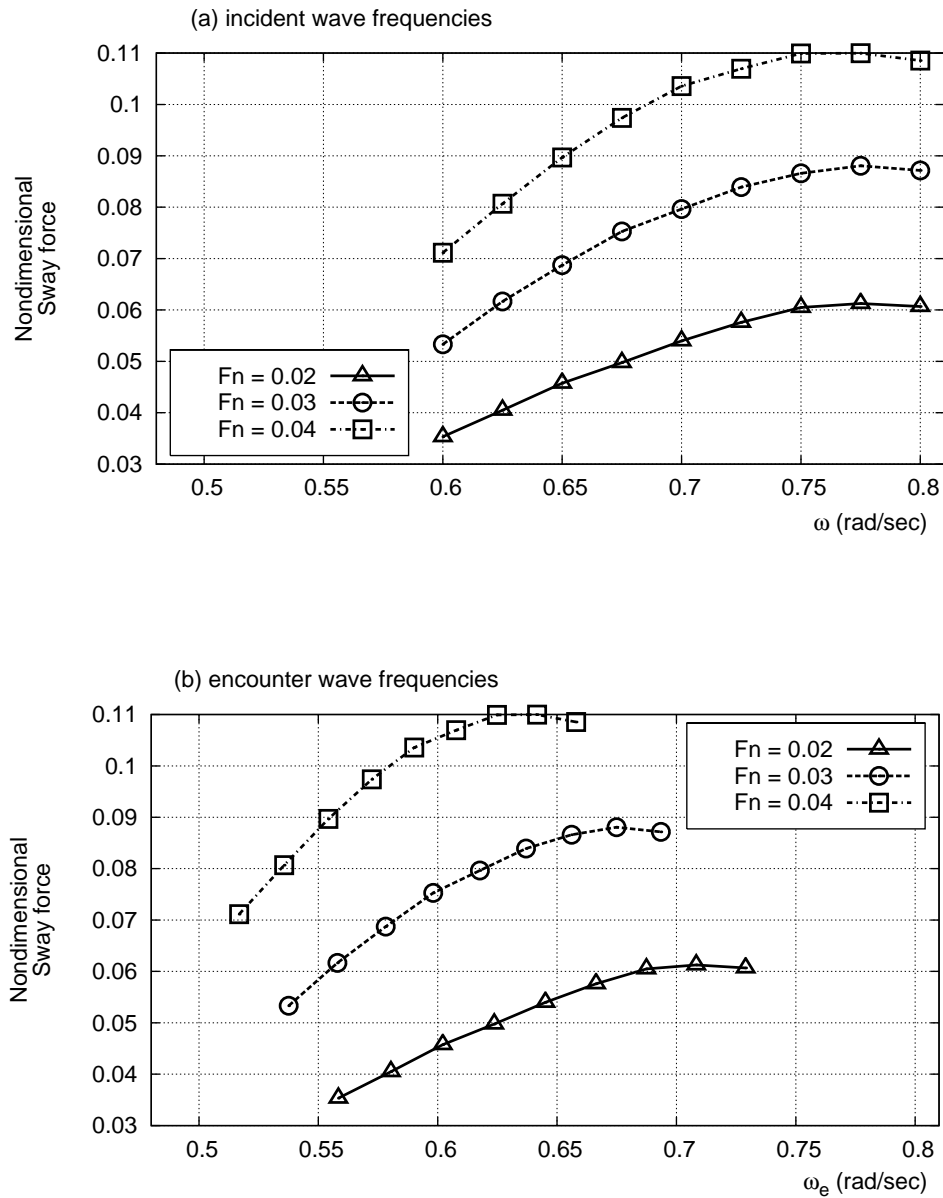


FIGURE F.50. Sway forces for diffracted waves in various frequencies with head sea (adverse current) effect. Wave and current heading angles are 30 and 150 degrees respectively.

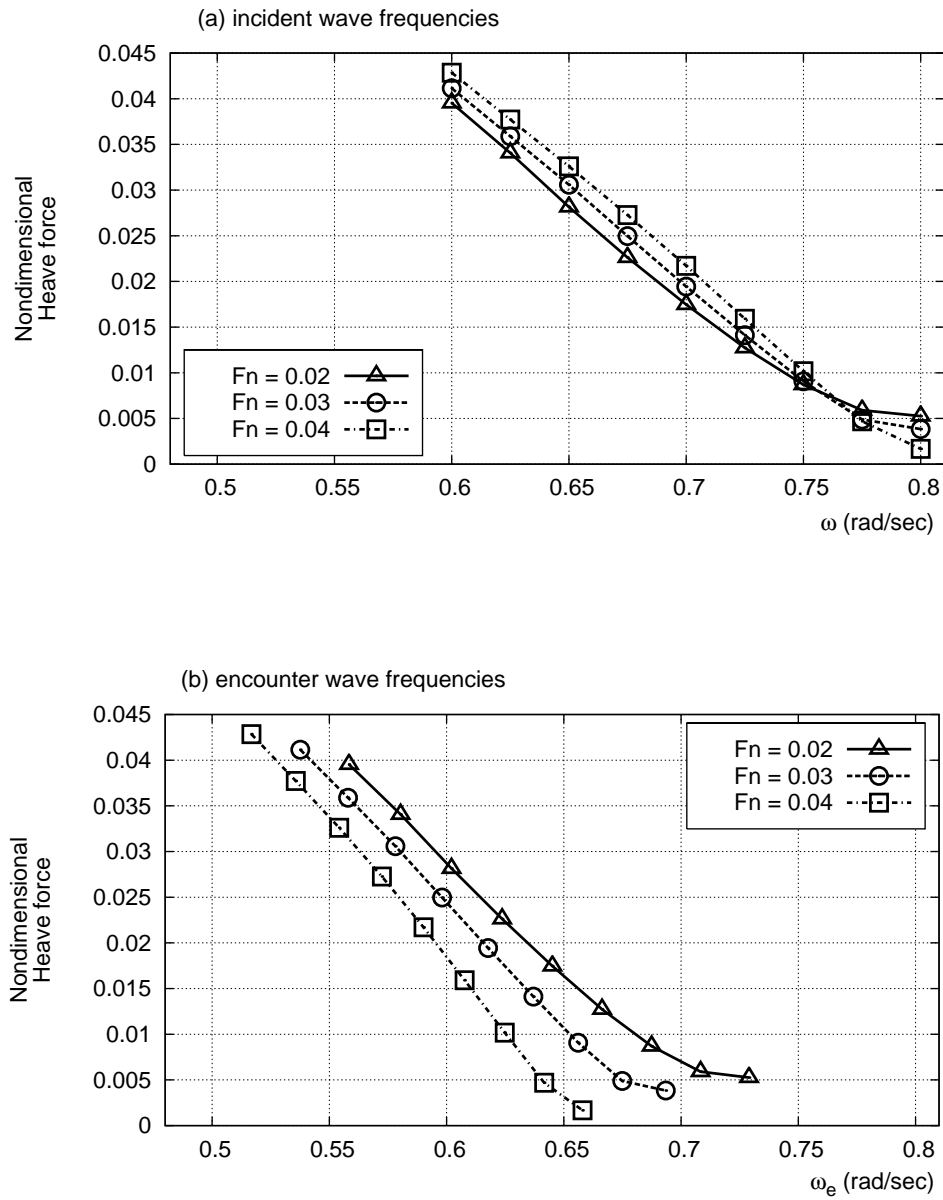


FIGURE F.51. Heave forces for diffracted waves in various frequencies with head sea (adverse current) effect. Wave and current heading angles are 30 and 150 degrees respectively.

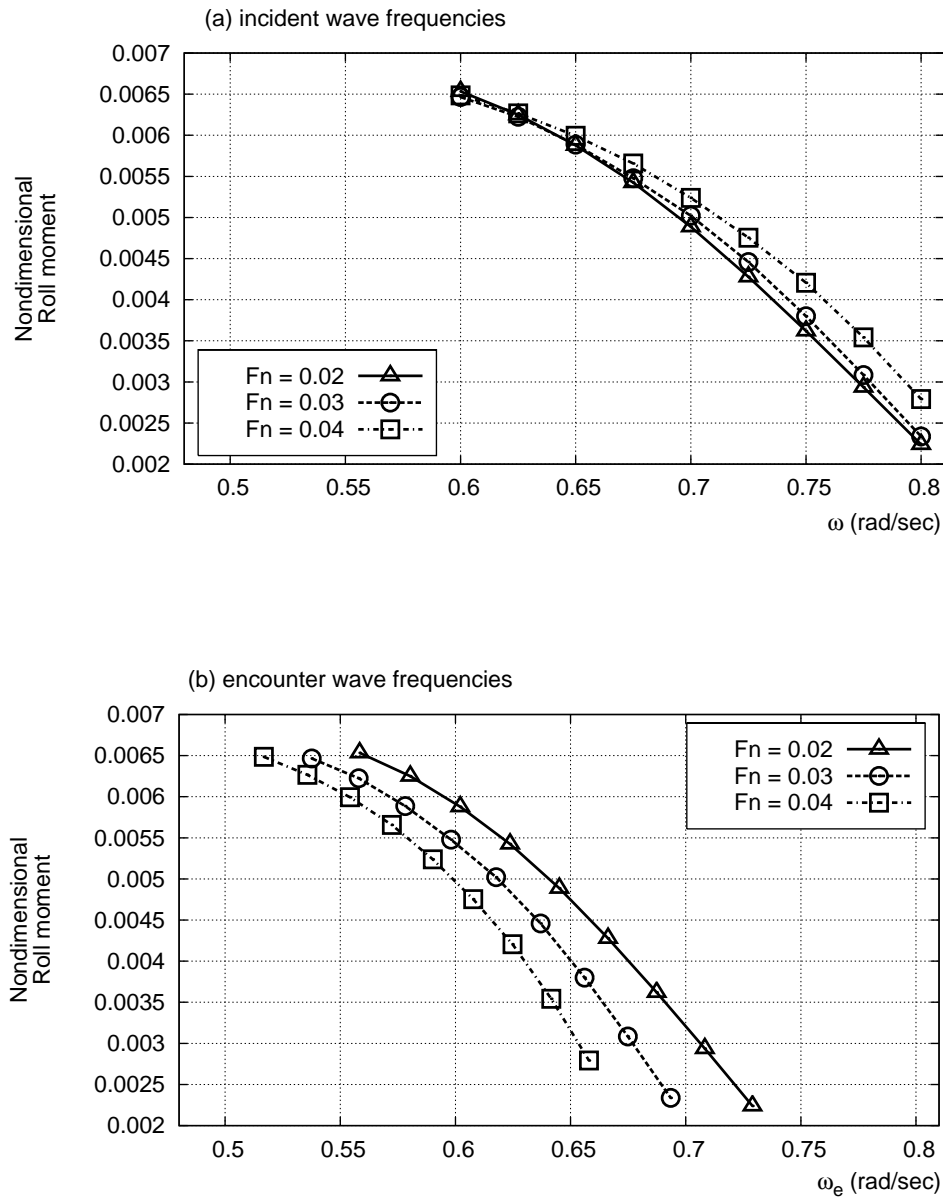


FIGURE F.52. Roll moments for diffracted waves in various frequencies with head sea (adverse current) effect. Wave and current heading angles are 30 and 150 degrees respectively.

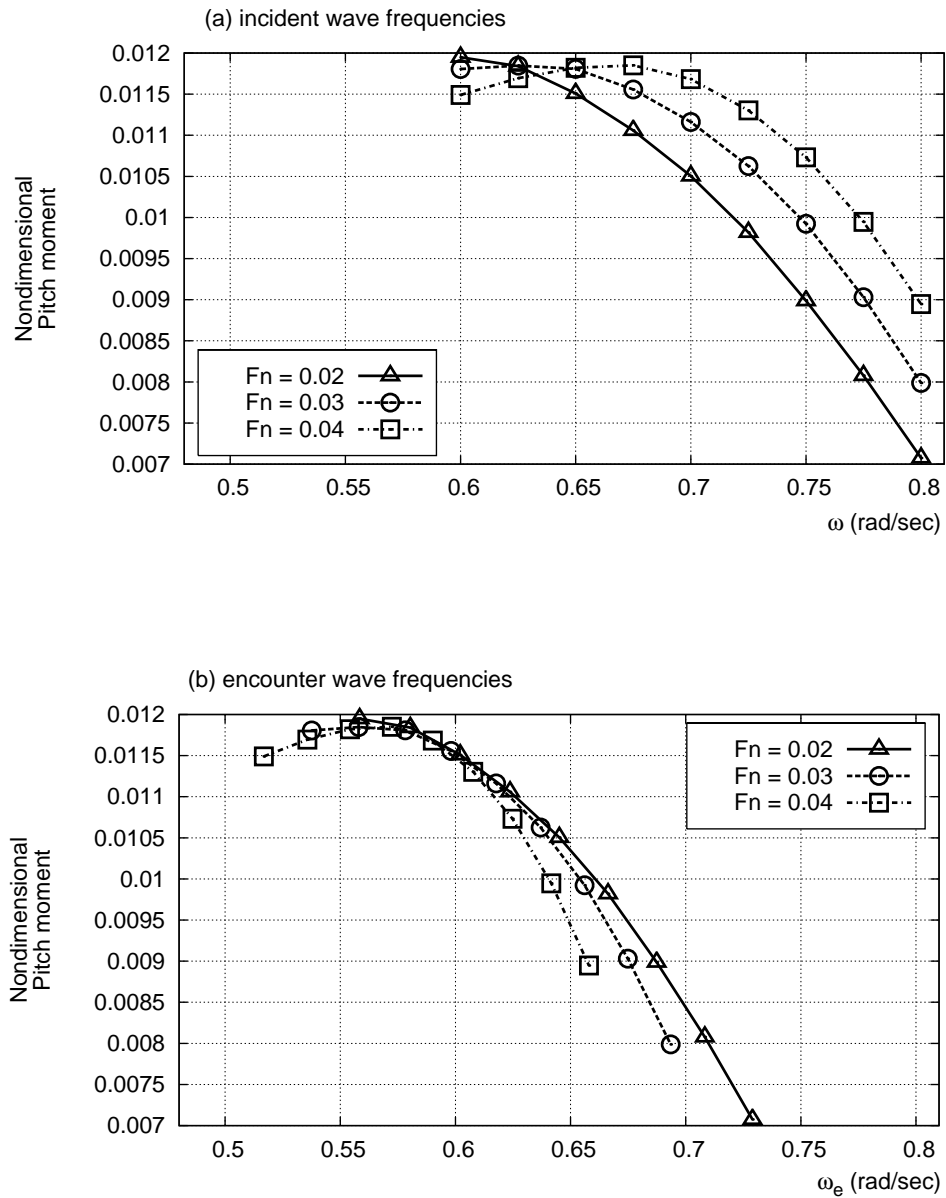


FIGURE F.53. Pitch moments for diffracted waves in various frequencies with head sea (adverse current) effect. Wave and current heading angles are 30 and 150 degrees respectively.

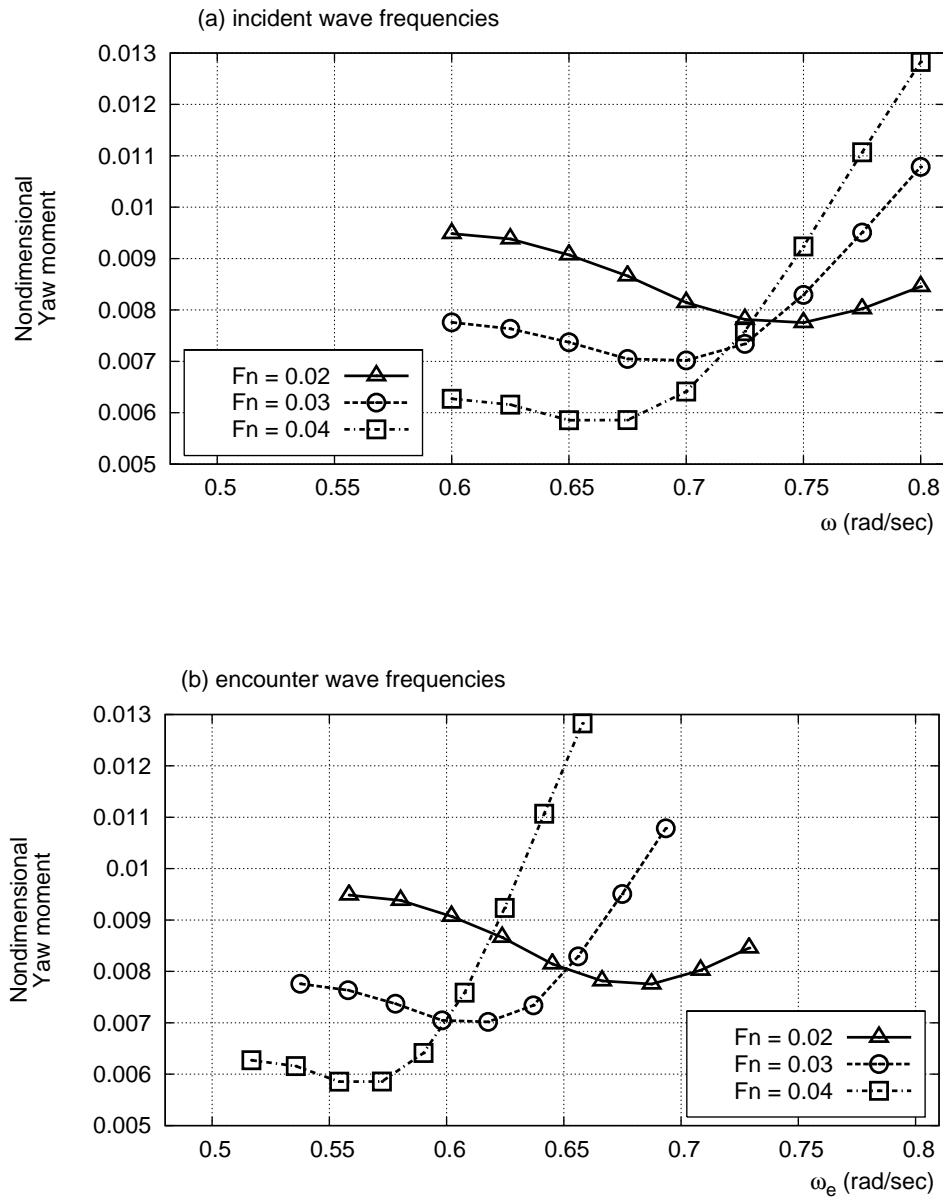


FIGURE F.54. Yaw moments for diffracted waves in various frequencies with head sea (adverse current) effect. Wave and current heading angles are 30 and 150 degrees respectively.

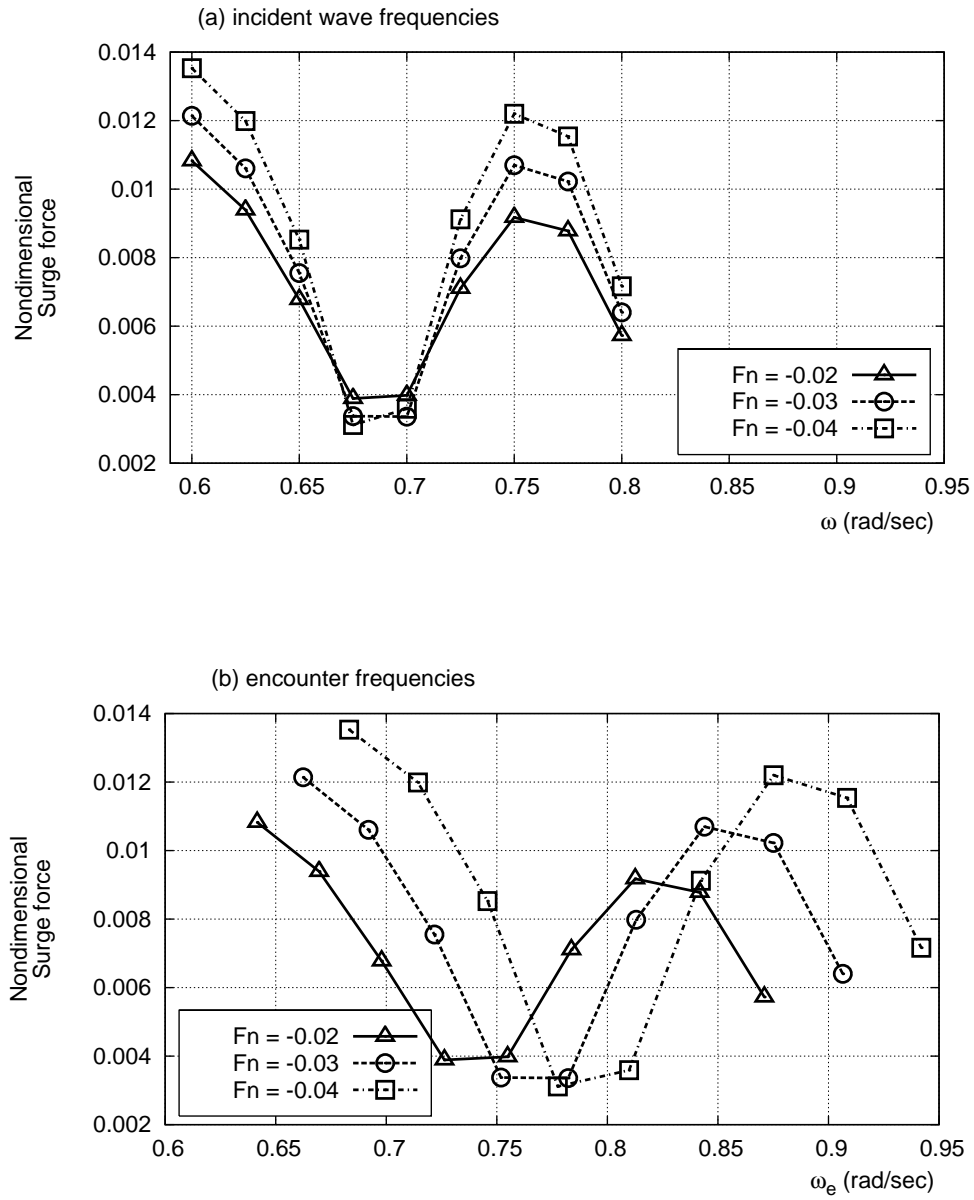


FIGURE F.55. Surge forces for diffracted waves in various frequencies with following sea (collinear current) effect. Wave and current heading angles are -5 degrees.

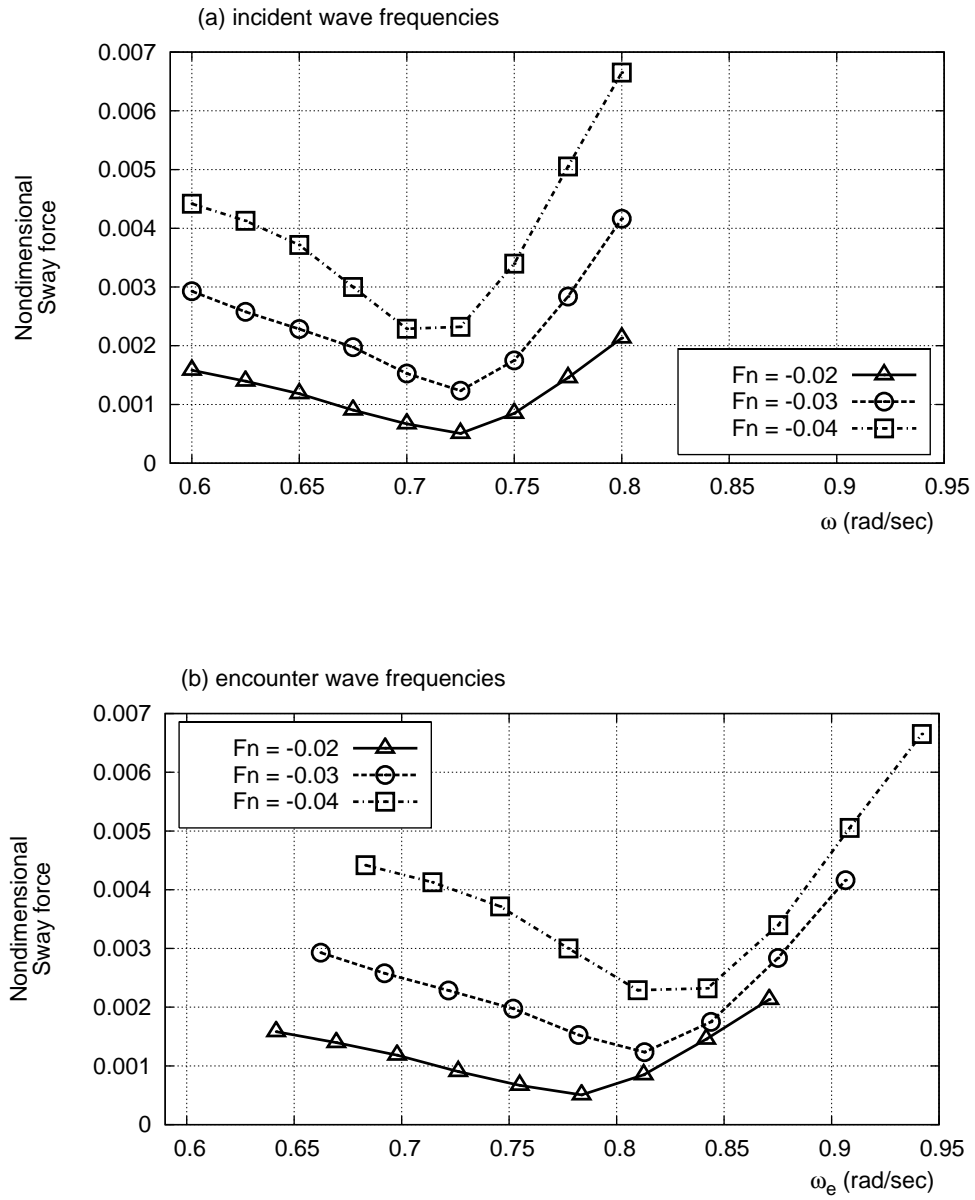


FIGURE F.56. Sway forces for diffracted waves in various frequencies with following sea (collinear current) effect. Wave and current heading angles are -5 degrees.

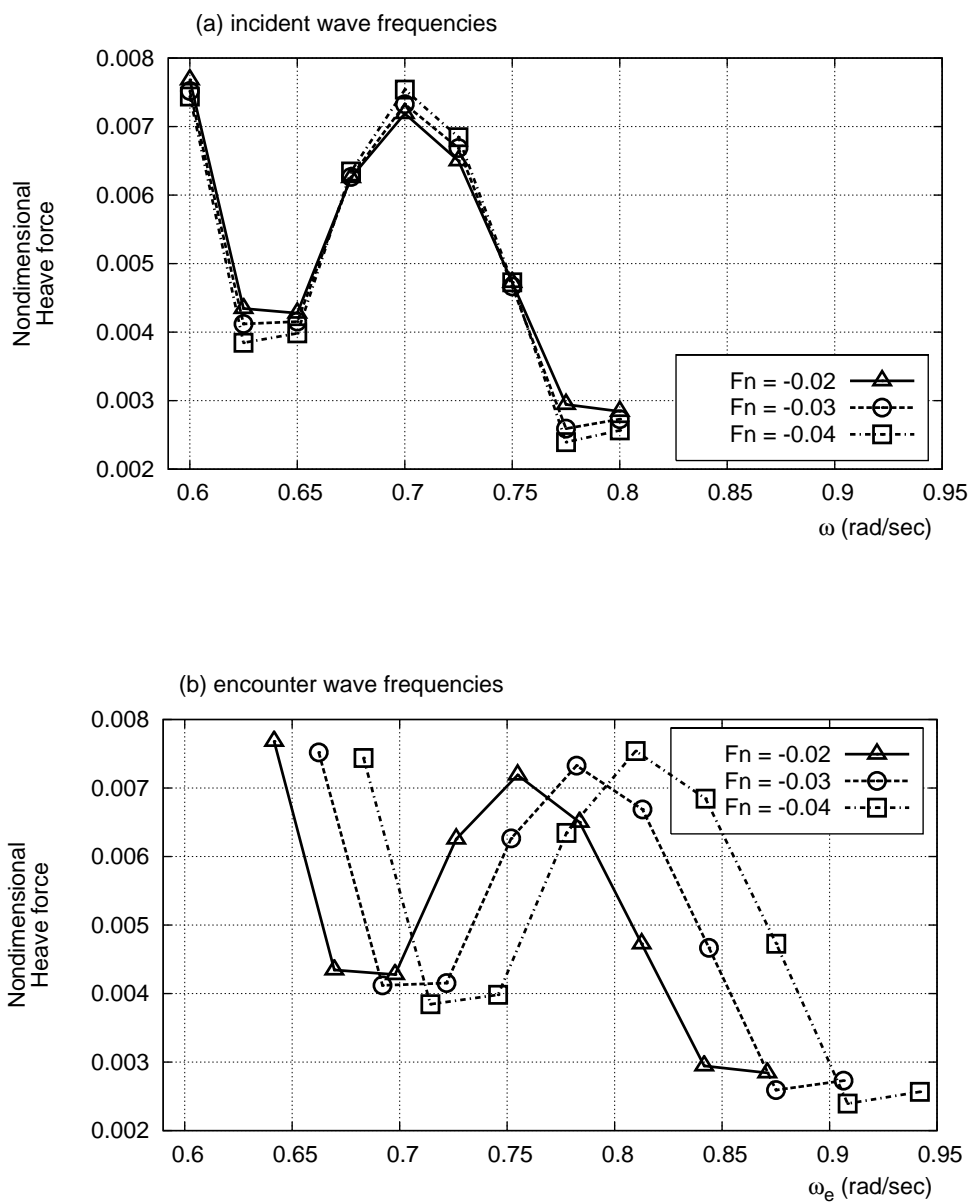


FIGURE F.57. Heave forces for diffracted waves in various frequencies with following sea (collinear current) effect. Wave and current heading angles are -5 degrees.

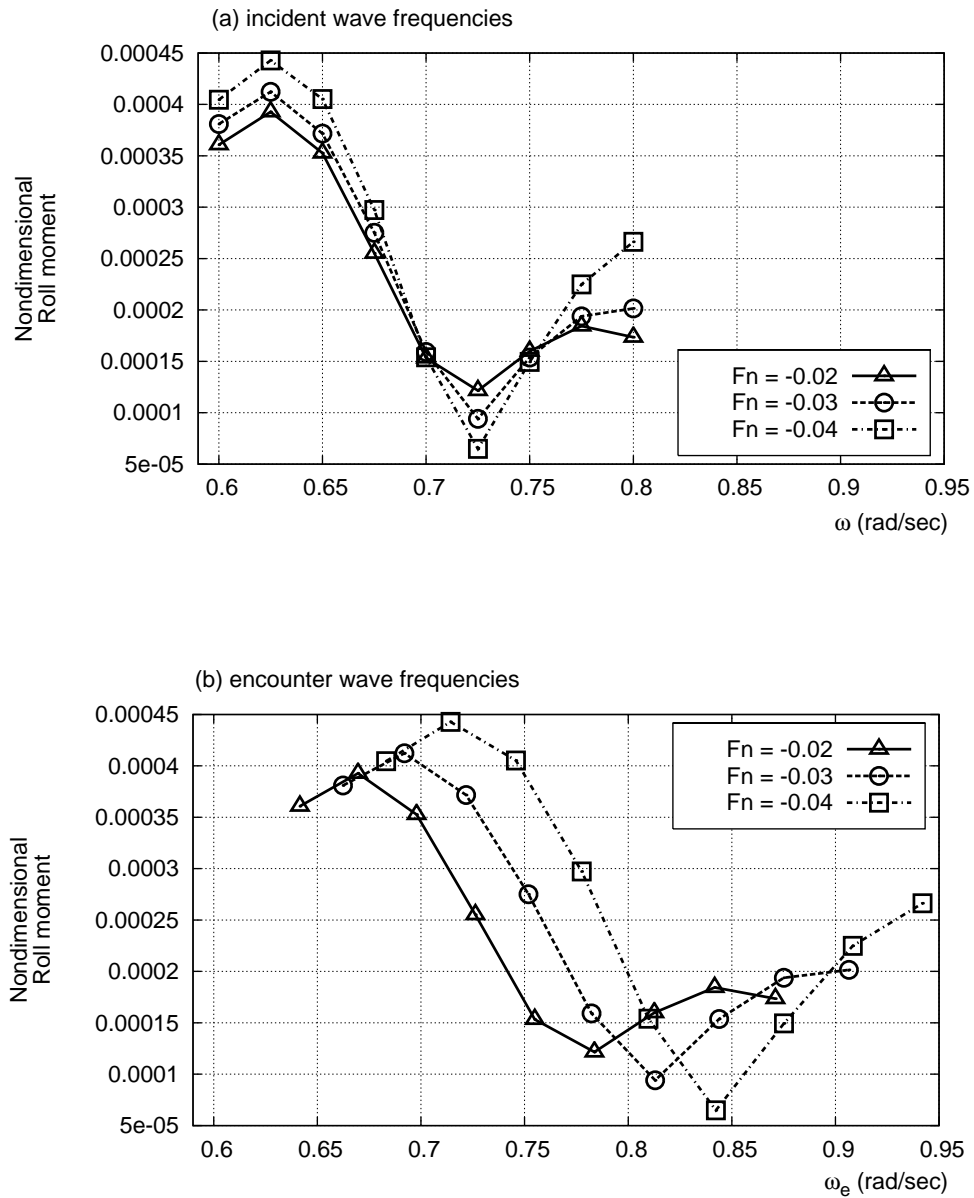


FIGURE F.58. Roll moments for diffracted waves in various frequencies with following sea (collinear current) effect. Wave and current heading angles are -5 degrees.

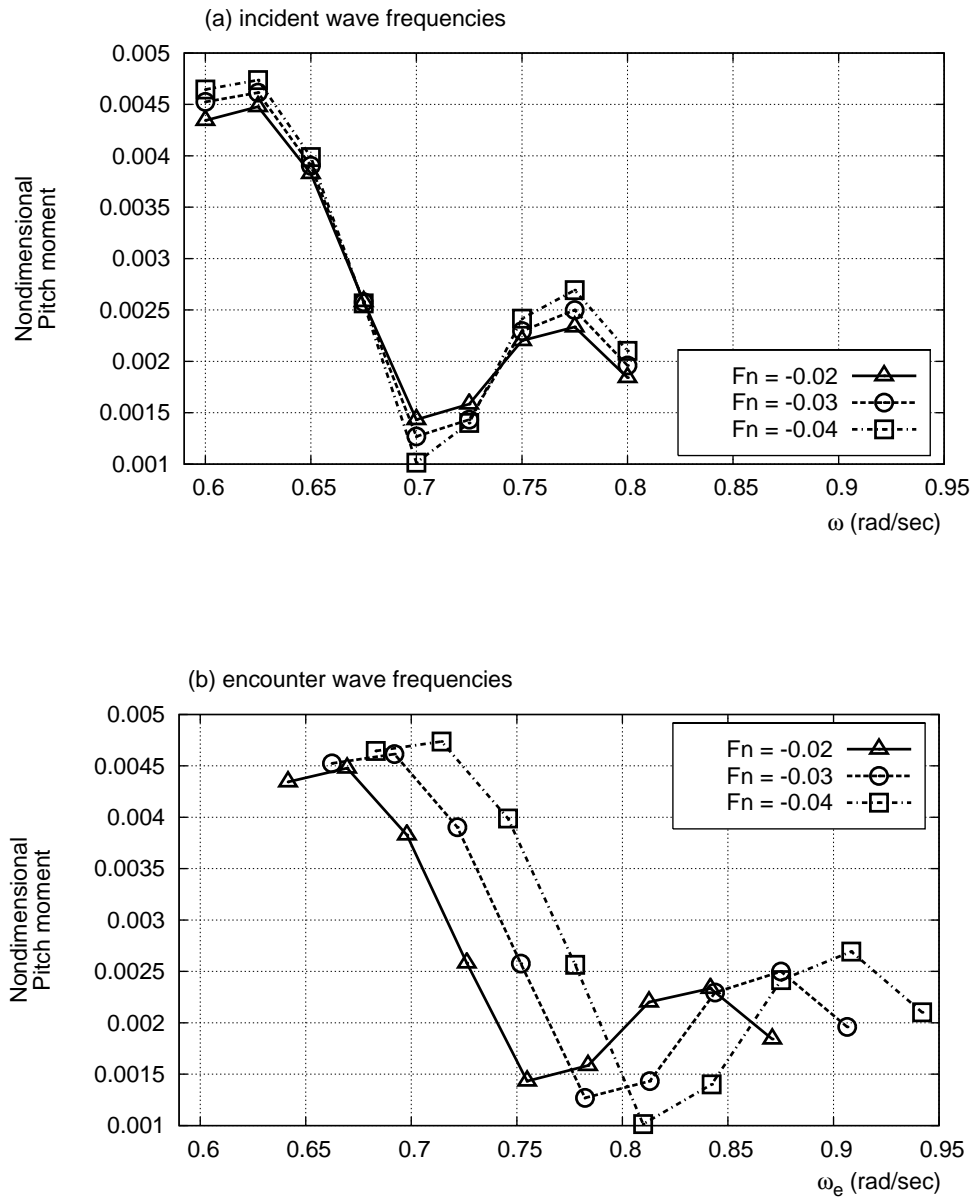


FIGURE F.59. Pitch moments for diffracted waves in various frequencies with following sea (collinear current) effect. Wave and current heading angles are -5 degrees.

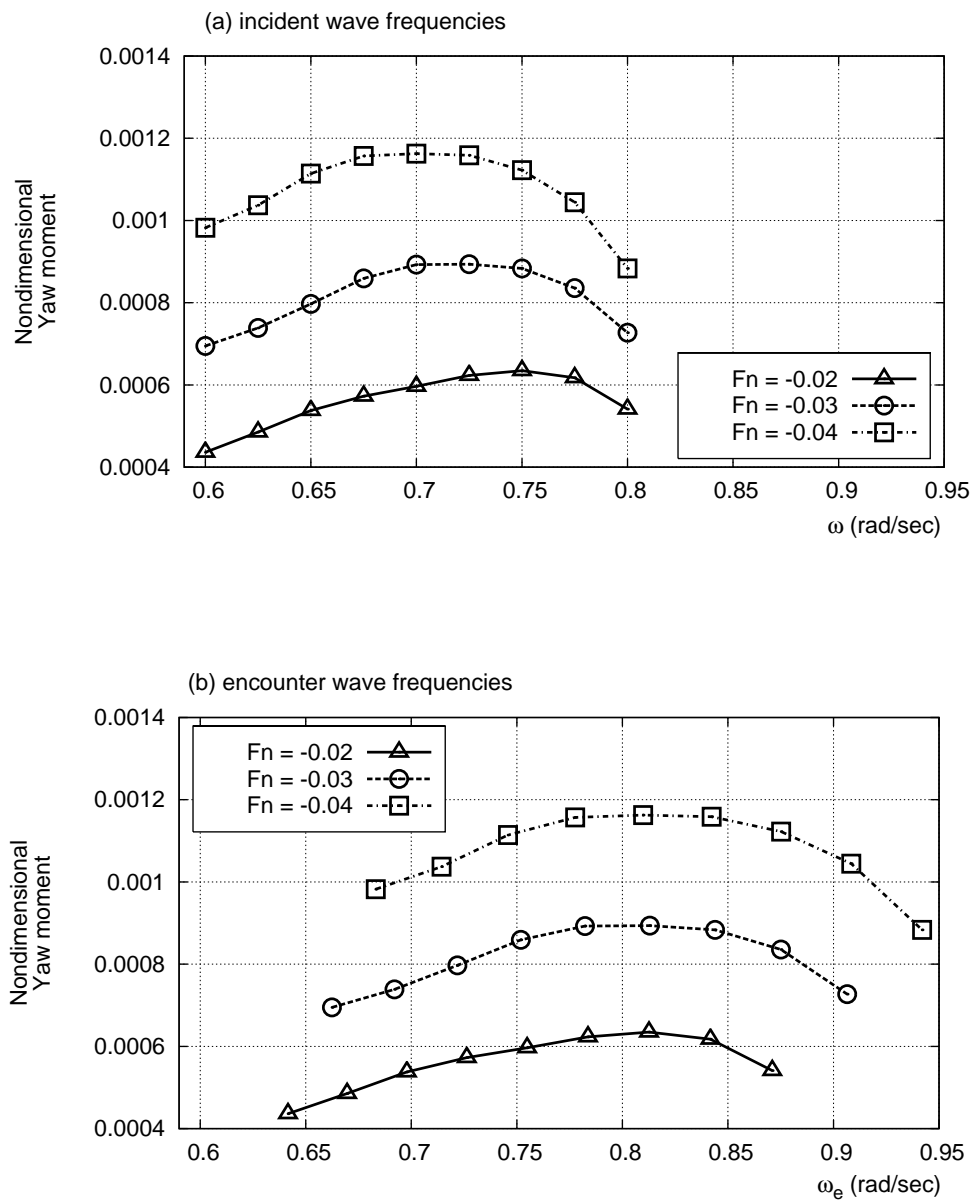


FIGURE F.60. Yaw moments for diffracted waves in various frequencies with following sea (collinear current) effect. Wave and current heading angles are -5 degrees.

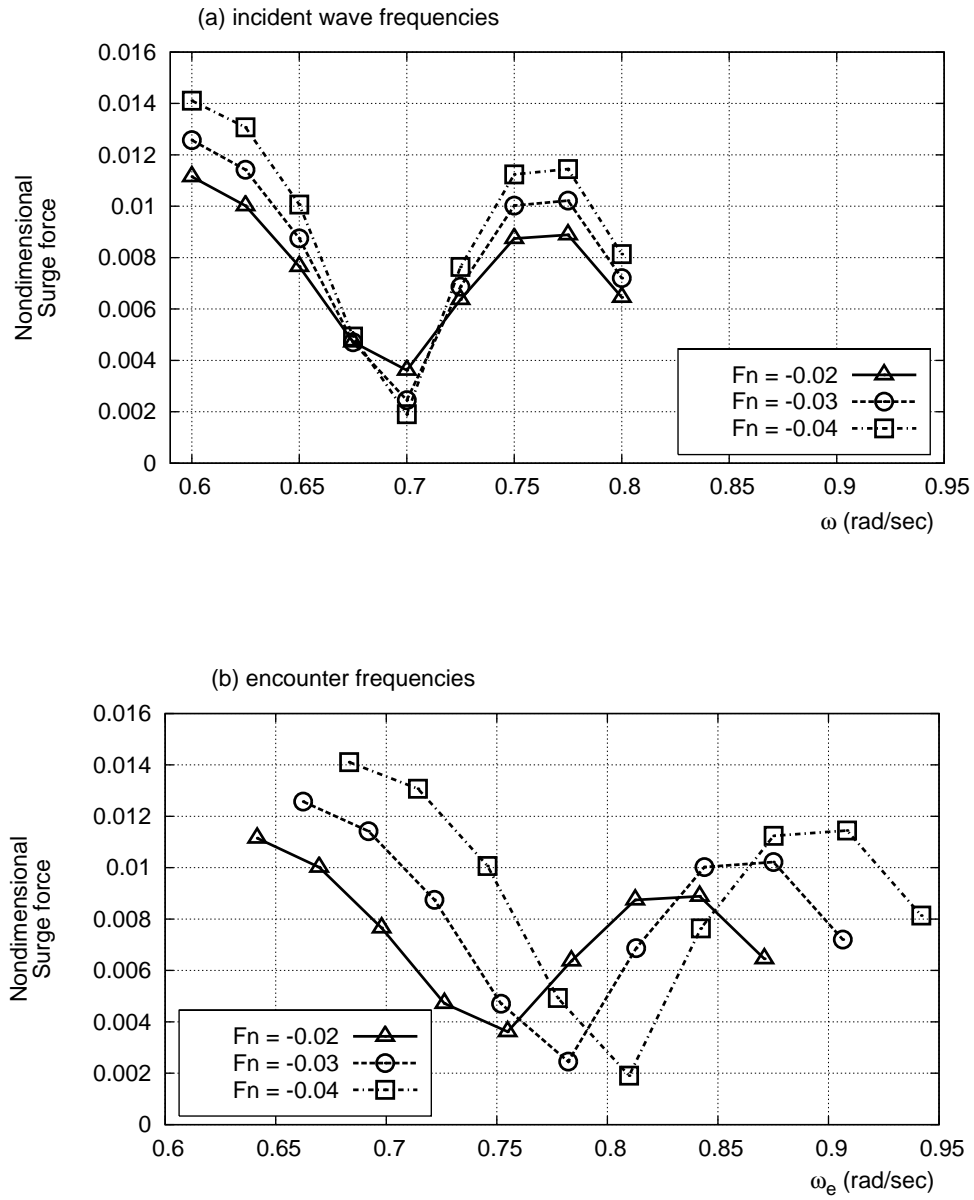


FIGURE F.61. Surge forces for diffracted waves in various frequencies with following sea (collinear current) effect. Wave and current heading angles are -10 degrees.

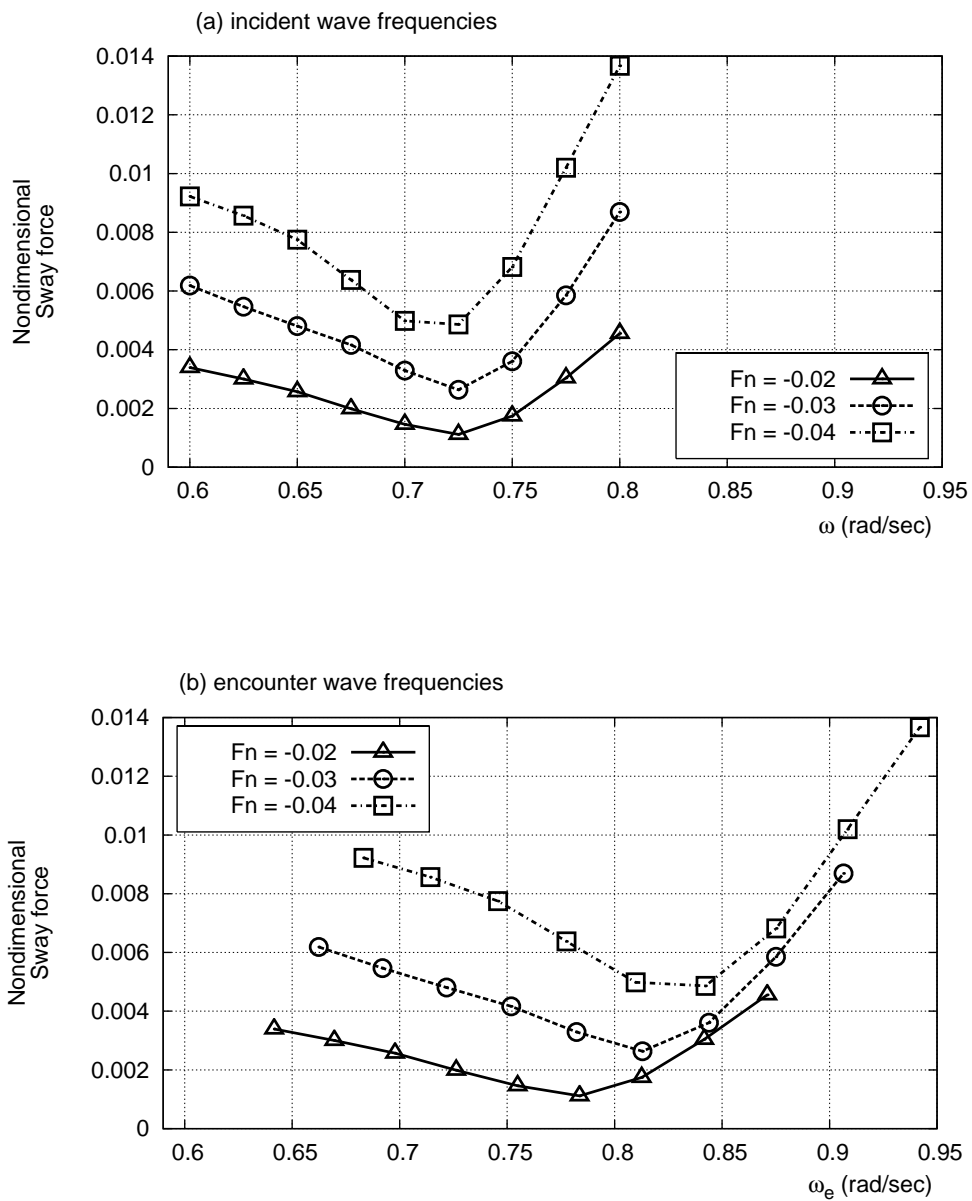


FIGURE F.62. Sway forces for diffracted waves in various frequencies with following sea (collinear current) effect. Wave and current heading angles are -10 degrees.

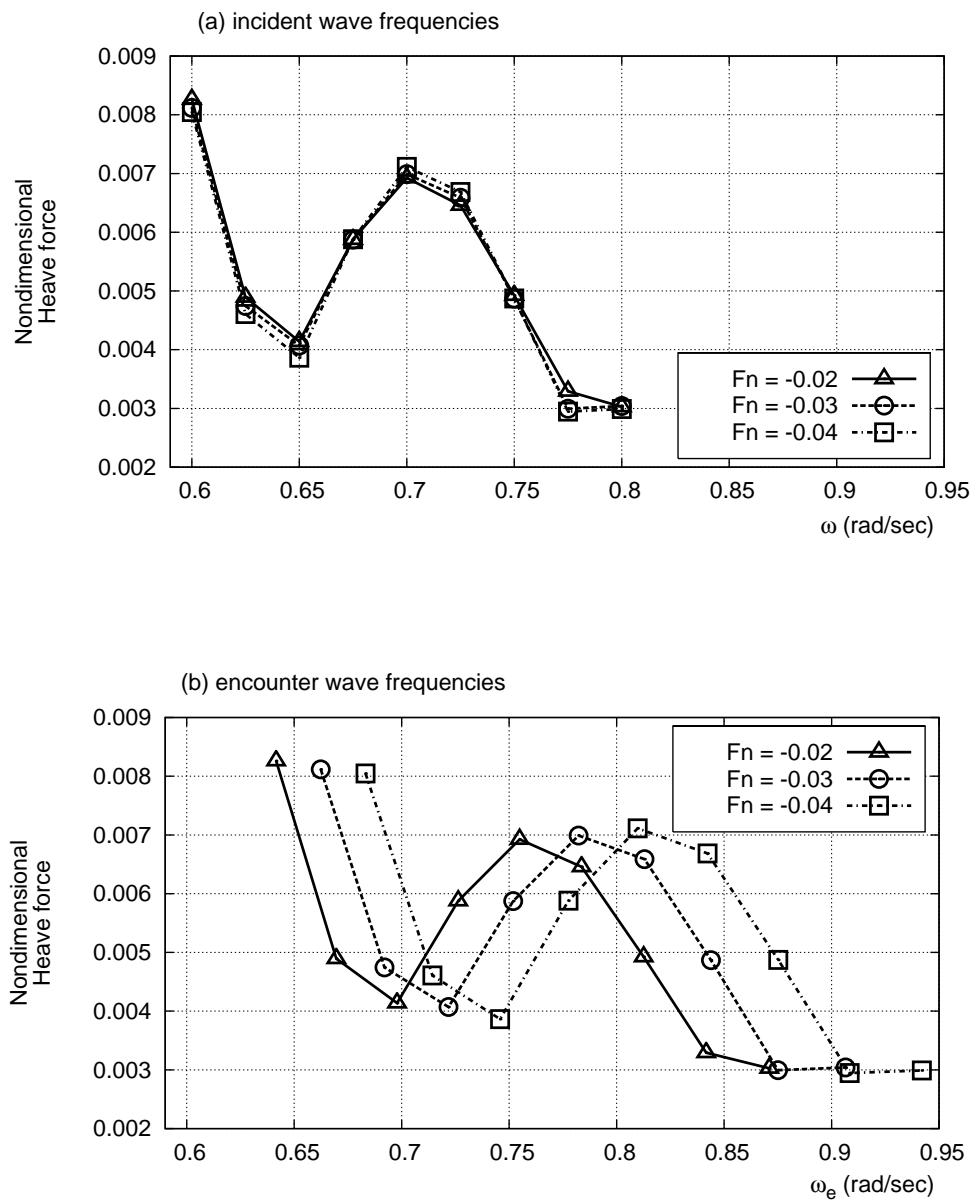


FIGURE F.63. Heave forces for diffracted waves in various frequencies with following sea (collinear current) effect. Wave and current heading angles are -10 degrees.

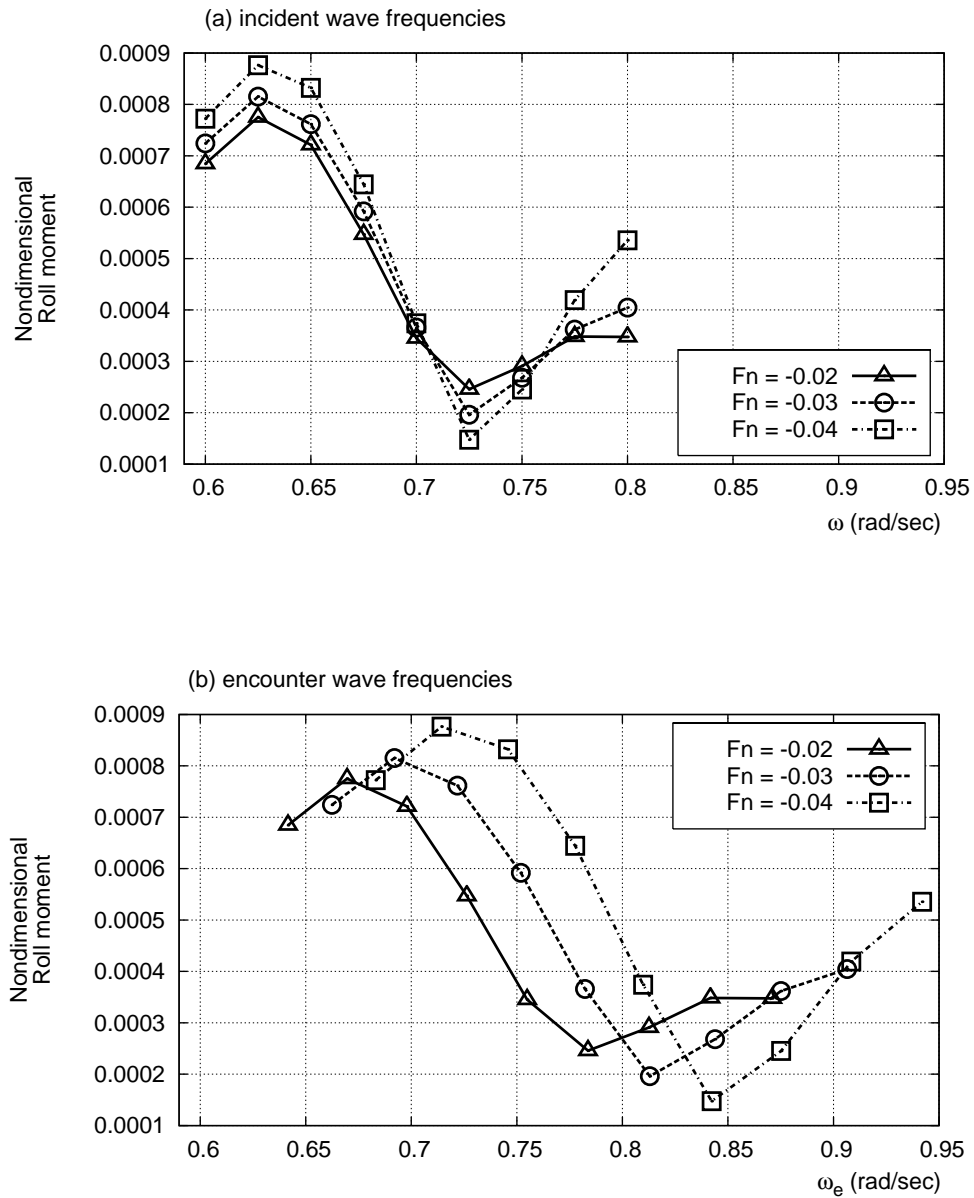


FIGURE F.64. Roll moments for diffracted waves in various frequencies with following sea (collinear current) effect. Wave and current heading angles are -10 degrees.

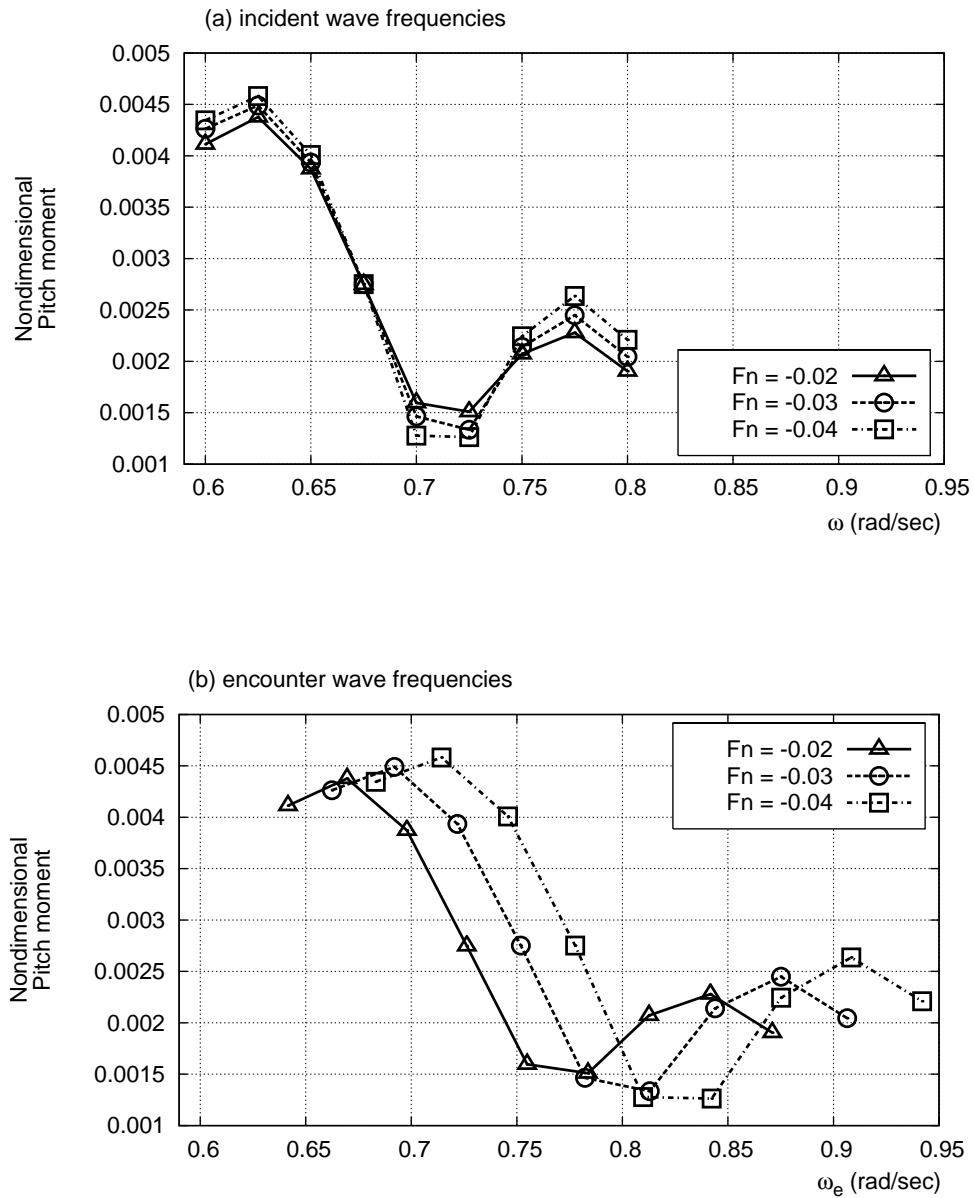


FIGURE F.65. Pitch moments for diffracted waves in various frequencies with following sea (collinear current) effect. Wave and current heading angles are -10 degrees.

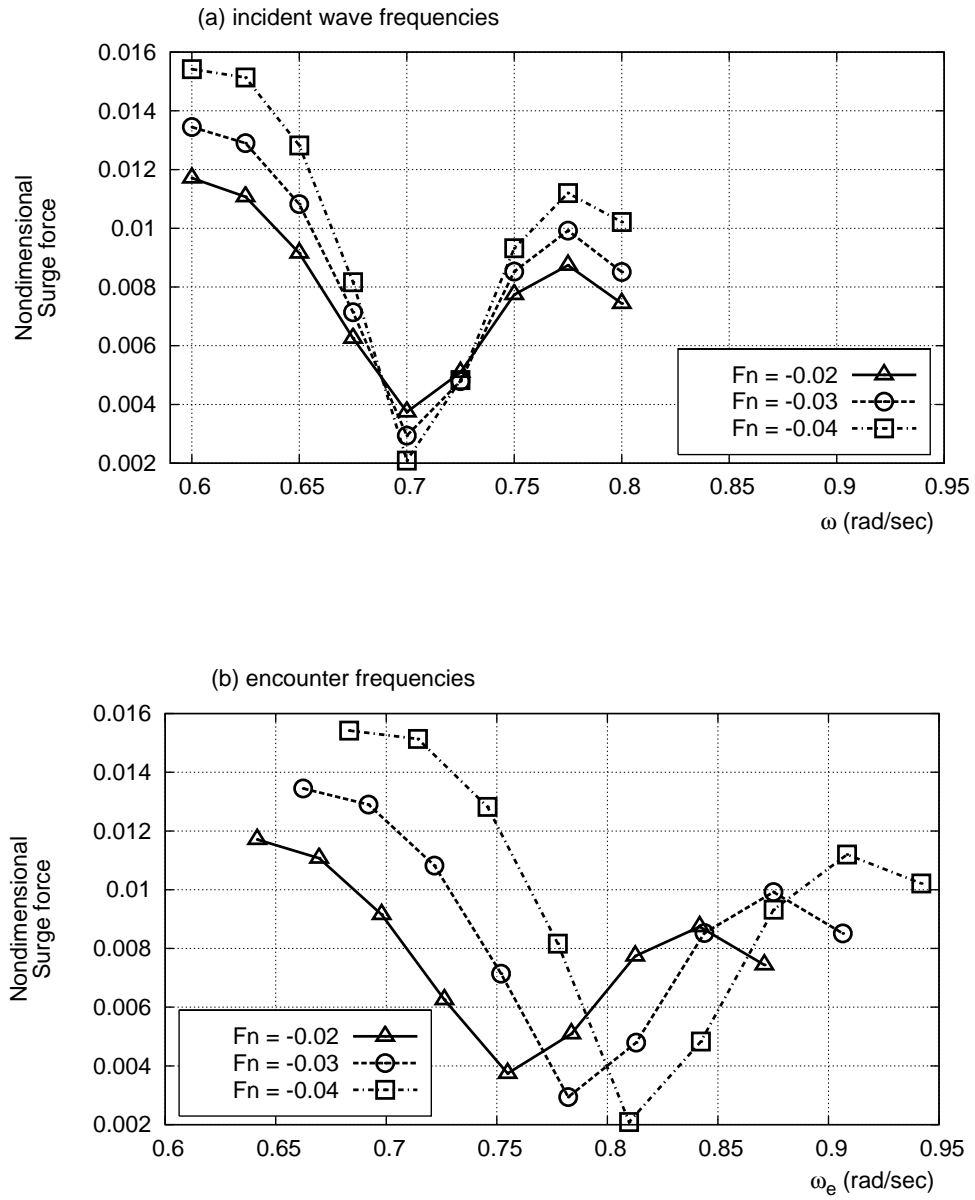


FIGURE F.66. Surge forces for diffracted waves in various frequencies with following sea (collinear current) effect. Wave and current heading angles are -15 degrees.

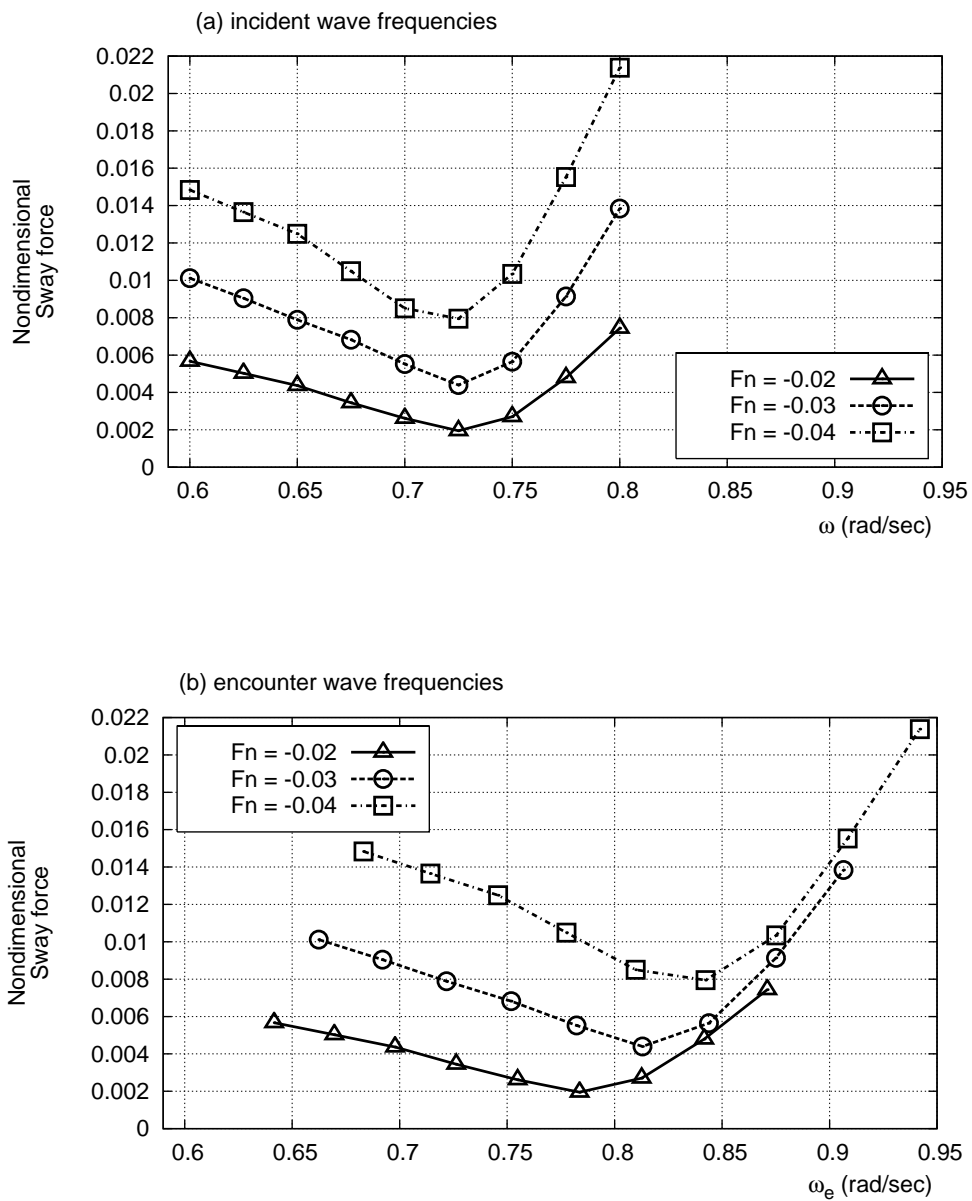


FIGURE F.67. Sway forces for diffracted waves in various frequencies with following sea (collinear current) effect. Wave and current heading angles are -15 degrees.

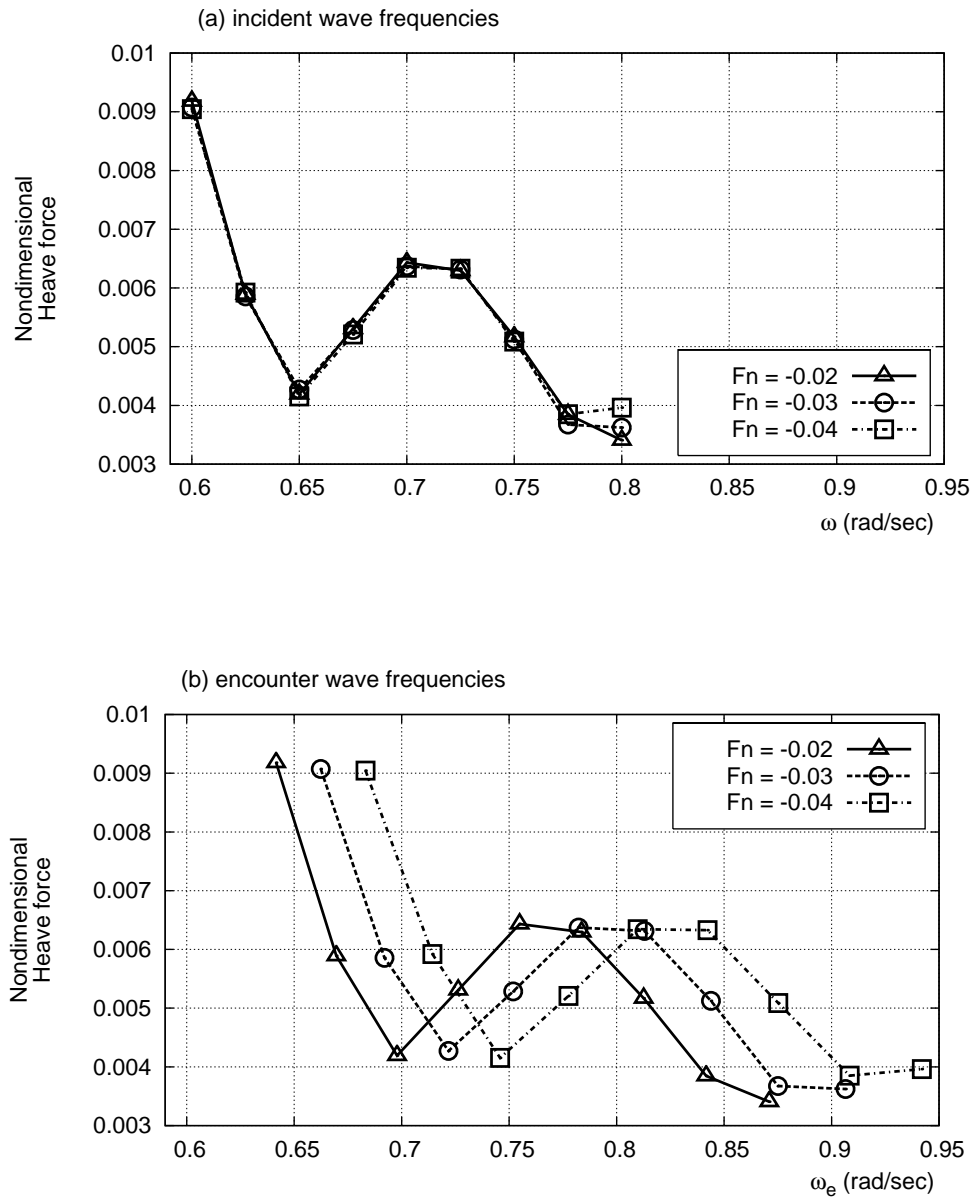


FIGURE F.68. Heave forces for diffracted waves in various frequencies with following sea (collinear current) effect. Wave and current heading angles are -15 degrees.

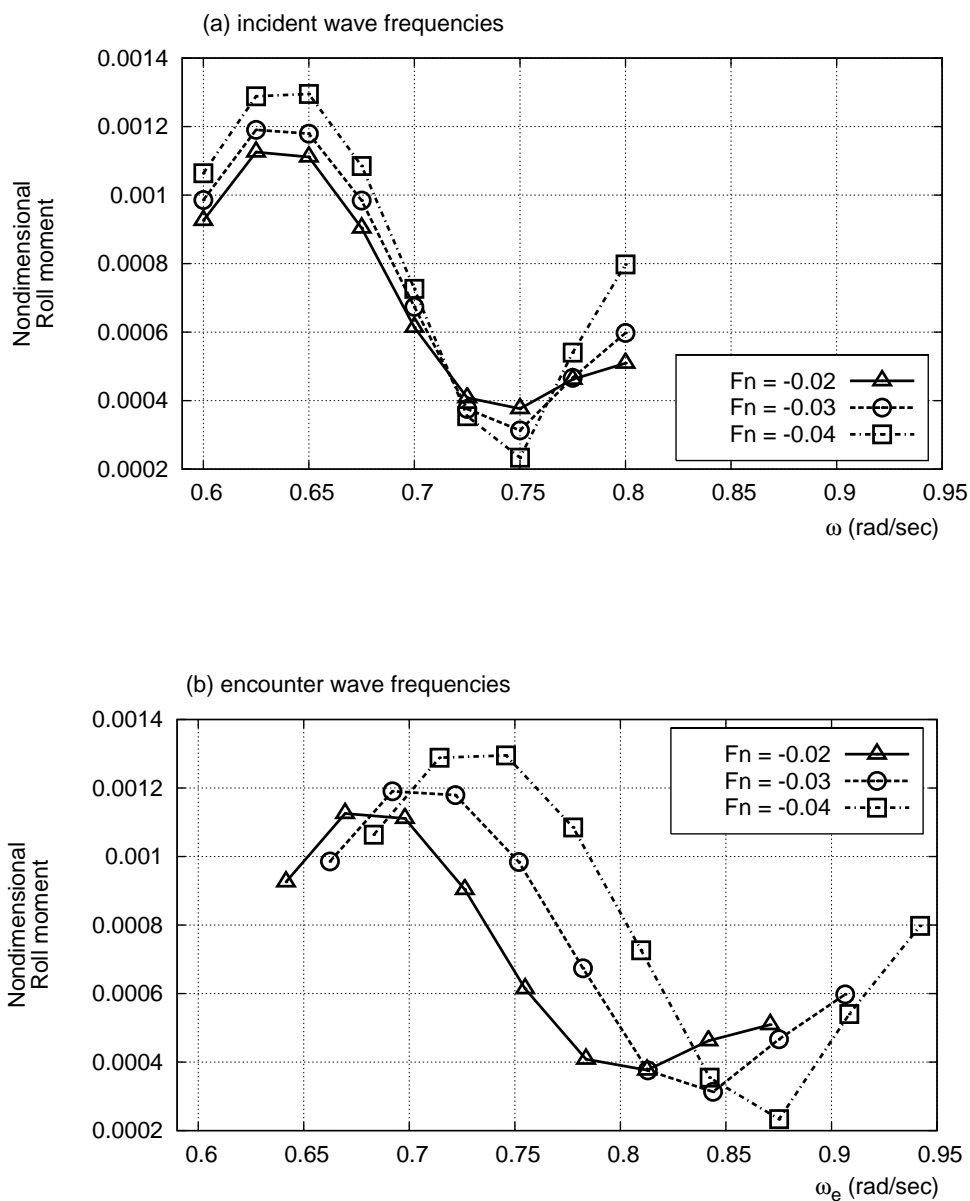


FIGURE F.69. Roll moments for diffracted waves in various frequencies with following sea (collinear current) effect. Wave and current heading angles are -15 degrees.

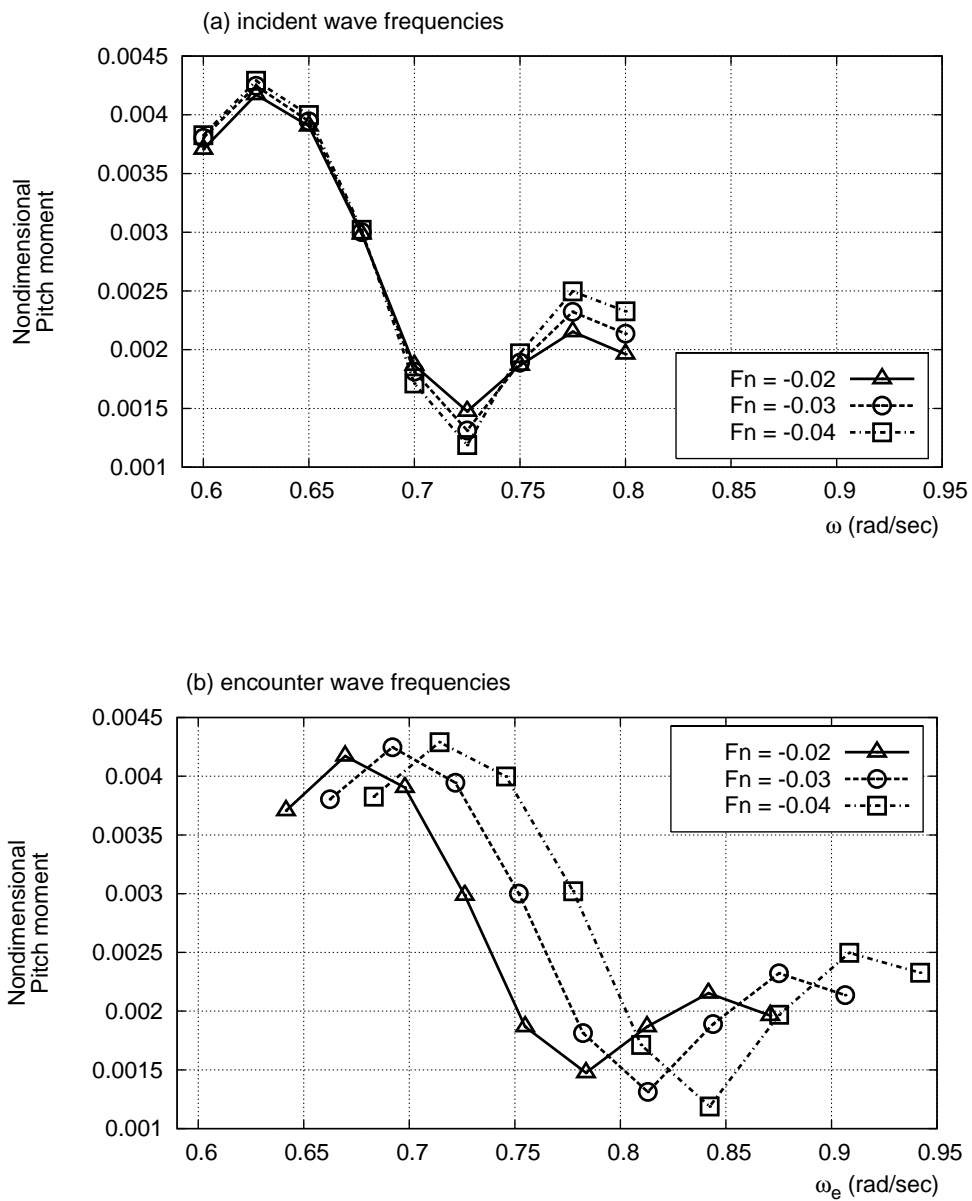


FIGURE F.70. Pitch moments for diffracted waves in various frequencies with following sea (collinear current) effect. Wave and current heading angles are -15 degrees.

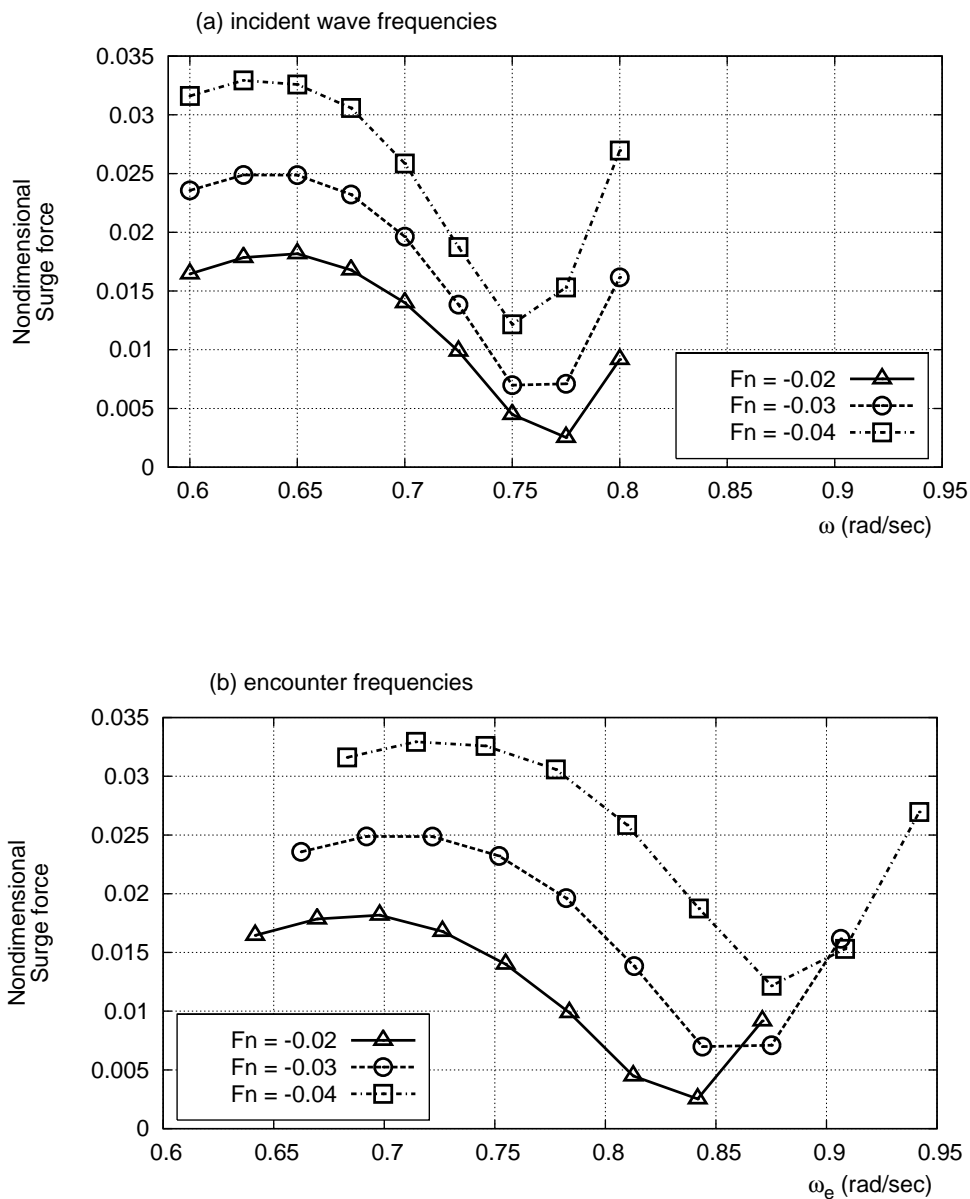


FIGURE F.71. Surge forces for diffracted waves in various frequencies with following sea (collinear current) effect. Wave and current heading angles are -30 degrees.

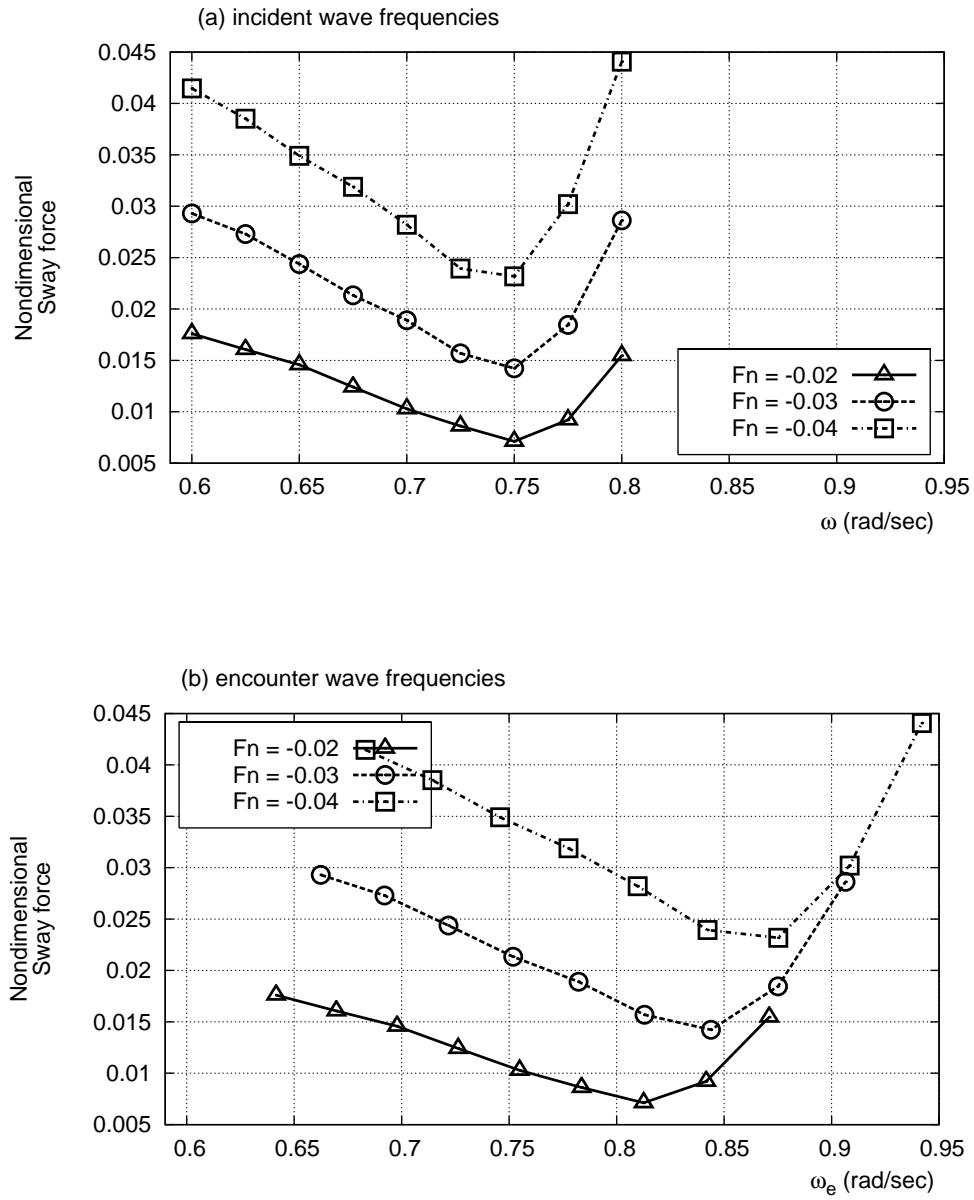


FIGURE F.72. Sway forces for diffracted waves in various frequencies with following sea (collinear current) effect. Wave and current heading angles are -30 degrees.

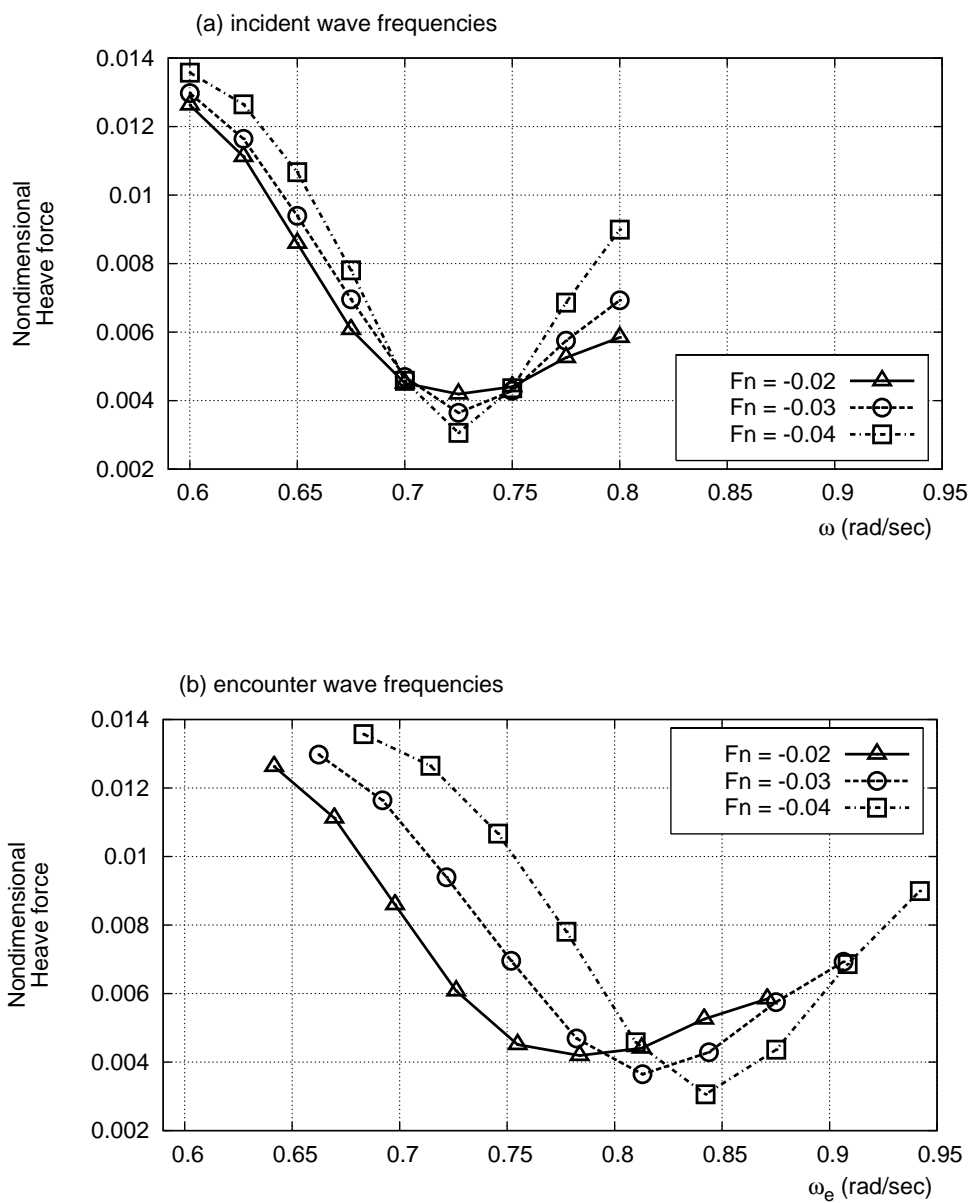


FIGURE F.73. Heave forces for diffracted waves in various frequencies with following sea (collinear current) effect. Wave and current heading angles are -30 degrees.

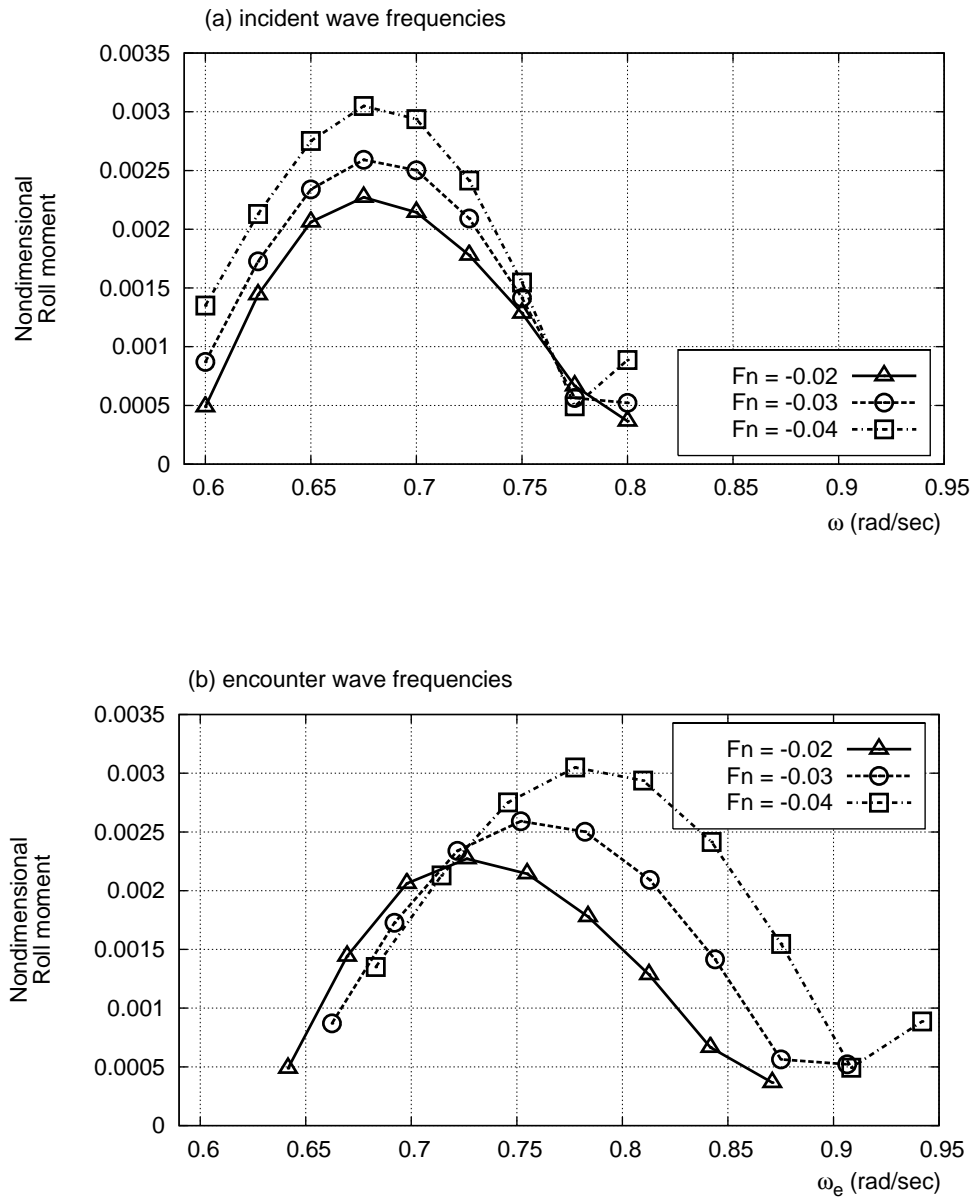


FIGURE F.74. Roll moments for diffracted waves in various frequencies with following sea (collinear current) effect. Wave and current heading angles are -30 degrees.

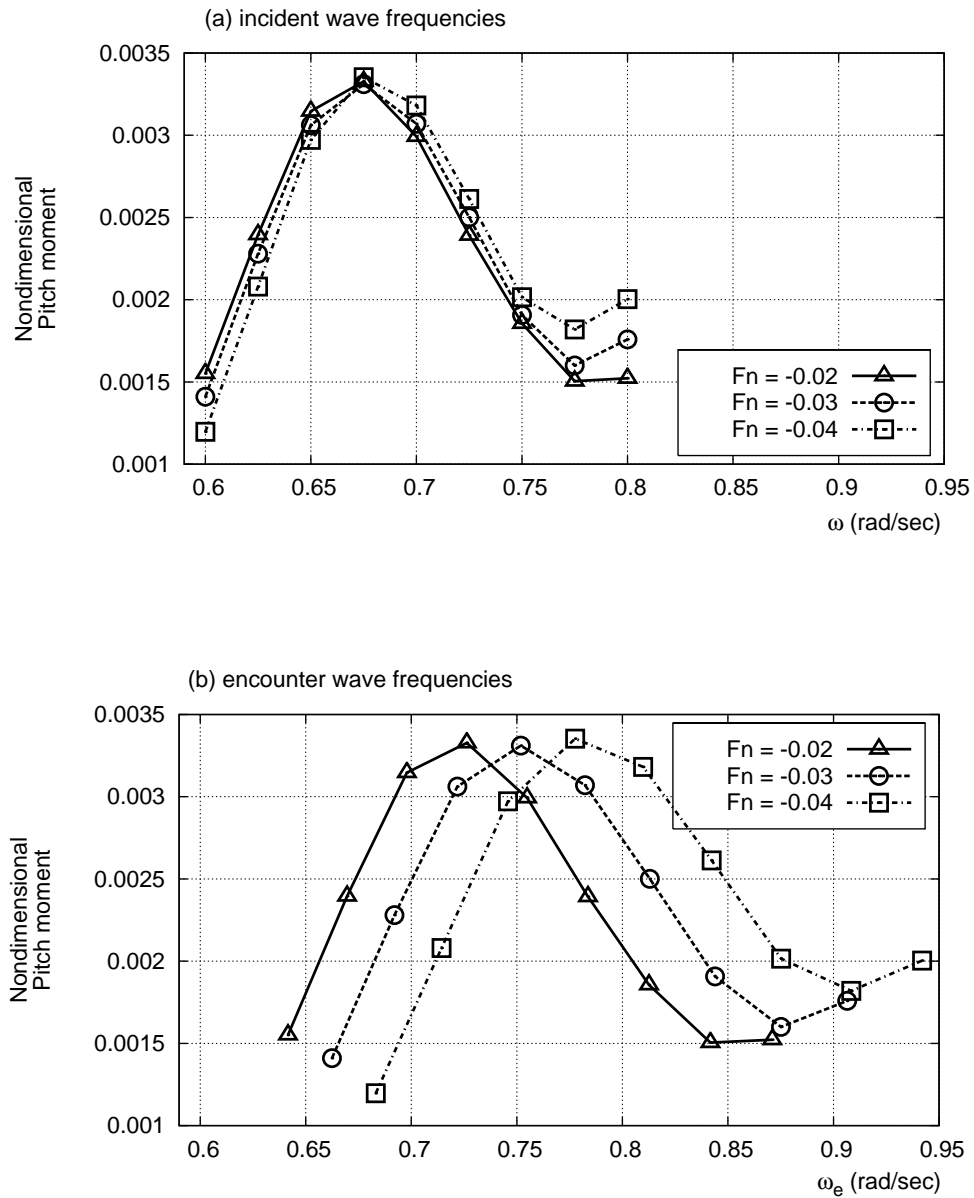


FIGURE F.75. Pitch moments for diffracted waves in various frequencies with following sea (collinear current) effect. Wave and current heading angles are -30 degrees.

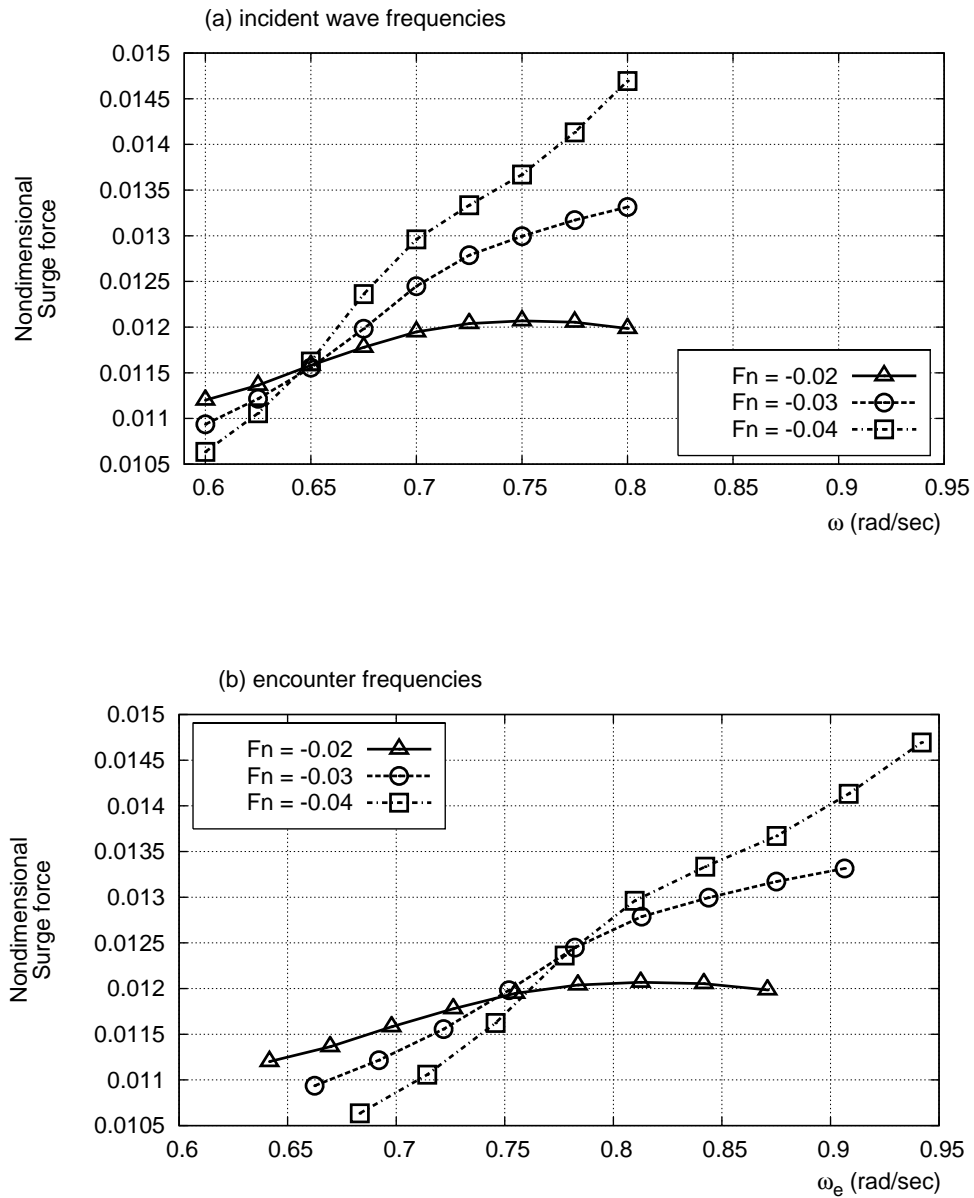


FIGURE F.76. Surge forces for diffracted waves in various frequencies with following sea (collinear current) effect. Wave and current heading angles are zero and -5 degrees respectively respectively.

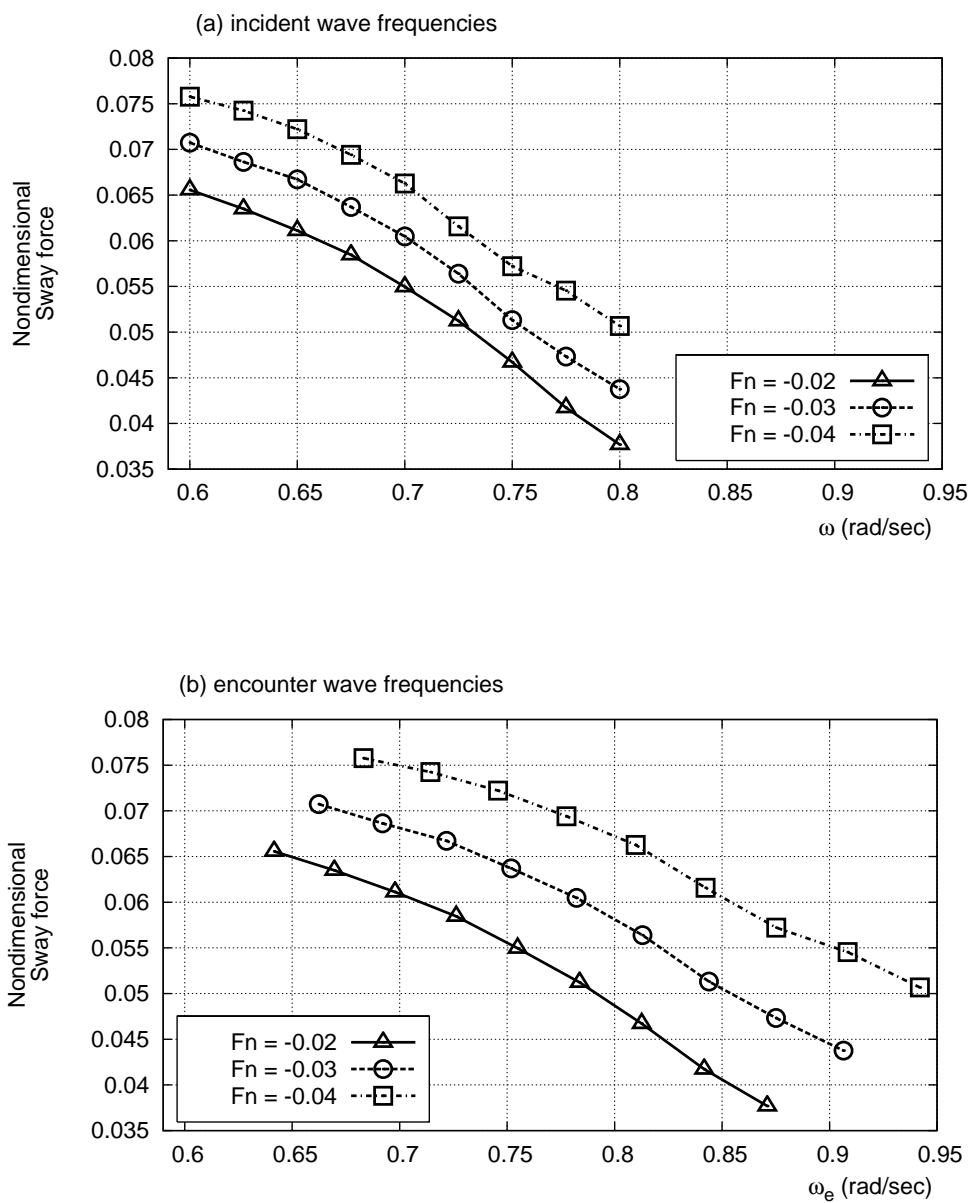


FIGURE F.77. Sway forces for diffracted waves in various frequencies with following sea (collinear current) effect. Wave and current heading angles are zero and -5 degrees respectively.

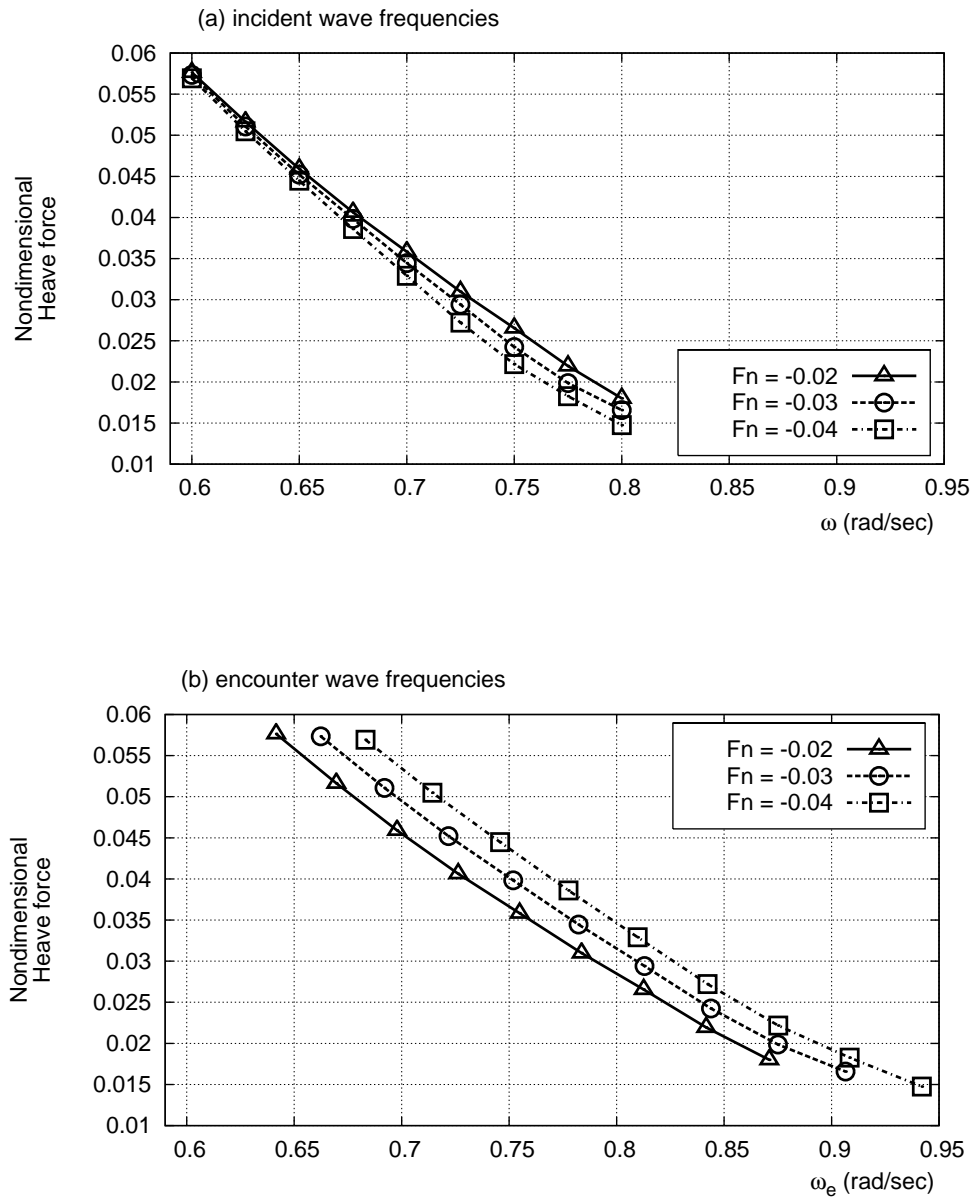


FIGURE F.78. Heave forces for diffracted waves in various frequencies with following sea (collinear current) effect. Wave and current heading angles are zero and -5 degrees respectively.

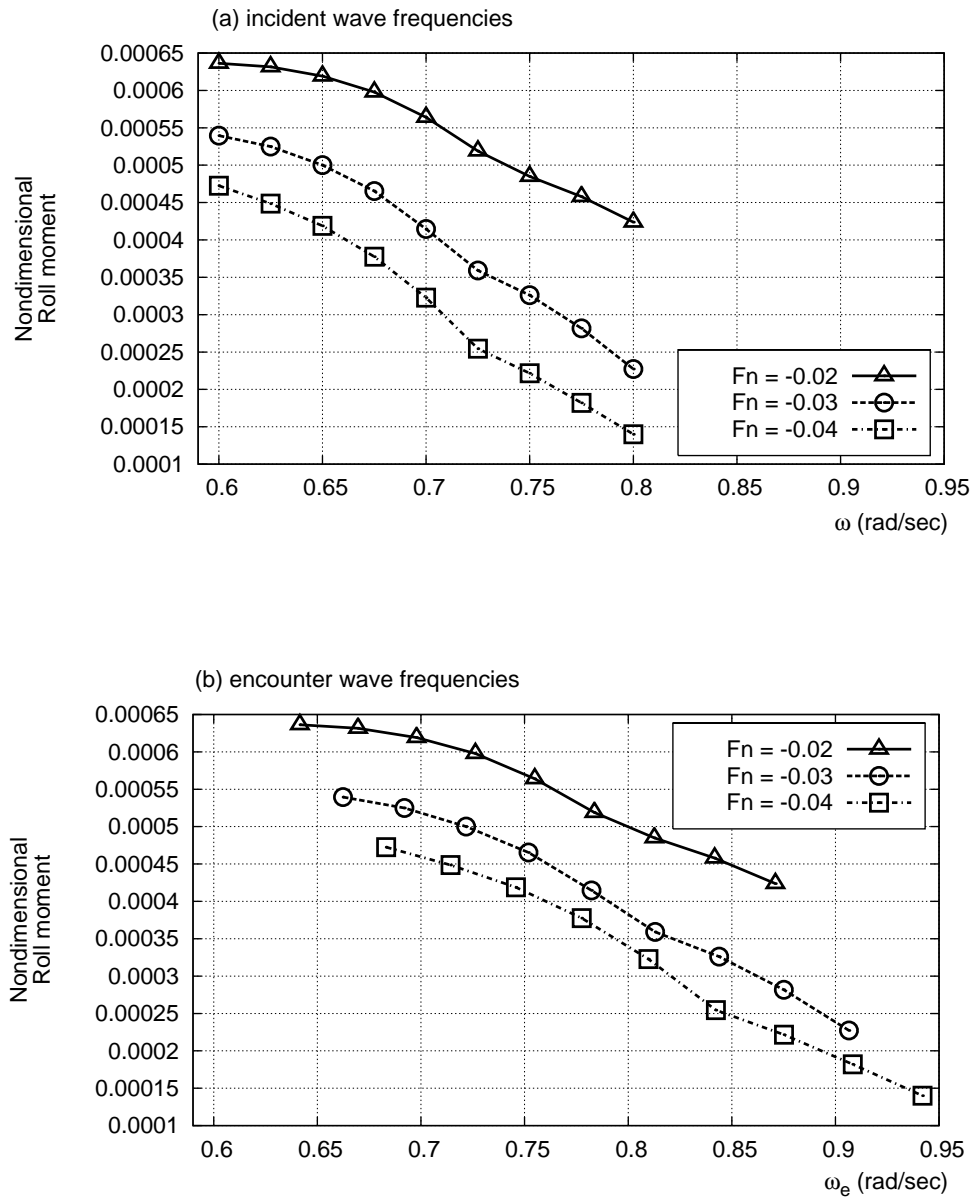


FIGURE F.79. Roll moments for diffracted waves in various frequencies with following sea (collinear current) effect. Wave and current heading angles are zero and -5 degrees respectively.

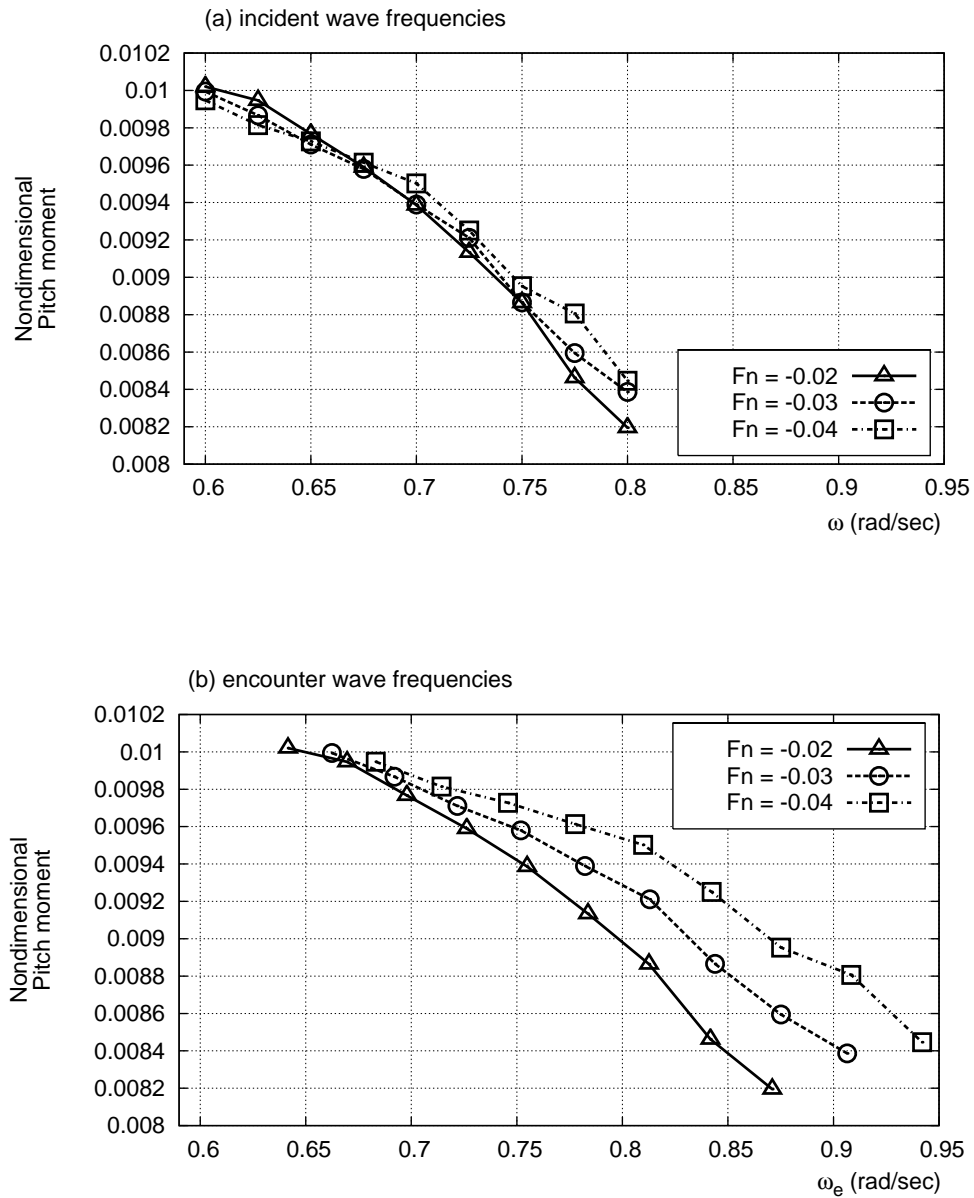


FIGURE F.80. Pitch moments for diffracted waves in various frequencies with following sea (collinear current) effect. Wave and current heading angles are zero and -5 degrees respectively.

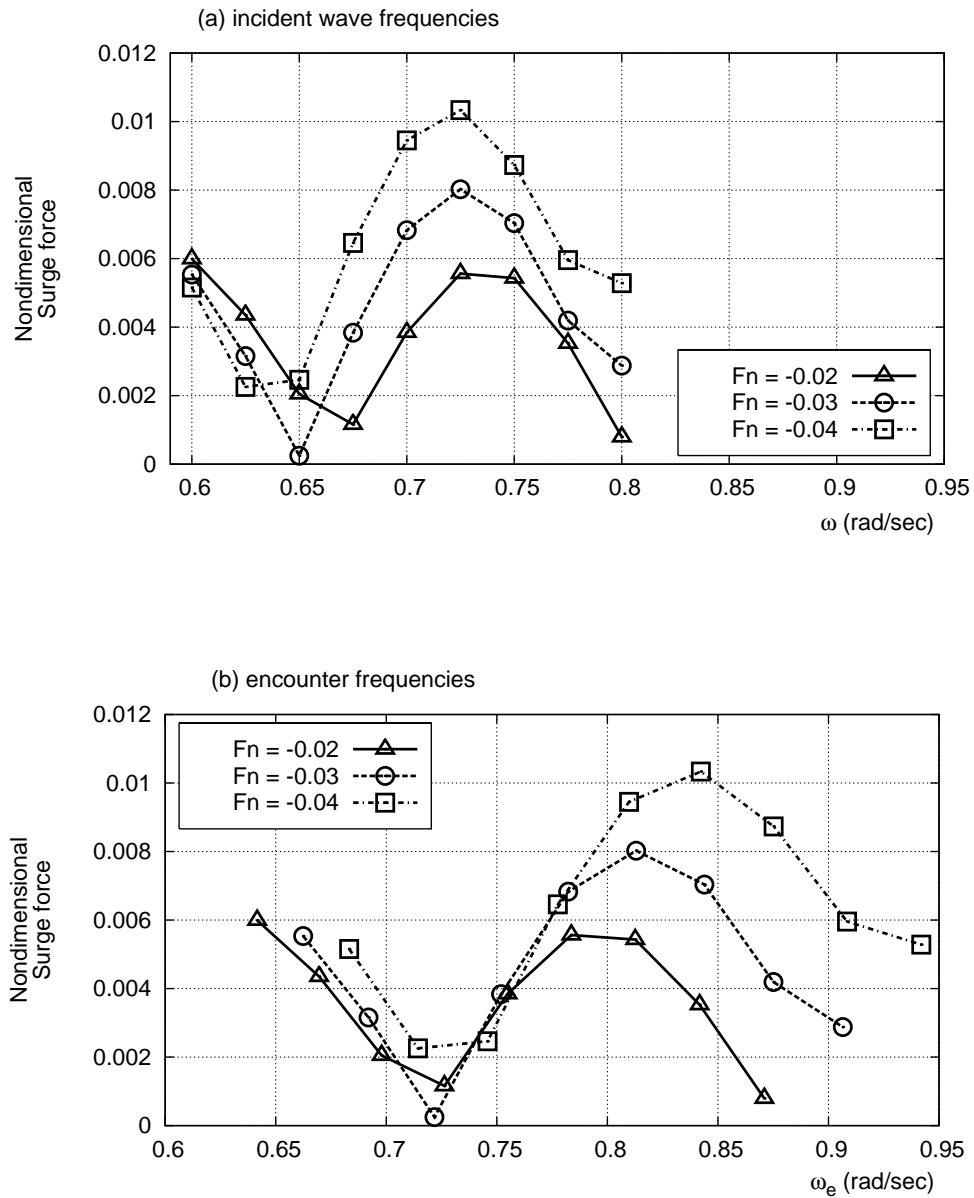


FIGURE F.81. Surge forces for diffracted waves in various frequencies with following sea (collinear current) effect. Wave and current heading angles are zero and -10 degrees respectively respectively.

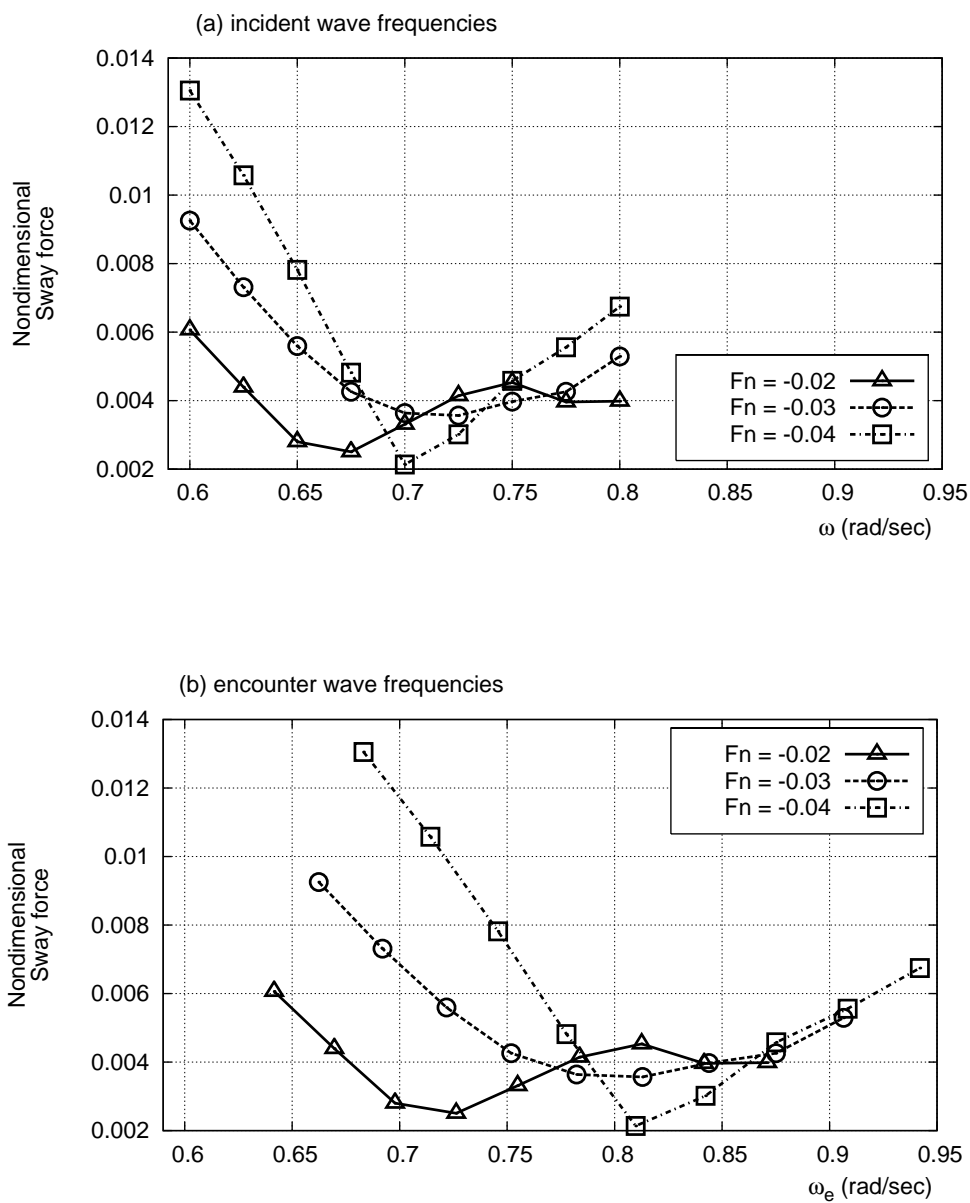


FIGURE F.82. Sway forces for diffracted waves in various frequencies with following sea (collinear current) effect. Wave and current heading angles are zero and -10 degrees respectively.

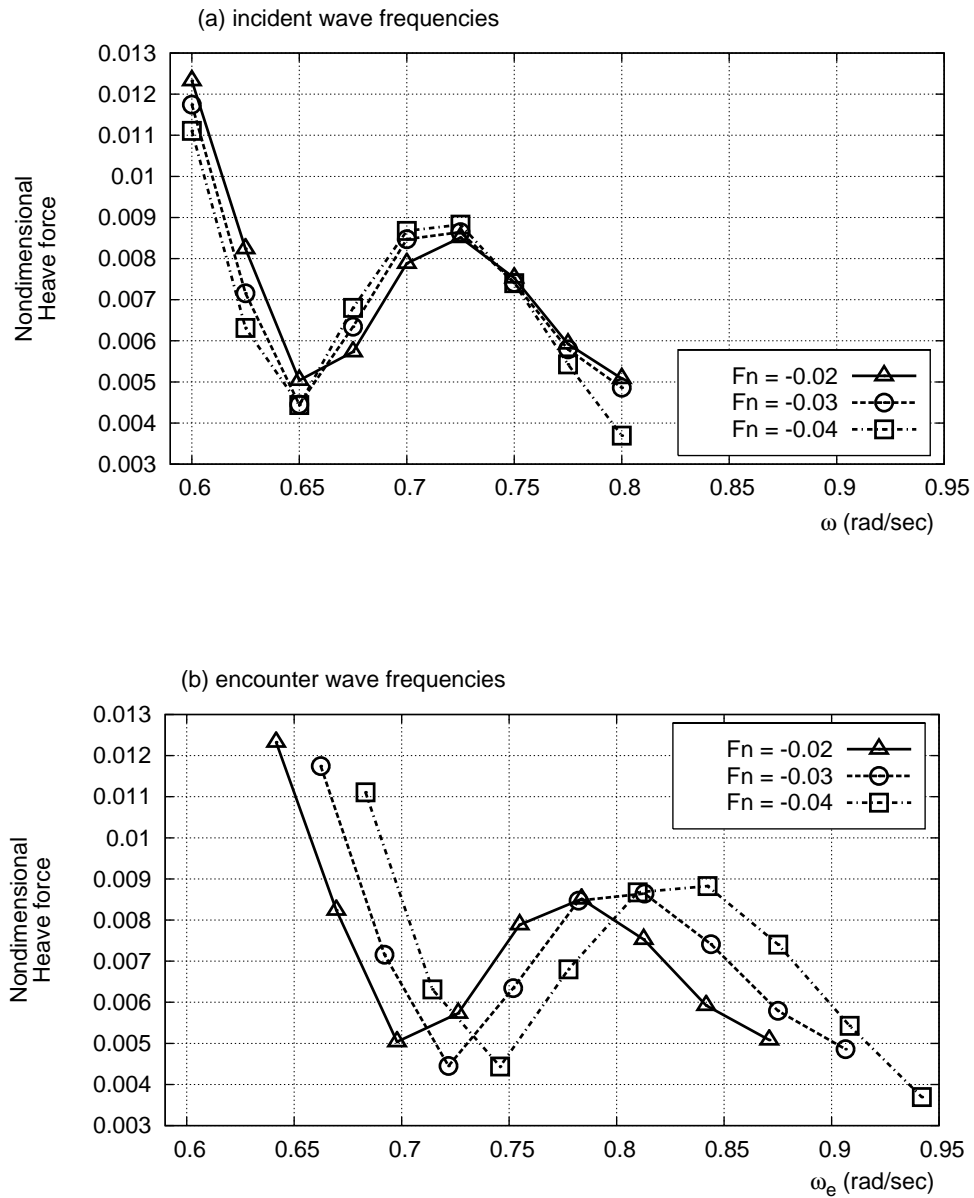


FIGURE F.83. Heave forces for diffracted waves in various frequencies with following sea (collinear current) effect. Wave and current heading angles are zero and -10 degrees respectively.

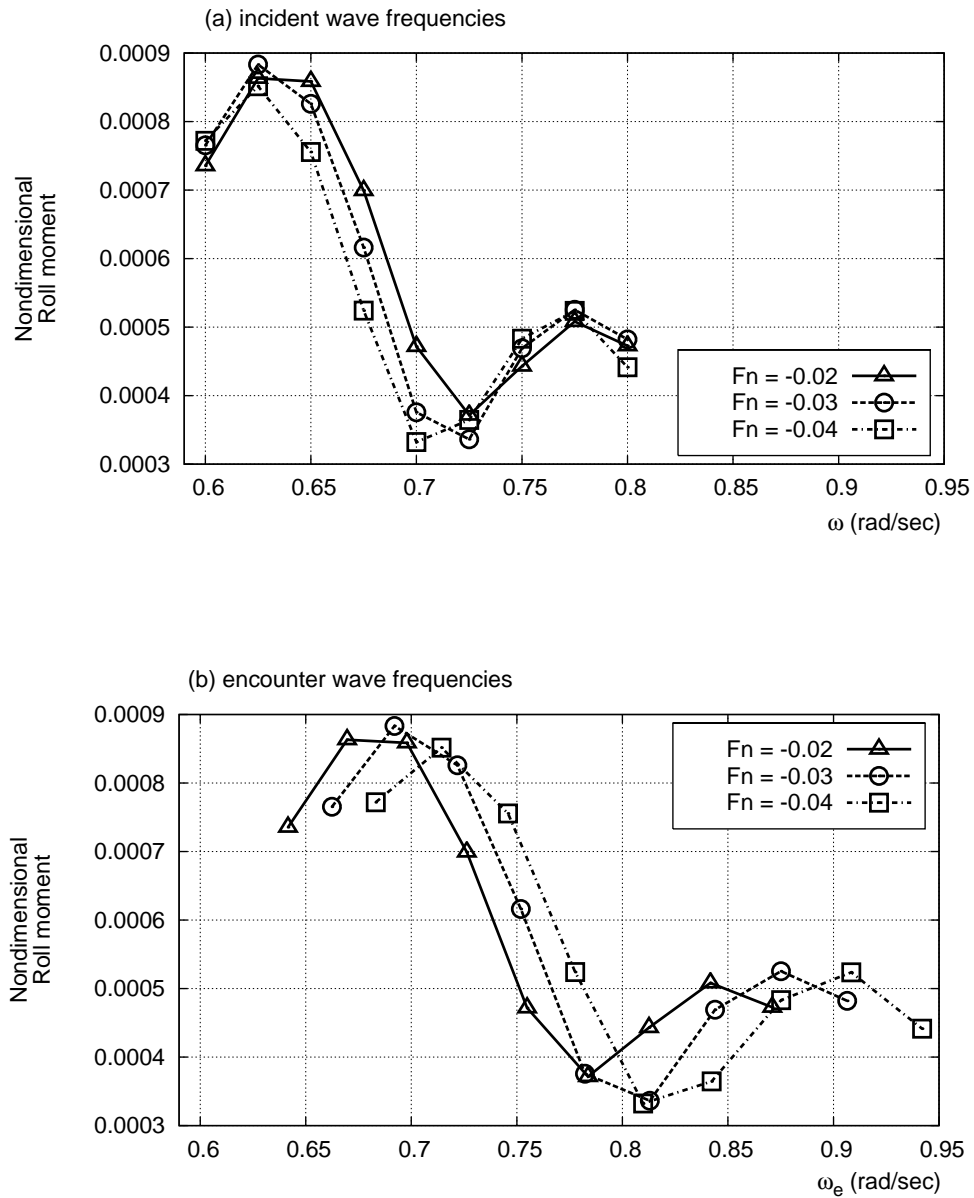


FIGURE F.84. Roll moments for diffracted waves in various frequencies with following sea (collinear current) effect. Wave and current heading angles are zero and -10 degrees respectively.

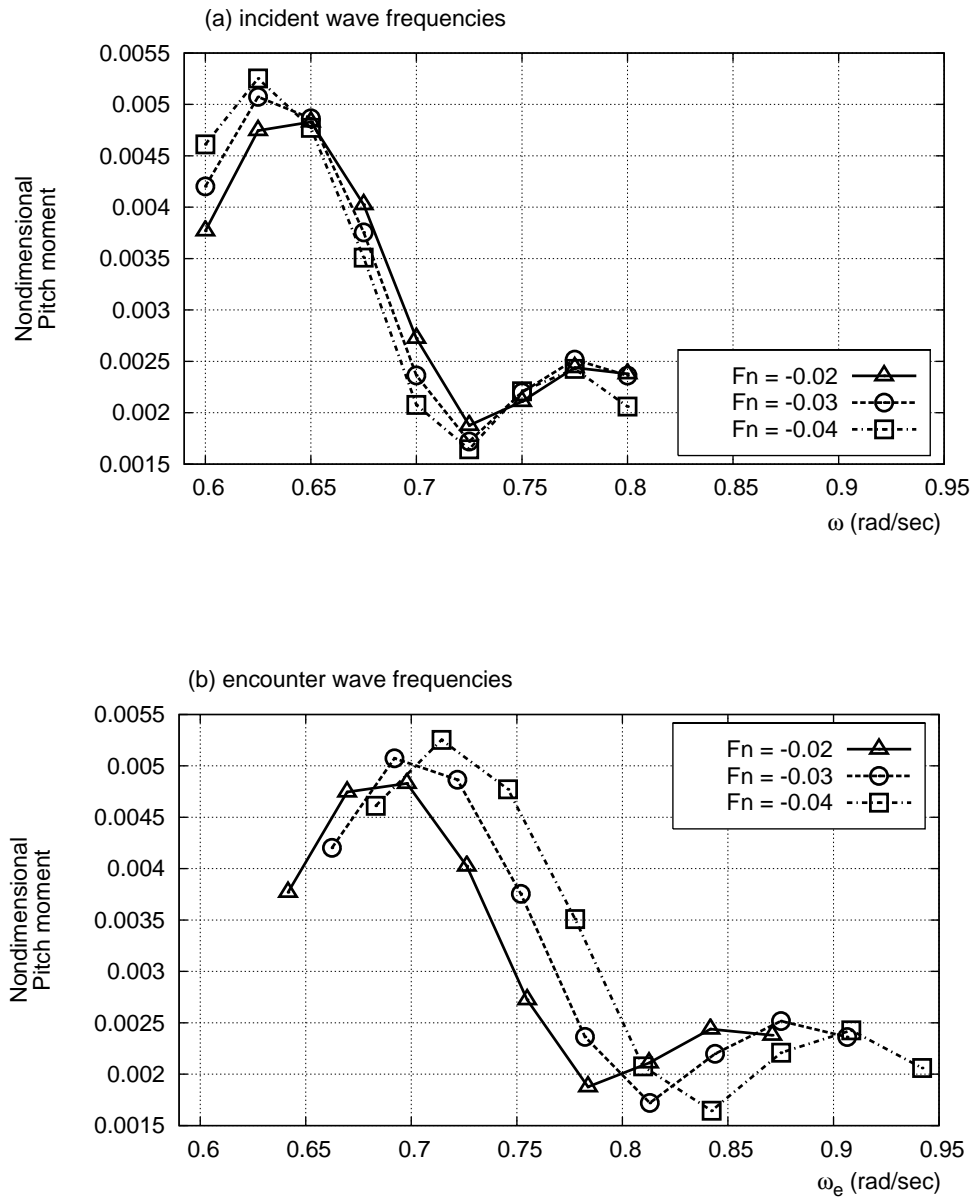


FIGURE F.85. Pitch moments for diffracted waves in various frequencies with following sea (collinear current) effect. Wave and current heading angles are zero and -10 degrees respectively.

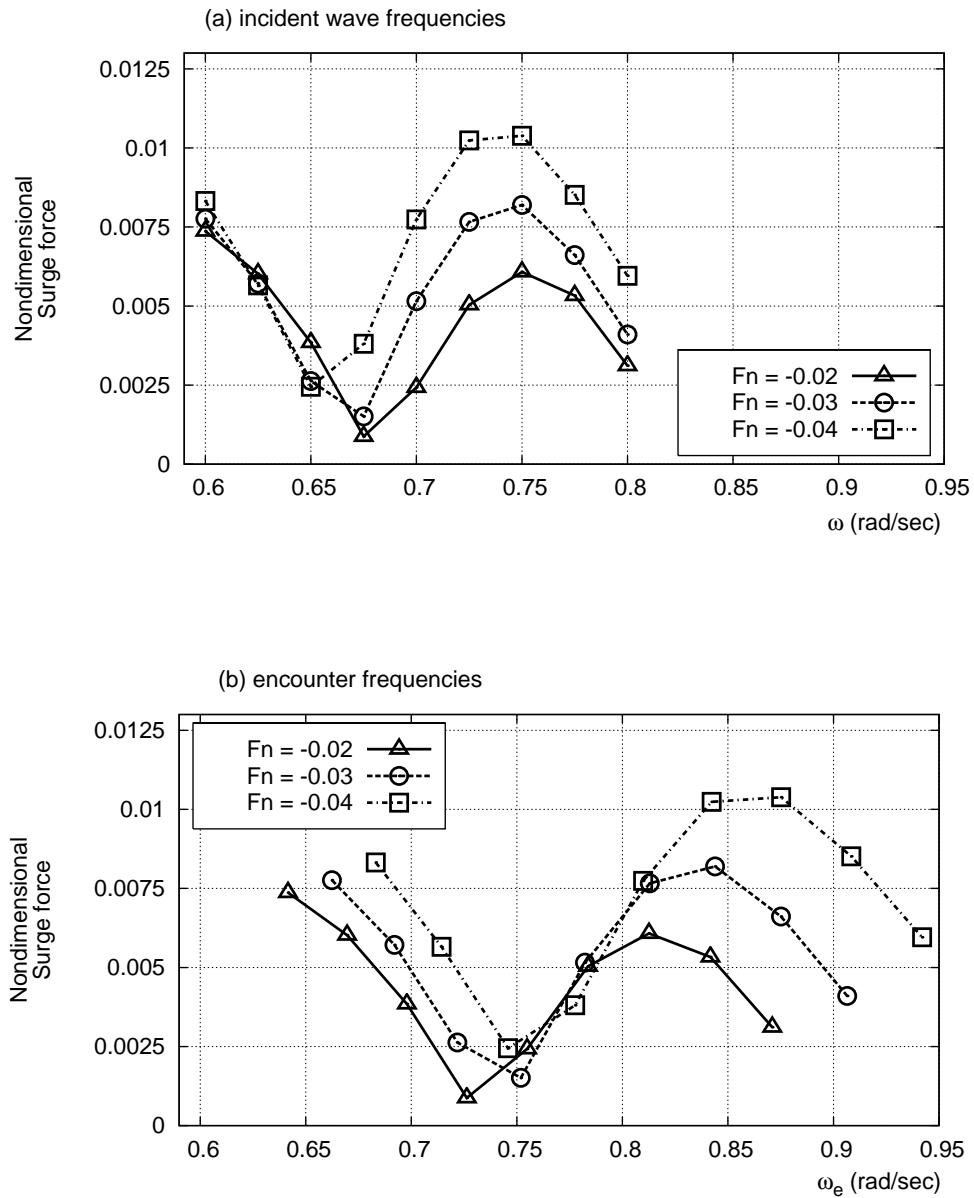


FIGURE F.86. Surge forces for diffracted waves in various frequencies with following sea (collinear current) effect. Wave and current heading angles are 5 and -5 degrees respectively respectively.

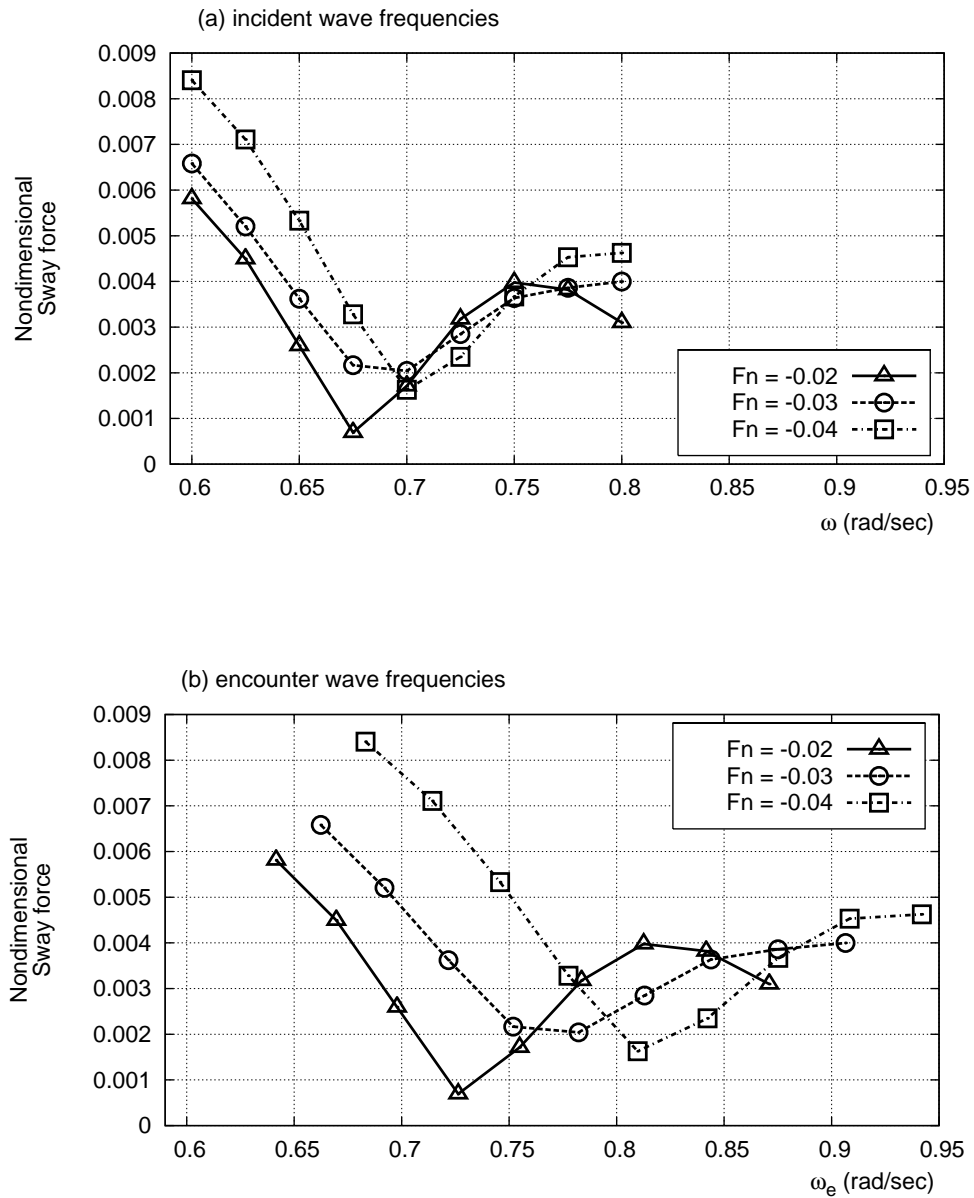


FIGURE F.87. Sway forces for diffracted waves in various frequencies with following sea (collinear current) effect. Wave and current heading angles are 5 and -5 degrees respectively.

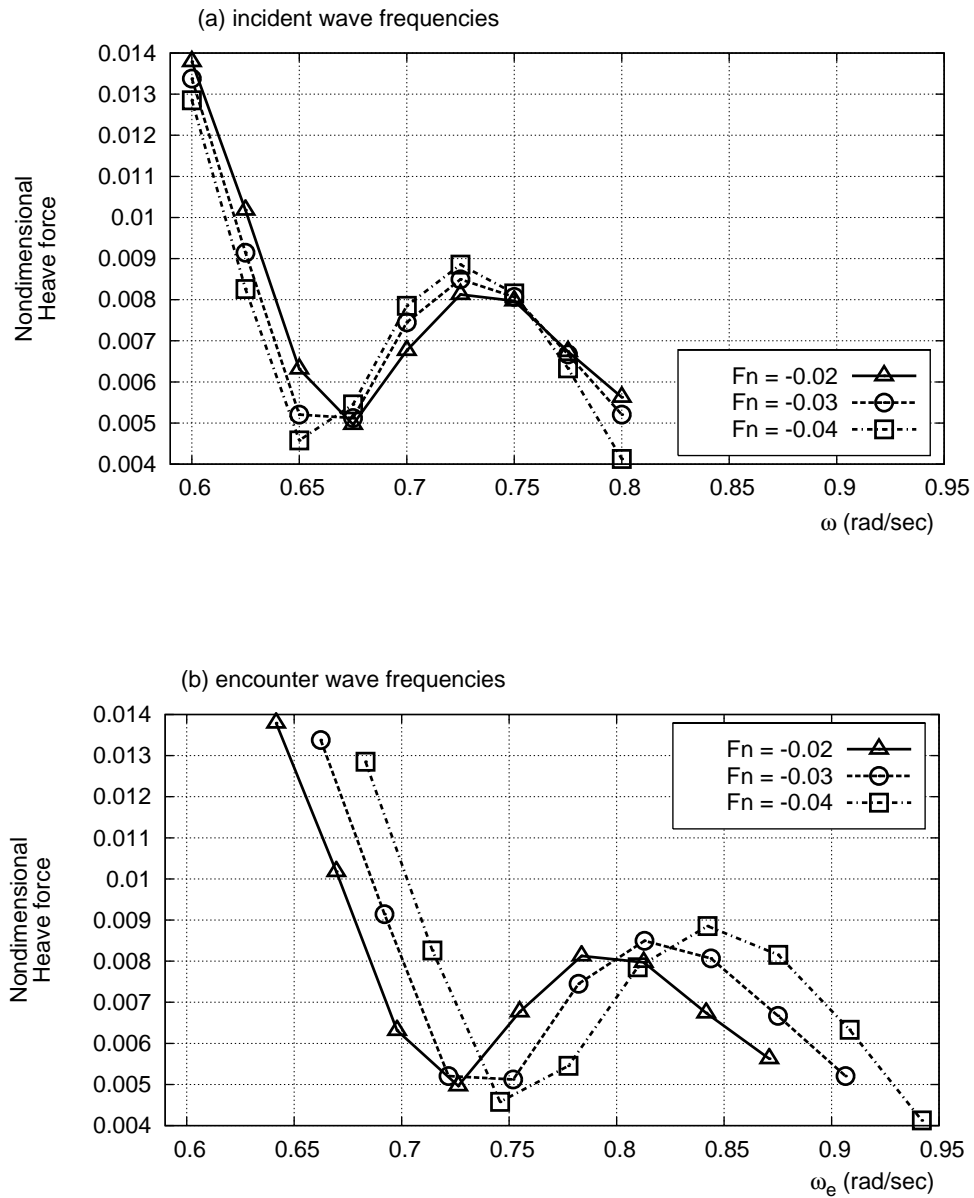


FIGURE F.88. Heave forces for diffracted waves in various frequencies with following sea (collinear current) effect. Wave and current heading angles are 5 and -5 degrees respectively.

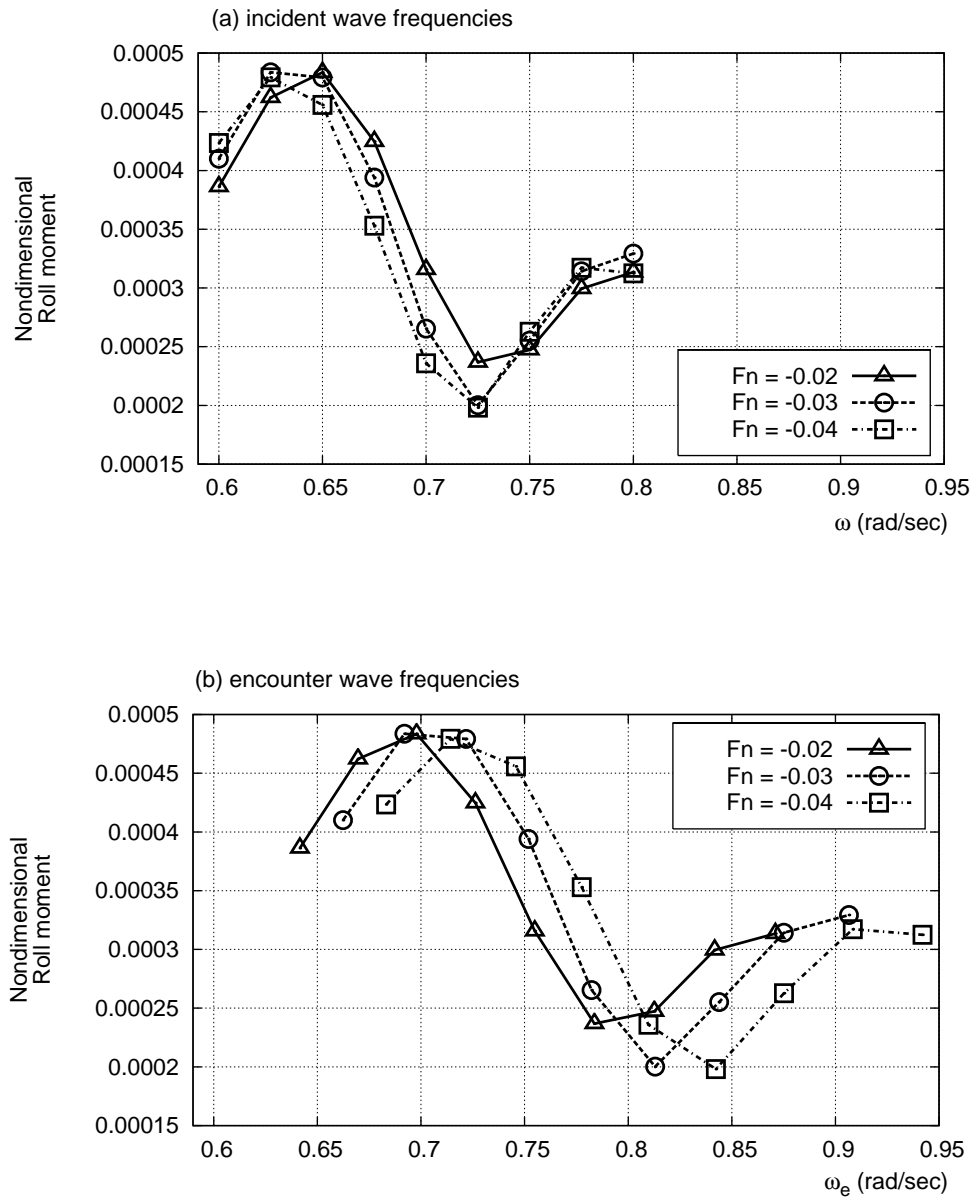


FIGURE F.89. Roll moments for diffracted waves in various frequencies with following sea (collinear current) effect. Wave and current heading angles are 5 and -5 degrees respectively.

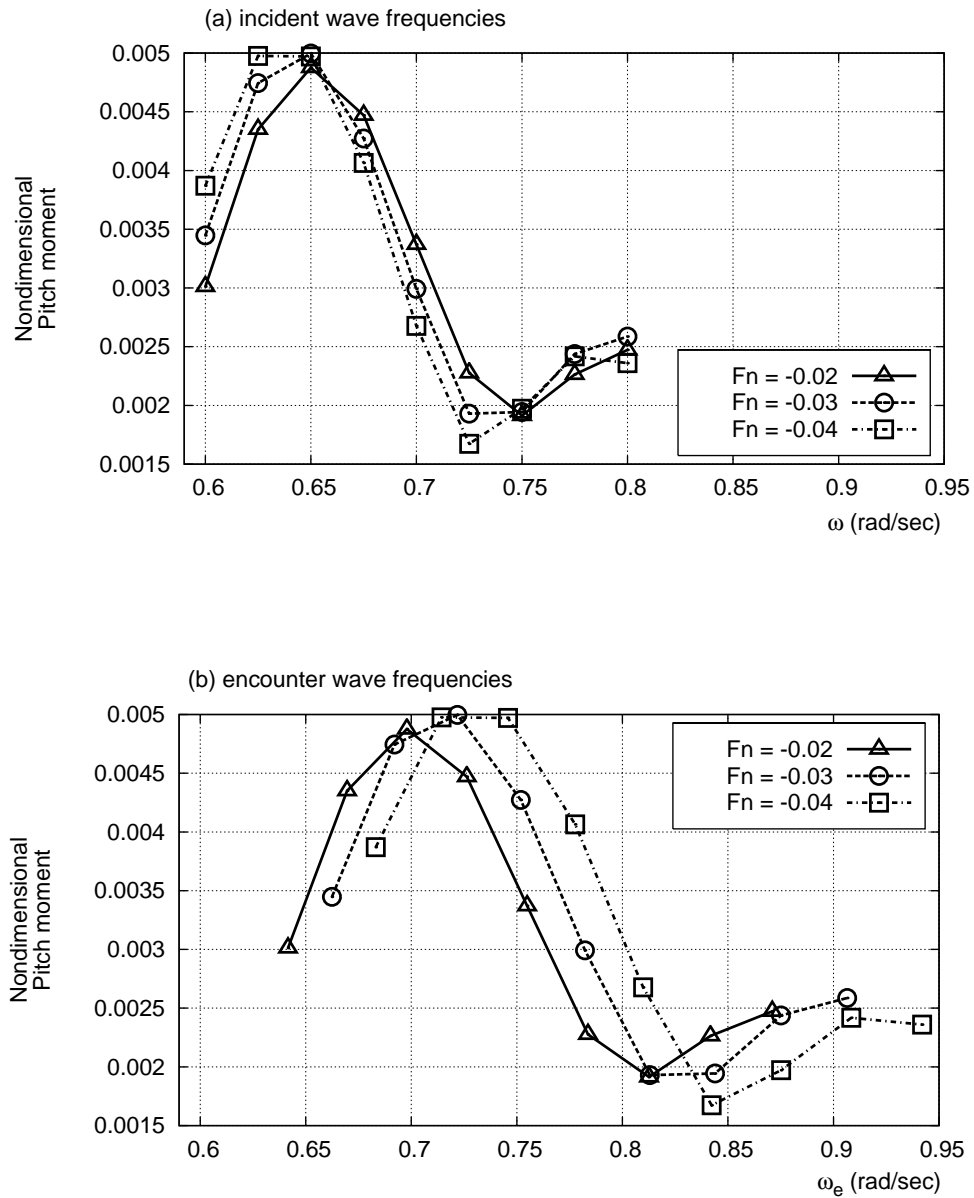


FIGURE F.90. Pitch moments for diffracted waves in various frequencies with following sea (collinear current) effect. Wave and current heading angles are 5 and -5 degrees respectively.

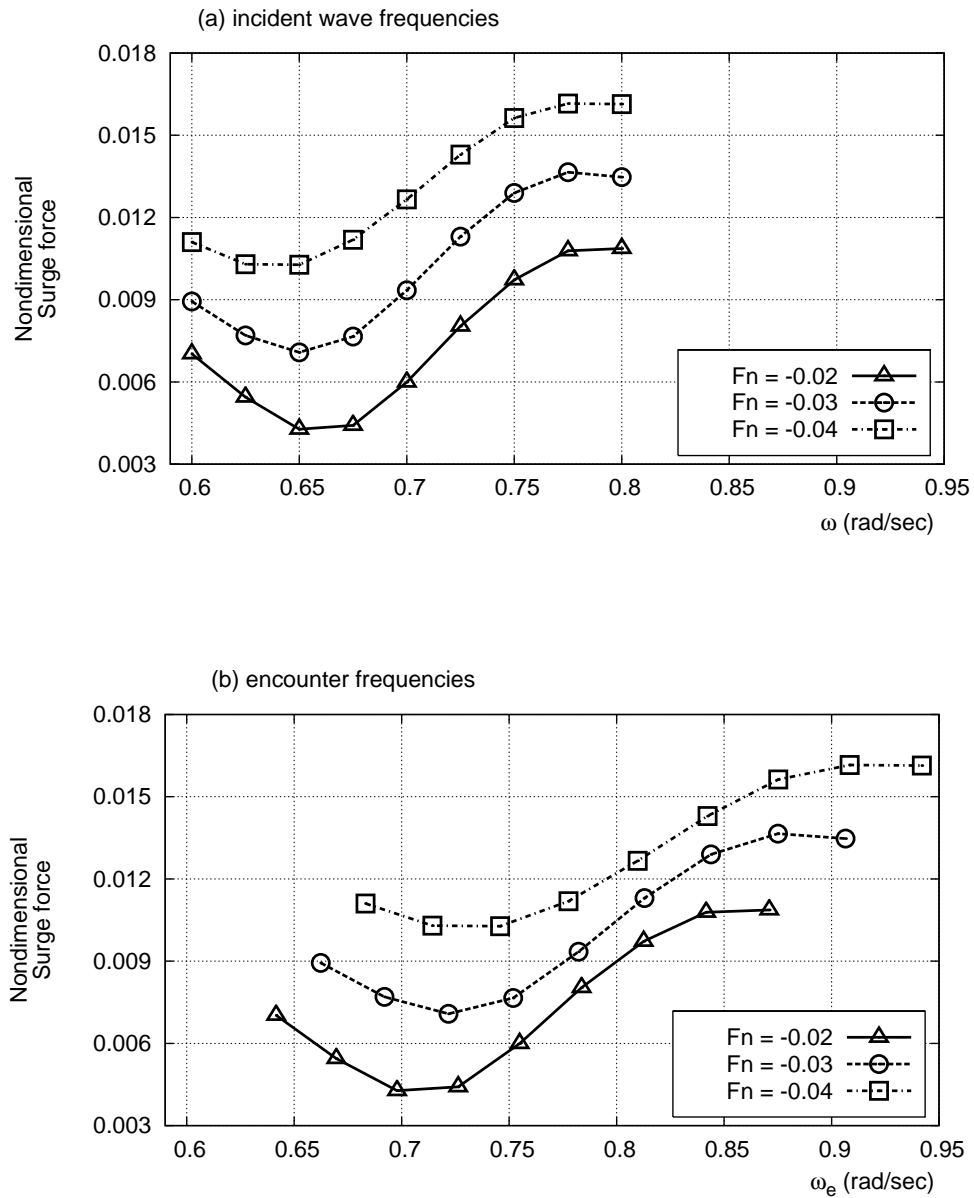


FIGURE F.91. Surge forces for diffracted waves in various frequencies with following sea (collinear current) effect. Wave and current heading angles are 10 and -10 degrees respectively respectively.

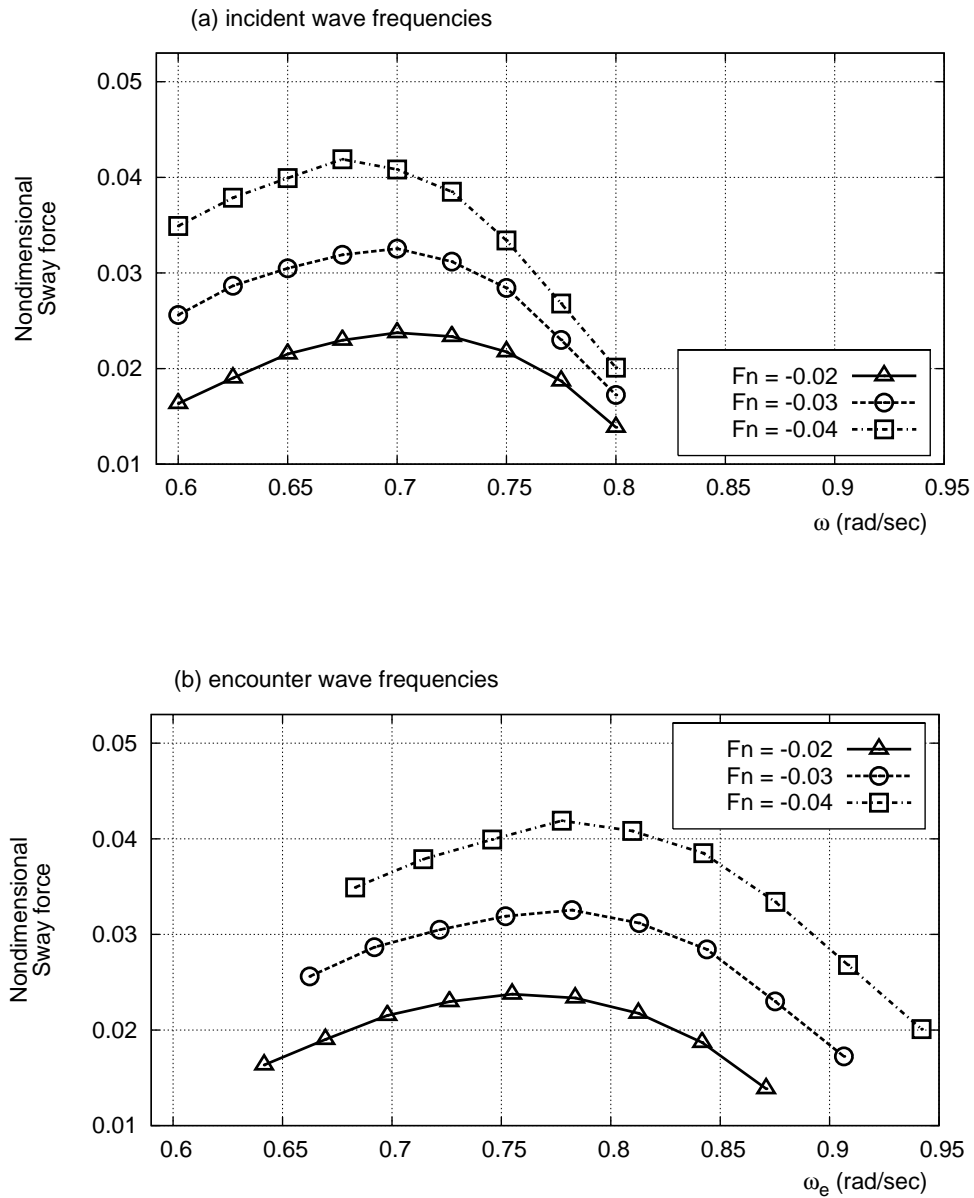


FIGURE F.92. Sway forces for diffracted waves in various frequencies with following sea (collinear current) effect. Wave and current heading angles are 10 and -10 degrees respectively.

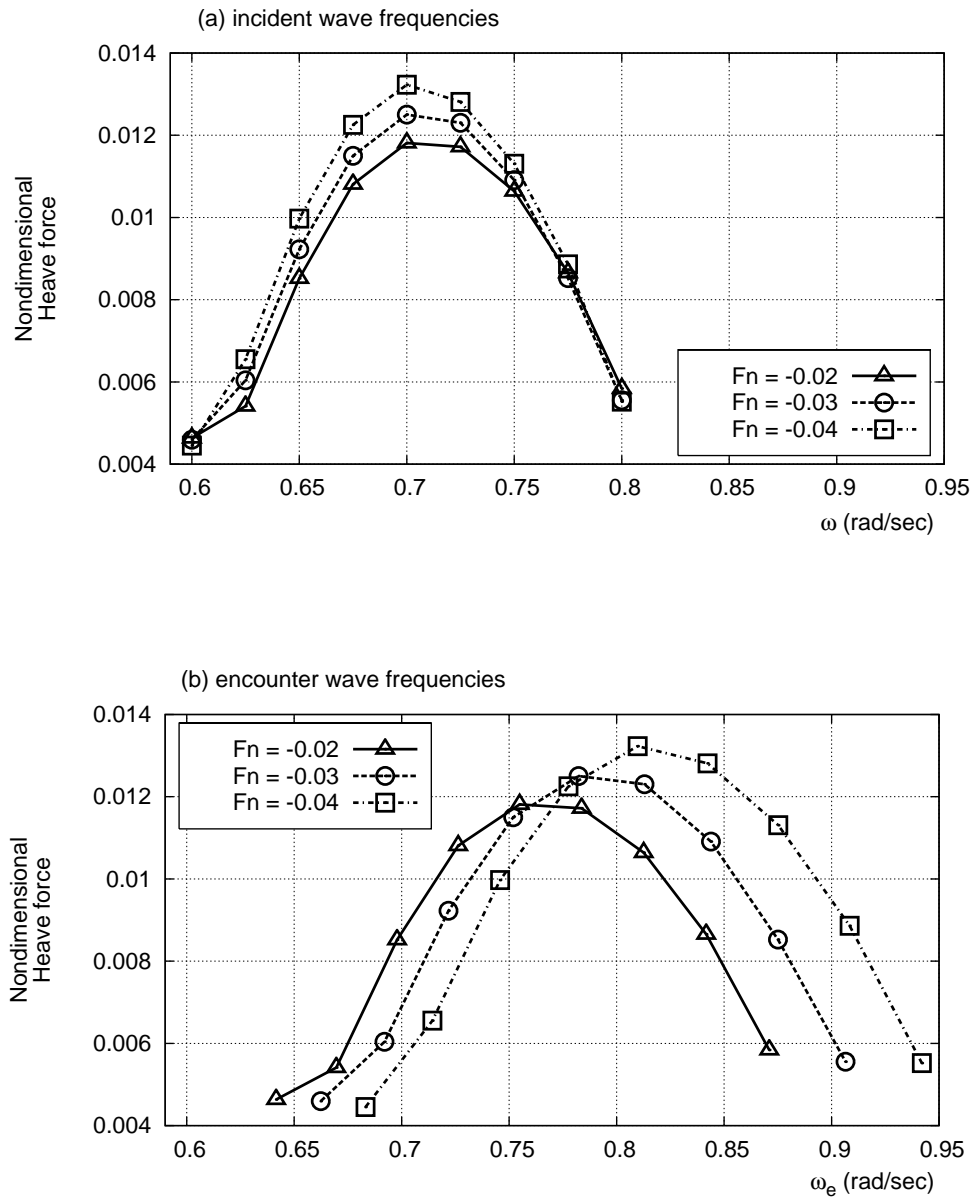


FIGURE F.93. Heave forces for diffracted waves in various frequencies with following sea (collinear current) effect. Wave and current heading angles are 10 and -10 degrees respectively.

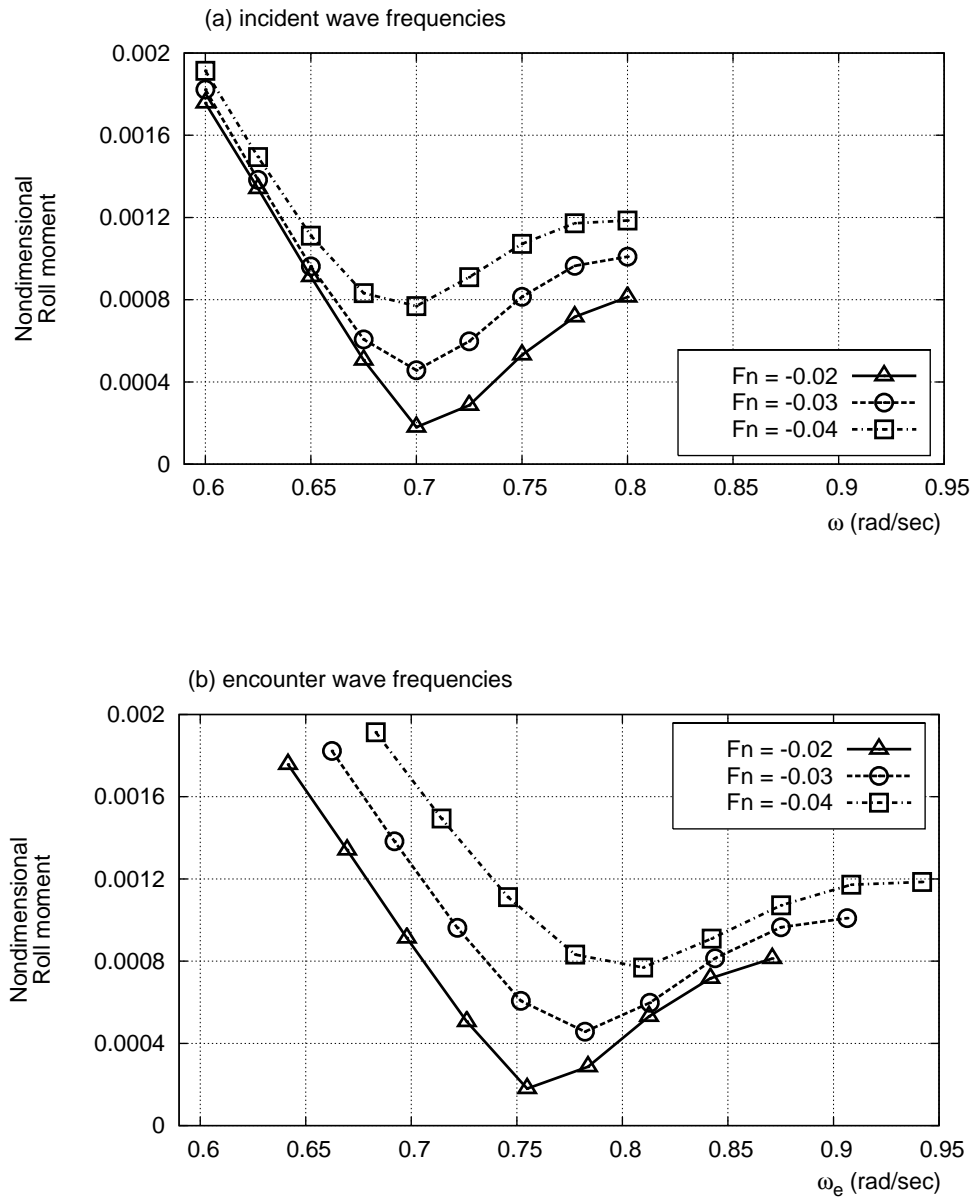


FIGURE F.94. Roll moments for diffracted waves in various frequencies with following sea (collinear current) effect. Wave and current heading angles are 10 and -10 degrees respectively.

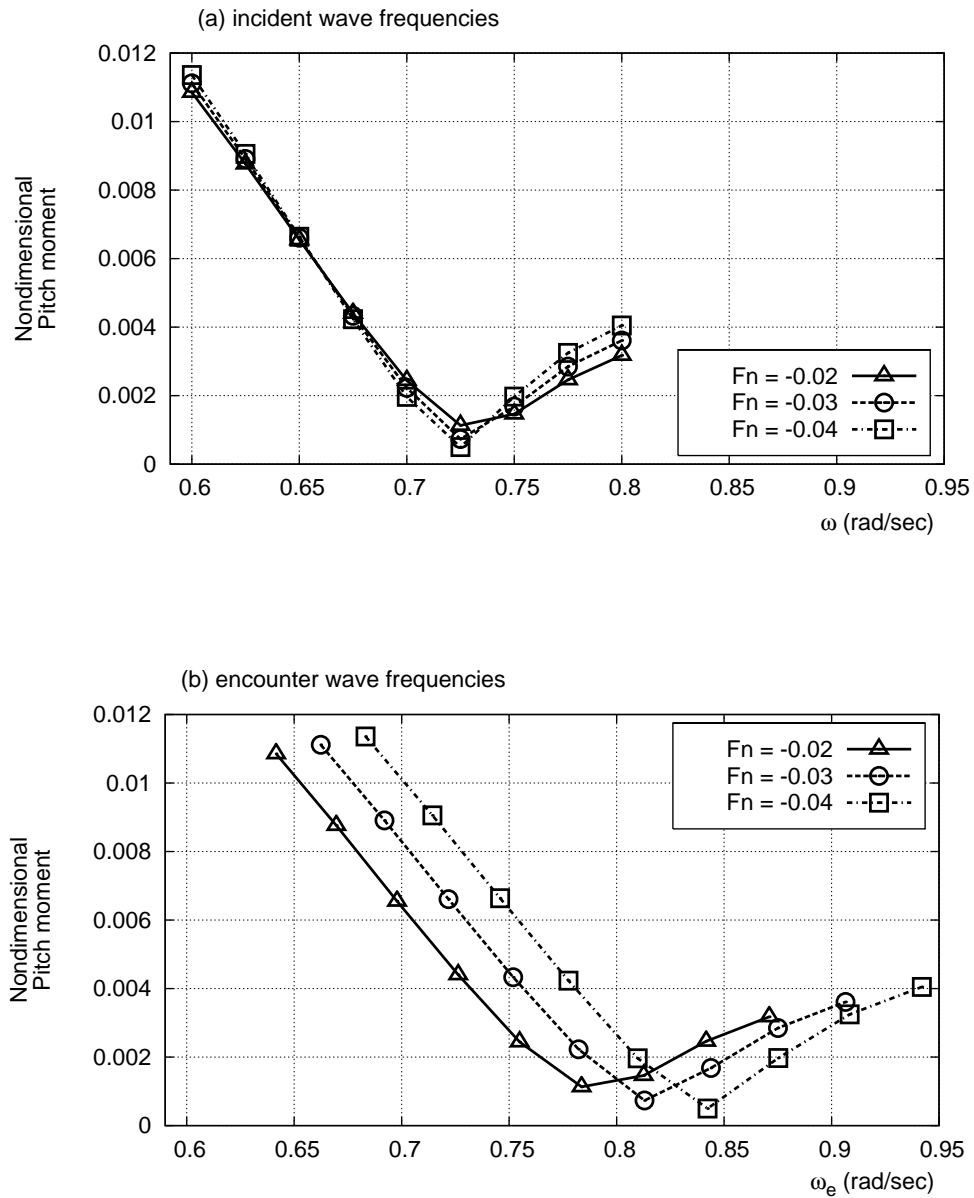


FIGURE F.95. Pitch moments for diffracted waves in various frequencies with following sea (collinear current) effect. Wave and current heading angles are 10 and -10 degrees respectively.

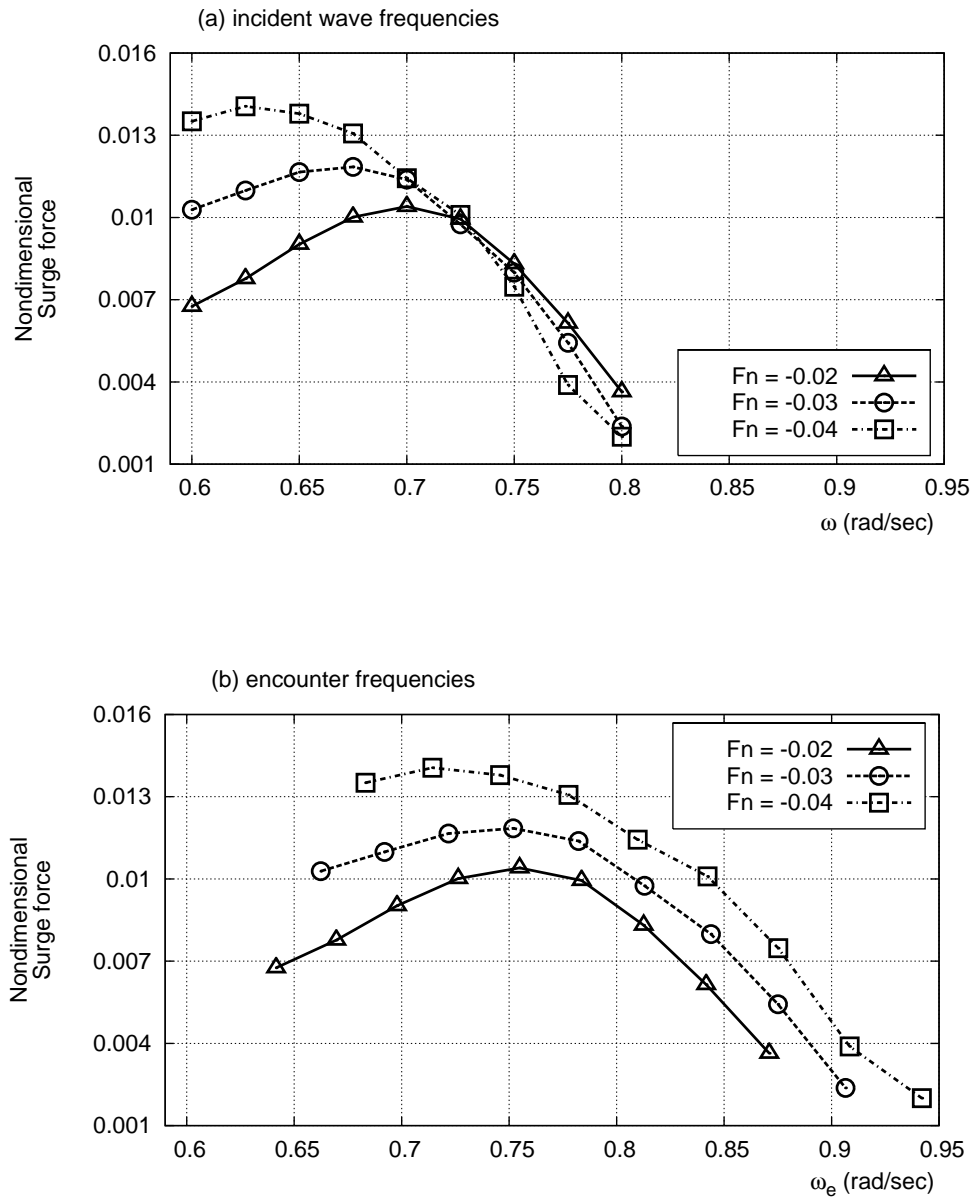


FIGURE F.96. Surge forces for diffracted waves in various frequencies with following sea (collinear current) effect. Wave and current heading angles are 15 and -15 degrees respectively respectively.

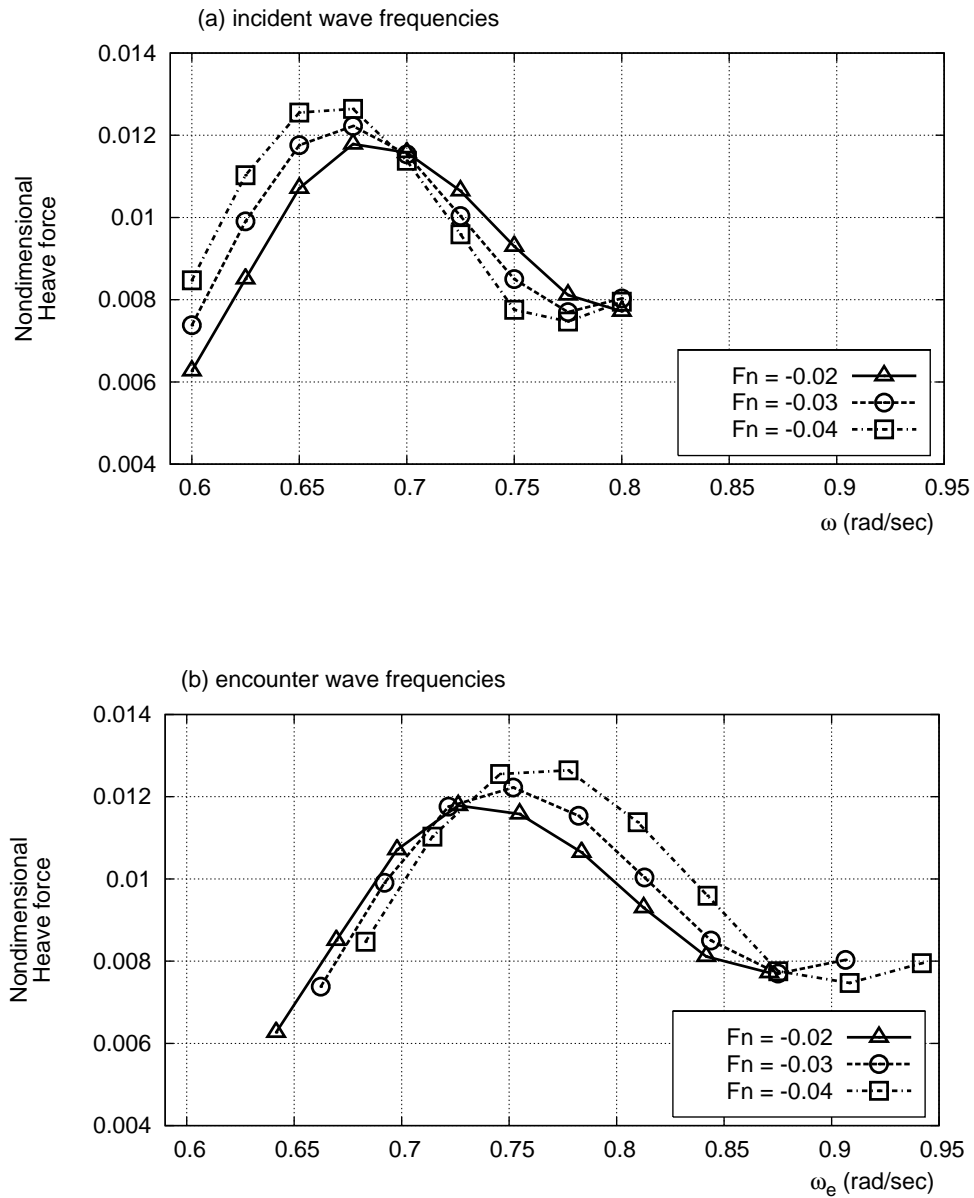


FIGURE F.97. Heave forces for diffracted waves in various frequencies with following sea (collinear current) effect. Wave and current heading angles are 15 and -15 degrees respectively.

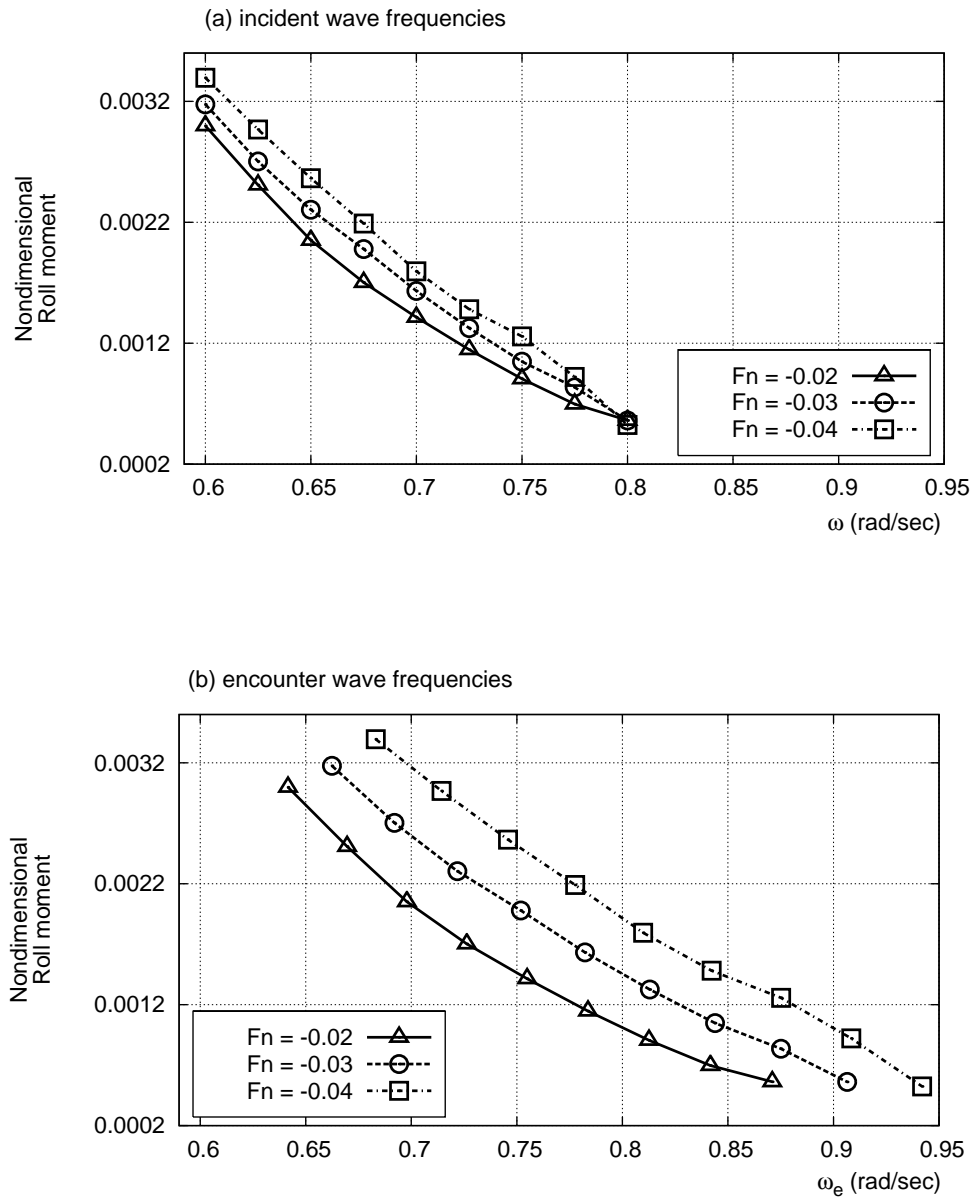


FIGURE F.98. Roll moments for diffracted waves in various frequencies with following sea (collinear current) effect. Wave and current heading angles are 15 and -15 degrees respectively.

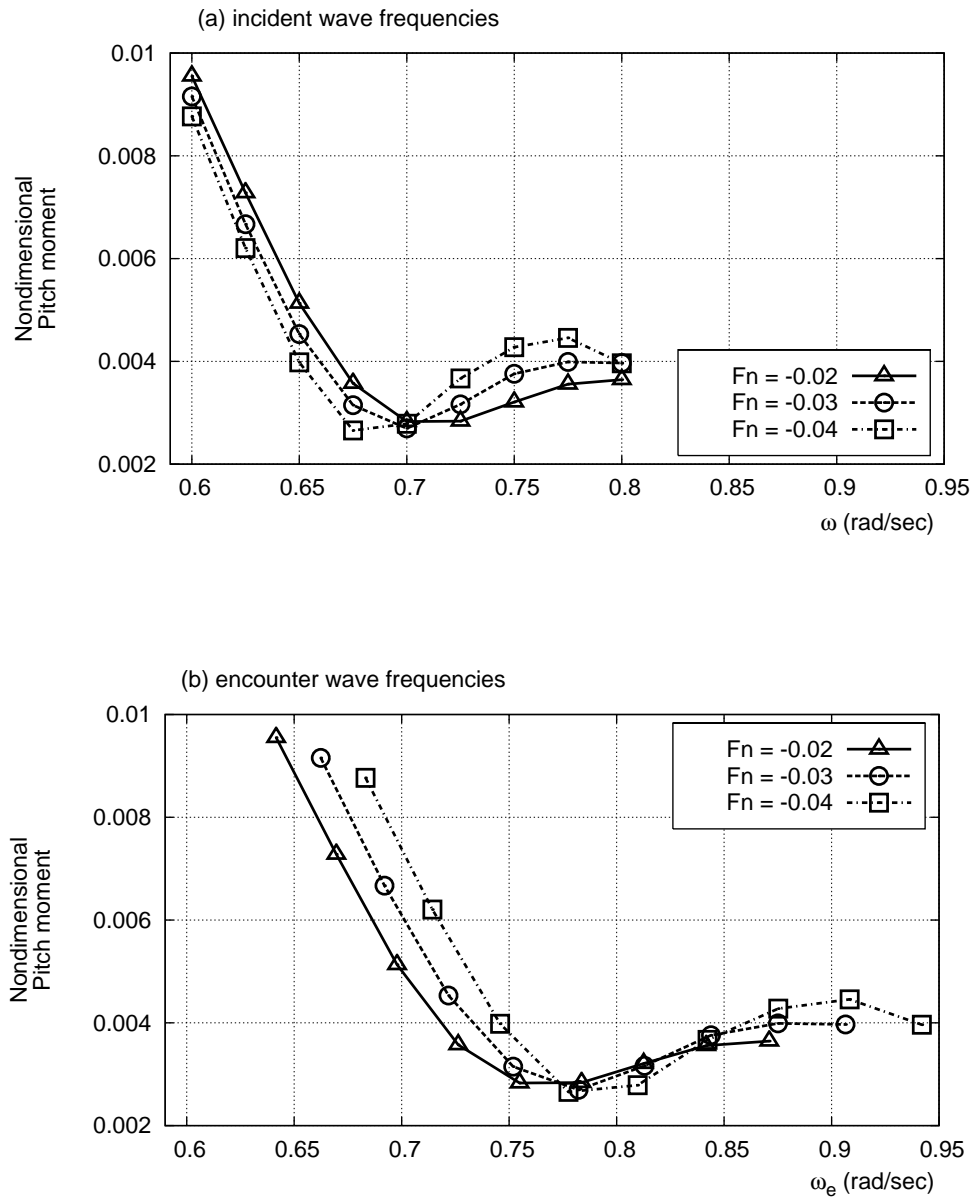


FIGURE F.99. Pitch moments for diffracted waves in various frequencies with following sea (collinear current) effect. Wave and current heading angles are 15 and -15 degrees respectively.

VITA**SANG-YUN BAE****Education**

B.S. (1996) Naval Architecture and Ocean Engineering, Inha University, Inchon, Korea

M.S. (1998) Naval Architecture and Ocean Engineering, Inha University, Inchon, Korea

Mailing Address

INTEC Engineering Partnership, Ltd. 15600 JFK Boulevard, 9th Floor, Houston, Texas, USA

Permanent Address

106-9 Kwangan1-dong Suyoung-ku, Pusan, Korea

The typist for this thesis was SANG-YUN BAE.